Universidad
del País Vasco

Euskal Herriko
Unibertsitatea

eman ta zabal zazu

ERRETAKO AZALEREN DETEKZIO AUTOMATIKOA BEREIZMEN ESPAZIAL ERTAINAREKIN ETA ESKUALDE- ETA MUNDU-MAILAN

DETECCIÓN AUTOMÁTICA DE ÁREAS QUEMADAS A MEDIA RESOLUCIÓN ESPACIAL Y A ESCALA REGIONAL Y GLOBAL

Ekhi Roteta Otaegik

aurkeztutako doktorego-tesia

Zuzendariak:

Aitor Bastarrika Izagirre – Meatze eta Metalurgia Ingeniaritza eta Materialen Zientzia Saila

Askoa Ibisate González de Matauco – Geografia, Historiaurrea eta Arkeologia Saila

Diziplinarteko Estrategia Zientifikoak Ondarean eta Paisaian Doktoregoa

Geografia, Historiaurrea eta Arkeologia Saila

Gasteizen, 2022ko urria

Esker-ematea

Tesiak neurri handi batean doktoregaiak eginiko lan pertsonalak izaten badira, ezinezkoa izango zen lan hau burutzea beste jende askoren laguntzarik gabe. Horrexegatik, nire esker ona erakutsi nahi nieke guztiei, inor ahaztuko ez dudalakoan.

Lehenik, ahaztu baino lehen, eskerrak eman nahi nizkioke Euskal Herriko Unibertsitateari, doktorego hau egin bitarteko denboran ikerketa diruz laguntzeagatik. Eta honekin batera, Geografia, Historiaurrea eta Arkeologia Sailari eta Diziplinarteko Estrategia Zientifikoak Ondarean eta Paisaian Doktorego-programari, hauek gabe ezin izango bainuen tesi hau egin.

Baina nire eskerrik beroenak doktorego honetan zuzendari izan ditudan Aitor Bastarrika eta Askoa Ibisate doktoreei eman nahi dizkiet, urte hauetan egindako gidaritza-lanagatik eta izandako pazientziagatik, artikuluen zuzenketekin igarotako orduengatik, eta orokorrean eskainitako denboragatik. Doktorego hau ezin izango zen burutu beraien laguntzarik gabe.

Unibertsitate honetatik irtenez, doktorego honen aurretik FireCCI proiektuarekin ikerketa-lanetan hastean ezagututako jendeari eta batik bat Alcalako lan-taldeari, beraietako askorekin lankidetzak oraintsu arte iraun baitu: Emilio Chuvieco eta M. Lucrecia Pettinari doktoreak, Rubén, Joshua, Gonzalo, etab.

Eta are urrunago joanez, Txileko Hémera ikerguneko kideak ere eskertu nahi nituzke, Patricia Oliva doktorea bereziki, bertan eginiko egonaldietan emandako laguntzagatik eta harrera onagatik, eta herrialde berri batean eroso sentitzea errazteagatik.

Nola ez, Gasteizko Ingeniaritza Eskolako Geomatika eta Topografia saileko kideei ere bai: Ortzi, Karmele, Ruper, Fran, Pili, Amaia (Leitzarango orduak tarteko), Leyre, ... Gasteizera bisitan joandako aldi bakoitzean inguruan izan ditudanak.

Eta azkenik, *last but not least*, etxekoei. Betidanik ondoan izan eta babesa eman didatelako, momentu txarrenetan batez ere.

Eskarrik asko danoi

Aurkibidea

Laburpena

Doktorego-tesi hau suteek erretako azalerak satelite-irudien bidez detektatzean datza, teledetekzio-teknikak erabiliz. Aurrez hainbat ikerketatan detektatu dituzte jada erretako azalerak, baina bereizmen espazial baxuko (250 m-ko pixelak edo handiagoak) irudiak erabili dira beti eta honek sute txikienak atzematea galarazten du; tesi honen berrikuntza nagusia Landsat eta Sentinel-2 sateliteek eskuratutako bereizmen ertaineko (10-30 m inguruko pixelak) irudiak erabiltzea da, hedadura txikiagoko erretako azalerak ere behatzea ahalbidetuz.

Erretako azalerak atzeman ahal izateko hainbat algoritmo automatiko sortu dira eskualde-, kontinente- eta mundu-mailan. Lehenengo biak espezifikoki Afrikako eta Txileko landaretza errea detektatzeko diseinatuta daude; azken algoritmoak, ordea, mundu osoko suteak atzeman ditzake, eskualde bakoitzeko ezaugarrietara egokituz. Gainera, erretako azalerak detektatzeko eta baliozkotzeko hainbat erreminta ere garatu dira, erabiltzaile baten gainbegiradapean betiere. Prozesu hauetako gehienak hodeian oinarritutako datu-prozesamendurako plataforma batean ezarri dira, azkarrago exekutatu ahal izateko.

Suteak bereizmen ertaineko irudiekin atzemateak duen garrantzia erakutsi dute emaitza guztiek, landaretza errea zehaztasun handiagoarekin aztertzea eta honi esker gizartearengan eta ingurugiroan dituzten efektuak hobekiago ezagutzea ahalbidetzen baitute; hain zuzen ere, erretako azalera osoaren zati bat bereizmen ertaineko irudiek bakarrik detektatzen dutela ikusi da, bereizmen baxuko irudiek atzeman ahal izateko sute txikiegiak izateagatik. Aurrerapen hauek hainbat aldizkari zientifikotan argitaratu dira artikulu moduan, beraz, artikuluen bilduma bidezko tesia da honako hau.

Resumen

La presente tesis doctoral trata de detectar áreas quemadas por incendios a partir de imágenes de satélite, empleando técnicas de teledetección. Las áreas quemadas ya han sido detectadas previamente en varios estudios, pero siempre partiendo de imágenes de baja resolución espacial (píxeles de al menos 250 m) y esto impide detectar los incendios más pequeños; la novedad de esta tesis es el uso de imágenes de media resolución (píxeles de 10-30 m) capturadas por los satélites Landsat y Sentinel-2, pudiendo así observar también áreas quemadas de menor extensión.

Se han creado varios algoritmos automáticos para la detección de áreas quemadas a escala regional, continental y global. Los primeros dos están diseñados específicamente para detectar la vegetación quemada en África y en Chile; sin embargo, el último algoritmo tiene el potencial de detectar incendios a través de todo el planeta, adaptándose a las características de cada región. Además, también se han desarrollado varias herramientas para la detección y validación de las áreas quemadas bajo la supervisión de un usuario. La mayoría de estos procesos han sido implementados en una plataforma de procesamiento de datos en la nube, para una ejecución más eficaz.

Todos los resultados han demostrado la necesidad de detectar incendios con imágenes de media resolución, ya que permiten analizar la vegetación quemada con mayor precisión y así estimar mejor sus efectos en la sociedad y en el medio ambiente; de hecho, se ha podido observar que parte de la superficie total quemada sólo es detectada con imágenes de media resolución, al tratarse de incendios demasiado pequeños para las imágenes de

baja resolución. Estos avances han sido publicados en varias revistas científicas, por lo que ésta es una tesis por compendio de artículos.

Abstract

The purpose of this doctoral thesis is detecting areas burned by fires from satellite images, by employing remote sensing techniques. Burned areas have already been detected previously by several studies, but from images at course spatial resolution (pixels at least 250 m wide and high), which prevents the detection of smallest fires; the novelty of this thesis is employing images at medium resolution (10–30 m) obtained by Landsat and Sentinel-2 satellites, thus allowing to observe smaller burned areas.

Several automatic algorithms were created to detect burned areas at a regional, continental and global scale. The first two are designed specifically for the detection of burned vegetation in Africa and Chile; however, the last one can detect fires through the whole planet, adapting itself to the characteristics in each region. Furthermore, some various tools were also designed with the aim of detecting and assessing burned areas under the supervision of a user. Most of these processes were implemented in a platform for data processing on the cloud, so that their execution is efficient.

All the results in this doctoral thesis have shown the need of images at medium resolution when detecting fires, since these allow analysing the burned vegetation with a greater accuracy and thus estimating better their effects on society and the environment; actually, it has been observed that part of the total burned surface is only detected by images at medium resolution, due to the presence of fires too small to be detected by images at course resolution. The achieved advances were published in several scientific journals, so this is a thesis by published papers.

1. Sarrera

Lurraren duela gutxiko historian ohiko gertakari naturalak izan dira suteak, baldintza klimatologiko eta meteorologikoekin erlazionatuta gehienbat, baina baita faktore geologiko eta astronomikoek eraginda ere. Ikatz-sedimentuen erregistroak analizatu zituen ikerketa baten arabera, suteak ez ziren orain bezain ohikoak Holozenoaren hasieran (orain dela 12.000 urte, azken glaziazioaren amaieran), baina ugaritu egin ziren glaziarrak urtu eta planetaren tenperatura igotzean (Marlon et al., 2013). Hainbat milurtekoren eskalan eta eremu boreal eta epeletan, landaretza gehien erretako garaiak bat datoz klima-aldaketekin eta tenperatura altu, prezipitazio urri eta hezetasun gutxiko aroekin; eremu tropikaletan, aldiz, suteek aurkako joera erakusten dute, landaretza gehiago erretzen baita tenperatura freskoago eta hezetasun gehiagoko garaietan (Daniau et al., 2013). Bi ikerketen arabera (Daniau et al., 2013; Marlon et al., 2013), ez dirudi gizakiak sua erabiltzeak eta nekazaritzaren zabaltzeak suteengan eragin handirik izan zutenik, gizakiak nekazaritzarako, deforestaziorako eta ehizatzeko sua erabili arren (Pyne, 1997).

Gaur egun, suteek eta landaretza erretzeak hainbat efektu negatibo dituzte ingurugiroan eta gizartean. Batetik, suak gas- eta aerosol-kantitate handiak igortzen ditu atmosferara landaretza erre heinean, klima-aldaketa areagotzen lagunduz; urtean batez beste $2,2 \cdot 10^{12}$ kg karbono aireratzen direla zenbatetsi dute (van der Werf et al., 2017). Suak igorritako gas hauek eta keak jendearen osasunean eta segurtasunean ere eragina dute (Goldammer et al., 2008; Reid et al., 2016; Roos et al., 2016). Sute katastrofikoenen kasuan, gainera, hainbat pertsona hiltzea eta inpaktu ekonomiko garrantzitsuak eragiten dituzte (Bowman et al., 2017).

Mundu-mailan, ez dirudi sute-kopurua eta erretako azalera osoa gorantz doazenik (Doerr eta Santín, 2016); izan ere, azken mende honetan suteak aurrekoetan baino urriagoak izan direla uste da, eta azken bi hamarkadetan erretako azalera osoaren murrizketa bat behatu da (Andela et al., 2017). Hala ere, gertatzen diren suteek larriagoak dirudite, gizartearengan duten eragina eta inpaktu ekonomikoak handiagoak dira, eta geroz eta maizago gertatzea espero da (Kramer, 2013; Stephens et al., 2013). Honako hauek dira azken urteetako sute larrienetako batzuk, doktorego-tesi hau landu bitartean gertatuak: Txileko 2017ko sute-denboraldia (National Geographic, 2018), Suediako 2018ko baso-suteak (The Local, 2018), Kanada mendebaldeko 2018 eta 2021ekoak (Lindsay, 2018; Kulkarni, 2021), Australiako 2019 eta 2020 arteko denboraldia (Bowman et al., 2020; Schweinsberg et al., 2020; Yu et al., 2020), edota Siberiako 2021eko suteak, beren kea Lurraren ipar polora lehen aldiz iritsi zelarik (Hayes, 2021). Sute hauek guztiak ezohiko bero- eta lehorte-boladen ondoren gertatu ziren. Izan ere, suteak larriagotzearen kausa nagusia klima-aldaketa da, honek dakartzan tenperatura-igoera eta prezipitazioak urritzearekin batera (Forkel et al., 2017; Parmesan et al., 2022). Aldi berean, suteek igorritako gasek eta aerosolek klima-aldaketa areagotzen dute (van der Werf et al., 2017), biek elkar eraginez.

Hau guztia dela eta, bereziki garrantzitsua da suteek kaltetutako azalerak, hau da, erretako azalerak (EA), behar adinako zehaztasunarekin detektatzea. Honek erretako landaretza-kantitatea eta atmosferara igorritako gasak zenbatestea, alde batetik, eta ingurugiroan, gizartearengan eta bere ondasunetan izandako kalteak balioztatzea, bestetik, ahalbidetzen ditu. EA detektatzeko metodorik zehatzena lekuan bertan neurtzea izango litzateke, baina honek duen kostua dela-eta urrunetik egiten da normalean (Mouillot et al., 2014; Chuvieco et al., 2019). EA detektatzeko modurik ohikoena teledetekzioa da, hau da, Lurraren inguruan orbitan dauden sateliteek modu sistematikoan eskuratzen dituzten irudiak aztertuz. Komunitate zientifikoak mundu-

mailako EA teledetekzio bidez detektatuz bi hamarkada badaramatza ere, bereizmen espazial baxuko (> 100 m) irudiak erabiltzen dira normalean, bereizmen ertaineko (10 – 100 m) irudiak globalki prozesatzeak dituen zailtasunak direla-eta. Honek tamaina guztietako suteak detektatu ahal izatea mugatzen du, eta txikienak alde batera uztea eta gutxiestea eragin (Randerson et al., 2012; Padilla et al., 2015; Boschetti et al., 2019).

Beraz, doktorego-tesi honen helburu nagusia EA bereizmen ertaineko irudien bidez detektatzea da. Honetarako hainbat algoritmo sortu dira, hasiera batean herrialde eta kontinente banatan, Txilen eta Afrikan, eta azkenik mundu-mailan EA detektatzeko algoritmo bat diseinatuz. Bereizmen ertaineko irudiekin lan egitean gorde eta prozesatu beharreko datu-kantitate handia dela-eta, tesi honetako lana datuak hodeian prozesatzeko plataforma batetara lekualdatu da pixkanaka, ikerketa aurre joan ahala, egin beharreko prozesuak asko erraztuz.

2. Marco teórico

En este apartado se detalla el marco teórico necesario para la comprensión de esta tesis doctoral, especialmente los principios fundamentales de la teledetección y del proceso de la detección de áreas quemadas. También se describen algunas herramientas metodológicas utilizadas en varias publicaciones, tales como la validación de productos y la plataforma Google Earth Engine.

2.1. Teledetección

La teledetección (en inglés *remote sensing*, "percepción remota") es una técnica que consiste en observar, detectar y analizar fenómenos naturales sobre la superficie terrestre a partir de imágenes digitales, normalmente adquiridas por sensores a bordo de satélites espaciales (Chuvieco, 2008). Para ello, las imágenes digitales suelen estar formadas por varias bandas espectrales, cada una representando la cantidad de luz o energía electromagnética recibida por el sensor en las longitudes de onda correspondientes; de este modo, se pueden diferenciar distintos objetos dependiendo de la absorción selectiva de las diferentes cubiertas en distintas bandas espectrales.

Principios físicos

Para comprender el correcto funcionamiento de la teledetección, primero hace falta conocer ciertos principios físicos. El espectro electromagnético se divide en varias regiones o dominios, según la longitud de onda de la energía electromagnética analizada. Entre estos dominios, son especialmente dos los que resultan importantes en teledetección y para esta tesis:

- Dominio óptico (longitudes de onda entre $0{,}4-2{,}5$ µm). Las bandas espectrales del dominio óptico pueden a su vez ser divididas en tres grupos:
    - Espectro o luz visible, que corresponde a las ondas de longitudes que nuestros ojos pueden percibir ($0{,}4-0{,}7$ µm).
    - Infrarrojo cercano o NIR (del inglés *Near Infrared*), entre $0{,}7-1{,}2$ µm.
    - Infrarrojo medio o MIR (del inglés *Middle Infrared*), con longitudes de onda entre $1{,}2-8$ µm. Dentro de esta parte del espectro, cabe destacar el infrarrojo de onda corta o SWIR (*Short Wave Infrared*), entre $1{,}2-2{,}5$ µm de longitud de onda.
- Dominio del infrarrojo térmico o TIR (del inglés *Thermal Infrared*) (longitudes de onda entre $8-14$ µm).

La diferencia principal entre bandas de estos dos dominios del espectro es el origen de la energía recibida por el sensor y por lo tanto la magnitud que se puede medir con ella. Según la ley de Planck, cualquier cuerpo de temperatura superior a 0 K emite radiación electromagnética, cuya intensidad depende de la temperatura de dicho cuerpo, y de la longitud de onda a la que se emite. El Sol, con una temperatura promedio de 6.000 K en su superficie, tiene su máxima emitancia en las longitudes de onda de la luz visible, mientras que la superficie terrestre, a 15°C (288 K) de promedio, emite más energía en el infrarrojo térmico (Figura 1).
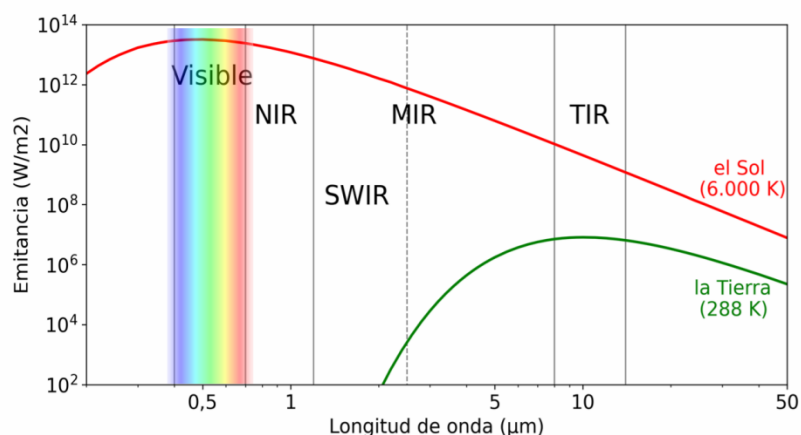
Figura 1. Emitancia del Sol y de la Tierra según la ley de Planck y los principales dominios del espectro, dependiendo de la longitud de onda. Ambos ejes tienen una escala logarítmica.

Así, el dominio óptico, entre los 0,4 – 2,5 μm (excluyendo las longitudes de onda del MIR que no forman parte del SWIR), cubre la parte del espectro donde el Sol emite energía con mayor intensidad, por lo que prácticamente toda la energía recogida por el sensor en estas longitudes de onda ha sido emitida por el Sol y reflejada en la superficie terrestre. Dado que se conoce la emitancia del Sol en cada longitud de onda, y el sensor registra en cada banda espectral la energía recibida desde cada objeto de la superficie en las longitudes de onda correspondientes a la banda, se calcula una variable física denominada reflectividad, es decir, la proporción de la energía reflejada en relación a la energía total recibida. La reflectividad de cada objeto varía según la longitud de onda, y por tanto esta información selectiva en diferentes bandas espectrales permite analizar, clasificar y detectar distintos fenómenos naturales.

En cambio, según la ley de Planck, el dominio del infrarrojo térmico agrupa las longitudes de onda donde la superficie terrestre, a una temperatura promedio de 15ºC o 288 K, emite energía electromagnética a mayor intensidad. Este hecho lo convierte en la mejor región del espectro electromagnético para detectar cambios de temperatura en la superficie, en función de la energía recibida en estas longitudes de onda. Por lo tanto, del mismo modo en que las bandas espectrales del dominio óptico se usan para calcular la reflectividad de los objetos representados en la imagen digital, las bandas térmicas se usan para estimar sus temperaturas.

Signaturas espectrales

Tal y como se ha mencionado en los párrafos anteriores, cada objeto responde de una forma específica ante la energía electromagnética recibida, ya que la proporción de energía reflejada por un objeto, o su reflectividad, depende de la longitud de onda de la energía y del tipo de objeto. Así, cada objeto tiene una signatura espectral, es decir, una curva que indica la reflectividad de ese objeto dependiendo de la longitud de onda de la energía electromagnética recibida. Conocer y diferenciar las signaturas espectrales de la vegetación antes y después de quemarse es crucial para poder detectar áreas quemadas (AQ).

Las firmas espectrales de la vegetación antes y después de un incendio están representadas en la Figura 2. En las longitudes de onda de la luz visible, la vegetación suele tener su máxima reflectividad en el centro, en el color verde, aunque sin llegar a valores altos; al quemarse, sin embargo, la reflectividad baja por debajo del 0,1 en todas las longitudes de esta región (Pereira et al., 1999). Las reflectividades más altas de la

vegetación sana se dan en el NIR donde, después de una subida repentina en la frontera con la luz visible, se mantiene bastante constante; al quemarse, en cambio, pierde gran parte de su reflectividad. Y por último, las reflectividades en el SWIR se encuentran invertidos con respecto al NIR, ya que la vegetación quemada refleja más energía que la no quemada. La información más valiosa para detectar AQ suelen ser las regiones espectrales del NIR y SWIR.
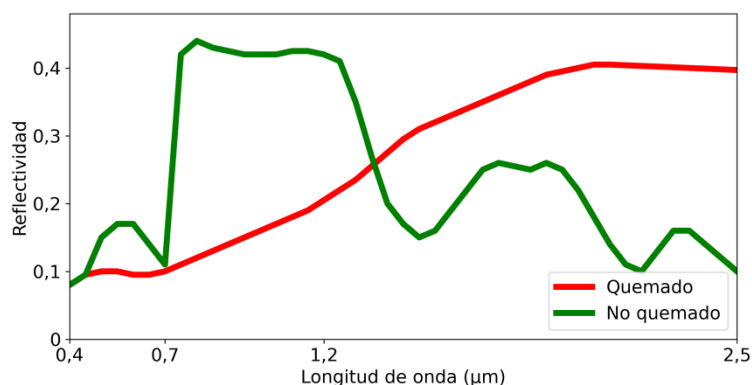
Figura 2. Signaturas espectrales de la vegetación quemada y no quemada en el dominio óptico del espectro. Las longitudes de onda señaladas marcan las fronteras entre la luz visible, el NIR y el SWIR.

Un problema común en la identificación de AQ suele ser la presencia de otros fenómenos que tienen una signatura espectral similar a las AQ, tales como bordes de nubes y sombras. Una confusión habitual en la literatura consultada es la de los campos de cultivo, ya que el cambio espectral que sufren estas cubiertas al recoger la cosecha es muy similar al de la vegetación quemada, y es un problema muy recurrente en muchos estudios (Goodwin y Collett, 2014; Vanderhoof et al., 2017; Giglio et al., 2018; Long et al., 2019; Hawbaker et al., 2020; van Dijk et al., 2021).

Satélites y sus imágenes

Las imágenes digitales que se usan en teledetección suelen ser capturadas por sensores instalados en satélites que orbitan alrededor de la Tierra. Hay dos tipos de sensores: activos y pasivos. Los sensores activos emiten la energía electromagnética que una vez reflejada por los objetos de la superficie terrestre retorna al propio sensor, registrando datos como su intensidad, la fase de la onda electromagnética y su polarización; a partir de estos datos, se pueden calcular variables como la rugosidad, la geometría y la altitud del terreno. Los sistemas activos funcionan con microondas con longitudes de onda que varían entre 1 mm y 1 m, lo que permite atravesar las nubes y así no depender de las condiciones meteorológicas para observar la superficie de la Tierra. Aunque hay trabajos recientes que utilizan sensores activos para la detección de AQ (Ban et al., 2020; Belenguer-Plomer et al., 2019, 2021), la literatura existente con sensores pasivos es mucho más frecuente (Roy et al., 2008; Giglio et al., 2009; Alonso-Canas y Chuvieco, 2015; Long et al., 2019; Hawbaker et al., 2020; Lizundia-Loiola et al., 2020). Éstos no emiten ningún tipo de energía, sino que sólo reciben y registran la energía electromagnética proveniente de la superficie de la Tierra, en bandas concentradas en dos dominios del espectro electromagnético: el óptico y el infrarrojo térmico. Por lo tanto, las magnitudes que se miden con los sensores pasivos son la reflectividad y la temperatura.

En la actualidad hay muchos satélites orbitando alrededor del planeta con sensores diseñados para la observación de la Tierra. Cada uno tiene sus propias características dependiendo del objetivo particular para el que se ha diseñado, pero se pueden distinguir

3 tipos de resoluciones a la hora de hablar de las imágenes digitales capturadas por estos sensores:

- Resolución espacial: consiste en el tamaño de cada píxel de la imagen digital, si ésta es proyectada sobre la superficie terrestre. Varía desde alrededor de 1 km, hasta la orden de unos pocos metros, y depende en gran medida de la altitud a la que orbita el satélite alrededor del planeta: a menor altitud, mayor resolución y mayor detalle en la imagen.
- Resolución espectral: se refiere a la cantidad de bandas espectrales que registra el sensor, y la posición de cada una de esas bandas en el espectro electromagnético (el rango de longitudes de onda que cubre).
- Resolución temporal: la frecuencia con la que el sensor adquiere una imagen de la misma región. Normalmente la resolución temporal hace referencia a la frecuencia medida sobre el Ecuador, ya que el satélite cubre las regiones de latitudes altas con mayor frecuencia.

De entre todos los tipos de sensores disponibles, son tres los que más se usan para la detección de AQ: MODIS (Moderate Resolution Imaging Spectroradiometer), los distintos sensores de los satélites Landsat (TM, ETM+ y OLI), y el sensor MSI (Multispectral Instrument) de Sentinel-2 (S2). Todos ellos tienen en común las siguientes bandas espectrales: una banda por cada color primario del espectro visible (azul, verde y rojo), una banda en el infrarrojo cercano (NIR), y dos bandas en el infrarrojo de onda corta (SWIR). Combinando los valores de reflectividad de cada objeto en estas seis bandas se obtiene su signatura espectral (Figura 3). El análisis de las signaturas espectrales de las cubiertas de vegetación sana y afectada por el incendio permiten deducir el cambio esperable de la vegetación al quemarse, ya que su reflectividad en el infrarrojo cercano (NIR, banda 8 de las imágenes MSI de Sentinel-2) disminuye drásticamente, por ejemplo.
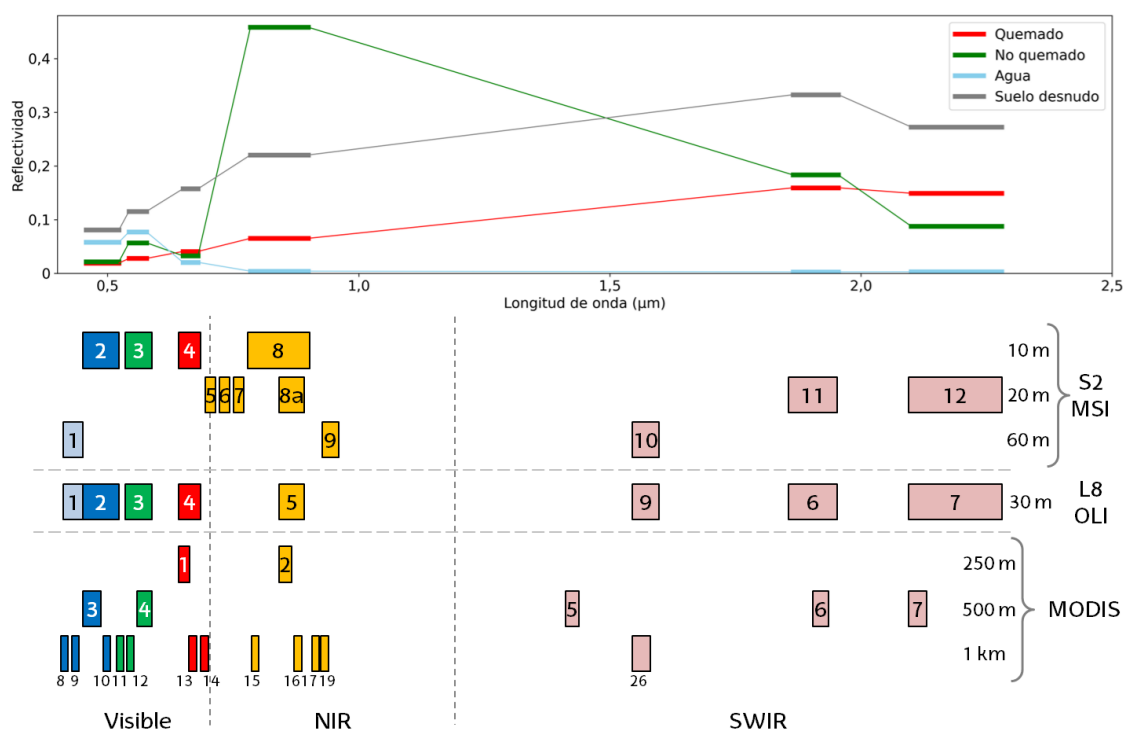
Figura 3. Signaturas espectrales de cuatro coberturas (vegetación quemada, vegetación no quemada, agua y suelo) según las seis bandas principales del sensor MSI (Sentinel-2); la distribución de las bandas de los sensores MSI, OLI (Landsat-8) y MODIS en el dominio óptico del espectro; y sus resoluciones espaciales.

De entre los 3 grupos de sensores mencionados, el sensor MODIS fue el primero en ser usado sistemáticamente para detectar AQ. Este sensor está instalado en los satélites Terra y Aqua de la Administración Nacional de Aeronáutica y el Espacio o NASA (del inglés *National Aeronautics and Space Administration*), que orbitan la Tierra a una altura de 700 km desde el principio del siglo XXI. Adquiere imágenes diarias de todo el planeta, con una baja resolución espacial de 250 m, 500 m o 1 km, dependiendo de la banda espectral; todas las bandas principales necesarias para la detección de AQ tienen 250 o 500 m de resolución (Figura 3).

La misión Landsat es anterior al sensor MODIS (comenzó en 1972), desarrollado también por la NASA junto con el USGS (*United States Geological Survey*), y consta de un total de 9 satélites, la mayoría de ellos ya fuera de servicio (USGS, s.f.); la altitud de la órbita es de alrededor de 700 km. La misión ha ido avanzando poco a poco y los sensores de los satélites más recientes son más completos aun manteniendo las características iniciales para estudios históricos: todos cubren cualquier parte del mundo cada 16 días a una resolución espacial media de 30 m (mejor resolución espacial que MODIS, con 250-1.000 m según la banda); la frecuencia aumenta a una imagen cada 8 días cuando hay dos satélites operativos. Los primeros tres satélites tenían a bordo el sensor MSS (Landsat-1, -2 y -3) que no tenía ninguna banda espectral en la región SWIR del espectro, lo que no los hace muy útiles para la detección de AQ. A partir del cuarto satélite, sin embargo, todos los sensores tienen bandas en los tres colores del espectro visible (azul, verde y rojo), una banda en el NIR, y dos en el SWIR (Figura 3). Los satélites Landsat-4, Landsat-5 y Landsat-7 completaron su ciclo de vida y ahora están fuera de servicio, el Landsat-6 sufrió un fallo técnico antes de alcanzar su órbita, pero el satélite Landsat-8 está todavía operativo en el momento de escribir este texto; recientemente se ha lanzado un noveno satélite (Landsat-9), con el mismo sensor OLI que el Landsat-8 (Tabla 1). En un principio las imágenes Landsat eran de uso comercial, pero el archivo histórico completo se abrió a la comunidad en 2008 de manera gratuita y pública, lo que facilita el empleo de estas imágenes en la realización de estudios que cubren regiones más extensas.

Satélite	Fecha de inicio	Fecha de finalización	Sensor
Landsat-4	Julio 1982	Diciembre 1993	Thematic Mapper (TM)
Landsat-5	Marzo 1984	Junio 2013	
Landsat-7	Abril 1999	Abril 2022	Enhanced Thematic Mapper Plus (ETM+)
Landsat-8	Febrero 2013	-	Operational Land Imager (OLI)
Landsat-9	Septiembre 2021	-	
Sentinel-2A (S2A)	Junio 2015	-	Multispectral Instrument (MSI)
Sentinel-2B (S2B)	Marzo 2017	-	

Tabla 1. Sensores habituales de media resolución espacial en AQ: misiones Landsat, a partir del Landsat-4, y Sentinel-2, con sus periodos operativos y los sensores a bordo.

La Agencia Espacial Europea o ESA (del inglés *European Space Agency*) ha desarrollado en la última década una misión para la observación de la Tierra dentro de su ambicioso programa Copernicus, similar a la misión estadounidense Landsat y denominada Sentinel-

2 (ESA, s.f.). Dicha misión consta de dos satélites, Sentinel-2A (S2A) y Sentinel-2B (S2B), lanzados en junio de 2015 y marzo de 2017 respectivamente (Tabla 1), a una órbita promedio de 780 km de altitud, y obtienen una imagen de la misma región cada 10 días, disminuyendo a 5 días a partir de marzo de 2017 al entrar en funcionamiento el segundo de los satélites. Ambos satélites llevan a bordo el sensor MSI, similar a los sensores de los satélites Landsat, pero con un mayor número de bandas espectrales y con mayor resolución espacial (10, 20 o 60 m dependiendo de la banda) (Figura 3).

Además de las bandas originales adquiridas por los sensores, resultan muy útiles los índices espectrales, es decir, nuevas bandas calculadas a partir de operaciones aritméticas entre las bandas originales diseñadas para resaltar alguna característica. Hay varios tipos de índices, y muchos de ellos consisten en diferencias normalizadas entre dos bandas, como el NDVI (*Normalized Difference Vegetation Index*), un índice que describe la vigorosidad de la vegetación (Rouse et al., 1973) y es ampliamente utilizado en estudios a partir de imágenes de teledetección. En esta tesis doctoral se han usado profusamente tres índices específicos para la detección de AQ: el NBR (*Normalized Burn Ratio*), también llamado NDII (*Normalized Difference Infrared Index*) (Key y Benson, 2003); NBR2 (*Normalized Burn Ratio 2*) (García y Caselles, 1991); y MIRBI (*Mid-Infrared Burned Index*) (Trigg y Flasse, 2001). La Figura 4 ilustra la mejora de estos índices a la hora de discriminar las áreas quemadas (e-d), ya que resultan más fáciles de identificar mediante los índices que con las bandas originales (b-d) o incluso la composición de color (a). En una de las publicaciones aportadas en esta tesis doctoral también se ha usado el índice RdNBR (del inglés *relative delta NBR*), que consiste en la relativa diferencia temporal del índice NBR (Miller y Thode, 2007).
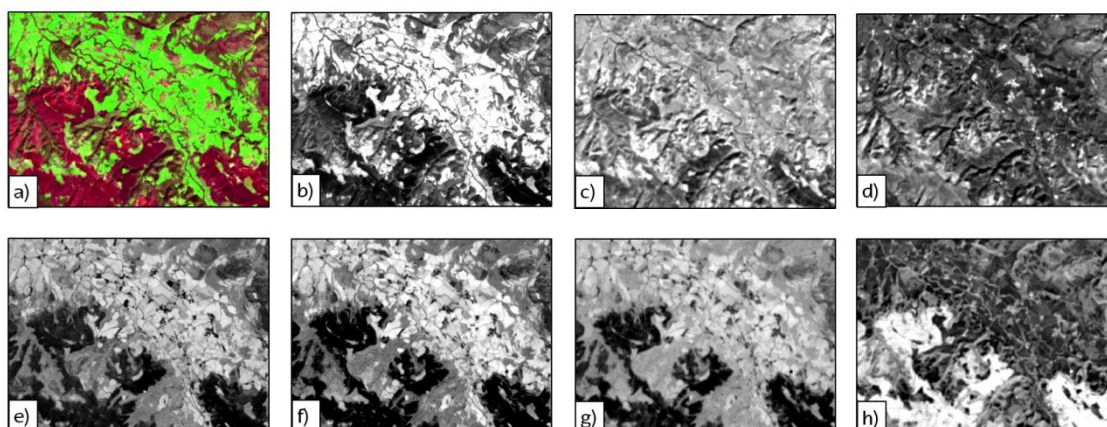
Figura 4. Representaciones de bandas de reflectividad e índices espectrales a partir de una imagen del sensor MSI (Sentinel-2) adquirida el 28 de febrero del 2019, en una zona de muestra ubicada en la tesela 30TXN, en el sur de Francia: a) composición en falso color SWIR-NIR-Rojo, con las AQ en color granate; b) banda 8 o NIR; c) banda 11 o SWIR corto; d) banda 12 o SWIR largo; e) índice espectral NDVI; f) índice NBR; g) índice NBR2; y h) índice MIRBI.

2.2. Antecedentes en la detección de áreas quemadas

Los primeros productos globales de AQ mediante teledetección fueron desarrollados en la primera década del siglo XXI, todos ellos a partir de imágenes de satélite de muy baja resolución espacial (> 1.000 m). Los primeros fueron GBA2000 (Tansey et al., 2004) y GLOBSCAR (Simon et al., 2004), derivados de las imágenes de los sensores SPOT-Vegetation y ATSR-2 respectivamente, ambos con una resolución espacial de 1 km. Más tarde se crearon dos productos a partir de imágenes MODIS, MCD45A1 (Roy et al., 2005) y

MCD64A1 (Giglio et al., 2009), ambos a 500 m de resolución. Los dos productos han sido mejorados en varias versiones, siendo hoy en día la colección 6 del producto MCD64A1 (MCD64A1c6) (Giglio et al., 2018) el producto estándar de AQ de la NASA. La Agencia Espacial Europea también ha desarrollado varios productos globales de baja resolución en los últimos años (antes y durante el desarrollo de esta tesis) dentro del proyecto Fire_CCI, cuyos objetivos son la detección de AQ, la estimación de los gases invernadero durante los incendios y su impacto en el cambio climático (https://climate.esa.int/en/projects/fire/, visitado por última vez en marzo de 2022). El primero de estos productos fue FireCCI41 (Alonso-Canas y Chuvieco, 2015), basado en imágenes MERIS a 300 m de resolución, y el segundo es FireCCI51 (Lizundia-Loiola et al., 2020), usando sólo las bandas 1 y 2 de las imágenes MODIS, ambas a 250 m de resolución (Figura 3); el algoritmo de este último producto también ha sido adaptado a las imágenes del sensor OLCI de los satélites Sentinel-3, creando así el producto C3SBA10 (Lizundia-Loiola et al., 2021). FireCCI51 es en la actualidad el producto global de AQ de baja resolución más preciso creado por la ESA (Padilla et al., 2018; Franquesa et al., 2022a). Tanto MCD61A1 como FireCCI51, generados a partir de imágenes MODIS aunque a distintas resoluciones, cubren el periodo desde el 2001 hasta la actualidad, siendo así conocidas las áreas que se han quemado en todo el planeta casi desde que empezó el siglo XXI con una precisión de 500 o 250 m, dependiendo del producto. Ambos son productos mensuales, es decir, constan de una imagen por cada mes donde se indica para cada píxel el día del mes de la quema si ésta se ha producido y el nivel de confianza de dicha detección.

Sin embargo, la baja resolución de estos productos globales de AQ implica que no se puedan detectar las áreas quemadas por los incendios más pequeños, ya que éstos no llegan a alterar la señal suficientemente para ser detectados en un único pixel. Se han realizado varios procesos de validación global de los productos mencionados de baja resolución (Padilla et al., 2015; Boschetti et al., 2019; Lizundia-Loiola et al., 2020; Franquesa et al., 2022a) que indican una omisión que varía entre 55-70%, es decir, omiten más de la mitad de las áreas realmente quemadas. En cuanto a los errores de comisión (áreas detectadas como quemadas que en realidad no lo están), esta proporción es menor y se sitúa entre 25–40%. Otro estudio de interés intentó estimar las AQ subestimadas por los productos de baja resolución analizando anomalías térmicas (Randerson et al., 2012). El resultado fue que las AQ globales aumentarían en un 35% si se detectaran los incendios pequeños con suficiente precisión, aunque este aumento podía estar por encima del 50% en la mayoría de las regiones, o incluso más de un 100% en regiones como Asia ecuatorial, Centroamérica o Europa, donde se estimó que la mayoría de las AQ correspondían a incendios pequeños no detectados por los productos de baja resolución. En esta línea, la comunidad científica está de acuerdo en la necesidad de productos de área quemada de media resolución espacial que puedan generar productos que integren los incendios de menor tamaño.

Los primeros estudios de detección de AQ a media resolución espacial (10 – 100 m) estaban basados en imágenes Landsat. Estos trabajos eran locales y a menudo estaban limitados a una o unas pocas escenas Landsat (185 x 180 km^2) (Chuvieco y Congalton, 1988; Jakubauskas et al., 1990; García y Caselles, 1991; White et al., 1996; García-Haro et al., 2001; Paganini et al., 2003; Hudak y Brockett, 2004; Koutsias et al., 2009). Sin embargo, en la década del 2010, una vez las imágenes Landsat se hicieron públicas, se desarrollaron varios estudios con el objetivo de detectar AQ sistemáticamente sobre largas series de datos y en áreas de estudio más extensos. Entre estos tenemos algoritmos aplicados regionalmente en la provincia australiana de Queensland (Goodwin y Collett, 2014), en Burkina Faso (Liu et al., 2018), o el producto BAECV en los Estados Unidos (Hawbaker et al., 2017, 2020); también cabe destacar un algoritmo regional que fusiona datos Landsat con

MODIS, también aplicado a los EEUU (Boschetti et al., 2015). Después del lanzamiento del primer satélite Sentinel-2 en 2015, se han llevado varios trabajos de detección de AQ regionales que se basan en estas imágenes aplicados en Italia (Filipponi, 2019), India (Bar et al., 2020), Australia (Gibson et al., 2020) o la Península Ibérica (Llorens et al., 2021), o que combinan imágenes S2 y Landsat (Roy et al., 2019). Aun así, todos estos estudios fueron desarrollados a escala regional, y sólo existe un producto global de AQ de media resolución hasta la fecha. El producto GABAM (*Global Annual Burned-Area Map*) consta de mapas anuales de AQ generados a partir de imágenes Landsat, a 30 m de resolución espacial (Long et al., 2019); inicialmente producido sólo para el año 2015, aunque en años posteriores han incluido toda la serie histórica entre los años 1985 y 2019 (Wei et al., 2021) (https://vapd.gitlab.io/post/gabam/, visitado por última vez en marzo de 2022). A pesar de ser el primer producto global de esta resolución, este producto indica únicamente si un píxel se ha quemado o no, sin detallar la fecha de la detección ni el nivel de confianza en el que se produce. Además, al disponer de una única banda, tampoco permite conocer si un píxel se ha quemado más de una vez en el mismo año.

2.3. Validación de productos de áreas quemadas

Según el CEOS-LPSV (del inglés *Committee on Earth Observing Satellites' Land Product Validation Subgroup*), la validación es el proceso que evalúa la precisión de un producto por medios independientes (Justice et al., 2000). Este comité definió cuatro escenarios de validación dependiendo de la precisión que se requiera, siendo el primero el más permisivo y el cuarto el más estricto donde se valida el producto constantemente siempre que este sufra alguna modificación. De entre estos, el tercer escenario es el que más se usa para validar productos de AQ (Padilla et al., 2014b, 2015; Vanderhoof et al., 2017; Boschetti et al., 2019; Lizundia-Loiola et al., 2020), y consiste en la evaluación en diferentes regiones geográficas seleccionadas de una forma estadísticamente robusta (NASA, s.f.). El producto se valida en varias áreas de validación normalmente seleccionadas con un muestreo estratificado aleatorio (Padilla et al., 2014b, 2015; Boschetti et al., 2016; Padilla et al., 2017), donde los estratos son el ecosistema predominante y la presencia de una baja o alta actividad de incendios. En cada una de estas áreas de validación se crean *perímetros o datos de referencia* a partir de imágenes independientes y de mayor resolución espacial que el producto a validar, normalmente entre cada par de imágenes consecutivas de una serie temporal.

Una vez se tienen los datos de referencia, la validación se realiza mediante una tabulación cruzada entre los datos de referencia y el producto de AQ (Congalton y Green, 2008), con lo que se obtiene una matriz de error (Tabla 2); las celdas de esta tabla indican el área que se encuentra en el cruce entre sus dos categorías correspondientes. A partir de esta tabla se pueden calcular varias métricas, entre las cuales las más conocidas y empleadas son el error de comisión (CE)

$$CE = \frac{E_{12}}{E_{1+}}$$ (1)

y el error omisión (OE)

$$OE = \frac{E_{21}}{E_{+1}}$$ (2)

además de otras como el coeficiente Dice (DC) (Dice, 1945; Fleiss, 1981; Padilla et al., 2017)

$$DC = \frac{2 \cdot E_{11}}{E_{+1} + E_{1+}}$$ (3)

y el sesgo relativo (relB, del inglés *relative bias*) (Padilla et al., 2014a, 2015, 2017)

$$relB = \frac{E_{12} - E_{21}}{E_{+1}}$$

(4)

		Referencia		
		Quemado	No quemado	
Producto	Quemado	E_{11}	E_{12}	E_{1+}
	No quemado	E_{21}	E_{22}	E_{2+}
		E_{+1}	E_{+2}	

Tabla 2. Matriz de error resultante de la tabulación cruzada. Los valores E_{1+}, E_{2+}, E_{+1} y E_{+2} son la suma de la fila/columna correspondiente.

La Figura 5 presenta como ejemplo el proceso de validación del producto MCD64A1 en una zona de muestra. Tanto la composición de color como los perímetros de referencia tienen una resolución espacial de 10 m, frente a los 500 m del producto de baja resolución, por lo que los errores del producto se ven con facilidad en la Figura 5d; las áreas blancas y grises (correspondientes a las categoría no quemada y quemada, respectivamente) fueron correctamente clasificadas en MCD64A1. En este caso, el error de omisión es del 19%, y el de comisión de un 16%.
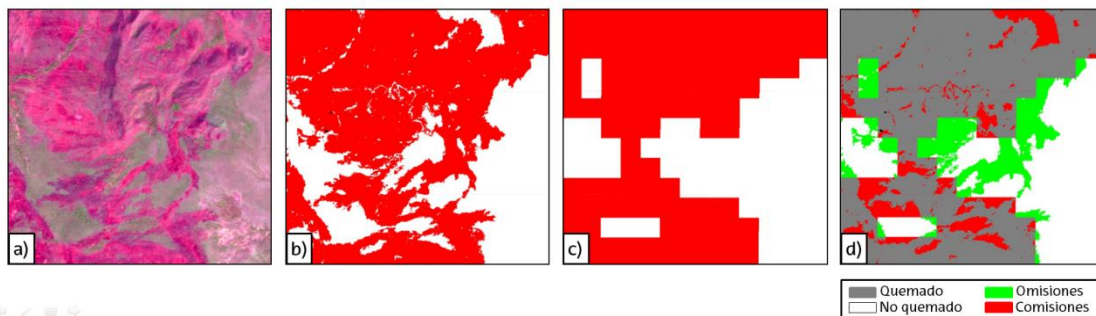
Figura 5. Ejemplo del proceso de la validación en una zona de ejemplo, en el norte de Benín: a) composición en falso color de las AQ al final del periodo de validación; b) perímetros de referencia a 10 m de resolución, generados a partir de imágenes S2; c) AQ según el producto MCD64A1, a 500 m de resolución; y d) cruce entre producto/referencia y errores resultantes.

2.4. Google Earth Engine

Google Earth Engine (GEE) es una plataforma en la nube desarrollada por Google que incluye varios catálogos de imágenes de satélite y proporciona una capacidad de geoanálisis a escala planetaria (Gorelick et al., 2017) (https://earthengine.google.com/, visitado por última vez en marzo de 2022). Debido a que está basado en la nube y a sus altas capacidades de procesamiento de datos, permite realizar análisis en un amplio conjunto de aplicaciones como deforestación, sequía, incendios, monitorización del clima, etc. Aunque el usuario tiene la opción de subir sus propios datos para operar con ellos, la plataforma incorpora varios tipos de datos como imágenes de distintos satélites (especialmente MODIS, Landsat y Sentinel), datos climatológicos, modelos digitales del terreno, usos del suelo y cartografía como fronteras internacionales y divisiones de países. Los resultados pueden ser visualizados en la interfaz de la plataforma, o exportados a la cuenta personal del usuario en Google Drive o Cloud Storage. Así GEE permite evitar la

descarga, el almacenamiento y el procesamiento de datos que conlleva trabajar con grandes series de imágenes para abarcar trabajos a escala regional, continental o global.

El primer estudio realizado en GEE fue publicado hace casi una década (Hansen et al., 2013) pero, aunque desde entonces se haya usado la plataforma en varios trabajos (Wang et al., 2020), ha habido pocas contadas en el campo de los incendios y las áreas quemadas. Casi todos estos estudios son de nivel regional (Soulard et al., 2016; Verheggen et al., 2016; Petrakis et al., 2018; Crowley et al., 2019; Daldegan et al., 2019; Gaveau et al., 2021; Seydi et al., 2021), y sólo uno se aplica a escala global, el producto GABAM anteriormente mencionado (Long et al., 2019).

3. Helburuak

Tesi honen helburu nagusia bereizmen ertaineko (10 – 30 m) satelite-irudien bidez EA detektatzeko algoritmo eta prozesuak garatzea da. Aurrekariei buruzko 2.2. atalean azaldu bezalaxe, orain arte existitzen diren EAen produktu globalak bereizmen baxukoak dira, eta sute txikienak ez dituzte behar bezala detektatzen; produktu hauek, duten bereizmena dela-eta, detektatzen ez duten azalera mundu-mailan urtero erretzen denaren %26 izan litekeela zenbatetsi da (Randerson et al., 2012). Beraz, sute txikiagoak ere barne hartuko dituzten bereizmen ertaineko EAen produktuen hutsunea betetzen saiatzen da doktorego-tesi hau. Honetarako hainbat algoritmo diseinatu dira, edonorentzat eskuragarri dauden Landsat eta Sentinel-2 sateliteen irudiak erabiliz, 10-30 m arteko bereizmen espazialarekin. Algoritmo hauek erabat automatikoak izan behar dute eskualde- edo mundu-mailan modu sistematikoan exekutatu ahal izateko, erabiltzaileak parte hartu beharrik gabe, bereizmen baxuko produktuak sortzen dituztenean bezalaxe. Algoritmoak EA edozein ekosistema eta lurzoru-motatan detektatzeko gai izan beharko du beraz, beste objektu batzuk (lainoen itzalak edota nekazal-soroak) EA bezala sailkatu gabe.

Algoritmo automatikoak diseinatzeaz gain, doktorego-tesi honen bigarren helburua komunitate zientifikoari hainbat erreminta eskuragarri jartzea da, zehaztasun handiko EAen kartografia sortu ahal izateko eta EAen baliozkotzea eta beharrezko neurri eta erroreak kalkulatzea errazteko. Erreminta hauek erabiltzaileak parte har dezan eskatzen dute, aurreko algoritmoek ez bezala, baina trukean EA zehatzagoak lortzen dituzte erabiltzailearen erabateko gainbegiratzeari esker.

Azkenik, tesi hau landu ahala, hodeian oinarritutako plataformetan lan egitearen garrantzia nabarmenduz joan da, Google Earth Engine bereziki. Plataforma honek aurrez sisteman kargatuta dauden satelite-irudien bildumak azkar atzitzea ahalbidetzen du, eta datuak prozesatzeko duen ahalmenak errendimendu handiko sistema informatiko lokal baten beharra ekiditen du. Plataforma honetan ezarritako aplikazioak komunitate zientifikoari zabaltzea errazagoa ere bada, ez baitu liburutegi espezifiko edo espezializaturik eskatzen.

Arlo hauetan aurrerapausoak egin ahala, hainbat artikulu argitaratu dira zientzia-aldizkarietan, egindako lana komunitate zientifikoari jakinarazi eta ezagutarazteko; beraz, artikuluen bilduma bidezko doktorego-tesia da honako hau. Lau artikulu garatu dira guztira, eta honako hauek izan dira bakoitzaren helburuak:

- Lehen artikulua (A1) – Afrikako EA: Sentinel-2 irudien bidez eta 20 m-ko bereizmen espazialarekin, kontinente-mailako algoritmo bat garatzea Afrikan, bereizmen baxuko produktuek detektatu ezin dituzten EA zehaztasunez aztertzeko, bertan baitago munduan erretako azaleraren %70a. Hau da datuak hodeian prozesatzeko plataforma bat erabiltzen ez duen artikulu bakarra.

- Bigarren artikulua (A2) – BAMT errremintak: EAen produktuak sortzeko eta baliozkotzeko errremintak lantzea, GEE plataforman inplementatuta. Horrela, dagoeneko existitzen diren metodologien erabilera komunitate zientifikoari erraztea da helburua, EAen kartografia sortzeko nahiz baliozkotzeko.

- Hirugarren artikulua (A3) – Txileko EA: algoritmo automatiko bat GEEn inplementatzeko lehen saiakera, Txilen Sentinel-2 irudien bidez, 20 m-ko bereizmen espazialarekin.

- Laugarren artikulua (A4) − EAen algoritmoa mundu-mailan: bereizmen ertaineko Landsat edo Sentinel-2 irudietan oinarrituta GEEn mundu-mailako algoritmo automatiko bat garatzea, Lurreko edozein lekutan bertako ekosistemarekiko mendekotasunik gabe funtzionatuko duena. Etorkizunean mundu-mailako algoritmo automatiko bat exekutatu ahal izateko oinarriak finkatzen ditu.

4. Artikuluen laburpenak

Atal honetan doktorego-tesi honetan landutako artikuluak laburbiltzen dira. Hauetako hiru aldizkari zientifikoetan argitaratu ziren: Afrikako FireCCISFD11 produktua (A1), BAMT erremintak (A2), eta mundu-mailako algoritmoa (A4). Txileko EAen algoritmoari buruzko artikulua (A3), ordea, nazioarteko kongresu batera bidali zen. Gainera, beste lau artikulu gehigarri ere (AG1, AG2, AG3 eta AG4) deskribatu egin dira modu laburrean, doktorego hau egin bitartean berauetan parte hartzeagatik, egile nagusi bezala izan ez bada ere; suteen detekzioari buruzkoak dira guztiak ere. Artikulu hauen izenburuak, egileak, aldizkariak, etab. eranskinetan ikus daitezke, baita artikuluak beraiek ere.

4.1. A1 – Afrikako EA

Lehen artikulu honen helburu nagusia Saharaz hegoaldeko Afrikan (SHA) EA bereizmen ertaineko irudiekin detektatzea izan zen. Artikulu hau idatzi zenean oraindik ez zegoen mundu- edo kontinente-mailako eta bereizmen ertaineko produkturik, GABAM produktua (Long et al., 2019) ez baitzen argitaratu 2019ko otsailera arte. EAen produktu honekin tamaina txikieneko suteak (< 25 ha) detektatu nahi ziren, horrela bereizmen baxuko produktuek detektatzen ez duten azalera osoa zenbatetsi ahal izateko. Ikerketa-eremu bezala SHA aukeratu zen, mundu osoan urtero erretzen den azaleraren %70 bertan baitago, eta 2016 urtea, Sentinel-2 irudiak dituen lehen urte osoa delako. Produktu hau ESAren Fire_CCI proiektuaren barnean garatu eta sortu zen, eta lehen SFD-a da (Small Fire Database); bere izen ofiziala FireCCISFD11 da.

Algoritmoa

Algoritmoa Sentinel-2A satelitearen MSI sentsoreak eskuratutako irudietan oinarrituta dago gehienbat, 20 m-ko bereizmen espazialarekin; S2 irudien bereizmen tenporala 10 egunekoa zen 2016an, artean Sentinel-2B satelitea ez baitzuten jaurti. Irudiez gain, MODIS sentsorearen datuetatik eratorritako bero-puntuak (*hotspots*) ere erabiltzen ditu algoritmoak, EAen gutxi gorabeherako kokapen bat aurkitzeko; bero-puntu hauek espektro elektromagnetikoko MIR eta TIR eremuetan energia-kantitate handia igortzen dutelako detektatzen dira, eta sentsoreak irudia eskuratzeko garaian aktibo zeuden suteak adierazten dituzte. Hemen erabilitako bero-puntuen produktua MODIS sentsoretik eratorrita dago, aurrez esan bezala, eta puntu bakoitzaren detektatze-data eta ordua, eta kokapena (1 km-ko bereizmenarekin) ematen ditu; bero-puntu hauen datuak FIRMS suteei buruzko sistema estatubatuarraren web-orritik deskarga daitezke (https://firms.modaps.eosdis.nasa.gov/download/, azken aldiz 2022ko martxoan ikusia).

Algoritmoa garatu aurretik Afrikako EAen analisi espektral bat egin zen erretakoa erre gabekotik bereizteko banda eta indize espektral egokienak zein ziren erabakitzeko. S2 irudien 52 bikote aukeratu ziren, SHA osoan zehar banatuta, bikote bakoitzeko bi daten artean suteren bat gertatu zelarik. Bikote bakoitzeko EA detektatzeko, sailkapen gainbegiratu batean oinarritzen den BAMS softwarearen metodologia erabili zen (Bastarrika et al., 2014), programa aldatu egin behar izan bazen ere S2 irudiekin erabili ahal izateko (BAMS softwareak Landsat irudiak bakarrik onartzen ditu). Ondoren, bikote bakoitzean bi daten artean erretako 10.000 lagin eta erre gabeko beste 10.000 hartu ziren. Banda espektral bakoitzarentzat eta hainbat indize espektralentzat, lagin hauek bi datetan zituzten balioak eta bien arteko aldaketak aztertu ziren, eta erretako eta erre gabeko pixelen artean bereizteko ahalmena edo banakortasun estatistikoa kalkulatu zen. Emaitzek adierazi zutenez, MIRBI eta NBR2 indize espektralak, biak SWIR bandetan

17

oinarrituta, eta NIR banda espektrala dira bi kategoriak hobekien bereizten dituztenak. Analisi honi esker aldagai bakoitzeko atalase bat ere lortu zen.

Algoritmoaren prozesu nagusia bi datatako irudi banaren artean burutzen da, sute-aurrea eta sute-ondorena deituak, eta bi daten artean erretako azalerak detektatzen dira. Lehenik lurrazala ongi behatzerik izan ez zen (laino edo hauen itzalengatik) edo erre ezin diren (elurra eta ura) pixelei maskara bat aplikatzen zaie, prozesu osoan zehar bazter batean uzteko. Honetarako irudiaren sailkapena edo SCL (ingelesezko *Scene Classification*) erabiltzen da, S2 irudi bakoitza 12 kategoriatan sailkatzen duelarik: daturik eza, pixel saturatuak edota akastunak, eremu ilunetako pixelak, lainoen itzalak, landaretza, lurzoru soila, ura, sailkatu gabea, probabilitate ertaineko lainoak, probabilitate altuko lainoak, zirru motako lainoak, eta elurra. SCL honetan identifikatutako laino-itzalak oso zehatzak ez direnez, SWIR luzeko B12 banda ere erabiltzen da itzalak aurkitzeko, banda honetan erreflektibitate baxueneko pixelak baztertuz. Ondoren hainbat irizpide erabiltzen dira erretako pixelen multzo gutxi batzuk identifikatzeko:

- Bi daten arteko MIRBI, NBR2 eta NIR diferentziak analisi espektralean lortutako atalaseak baino handiagoak izan behar dira.
- Sute-ondoreneko MIRBI, NBR2 eta NIR balioak irudiko batez besteko balioa baino altuagoak izan behar dira.
- Erretako pixelen multzo bakoitzak gutxieneko 30 ha-ko azalera izan behar du (750 pixel).
- Bi daten artean bero-puntu bat egon behar da pixel-multzotik 1 km baino gutxiagora.

Bi irudien daten artean erre diren pixel-multzo hauetan eta erre gabeko pixeletan oinarrituz, bi probabilitate-kurba sortzen dira %0 eta 100 balioen artean (erre gabe eta erreta, hurrenez hurren), bi irudien arteko MIRBI eta NBR2 diferentzientzako bana. Eszena osoa bi aldiz sailkatzen da honela, indize bakoitzak bi daten artean izan duen bilakaeraren arabera; ondoren, bi balioak biderkatuz azken probabilitate-irudia lortzen da, eta atalase baten bidez EA lortzen dira. Azkenik, hazien irudi bat ere lortzen da aurreko erretako pixel-multzoen hainbat estatistiketan oinarrituz; haziak erre izanaren oso seinale indartsua erakusten duten pixelak dira. Honela, probabilitate-iruditik lortutako EA baztertu egiten dira barnean hazirik ez badute, hau da, probabilitate altuko pixel errerik ez badute.

Prozesu osoa serie tenporal bateko hainbat irudi-bikotetan aplikatzen da, data bakoitzeko irudia aurreko lau datetako irudiekin konparatuz; kasu honetan 2016 urteko S2 irudi guztiak erabili ziren. Berez irudi bakoitza aurrekoarekin konparatzea nahikoa izan behar litzateke, baina baliteke irudiaren zati bat lainoek estalita egon eta behatzerik ez izatea. Hori dela-eta, irudi bakoitza aurreko hainbatekin konparatzen da, sute-aurreko irudi batean behatu gabe egon daitekeen hutsunea besteekin betetzeko. Horrela, serie tenporaleko data bakoitzeko EAen irudi bat lortzen da. Amaierako produktua hilerokoa da, eta pixel bakoitza hilabete osoko egunen batean behatu ote zen, behatu bazen erre ote zen, eta erre bazen hileko zein egunetan erre zen adierazten du.

Emaitzak

Algoritmo hau SHA osoan 2016ko irudi guztiekin exekutatu zen, urte horretan gertatutako sute guztiak detektatuz; lortutako produktuak FireCCISFD11 du izena, Fire_CCI proiektuko SFDaren lehen bertsioa (v1.1) izanik. Produktuaren baliozkotzea erreferentzia-datuekin konparatuz egin zen, Landsat irudietatik eratorriak; normalean erreferentzia-datuek baliozkotu beharreko produktuak baino bereizmen altuagoa behar izaten dute, baina kasu honetan ezin izan zen hala egin, ez baitago Sentinel-2 baino bereizmen altuagoko irudi ez-komertzialik. SHA osoan zehar banatutako 45 baliozkotze-eremu aukeratu ziren

guztira, baliozkotze-eremuak aukeratzeko ausazko laginketa-metodologia bat erabiliz, eremuko ekosistema nagusiaren eta sute-kopuruaren araberako estratu batzuetan oinarrituz (Padilla et al., 2017). Baliozkotze-eremuetako irudi-bikote bakoitzaren arteko erreferentzia-datuak sailkapen gainbegiratu baten bidez sortu ziren, ikerketa honen hasierako analisi espektralean egin antzera. Erreferentzia-datu hauek FireCCISFD11, MCD64A1 eta FireCCI51 produktuekin konparatuz baliozkotze-neurriak lortu ziren; kontuan izan behar da hemen azaldutako FireCCI51 produktuaren datuak ez direla jatorrizko artikuluan aipatzen, produktu hau ez baitzen argitaratu 2020 urtera arte.

Lortutako komisio-erroreak %19,3koak izan ziren, produktu globalenak baina apur bat gutxixeago (%20,4 eta 25,7 MCD64A1 eta FireCCI51entzat, hurrenez hurren). Errore hauen zati handiena uzta bildu berria den nekazal-soroetan kokatuta dago, EAekin maiz nahasten den lurzoru-mota baita (van Dijk et al., 2021), baina baita algoritmoaren lehen fasean maskara aplikatzean ongi baztertu ez ziren lainoen ertzetan ere. Halere, bereizmen baxuko produktu globalekin konparatuta omisioa asko hobetu zen; erretako azalera osoaren %26,5 bakarrik ez zuen detektatu FireCCISFD11ek baliozkotze-eremuetan, baina %55-60 artean MCD64A1 eta FireCCI51ek. Bereizmen baxuko produktuekiko omisioaren jaitsiera honen zergatia bereizmen espaziala da, MODIS irudien 250 (FireCCI51) edo 500 m-ko (MCD64A1) pixelak ez baitira sute txikienak atzemateko gai, baina S2 irudien 20 m-ko pixelekin errazago beha daitezke.

Gure FireCCISFD11 produktuaren arabera, 2016an 4,9 milioi km^2 erre ziren guztira SHAn, sute gehienak maiatzetik urrira gertatuz hego-hemisferioan, eta azaro eta martxo artean ipar-hemisferioan. Suteen banaketa espazial nahiz tenporala hiru produktuen artean berdinak diren arren, FireCCISFD11ek azalera handiagoa detektatzen du hilabetero (6. irudia), MCD64A1 eta FireCCI51 produktuen arabera guztira erretako azalera txikiagoa baita (2,7 eta 3,2 milioi km^2, hurrenez hurren). Halere, tamaina ezberdineko EA konparatzean, aldeak nabarmenagoak dira produktuen artean. Sute handienek (> 250 ha) antzeko azalera osoa eta banaketa espaziala dituzte, baina alde handiagoak ikus daitezke produktuen artean sute txikiak bakarrik kontuan hartuz gero. EA txikienekin (≤ 25 ha, hau MCD64A1 produktuko pixel baten azalera izanik), FireCCISFD11eko EAen %3 bakarrik detektatu zuen bereizmen baxuko MCD64A1 produktuak.
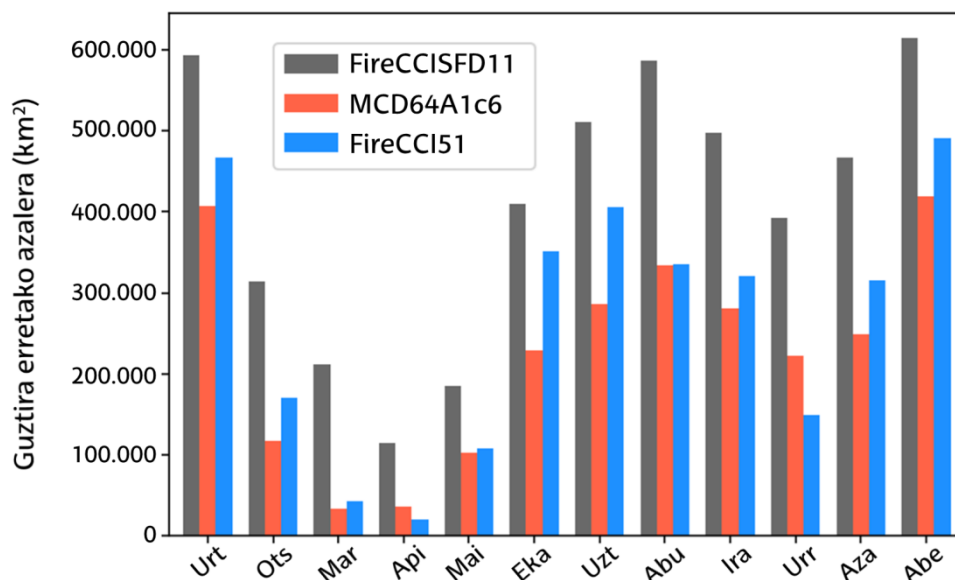
6 irudia. 2016an Saharaz hegoaldeko Afrikan erretako azalera osoa, hilabeteka, FireCCISFD11, MCD64A1 eta FireCCI51 produktuen arabera.

Azkenik, EA detektatzeko zehaztasun tenporala ere aztertu zen, algoritmoen sarrera-datu bezala erabilitako irudiek bereizmen tenporal ezberdinak baitituzte: egun bakarra MODISek baina 10 egun S2 irudiek. Bero-puntuen datak erreferentzia bezala erabiliz, MCD64A1ek EAen %70 erre ondorengo lehen egunean detektatzen duela ikusi zen, eta %80 lehen lau egunetan. FireCCISFD11 produktuak, ordea, denbora gehiago behar du EA detektatzeko: 10 egun %75 detektatzeko (erre zenetik lehen S2 irudia), eta 20 egun %89rentzat (bi irudi).

FireCCISFD11 produktu hau kontinente-mailan bereizmen ertainarekin sortutako lehena izan zen, eta bereizmen ertaineko produktuak zenbat sute txiki gutxiesten ari ziren jakiteko oso baliagarria izan zen. Hain zuzen ere, MCD64A1ek erretako azalera osoaren %55 ez zuela detektatzen ikusi zen; gure produktu berriak honekiko %80ko igoera erakusten zuen, beraz. Honek eragin zuzena du mundu-mailako EAengan eta hauek igorritako gasengan, lan honen ikerketa-eremuan, SHAn, baitago munduko suteen %70 inguru. Algoritmoa Afrikako suteen ezaugarri espektraletara egokituz diseinatu zen hasieratik, eta baliteke hain ongi ez funtzionatzea bertatik kanpora probatuz gero.

4.2. A2 – BAMT erremintak

FireCCISFD11 produktua garatzeko aurreko artikulua (A1) lantzean, hainbat arazo edota gabezia nabaritu ziren EAen detekzioaren arloan. Honako hauek dira aurkitutako gabezia nagusiak:

1. Eskualde-, kontinente- edo mundu-mailan, bereizmen ertaineko irudi-multzo baten bidez, EAen kartografia bat lortzen lagunduko duten erreminta batzuen hutsunea. Kasu honetan BAMS (Burned Area Mapping Software) softwarea bazegoen aurretiaz (Bastarrika et al., 2014), EA detektatzeko sailkapen gainbegiratu bat egiten duelarik, baina hainbat muga ditu. Batetik, bere erabilera GIS (Geografia-Informazioko Sistemak) software komertzial bati lotuta dago, ArcGIS (https://www.esri.com/en-us/arcgis/products/arcgis-desktop/overview, azken aldiz 2022ko martxoan ikusia); gainera, honek BAMS softwarea etengabe eguneratzea eskatzen du, ArcGISen bertsio berrien ongi funtzionatzen jarrai dezan. Eta, bestetik, BAMSek Landsat irudiak bakarrik onartzen ditu (S2 sateliteak oraindik ez ziren existitzen software hau garatzean), eta aldiko eszena bakarraren (path-row) prozesamendura mugatuta dago, eremu handiagoetako kartografia sortzea zailduz. EA detektatzeko algoritmoa ere nahiko mugatuta dago, erretako pixelen kategoria bakarrik entrena baitaiteke, eta erre gabekoen kategoria kontrolatzea nahiko zaila da, nekazal-soroetan batez ere.
2. Baliozkotze-eremuen aukeraketa estratu bidezko eta ausazko laginketa-metodologia baten bidez egitea komeni da (Padilla et al., 2017), bertan beranduago erreferentzia-datuak sor daitezen. Hasierako elementuak Landsat edo S2 eszenak direnean, metodologia honek eszenako Olsonen ekosistema nagusiaren (Olson et al., 2001), espero den sute-kopuruaren eta erabilgarri dauden lainorik gabeko irudi-kopuruaren arabera hainbat estratutan sailkatzen ditu elementu guztiak; ondoren, estratu bakoitzean elementu-kopuru jakin bat ausaz lagintzen da. Metodologia hau ezartzea korapilatsua izan daiteke erabiltzaile askorentzat, erabilgarri dauden lainorik gabeko irudiak aztertzea batez ere.
3. EAen kartografia edo bere baliozkotzerako beharrezko erreferentzia-datuak sortzeko irudi-kantitate handia deskargatu eta prozesatu behar izaten da sistema informatiko batean, eta honek biltegiratzeko eta prozesatzeko ahalmen handia eskatzen du, ikertzaile askok agian izango ez duena: A1eko FireCCISFD11

produktuaren kasuan, adibidez, deskargatutako S2 irudiak biltegiratzeko bakarrik 63 TB edukiera behar izan zen, eta beste 87 TB sortu ziren tarteko datuetan azken produktua lortu aurretik.

Gabezia hauei konponbide bat emateko, hainbat erreminta inplementatu ziren Google Earth Enginen, hau da, hodeian lan egiten duen eta erabiltzaileari datu-kantitate handiekin lan egitea saihesten laguntzen dion plataforma batean. Erreminta hauei Burned Area Mapping Tools (BAMT) izena eman zitzaien, eta EA detektatzeko eta baliozkotzeko prozesu osoa betetzen dute, erabiltzaileari bere EAen kartografia sortzea, estatistikoki adierazgarriak diren baliozkotze-eremuak aukeratzea eta hauetan erreferentzia-datuak sortzea ahalbidetuz. Eskakizun bakarrak Google Earth Enginen kontu bat (doakoa da) eta internetera konexio on bat dira; prozesu osoa hodeian burutzen da, eta azken emaitzak soilik esportatzen dira, erabiltzailearen Google Drive kontu pertsonalera. Erreminta hauetarako loturak https://github.com/ekhiroteta/BAMT web-orrian aurki daitezke.

Erremintak

BAMT erremintekin egin daitezkeen prozesuak erakusten ditu 7. irudiak, bi bloketan zatituta. Batetik, *BA Cartography* erremintak eremu handi bateko EAen mapak sortzea ahalbidetzen du, sailkapen gainbegiratu baten bidez (erretako eta erre gabeko lagin batzuk entrenatuz). Bestetik, gainerako erremintak EAen edozein kartografia baliozkotzeko dira, *BA Cartography* erremintak sortutako mapak nahiz beste edozein produktu (FireCCISFD11 edo MCD64A1, adibidez). Artikulu honetan *VA*, *VA Dates* eta *RP* erremintak bakarrik aurkeztu ziren; hauek baliozkotze-eremuak aukeratzea eta bertan erreferentzia-datuak sortzea ahalbidetzen dute, baina baliozkotzea bera sistema informatiko lokal batean egin behar zen, erreferentzia-datuak deskargatu ondoren. Tesi honetan beste erreminta bat ere aurkezten da ordea, artikulua argitaratu ostean garatu zena: *Assessment*. Honek baliozkotzea, erreferentzia-datuak sortu eta gero, GEE plataforman bertan burutzea ahalbidetzen du, datuak deskargatu eta baliozkotu beharreko kartografiarekin sistema lokal batean konparatu gabe.
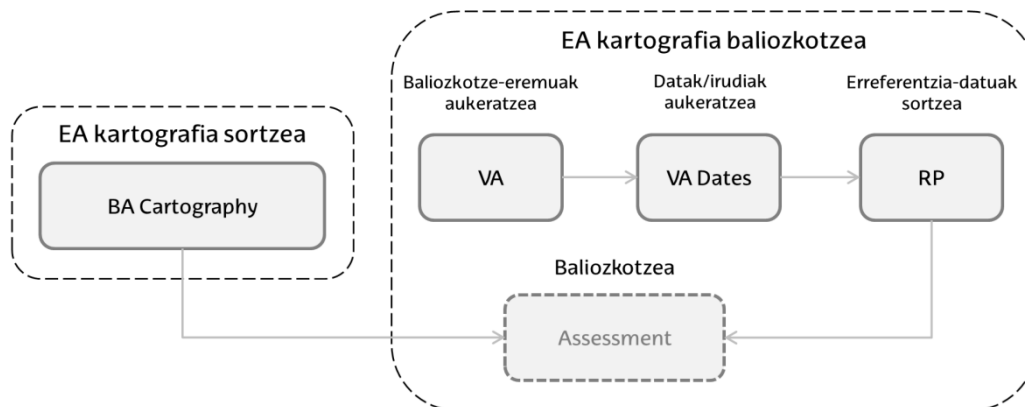
7 irudia. BAMT erremintekin EAen kartografia sortzeko eta baliozkotzeko prozesuaren fluxu-diagrama.

BA Cartography erremintak Landsat edo S2 irudi baten eszena baino zabalagoak diren eremuetan EAen mapak sortzea ahalbidetzen du sailkapen gainbegiratu baten bidez. Elkarren segidako bi periodo definitu behar zaizkio, sute-aurreko eta sute-ondoreneko bezala erabiliko direnak; lehenengoan oraindik erre gabe baina bigarrenean jada erreta azaltzen diren azalerak bakarrik atzemango ditu errerremintak. Emaitzaren bereizmen espaziala erabilitako datuen araberakoa da: 30 m-koa Landsat irudiak erabiltzen badira, edo 20 m-koa S2 irudiekin.

EA detektatzeko prozesua sailkapen gainbegiratu baten bidez egiten da. Erabiltzaileak hainbat poligono definitu behar ditu, erretako nahiz erre gabeko kategorien barruan. Algoritmoak *Random Forest* sailkatzaile bat (Breiman, 2001) entrenatzen du, aurrez definitutako poligonoetako pixelen balioak erabiliz. Behin sailkatzailea entrenatuta, EA aurkitu nahi diren eremu osoa sailkatzen da, eta emaitza interfazeko mapan erakusten da; emaitza oraindik ez dela egokia baderitzo, erabiltzaileak poligonoak ezabatu, aldatu edo berri batzuk defini ditzake, eta prozesua errepikatu behin eta berriz nahi duen emaitza lortu arte. Azken emaitza erabiltzailearen Google Drive kontura esportatzen da geruza bektorial moduan, poligono bakoitzak atributu bat duelarik zein datatan erre den adieraziz.

Bigarren blokeko lehen erreminta, **VA**, aurrez aipatutako ausazko laginketa-metodologiaren inplementazio bat da (Padilla et al., 2017), baliozkotze-eremuak aukeratzeko hainbat estratutan eta irizpide estatistikotan oinarrituz. Honako sarrera-datu hauek behar ditu: ondoren erreferentzia-datuak sortzeko erabiliko diren irudi-motak (Landsat edo S2), baliozkotu beharreko EAen produktuaren edo kartografiaren hedadura eta periodoa, erretako azaleraren erreferentzia bezala MCD64A1 edo FireCCI51 produktua erabiliko den, eta baliozkotze-eremu bakoitzean lainorik gabeko nahiko irudi egongo dela ziurtatzeko hainbat parametro. Erremintak, trukean, aukeratutako baliozkotze-eremuak ematen ditu, baita bakoitzean lainorik gabeko nahiko irudi zein periodotan dauden ere. Zoritxarrez GEEk prozesamendurako dituen mugek nahiko baldintzatzen dute erreminta hau, eta hedadura handietan blokeatu egin daiteke. Lainorik gabeko irudiak nahiko maiztasunekin zein garaitan dauden bai, baina data konkretuak oraindik ezagunak ez direnez, *VA Dates* erreminta erabili behar da ondoren irudi hauek aurkitzeko.

Baliozkotze-eremu bakoitzean erabilgarri dauden irudiak eta beren datak ezagutzean, *VA* eta *VA Dates* errementei esker, erreferentzia-datuak sor daitezke *RP* erreminta erabiliz. *BA Cartography* erremintaren prozesu bera da, ezberdintasun gutxi batzuekin. Batetik, bi irudiren artean bakarrik detekta daitezke EA eta, beraz, eremuaren hedadura oso mugatua da (100 x 100 km^2), EAen produktuak baliozkotzeko erabilia izan dadin. Bestalde, EA 10 m-ko bereizmen espazialarekin ere detekta daitezke, S2 irudiak erabiltzen direnean, baliozkotzeko benetan erabilgarria izan daitekeena (baliozkotze-prozesuan bereizmen handiagoko datuak behar baitira, aurrez esan bezala).

Erreminta hauek EAen kartografia bat eta, gainera, kartografia hau edo beste produkturen bat baliozkotzeko beharrezko erreferentzia-datuak sortzea ahalbidetzen dute. Ondoren, bien arteko konparaketa eta baliozkotze-neurrien kalkulua (komisio- eta omisio-erroreak, adibidez) sistema informatiko lokal batean egin behar ditu erabiltzaileak. Artikulu honen ondoren, ordea, beste erreminta bat diseinatu da, **Assessment**, baliozkotzea GEEn bertan egitea ahalbidetzen duena. Erreminta honek EAen produktu bat eta erreferentzia-datuak, raster formatuan nahiz bektorialean, behar ditu baliozkotzea egin ahal izateko; sarrera-datu guztiak aurrez GEEn kargatuta egon behar dira, plataformako berezko produktuak direlako edo erabiltzaileak berak igo dituelako. Emaitza bezala baliozkotze-eremu bakoitzean kalkulatutako neurriak ematen ditu, eta baita produktu osoarenak ere. Erreminta hau ez zen argitaratutako artikuluan azaldu, ordea, gaur egun jada erabilgarri egon arren.

Kasu praktikoak

BAMT erreminta hauek bi kasu praktikotan baliatu ziren beraien erabilgarritasuna egiaztatzeko. Lehen kasua 2019 eta 2020 artean Australia hego-ekialdean gertaturiko sute-denboraldia izan zen, ohiz kanpoko lehorte luze batek hainbat sute eragin baitzituen (Bowman et al., 2020; Schweinsberg et al., 2020; Yu et al., 2020). *BA Cartography*

erremintarekin milioi bat km^2 baino hedadura handiagoko eremu batean 2019ko irailaren eta 2020ko apirilaren artean erretako azalerak detektatu ziren, denboraldi osoa bi hilabeteko lau periodotan zatituz. 86 entrenamendu-poligono definitu ziren guztira, eta GEEk hiru egun baino gutxiago behar izan zituen 3.600 Landsat irudi prozesatzeko, 30 m-ko bereizmenarekin. Ikerketa honen arabera, 52.700 km^2 inguru (aztertutako eremuaren %5) erre ziren sute-denboraldi honetako zortzi hilabeteetan; sute guztiak ekialdeko itsasertzean izan ziren, itsasotik 250 km baino gertuago. Lortutako EAen kartografia baliozkotzeko 10 eremu aukeratu ziren VA erreminta erabiliz, eta hauetako bakoitzean erreferentzia-datuak sortu ziren RP erremintarekin elkarren segidako S2 irudien artean, 20 m-ko bereizmenarekin. Baliozkotzean lortutako emaitzen arabera %11,8 eta %8,9ko komisio- eta omisio-erroreak, hurrenez hurren, zituen sortutako kartografiak.

Bigarren kasu praktikoak Kanadako probintziak hartzen ditu, iparraldeko hiru lurraldeak (Yukon, Ipar-mendebaldeko Lurraldeak eta Nunavut) alde batera utziz; 6 milioi km^2 inguruko eremua, beraz. Australiako ikerketa-eremua baino askoz handiagoa zenez, periodo bakarra prozesatu zen, 2018ko uztailetik irailera arteko suteak bakarrik detektatuz. 19 entrenamendu-poligono bakarrik behar izan ziren, eta GEEk Sentinel-2 sateliteen 255.000 irudi baino gehiago prozesatu zituen, 20 m-ko bereizmen espazialarekin, 10 egunez. Ikerketa honen arabera, 16.000 km^2 baino gehiago erre ziren aztertutako periodoan, horietatik erdia baino gehiago Columbia Britainiarrean (10.000 km^2) baina erretako azalera handiekin Ontario, Alberta, Manitoba, Saskatchewan eta Quebec probintzietan ere (800-1.800 km^2 artean bakoitzean). EAen mapa hau baso-suteen zerbitzu kanadarraren datu ofizialekin konparatu zen, baliozkotze moduan. Datu hauen arabera erretako azalera osoa oso antzeko bazen ere (16.500 km^2), hauetatik 10.000 km^{2}tan bakarrik zetozen bat espazialki, gainerakoa kokapen ezberdinetan baitzegoen. Bisualki eginiko alderaketa batek, ordea, BA Cartography erremintarekin detektatutako EA zehatzagoak zirela eta datu ofizialek baino detaile gehiago zituztela erakutsi zuen.

BAMT erremintak erabilgarriak direla ikusi da hedadura handietan EA detektatzeko, milaka irudi egun gutxi batzuetan prozesatuz, nahiz EAen mapak edo produktuak baliozkotzeko. Australian detektatutako suteek FireCCISFD11 edo MCD64A1 bezalako produktu global askok beren baliozkotzeetan baino errore gutxiago zituztela ikusi zen, eta Kanadako suteak ere perimetro ofizialak baino zehatzagoak ziren, bisualki behintzat. Doktorego-tesi honetan garatutako erreminta hauek, beraz, komunitate zientifikoari bereizmen ertaineko EAen detekzioa eta baliozkotzea nabarmen erraztea espero da.

4.3. A3 – Txileko EA

Ikerketa honen helburua bereizmen ertaineko irudiekin EA detektatzeko algoritmo automatiko bat sortzea da, A1ean bezala, baina GEEn inplementatuta eta Txilen aplikatuta oraingo honetan, prozesu guztia hodeian automatizatuz eta burutuz. FireCCISFD11 produktuaren algoritmoa espezifikoki kontinente afrikarrerako diseinatuta zegoen bezalaxe, algoritmo hau Txileko ingurugiro-baldintzetara egokituta dago, eta 2017ko urtarrilaren eta martxoaren arteko sute-denboraldian aplikatu zen, bereziki bortitza izan baitzen eta normalean erretzen den azalera bost aldiz erre baitzen (5.000 km^2 normalean izaten ziren 1.000 km^{2}en aldean).

Algoritmoa

GEEn inplementatutako algoritmo hau oso prozesu erraz batean oinarrituta dago, Random Forest sailkatzaile baten bidez (Breiman, 2001) Txile osoko EAen kartografia sortzen baitu; honetarako 20 m-ko bereizmeneko S2 irudiak erabiltzen ditu, sute-aurre eta

sute-ondoren bezala balio duten bi periodotan banatuta. *Random Forest* sailkatzailearentzako entrenamendu-laginak ausaz aukeratzen dira hainbat entrenamendu-eremutako erreferentzia-perimetroetatik (ausazko 1.000 puntu kategoria bakoitzeko, 2.000 puntu entrenamendu-eremu bakoitzeko), A2ko *RP* erreminta erabiliz.

Algoritmo honen zatirik konplexuena herrialde osoa ordezkatuko zuten entrenamendu-datuak lortzea izan zen, Txilek hainbat ekosistema baititu latitudearen arabera: Atacamako basamortua iparraldean; klima mediterraneo eta epeletako basoak erdialdean, EA gehienak gertatzen diren inguruan; eta baso borealak hegoaldean. Herrialde osoa algoritmo berarekin sistematikoki prozesatu nahi denez, entrenamendu-datuek ekosistema hauek guztiak izan behar dituzte kontuan. Beraz, algoritmoaren hiru bertsio sortu ziren, pixkanaka entrenamendu-puntu gehiago erabiliz eta herrialdearen baldintzetara hobeto egokituz. Lehen bertsioan 10 entrenamendu-eremutako puntuak erabili ziren, guztiak herrialdearen erdialdean kokaturik. Bigarren bertsioan lau eremu gehiago hartu ziren kontuan: bi nekazal-soroetako komisio-erroreak zuzentzeko, eta beste bana basamortuan eta baso borealean. Azken bertsioan zortzi entrenamendu-eremu gehitu ziren, errore gehien aurkitu ziren eskualdeen artean banatuta.

Emaitzak

Hiru bertsioetan aurkitutako errore gehienak uzta bildu-berria zuten nekazal-soroetan (EAekin maiz nahasten den lurzoru-mota hau) eta lainoen eta erliebearen itzaletan aurkitu ziren. Halere, erroreak gutxiagotu egin ziren arazo hauek konpontzeko entrenamendu-eremu gehiago erabili ahala. EA detektatzeko erabilitako aldagai guztien artean, bertsio bakoitzean entrenatutako *Random Forest* sailkatzailearen arabera, RdNBR indizea izan zen aldagai garrantzitsuena, NBR eta NBR2 indizeen aurretik.

Algoritmoaren azken bertsioaren (v3) emaitzak Txileko baso-korporazio nazionalaren edo CONAFen (gaztelerazko *Corporación Nacional Forestal*) datu ofizialekin konparatu ziren bisualki. Ikerketa honetako emaitzek zehaztasun handiagoa zutela egiaztatu zen, CONAFen perimetroek bereizmen espazial baxuagoa baitzuten eta EAen barruan erre gabeko uharteak ere ez baitzituzten adierazten. Hala ere, gure emaitzetan omisio-erroreak ere aurkitu ziren, erre gabeko zuhaitzen adaburuek oihanpe errearen seinalea behatzea oztopatzen zuten basoetan batez ere.

Algoritmo honen arabera, 2017 hasieran Txilen 5.460 km²ko azalera erre zen guztira, gehiengoa 10 km² baino gehiagoko sute handietan. Azalera honen %41, 2.240 km², Maule eskualdean kokatuta zegoen, O'Higgins, Biobío, Araucanía, Ñuble eta Santiago eskualdeek jarraituta, bakoitzak 300-750 km² arteko azalera errea zuelarik; eskualde hauek guztiak herrialdearen erdialdean kokatuta daude.

4.4. A4 – EAen algoritmoa mundu-mailan

Azken artikulu honen helburua mundu-mailan funtzionatuko duen bereizmen ertaineko algoritmo automatiko bat sortzea da; gainera, BAMT erremintak (A2) eta Txileko algoritmoa (A3) bezalaxe, GEEn diseinatuta eta inplementatuta dago. EA hiru bereizmen espazialetan detekta ditzake, erabiltzen dituen irudien arabera: 10 edo 20 m (Sentinel-2), eta 30 m (Landsat). Baliozkotze-eremuetan nahiz hiru proba-eremu handitan emaitza onak lortu arren, artikulu honetan aurkeztutakoa lehen bertsio bat baino ez da oraindik, eta hobekuntza batzuen beharra izan dezake mundu-mailan modu sistematikoan aplikatzen hasi aurretik.

Algoritmoa

Aurreko artikuluetako algoritmoak zegozkien inguruneetako ezaugarri espektralentzat diseinatuta zeuden: lehena (A1), Afrikan, MIRBI eta NBR2 indizeetan eta NIR bandan bakarrik zegoen oinarrituta, atalase finko batzuk erabiliz; Txilekoa (A3) bertan kokatutako entrenamendu-eremuetara egokitutako sailkatzaile bat zen; eta BAMTen parte diren *BA Cartography* eta *RP* erremintak (A2), malguagoak badira ere, erabiltzaileak definitutako entrenamendu-poligonoen menpe eta beraz tokiko baldintza espektraletara egokituta daude. Litekeena da hiru algoritmo hauetako bakar batek berak ere dagokien eremutik kanpo behar bezala ez funtzionatzea, EAen seinale espektrala asko alda baitaiteke ekosistemaren, lurzoru-motaren edota sutea gertatu zenetik igaro den denboraren arabera. Algoritmo berri honek, beraz, edozein kasutako tokiko ezaugarrietara moldatzeko behar bezain malgua izan behar du, gero Lurreko edozein eskualdetan aplikatu ahal izateko.

Algoritmo global hau exekuzio bakoitzean hilabete batez MGRS tesela batean (ingelesezko *Military Grid Reference System*, S2 irudiak banatzeko erabiltzen den sistema) erre diren azalerak prozesatzeko eta detektatzeko diseinatuta dago. Behar den bereizmenaren arabera, Landsat edo Sentinel-2 irudiak erabiltzen ditu; algoritmoaren prozesua berbera da bi kasuetan, espektro elektromagnetikoaren eremu berberetan baitauzkate bandak eta beraz baliokideak dira. Satelite-irudi hauez gain, MODIS sentsorearen irudietatik eratorritako bero-puntuak edo *hotspot*-ak ere behar ditu, 1 km-ko bereizmen espazialarekin, A1eko FireCCISFD11 produktuaren algoritmoak bezalaxe. Erabilgarri dauden lehen Landsat irudiak 1982koak badira ere, algoritmo hau 2000ko azarotik aurrera bakarrik exekutatu daiteke, data honetatik aurrera bakarrik baitaude MODISen bero-puntuak.

Algoritmoaren lehen pausuan, aurre-prozesuan, bi fase nagusietarako irudiak prestatzeaz arduratzen da. Horretarako, prozesatu beharreko teselan bost hilabetez eskuratutako irudiak kargatzen dira, detektatu beharreko suteak gertatu ziren hilabetearen inguruan zentratuta; irudien seriea luzeegia bada, laino-portzentajea altueneko datak ezabatu egiten dira GEEk bere memoria- eta prozesamendu-mugak gaindi ez ditzan. EAen detekzioan kontuan izan behar ez liratekeen elementu guztiei ere (lainoak, itzalak, elurra edota ura) maskara bat aplikatzen zaie, analisitik kanpo uzteko. Azkenik, hiru indize espektral kalkulatzen dira irudi bakoitzarentzat: NBR, NBR2 eta MIRBI.

Lehen fasearen helburua hilabete honetan erre diren pixel batzuk aurkitzea da, aurrez ezarritako irizpide batzuetan oinarrituz, gero pixel hauetatik erretako eta erre gabeko kategorien hainbat balio lortzeko NBR, NBR2 eta MIRBI indizeentzat eta NIR bandarentzat. Honetarako, MODISen bero-puntu baten inguruan NBR indizearen bat-bateko jaitsiera izan duten pixelen bilakaera aztertzen da, jaitsiera hori bero-puntuaren dataren inguruan izan bada pixela benetan erre delako izan baitaiteke; NBR indizearen jaitsiera honen alde banatako datekin bi irudi sortzen dira, sute-aurreari eta sute-ondorenari dagozkienak. Bi irudi hauetatik indize edo banda bakoitzarentzat hainbat atalase kalkulatzen dira, sute-ondoreneko balioenak nahiz bi daten arteko aldaketenak. Atalase hauetan oinarritutako hainbat baldintza aplikatuz, erretako pixelen multzo bat aukeratzen da. Lehen fase hau amaitzeko, multzo honetatik 1.000 pixeleko lagin bat hartzen da, eta NBR indizearen jaitsieraren aurretik eta ondoren zituzten balioak erre gabeko eta erretako kategoria bezala hartzen dira, hurrenez hurren.

Algoritmoaren bigarren fasea aurreko laginean oinarrituz probabilitate-funtzioak sortzeaz eta funtzio hauekin irudiak sailkatzeaz arduratzen da. Erabili beharreko aldagai bakoitzeko (NBR, NBR2 eta MIRBI, eta NIR) %0 (erre gabe) eta %100 (erreta) arteko balioak dituen funtzio logistiko bat sortzen da; probabilitate-funtzio hauek datu-serieko irudi

guztiak sailkatzea ahalbidetzen dute, banda edo indize bakoitzean besteekiko menpekotasunik gabeko probabilitate-balioak lortuz. Irudi bakoitzeko lau probabilitate-irudi hauekin beste probabilitate-irudi bat kalkulatzen da batezbesteko haztatuaren bidez, dagokion banda edo indizearen banakortasunaren karratua erabiliz pisu bezala; banda baten banakortasuna aldagai batek bi kategoria bereizteko duen ahalmena da (Kaufman eta Remer, 1994). Banakortasunaren menpeko batezbesteko haztatu honek algoritmoa tokiko EAen seinale espektralera hobekiago egokitzea ahalbidetzen du, seinale hau bertako ingurugiro-baldintzen araberakoa baita maiz. Azken probabilitate honi *probabilitate estatikoa* deritzo, eta pixel bakoitza dagokion datan erreta zegoen ala ez adierazten du, aurreko datetan ere erreta ote zegoen kontuan izan gabe. Ondoren, pixel bakoitzaren probabilitate estatikoak denboran zehar duen bilakaera aztertuz, *probabilitate dinamikoa* kalkulatzen da, hau da, pixela erre berria izan eta data honetan lehen aldiz behatu ahal izan den ala ez dioen probabilitatea. Probabilitate dinamiko honek balio altua du aurreko datetan probabilitate estatiko baxuak baina kalkulatu nahi den datan eta ondorengoetan altuak izan baditu. Azkenik, pixel bat erretakotzat jotzen da probabilitate dinamiko altueneko datan duen balioa %50 baino altuagoa bada. Prozesua amaitzeko iragazki bat aplikatzen da, erretako pixel isolatuak ezabatu eta EA konpaktuagoak lortzeko.

Algoritmoa exekutatzen den bakoitzean MGRS tesela batek mugatutako irudi bat lortzen da, aurrez definitutako hilabetean erre diren azalerekin. Irudi bakoitzak bi banda ditu: pixel bakoitza urteko zenbatgarren egunean erre zen, 1 eta 365 arteko balioekin (0 balioa erre ez bazen); eta %50-100 arteko segurtasun-maila erre diren pixelentzat (%0 erre ez direnentzat). Emaitza UTM koordenatuekin georreferentziatuta dago 10, 20 (S2) edo 30 (Landsat) m-ko bereizmen espazialarekin.

Baliozkotzea

Guztira 50 baliozkotze-eremu aukeratu ziren A2ko *VA* erreminta erabiliz; hauetatik erdiak Afrikan kokatuta daude, bertan gertatzen baita mundu osoko suteen %70. Eremu hauetako bakoitzak 2-12 hilabeteko periodo bat du, 2019an hodei gutxiko irudiak behar adinako maiztasunarekin dituena. Ondoren, eremu bakoitzeko irudi-bikote bakoitzaren artean EAen erreferentzia-perimetroak sortu ziren, *RP* erremintarekin eta 10 m-ko bereizmen espazialarekin. Aldi berean, baliozkotze-eremu hauetan guztietan algoritmo automatikoa exekutatu zen, eremu bakoitzari zegokion periodo osoa estaltzeko beharrezko hilabete guztiak prozesatuz. Hiru aldiz exekutatu zen algoritmoa, bakoitzean bereizmen espazial ezberdin batekin, eta, beraz, hiru produktu lortu ziren kasu bakoitzean, BAS2-10 (10 m), BAS2-20 (20 m) eta BAL-30 (30 m) deritzenak. Algoritmo honekin sortutako hiru produktuak erreferentzia-perimetroekin konparatuz baliozkotu ziren, baita GEEn eskuragarri dauden bereizmen baxuko produktu bi globalak ere (FireCCI51 eta MCD64A1, 250 eta 500 m-ko bereizmen espazialarekin, hurrenez hurren).

Lortutako estatistikek erakusten dutenez, erroreak murritzagoak dira bereizmen espaziala handiagotu ahala. Komisio-erroreak %18-19 artekoak dira FireCCI51 eta MCD64A1 produktuentzat, baina %11koak BAL-30entzat eta %9 ingurukoak S2 irudietatik sortutako produktuentzat (BAS2-20 eta BAS2-10). Modu berean, bereizmen baxuko produktuek %50 baino gehiagoko omisioa zuten, baina %35ekoa BAL-30 produktuak eta %27-28 artean BAS2-20 eta BAS2-10ek. Neurketa hauexek berberak lurzoru-motaren arabera ere kalkulatu ziren, eta gure algoritmoa sabanetan eta larreetan zehatzagoa dela ikusi zen, eta ez hainbeste sastrakadi eta basoetan; emaitza okerrenak nekazal-soroetan aurkitu ziren. Detektatutako suteen datak VIIRS sute aktiboen (375 m-ko bereizmen espazialarekin, MODIS *hotspot*-en 1 km-en aldean) datekin konparatzeak erakutsi zuenez, bereizmen ertaineko hiru produktuek EAen %81-84 artean sutearen ondoren eskuragarri

dagoen lehen irudian detektatzen dute (5 egun Sentinel-2 irudien kasuan, edo 8 egun Landsat datuekin). Bereizmen baxuko produktuei dagokienez, FireCCI51ek antzeko denbora behar du suteen ehuneko bera detektatzeko (5 egun), baina 2 egun baino ez MCD64A1ek; azken honek, gainera, suteen %78 detektatzen du lehen egunean bertan.

Gure algoritmoak 10 m-ko bereizmenarekin detektatutako suteak 20 m-rekikoak baino zehatzagoak izan baziren ere, hobekuntza ez zen oso nabarmena izan. Gainera, 20 m-ko bereizmenarekin burutzen du algoritmoak azkarren detekzioa, MGRS tesela batean hilabete bakoitzeko 4,2 min behar baititu bataz beste; 10 m-rekin prozesatuta, aldiz, 5,9 min, eta 4,5 min Landsat irudiekin eta 30 m-ko bereizmenarekin. Hau dela-eta, EA Sentinel-2 irudien bidez 20 m-ko bereizmen espazialarekin detektatzeak dirudi algoritmo honen aukera hoberena.

Proba-eremuak

Baliozkotzea 50 eremutan egin arren, algoritmoak zer moduz funtzionatzen ote zuen probatu nahi izan zen beste hiru proba-eremu handitan, bakoitzak 5x5 graduko azalera estaltzen zuelarik. Hiru eremu hauek mundu-mailan sute gehien dituzten hiru ekosistemetan daude: bat Afrika Erdiko Errepublikan dago, sabana tropikal eta subtropikalez osatua; bestea, Mexiko eta Guatemala artean kokatuta, oihan tropikalek osatzen dute gehienbat; eta hirugarrenak baso borealak ditu, Siberian, Baikal lakuaren iparraldean. Eremu hauetako bakoitzean 2019ko 12 hilabeteetan exekutatu zen algoritmo automatikoa, EA 20 m-ko bereizmen espazialarekin detektatuz (BAS2-20), hau baita baliozkotzearen emaitzen eta prozesatze-denboraren artean oreka egokiena duen bereizmena. Proba-eremuetako emaitzak bereizmen ezberdineko hiru produktu globalekin konparatu ziren: FireCCI51 250 m-rekin, MCD64A1 500 m-rekin, eta GABAM 30 m-rekin, azken hau Landsat irudien bidez sortua. GABAM produktuak ez du erretako pixela zein egunetan edo hilabetetan detektatu zen adierazten, zoritxarrez, baina urte osoan erretako azalerak konparatzeko balio dezake.

Gure BAS2-20 produktuak detektatu zuen erretako azalera handiena hiru proba-eremuetan, ondoren FireCCI51 eta MCD64A1 zetozen, eta GABAMek zituen azalera txikienak. Erretako azaleraren ehunekoa ere kalkulatu zen lau produktuetako bakoitzarentzat, 0,05 graduko gelaxkak dituen sare batean, horrela produktuen arteko erregresio lineala eta korrelazio espaziala aztertuz. BAS2-20-rekiko korrelazio handiena MODIS irudietatik eratorritako produktuek zuten (0,48 eta 0,79 arteko r^2 balioekin), erregresio-zuzenen maldak 0,75 eta 1,14 artean zeudelarik, baina 1 balioaren azpitik kasu gehienetan; honek produktu globalek azalera txikiagoak detektatzen dituztela esan nahi du. GABAM produktuak oso korrelazio txikiak erakutsi zituen ($r^2 < 0,54$), 0,30 eta 0,44 arteko maldekin erregresio-zuzenentzat, omisio-errore altuak erakutsiz.

4.5. Artikulu gehigarriak

Aurrez esan bezala, beste lau artikulutan ere parte hartu da tesi hau burutu bitartean, guztiak EAen detekzioari buruzkoak. Tesiaren ikerketa nagusia osatzen ez badute ere, artikulu bakoitzaren laburpen bat irakur daiteke atal honetan.

AG1 – algoritmoen arteko konparaketa

A1 lehen artikulurako Sentinel-2 irudietan oinarritutako algoritmo bat garatu zen SHAn EA detektatzeko. Irudi hauen banda espektralak espektroaren domeinu optikoan daude, hodeiek energia elektromagnetikoa guztiz islatzen duten uhin-luzeretan kokaturik. Honek

hodeien azpiko lurrazala behatzea galarazten du, uhinek ezin baitituzte zeharkatu, eta arazo bihur daiteke eremu hodeitsuetan EA behatu nahi badira. Kasu hauetan mikrouhinak erabilgarriagoak izan daitezke, hau da, 1 mm eta 1 m arteko uhin-luzera duen energia, hauek hodeiak zeharkatu eta azpian dagoen beha baitezakete. Banda espektralak uhin-luzera hauetan dituzten irudiak sistema aktiboek eskuratzen dituzte normalean, lehenik energia igorriz eta gero lurrazalean islatu eta itzuli dena erregistratuz. Sentinel-1 (S1) sateliteek, Sentinel-2 bezalaxe ESAren Copernicus programaren barnean daudenek, sistema aktiboen bidez eskuratzen dituzte beren irudiak.

Artikulu honen helburua hainbat algoritmoren emaitzak konparatzea eta bakoitzak gune hodeitsuetan EA detektatzeko duen errendimendua zenbatestea da; algoritmo hauek, batetik, A1en S2 irudi optikoetan oinarritutakoa eta, bestetik, S1 irudiak erabiltzen dituzten bi dira. Guztien arteko konparaketa Afrikan ekuatorearen eta Sahara basamortuaren artean kokaturiko 10 ikerketa-eremutan egin zen, sute asko eta hodei dezente dituztenak (baina %75etik beherako hodeitza, S2 irudietan EA behatzea gehiegi ez oztopatzeko). Erreferentzia-datuekin buruturiko baliozkotzearen arabera, S2 irudiak erabiltzen dituen A1eko algoritmoak komisio-errore gutxiago egiten ditu, hodei asko izan arren. Algoritmo hau lurzoru-mota guztietan orokorki zehatzagoa izan arren, S1 irudietan oinarrituriko algoritmoetako batek komisio-errore baxuagoa zuen larreetan eta baso tropikaletan.

AG2 – erreferentzia-datuen datu-basea

EAen produktuak baliozkotu egin behar dira beraien errendimendua ezagutzeko, aurrez azaldu bezala, bereizmen handiagoko erreferentzia-datuekin konparatuz. Mundu-mailako erreferentzia-daturik ez dago, ordea, komunitate zientifikoak erabiltzeko prest, eta berauek sortzea oso prozesu luzea da, analisi bisual eta eskuzko edizio bidez. Hori dela-eta, artikulu honetan datu-base bat sortzen da, Burned Area Reference Database (BARD) deitua, hainbat ikerketatan jadanik sorturiko erreferentzia-datuak dituena, publiko eginak edonork erabil ditzan. Erreferentzia-datu guztiak Landsat edo Sentinel-2 irudiak erabiliz sortu ziren, 30 edo 20 m-ko bereizmenarekin, eta formatu berean jarri dira errazago erabili ahal izateko. Honela, A1eko algoritmoa garatu aurretik eginiko analisi espektralerako sortutako erreferentzia-datuak bertan sartuta daude, 52 eremutan bi S2 irudiren artean detektatuak, eta baita artikulu berean FireCCISFD11 produktua baliozkotzeko erabilitako erreferentzia-datuak ere, Landsat irudiekin 45 baliozkotze-eremutan sortuak.

AG3 – sute txikien emisioak

A1ek erakutsi zuenez, bereizmen baxuko MCD64A1 produktuak Afrikan zituen EAek ez zuten benetan erretako azaleraren zati handi bat atzematen, MODIS irudien 500 m-ko bereizmenak ezin baitzituen sute txikienak detektatu. Hori dela-eta, artikulu berri honetan sute txikiei esker erretako azalera osoaren igoera analizatu nahi izan zen, baita orain arte detektatu gabeko sute hauek landaretza erretzeagatik atmosferara igorritako gasak ere. FireCCISFD11 produktuak, 20 m-ko bereizmenarekin, ez zuen bereizmen baxuko produktuekiko aldaketa handirik erakutsi sute handienei zegokienez, baina MCD64A1ek baino 15 aldiz azalera handiagoa detektatu zuen 100 ha baino gutxiagoko suteak bakarrik kontuan hartuz gero. FireCCISFD11en laguntzaz zenbatetsitako karbono-emisioak 1,44 Pg izan ziren 2016 urtean SHAn; honen aldean, 0,71 Pg karbono bakarrik igorri zirela zenbatetsi zen MCD64A1 produktuan oinarrituz, edo 1,09 Pg estatistikoki zenbatetsitako sute txikien ekarpena kontuan hartuz.

AG4 – Afrikako EAen bigarren produktua

A1eko FireCCISFD11 produktua ESAren Fire_cci proiektuaren barnean garatu eta sortu zen, eta SHAn 2016 urtean erretako azalerak erakusten zituen. Proiektu honetan bertan, beranduago, produktu honen bertsio berri bat sortu da, FireCCISFD20 deitua, eremu bereko baina 2019 urteko EA detektatzen dituena, eta honen garapena eta emaitzak azaltzen ditu azken artikulu honek. 2016ko produktuarekiko ezberdintasun garrantzitsuenak bi dira: a) erabilgarri dauden S2 irudien kopurua bikoiztu egin da, 2019an bi satelite baitaude (Sentinel-2B espazioratu gabea zen artean 2016an), eta b) bereizmen handiagoko VIIRS sentsorearen datuetatik eratorritako sute aktiboen produktua erabiltzen du, MODIS irudien 1 km-ko bereizmenarekin aldean 375 m dituelarik.

Bereizmen baxuko FireCCI51 eta MCD64A1 produktuek baino FireCCISFD20k nabarmen errore gutxiago zituela ikusi zen A1ean bezalaxe, omisioari zegokionez batez ere. 2019 urtean guztira erretako azalera 2016koaren berbera izan zen ia: 4,8 eta 4,9 milioi km^2, hurrenez hurren. Honek FireCCI51 eta MCD64A1ekiko %100 inguruko igoera esan nahi du, hau da, bereizmen baxuko produktuek EAen erdia baino ez zuten detektatzen, beste erdia sute txikiek osatzen baitzuten.

5. Conclusiones

Esta tesis ha cumplido su principal objetivo mediante la creación de varios procesos y algoritmos para la detección de áreas quemadas, basados en imágenes de media resolución espacial: Sentinel-2 (10-20 m) y Landsat (30 m). Los tres algoritmos creados a escala regional (Chile, P3), continental (África, P1) y global (P4) son totalmente automáticos, por lo que no exigen ningún tipo de intervención por parte del usuario y se pueden aplicar sistemáticamente para detectar AQ de cualquier período a partir de las primeras adquisiciones de imágenes de media resolución espacial (década de los 80 para Landsat, finales de 2015 para S2) o productos de fuegos activos (finales de 2000 para los *hotspots* de MODIS, 2012 en el caso de VIIRS). Las herramientas BAMT de la P2, en cambio, requieren de la supervisión de un usuario para el entrenamiento del algoritmo, pero los resultados son más precisos y permiten generar perímetros de referencia suficientemente fiables para validar otros productos de AQ.

La primera publicación (P1) consistió en la creación de un algoritmo que detectara AQ en el África subsahariana a partir de imágenes de Sentinel-2 a 20 m de resolución, y aplicar dicho algoritmo sobre datos de un año completo (2016). El proceso consistía en comparar la imagen de cada fecha con cada una de varias imágenes previas, para así compensar la falta de datos en zonas nubladas. En cada uno de estos pares de imágenes se ejecutaba el proceso principal del algoritmo para detectar AQ. Este proceso se basa principalmente en la banda de reflectividad del infrarrojo cercano (NIR) y los índices espectrales MIRBI y NBR2 de ambas imágenes S2, y en los fuegos activos derivados del sensor MODIS con 1 km de resolución espacial. Estas bandas e índices de las imágenes fueron seleccionadas en el análisis espectral realizado inicialmente porque mostraron mayor capacidad de discriminar áreas quemadas de las no quemadas que otras bandas, tanto en las fechas post-incendio como en las diferencias temporales entre ambas fechas. La banda espectral NIR y las dos del SWIR (en las que se basan los índices MIRBI y NBR2) ya han sido ampliamente usadas en los productos globales de AQ hasta la fecha (Simon et al., 2004; Tansey et al., 2004; Roy et al., 2008; Giglio et al., 2018; Long et al., 2019; Lizundia-Loiola et al., 2020). La estrategia de usar los incendios activos para elegir candidatos de píxeles quemados según su cercanía a los *hotspots* tampoco es nueva y ha sido empleada en varios algoritmos (Roy et al., 2008; Alonso-Canas y Chuvieco, 2015; Giglio et al., 2018; Lizundia-Loiola et al., 2020), ya que ayuda a descartar posibles falsos positivos y reducir errores de comisión. El empleo del producto de incendios activos del sensor VIIRS habría sido preferible, pero éste aún no estaba disponible cuando se desarrolló este algoritmo.

Gran parte de los errores de comisión observados en la validación del producto FireCCISFD11 se debe a nubes y sombras de nubes que no se enmascararon adecuadamente al principio del algoritmo, y que por tanto fueron detectadas como quemadas. Además, usar diferencias simples entre dos imágenes sin observar la evolución en otras fechas adyacentes facilita este tipo de comisión (este problema se soluciona satisfactoriamente en la P4). Otro origen de comisión fueron los campos de cultivo, ya que su señal espectral antes y después de recoger la cosecha suele parecerse a los cambios observados en la vegetación afectada por los incendios; su confusión con las AQ es también un problema frecuente en otros productos (Goodwin y Collett, 2014; Vanderhoof et al., 2017; Giglio et al., 2018; Long et al., 2019; Hawbaker et al., 2020). A pesar de todo, los errores de omisión fueron mayores que los de comisión, ubicados en áreas quemadas de menor severidad cuya señal espectral no era tan fuerte para detectarlos. Este trabajo confirmó la importancia de detectar AQ a partir de imágenes de media resolución, pero también mostró las altas capacidades de almacenaje y procesamiento de datos que requiere, ya que se llegó a necesitar espacio de almacenaje de hasta 150 TB para las

imágenes iniciales y los datos intermedios creados durante la ejecución del algoritmo. Debido a esto, todos los siguientes trabajos están implementados en una plataforma para procesamiento de datos en la nube, Google Earth Engine (GEE).

La P3 fue un primer intento de implementar un algoritmo automático regional en GEE en Chile, a 20 m de resolución con imágenes de S2. El algoritmo consistía en un clasificador *Random Forest* aplicado sobre dos imágenes correspondientes a los periodos pre- y post-incendio. Debido a que el proceso era muy simple, su ejecución fue rápida y permitió procesar todo el territorio chileno en poco tiempo. Se crearon tres versiones diferentes, cada una con más áreas de entrenamiento que la anterior, lo que demostró la importancia de entrenar bien ambas categorías para una adecuada clasificación; la categoría más complicada de entrenar fue la no quemada. Al igual que en la P1, los errores de comisión más complejos de eliminar fueron los campos de cultivo, y las nubes y sus sombras no enmascaradas adecuadamente. Una vez más, los errores de omisión resultaron ser píxeles quemados de menor severidad, en general ubicados en zonas boscosas.

La cuarta publicación (P4) trata de solventar los puntos débiles de los algoritmos previos y así crear uno global y totalmente automático en GEE. A diferencia de los dos algoritmos anteriores, que se basaban en diferencias simples entre dos imágenes correspondientes a los periodos pre- y post-incendio, en este caso se evalúa la evolución de cada píxel a lo largo de varias imágenes de la serie temporal. Esto permite evitar errores de comisión en sombras y nubes, ya que su señal, aunque pueda ser similar, no permanece en fechas posteriores al contrario de las AQ; al trabajar con diferencias simples estos píxeles suelen ser detectados como quemados. El algoritmo también es suficientemente flexible para adaptarse a las características espectrales de las AQ en cada ecosistema y región del planeta: aunque utilice las mismas cuatro bandas e índices espectrales, el algoritmo analiza la capacidad de cada una para discriminar AQ en cada caso, y otorga más importancia a ciertas bandas o índices dependiendo de esta capacidad de discriminación. Los primeros dos algoritmos eran más rígidos en este sentido, ya que el de FireCCISFD11 empleaba umbrales fijos para toda el África subsahariana, y el algoritmo de Chile se basaba en puntos de entrenamiento seleccionados exclusivamente dentro del país.

Este último algoritmo, además, está diseñado para procesar imágenes de los satélites tanto Landsat como Sentinel-2, ya que las bandas en ambas imágenes cubren similares regiones del espectro y son por tanto relativamente comparables. Siempre que haya imágenes disponibles, puede basarse en cualquiera de los dos conjuntos de imágenes, detectando así AQ a una resolución de 10, 20 o 30 m, dependiendo del tipo de imagen que se haya usado. Esto permite procesar toda la serie temporal desde 2016 hasta la actualidad a 10 o 20 m de resolución con imágenes S2, o desde 2001 hasta la actualidad con imágenes Landsat; en realidad hay datos Landsat anteriores a esa fecha, pero el algoritmo también requiere el producto de incendios activos derivado de datos MODIS que sólo está disponible a partir del año 2001. Al estar el algoritmo directamente implementado en GEE, resulta muy simple elegir el tipo de imágenes y la correspondiente resolución.

Los resultados de cada uno de los tres algoritmos han sido comparados con datos de referencia, aunque sólo FireCCISFD11 y los productos del algoritmo global de la P4 (BAS2-10, BAS2-20 y BAL-30) han sido comparados con productos de baja resolución y validados en realidad (con datos de referencia de mayor resolución espacial). Tanto los productos de baja resolución como los de media resolución presentan un mayor error de omisión que de comisión. El primer producto presenta errores de comisión de 19% y de omisión de 26%. Los tres productos de la última publicación (P4), en cambio, presentan errores de comisión cercanos al 10%, pero un aumento significativo de la omisión a valores entre 27–35%,

aumentando a medida que la resolución espacial disminuye. Los productos derivados a partir de imágenes S2 presentan prácticamente los mismos errores en ambas resoluciones (10 y 20 m), pero las AQ a 20 m son procesadas con más rapidez; las AQ a 30 m a partir de imágenes Landsat son las que mayores errores contienen. En comparación, los errores de los productos de baja resolución (MCD64A1 y FireCCI51) son más visibles: comisión entre 20–55% y omisión superior al 50%, según esta misma publicación y otros estudios (Padilla et al., 2015; Boschetti et al., 2019; Lizundia-Loiola et al., 2020; Franquesa et al., 2022a).

El producto FireCCISFD11 fue la primera vez que se usaban imágenes de media resolución en un área tan extensa (casi continental), y demostró que los únicos productos hasta la fecha, todos de baja resolución, estaban omitiendo considerablemente los incendios más pequeños y por tanto subestimando la superficie total quemada. Según FireCCISFD11, la inclusión de las AQ más pequeñas supuso un aumento del 80% en comparación con la superficie detectada por el producto MCD64A1, o de más de un 50% en comparación con FireCCI51, frente al aumento de tan solo 32% en el mismo continente estimado por un estudio previo donde se simulaba la aportación de los incendios más pequeños a partir de incendios activos (Randerson et al., 2012). Este es un dato importante si se tiene en cuenta que el área de estudio, el África subsahariana, contiene el 70% de la superficie quemada global. En las tres áreas de prueba de la P4, el aumento del área quemada en el producto BAS2-20, aunque menor, es del 35 o 65%, dependiendo de si se compara con FireCCI51 o MCD64A1 respectivamente.

La Figura 8 compara, en una zona de muestra del suroeste de Mali, varios productos de AQ: dos productos globales de baja resolución, y los de media resolución creados en dos publicaciones de esta tesis. Las AQ más grandes presentan tamaños y formas parecidas en todos los productos, pero los incendios más pequeños, sobre todo ubicados en el centro y sur de la zona de muestra, no fueron detectados por FireCCI51 y MCD64A1. Entre los productos de media resolución, parece que FireCCISFD11 detecta mejor las AQ, siendo estas más compactas que en los tres productos de la P4; esto era algo esperable, ya que el algoritmo de FireCCISFD11 está específicamente diseñado para las características espectrales de los incendios africanos, mientras que el algoritmo de la última publicación es global, y tiene que adaptarse a las características locales de cada caso en la mejor manera posible. En cuanto a las fechas detectadas de los incendios, los productos de baja resolución suelen detectar las AQ al mismo tiempo o antes que los productos de media resolución, debido a la frecuencia de imágenes de cada sensor: un solo día para las imágenes MODIS, pero 10 días para Sentinel-2 (en 2016 sólo había un satélite todavía) y 8 días para Landsat (combinando los satélites Landsat-7 y -8). Así, al adquirir el sensor MODIS imágenes con mayor frecuencia, es más probable que observe antes un área quemada que los satélites S2 y Landsat. Cabe destacar que las áreas quemadas a principios de diciembre no fueron detectadas hasta finales del mismo mes por el producto FireCCISFD11, aunque los mapas BAS2-10 y BAS2-20, creados a partir de las mismas imágenes S2, no muestren este retraso.
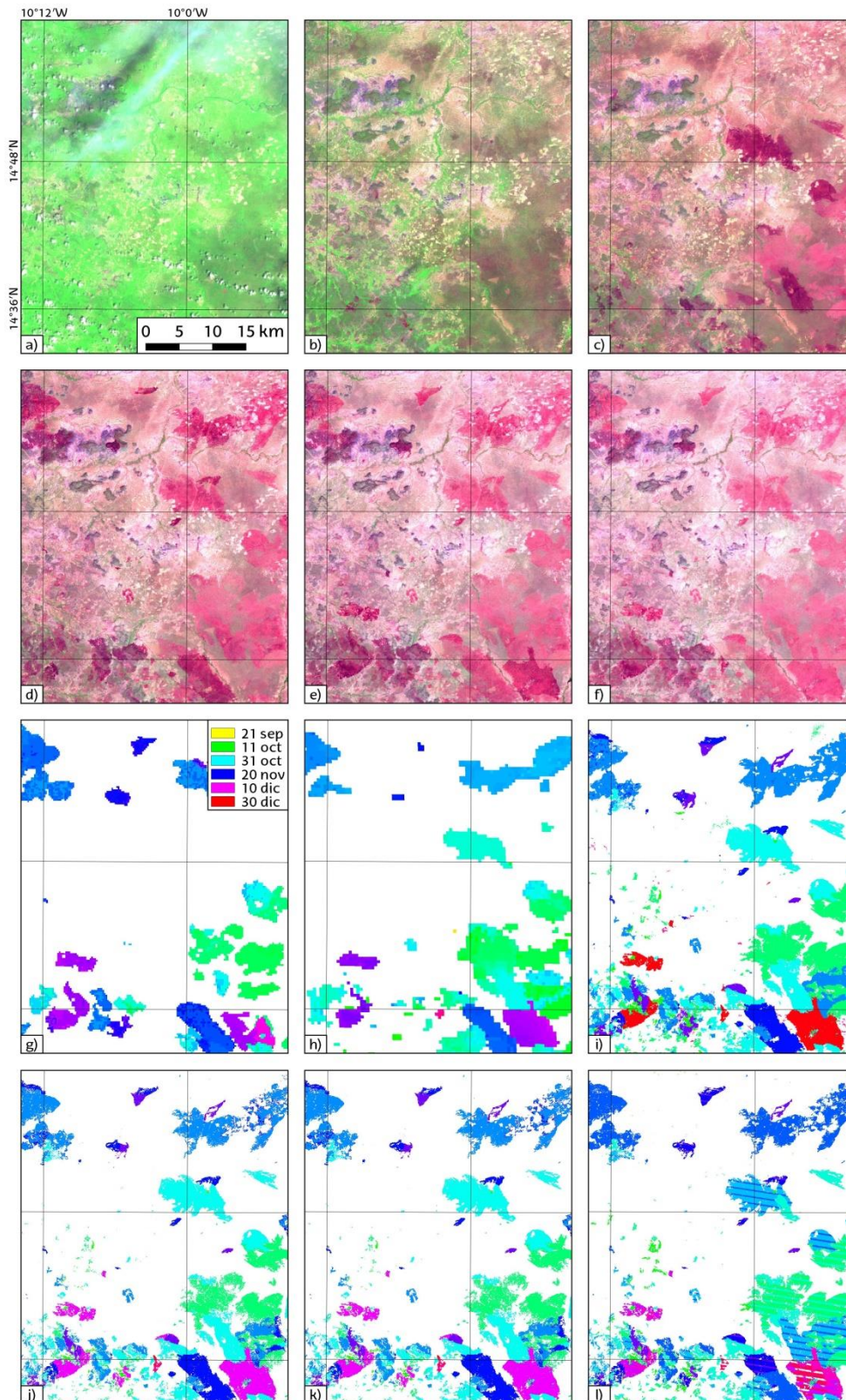
Figura 8. Comparación de varios productos en una zona de muestra, ubicada en el suroeste de Mali, con áreas quemadas a finales de 2016. Las imágenes a-f muestran composiciones en falso color para las siguientes fechas: 21 de septiembre, 11 de octubre, 31 de octubre, 20 de noviembre, 10 de diciembre y 30 de diciembre, separadas entre sí por 20 días. A continuación se muestran los productos de baja resolución FireCCI51 (g) y MCD64A1 (h), y los mapas creados durante esta tesis: FireCCISFD11 (i) en la P1, y BAS2-10 (j), BAS2-20 (k) y BAL-30 (l) en la P4. Las fechas de la detección de los incendios en la leyenda corresponden a las imágenes en color a-f.

Por último, es importante recalcar que las herramientas BAMT de la P2 permiten a cualquier usuario que disponga de una cuenta de Google Earth Engine crear mapas de AQ de media resolución espacial en regiones extensas como un país, o incluso en un continente, y además generar perímetros de referencia para validar estos mapas (o algún otro producto de AQ). Los procesos para detectar AQ (tanto cartografías extensas de AQ como perímetros de referencia) consisten en una supervisión clasificada, y son una continuación del software BAMS (Bastarrika et al., 2014) con varias mejoras: se basan exclusivamente en una plataforma no comercial, se permite trabajar con imágenes S2, y el algoritmo se basa en un clasificador más robusto (*Random Forest*) permitiendo el entrenamiento de la categoría quemada y no quemada (en BAMS únicamente se podía entrenar la categoría quemada). La herramienta para la selección de áreas de validación es también la primera implementación de la metodología de muestreo estratificado aleatorio (Padilla et al., 2017) que se puede acceder de forma libre. La validez de estas herramientas fue confirmada en dos casos prácticos. En Australia, las AQ detectadas a partir de imágenes Landsat a 30 m de resolución fueron validadas con datos de referencia creados con imágenes S2 a 20 m, y se obtuvieron errores alrededor del 10%, los más bajos de todos los trabajos realizados en esta tesis doctoral. En el caso de Canadá, los resultados no fueron validados pero sí comparados con datos oficiales canadienses, y nuestras AQ resultaron ser visualmente más precisas.

Diseñar estas herramientas y aplicarlas en casos reales permitió comprender mejor las limitaciones de la plataforma GEE. Por un lado, se ha demostrado que las herramientas desarrolladas permiten generar una cartografía de AQ en una extensión de varios millones de km^2, procesando en unos pocos días ingentes cantidades de imágenes equivalentes a varios TB de datos, aunque el proceso de entrenamiento del clasificador requiere de bastante tiempo y paciencia por la cantidad de información que debe gestionar. Por otro lado, la mayoría de los algoritmos de AQ desarrollados durante esta tesis doctoral aplica un proceso donde primero se identifican las semillas (píxeles con una señal fuerte de estar quemados), y luego se expanden las regiones a su alrededor hasta llegar a cierto valor de corte. De entre todas las funciones disponibles en GEE, la mejor opción encontrada para implementar esta cartografía en dos fases fue vectorizar el resultado para identificar los polígonos que no contenían ninguna semilla y eliminarlos; sin embargo, la vectorización de una capa ráster consume mucha memoria en GEE, y en algunos casos excede el límite disponible para cada usuario. Por último, la herramienta para la selección de áreas de validación está aún bastante limitada por las propias limitaciones de memoria de GEE a la hora de consultar todo el catálogo de imágenes. Conocer estas limitaciones resultó valioso para los trabajos de la última publicación (P4), también implementada en GEE.

Como resumen, se ha logrado mejorar la detección de AQ a partir de imágenes de media resolución espacial, en el rango de 10-30 m. Si bien dos de los algoritmos son regionales o continentales y el único algoritmo global necesita una mayor investigación para ser aplicado operativamente, se espera lanzar en un breve espacio de tiempo el algoritmo a escala global. Ha quedado demostrada también la importancia de detectar AQ a estas resoluciones espaciales, ya que los productos de baja resolución omiten una buena proporción de los incendios. Según datos extraídos de la P1, la inclusión de incendios pequeños en África aumenta en un 80% la superficie quemada total con respecto a MCD64A1; en las tres áreas de prueba de la P4, el aumento, aunque menor, es entre el 35 y el 65%, dependiendo de si se compara con FireCCI51 o MCD64A1. La inclusión de estos incendios permitirá conocer mejor los impactos que tiene en la sociedad y estimar los gases y aerosoles emitidos a la atmósfera con mayor precisión (PA3), de cara a una modelización más precisa del cambio climático. Por último, las herramientas BAMT

permiten a cualquier usuario crear sus propios mapas de AQ, así como validar estos mapas u otros productos mediante la creación de perímetros de referencia de gran precisión. Mientras se está redactando esta tesis, este artículo lleva año y medio publicado, y las herramientas están empezando a ser utilizados en otros estudios (Chuvieco et al., 2022; Franquesa et al., 2022a, 2022b; Majdalani et al., 2022).

De esta tesis doctoral se pueden extraer dos líneas futuras principales de investigación. La primera gira en torno al desarrollo de las herramientas BAMT. Éstas, aunque ya están listas para ser usadas por la comunidad científica, requieren de una investigación más profunda de cara a mejorar su rendimiento, tanto en lo que se refiere a la selección de áreas de validación, así como en la implementación de los algoritmos en dos fases en formato ráster y evitando así la vectorización.

La segunda línea, más importante, debería enfocarse en finalizar el algoritmo preliminar publicado (P4) de manera que éste pueda ser aplicado de forma sistemática y global. Por un lado, debería mejorarse la implementación en dos fases, contemplada también para las herramientas BAMT. Por otro lado, la sustitución del producto de fuegos activos VIIRS también podría mejorar los resultados, debido a su mayor resolución espacial de 375 m frente a 1 km de los *hotspots* MODIS que se usan actualmente. Idealmente, el algoritmo de detección de AQ debería ser independiente de los fuegos activos, siguiendo el enfoque de GABAM, el único algoritmo automático global que no depende de ellos; el resto de estudios que tiene dicha independencia son algoritmos locales o regionales (Liu et al., 2018; Filipponi, 2019; Roy et al., 2019; Hawbaker et al., 2020; Llorens et al., 2021; Pinto et al., 2021). Para prescindir de los fuegos activos, debería utilizarse una ingente cantidad de datos de muestra de manera que el sistema fuera suficientemente robusto como para entender la señal de los incendios en diferentes ecosistemas y fechas, evitando la confusión con otras cubiertas. En este sentido, métodos basados en el aprendizaje automático (en inglés *maching learning*) y el aprendizaje profundo (en inglés *deep learning*) podrían resultar extremadamente útiles; de hecho, recientemente se han publicado varios estudios que emplean estas técnicas para la detección de AQ (Knopp et al., 2020; Hu et al., 2021; Martins et al., 2022; Prabowo et al., 2022).

6. Erreferentziak

Alonso-Canas, I., Chuvieco, E., 2015. Global burned area mapping from ENVISAT-MERIS and MODIS active fire data. *Remote Sens. Environ.* 163, 140–152. https://doi.org/10.1016/j.rse.2015.03.011

Andela, N., Morton, D.C., Giglio, L., Chen, Y., Van Der Werf, G.R., Kasibhatla, P.S., DeFries, R.S., Collatz, G.J., Hantson, S., Kloster, S., Bachelet, D., Forrest, M., Lasslop, G., Li, F., Mangeon, S., Melton, J.R., Yue, C., Randerson, J.T., 2017. A human-driven decline in global burned area. *Science* 356, 1356–1362. https://doi.org/10.1126/science.aal4108

Ban, Y., Zhang, P., Nascetti, A., Bevington, A.R., Wulder, M.A., 2020. Near Real-Time Wildfire Progression Monitoring with Sentinel-1 SAR Time Series and Deep Learning. *Sci. Rep.* 10, 1322 (2020). https://doi.org/10.1038/s41598-019-56967-x

Bar, S., Parida, B.R., Pandey, A.C., 2020. Landsat-8 and Sentinel-2 based Forest fire burn area mapping using machine learning algorithms on GEE cloud platform over Uttarakhand, Western Himalaya. *Remote Sens. Appl. Soc. Environ.* 18, 100324. https://doi.org/10.1016/j.rsase.2020.100324

Bastarrika, A., Alvarado, M., Artano, K., Martinez, M., Mesanza, A., Torre, L., Ramo, R., Chuvieco, E., 2014. BAMS: A Tool for Supervised Burned Area Mapping Using Landsat Data. *Remote Sens.* 6, 12360–12380. https://doi.org/10.3390/rs61212360

Belenguer-Plomer, M.A., Tanase, M.A., Fernandez-Carrillo, A., Chuvieco, E., 2019. Burned area detection and mapping using Sentinel-1 backscatter coefficient and thermal anomalies. *Remote Sens. Environ.* 233, 111345. https://doi.org/10.1016/j.rse.2019.111345

Belenguer-Plomer, M.A., Tanase, M.A., Chuvieco, E., Bovolo, F., 2021. CNN-based burned area mapping using radar and optical data. *Remote Sens. Environ.* 260, 112468. https://doi.org/10.1016/j.rse.2021.112468

Boschetti, L., Roy, D.P., Justice, C.O., Humber, M.L., 2015. MODIS–Landsat fusion for large area 30m burned area mapping. *Remote Sens. Environ.* 161, 27–42. https://doi.org/10.1016/j.rse.2015.01.022

Boschetti, L., Stehman, S. V., Roy, D.P., 2016. A stratified random sampling design in space and time for regional to global scale burned area product validation. *Remote Sens. Environ.* 186, 465–478. https://doi.org/10.1016/j.rse.2016.09.016

Boschetti, L., Roy, D.P., Giglio, L., Huang, H., Zubkova, M., Humber, M.L., 2019. Global validation of the collection 6 MODIS burned area product. *Remote Sens. Environ.* 235, 111490. https://doi.org/10.1016/j.rse.2019.111490

Bowman, D.M.J.S., Williamson, G.J., Abatzoglou, J.T., Kolden, C.A., Cochrane, M.A., Smith, A.M.S., 2017. Human exposure and sensitivity to globally extreme wildfire events. *Nat. Ecol. Evol.* 1, 0058 (2017). https://doi.org/10.1038/s41559-016-0058

Bowman, D., Williamson, G., Yebra, M., Lizundia-Loiola, J., Pettinari, M.L., Shah, S., Bradstock, R., Chuvieco, E., 2020. Wildfires: Australia needs national monitoring agency. *Nature.* https://doi.org/10.1038/d41586-020-02306-4

Breiman, L., 2001. Random Forests. *Mach. Learn.* 45, 5–32. https://doi.org/10.1023/A:1010933404324

Chuvieco, E., Congalton, R.G., 1988. Mapping and inventory of forest fires from digital processing of tm data. *Geocarto Int.* 3, 41–53. https://doi.org/10.1080/10106048809354180

Chuvieco, E., 2010. Teledetección ambiental: La observación de la Tierra desde el Espacio. *Editorial Ariel*, ISBN: 9788434434981

Chuvieco, E., Mouillot, F., van der Werf, G.R., San Miguel, J., Tanase, M., Koutsias, N., Garcia, M., Yebra, M., Padilla, M., Gitas, I., Heil, A., Hawbaker, T.J., Giglio, L., 2019. Historical background and current developments for mapping burned area from satellite Earth observation. *Remote Sens. Environ.* 225, 45–64. https://doi.org/10.1016/j.rse.2019.02.013

Chuvieco, E., Roteta, E., Sali, M., Stroppiana, D., Boettcher, M., Kirches, G., Storm, T., Khairoun, A., Pettinari, M.L., Franquesa, M., Albergel, C., 2022. Building a small fire database for Sub-Saharan Africa from Sentinel-2 high-resolution images. *Sci. Total Environ.* 845, 157139. https://doi.org/10.1016/j.scitotenv.2022.157139

Congalton, R.G., Green, K., 2008. Assessing the Accuracy of Remotely Sensed Data. *CRC Press.* https://doi.org/10.1201/9781420055139

Crowley, M.A., Cardille, J.A., White, J.C., Wulder, M.A., 2019. Generating intra-year metrics of wildfire progression using multiple open-access satellite data streams. *Remote Sens. Environ.* 232, 111295. https://doi.org/10.1016/j.rse.2019.111295

Daldegan, G.A., Roberts, D.A., Ribeiro, F. de F., 2019. Spectral mixture analysis in Google Earth Engine to model and delineate fire scars over a large extent and a long time-series in a rainforest-savanna transition zone. *Remote Sens. Environ.* 232, 111340. https://doi.org/10.1016/j.rse.2019.111340

Daniau, A.L., Goñi, M.F.S., Martinez, P., Urrego, D.H., Bout-Roumazeilles, V., Desprat, S., Marlon, J.R., 2013. Orbital-scale climate forcing of grassland burning in southern Africa. *Proc. Natl. Acad. Sci. USA* 110, 5069–5073. https://doi.org/10.1073/pnas.1214292110

Dice, L.R., 1945. Measures of the Amount of Ecologic Association Between Species. *Ecology* 26, 297–302. https://doi.org/10.2307/1932409

Doerr, S.H., Santín, C., 2016. Global trends in wildfire and its impacts: Perceptions versus realities in a changing world. *Philos. Trans. R. Soc. B Biol. Sci.* 371. https://doi.org/10.1098/rstb.2015.0345

European Space Agency (ESA), s.f. *Sentinel-2.* https://www.esa.int/Applications/Observing_the_Earth/Copernicus/Sentinel-2

Filipponi, F., 2019. Exploitation of sentinel-2 time series to map burned areas at the national level: A case study on the 2017 Italy wildfires. *Remote Sens.* 11, 622. https://doi.org/10.3390/rs11060622

Fleiss, J.L., 1981. Statistical methods for rates and proportions. *Wiley*, ISBN: 9780471064282

Forkel, M., Dorigo, W., Lasslop, G., Teubner, I., Chuvieco, E., Thonicke, K., 2017. A data-driven approach to identify controls on global fire activity from satellite and climate observations (SOFIA V1). *Geosci. Model Dev.* 10, 4443–4476. https://doi.org/10.5194/gmd-10-4443-2017

Franquesa, M., Lizundia-Loiola, J., Stehman, S. V., Chuvieco, E., 2022a. Using long temporal reference units to assess the spatial accuracy of global satellite-derived burned area products. *Remote Sens. Environ.* 269, 112823. https://doi.org/10.1016/j.rse.2021.112823

Franquesa, M., Rodríguez-Montellano, A.M., Chuvieco, E., Aguado, I., 2022b. Reference Data Accuracy Impacts Burned Area Product Validation: The Role of the Expert Analyst. *Remote Sens.* 14, 4354. https://doi.org/10.3390/rs14174354

García, M.J.L., Caselles, V., 1991. Mapping burns and natural reforestation using thematic Mapper data. *Geocarto Int.* 6, 31–37. https://doi.org/10.1080/10106049109354290

García-Haro, F.J., Gilabert, M.A., Meliá, J., 2001. Monitoring fire-affected areas using Thematic Mapper data. *Int. J. Remote Sens.* 22, 533–549. https://doi.org/10.1080/01431160050505847

Gaveau, D.L.A., Descals, A., Salim, M.A., Sheil, D., Sloan, S., 2021. Refined burned-area mapping protocol using Sentinel-2 data increases estimate of 2019 Indonesian burning. *Earth Syst. Sci. Data* 13, 5353–5368. https://doi.org/10.5194/essd-13-5353-2021

Gibson, R., Danaher, T., Hehir, W., Collins, L., 2020. A remote sensing approach to mapping fire severity in south-eastern Australia using sentinel 2 and random forest. *Remote Sens. Environ.* 240, 111702. https://doi.org/10.1016/j.rse.2020.111702

Giglio, L., Loboda, T., Roy, D.P., Quayle, B., Justice, C.O., 2009. An active-fire based burned area mapping algorithm for the MODIS sensor. *Remote Sens. Environ.* 113, 408–420. https://doi.org/10.1016/j.rse.2008.10.006

Giglio, L., Boschetti, L., Roy, D.P., Humber, M.L., Justice, C.O., 2018. The Collection 6 MODIS burned area mapping algorithm and product. *Remote Sens. Environ.* 217, 72–85. https://doi.org/10.1016/j.rse.2018.08.005

Goldammer, J.G., Statheropoulos, M., Andreae, M.O., 2008. Chapter 1 Impacts of Vegetation Fire Emissions on the Environment, Human Health, and Security: A Global Perspective. In: Bytnerowicz, A., Arbaugh, M.J., Riebau, A.R., Andersen, C. (eds.). Wildland Fires and Air Pollution. *D. in E. S.* 8, 3–36. https://doi.org/10.1016/S1474-8177(08)00001-6

Goodwin, N.R., Collett, L.J., 2014. Development of an automated method for mapping fire history captured in Landsat TM and ETM+ time series across Queensland, Australia. *Remote Sens. Environ.* 148, 206–221. https://doi.org/10.1016/j.rse.2014.03.021

Gorelick, N., Hancher, M., Dixon, M., Ilyushchenko, S., Thau, D., Moore, R., 2017. Google Earth Engine: Planetary-scale geospatial analysis for everyone. *Remote Sens. Environ.* 202, 18–27. https://doi.org/10.1016/j.rse.2017.06.031

Hansen, M.C., Potapov, P. V., Moore, R., Hancher, M., Turubanova, S.A., Tyukavina, A., Thau, D., Stehman, S. V., Goetz, S.J., Loveland, T.R., Kommareddy, A., Egorov, A., Chini, L., Justice, C.O., Townshend, J.R.G., 2013. High-resolution global maps of 21st-century forest cover change. *Science* 342, 850–853. https://doi.org/10.1126/science.1244693

Hawbaker, T.J., Vanderhoof, M.K., Beal, Y.-J., Takacs, J.D., Schmidt, G.L., Falgout, J.T., Williams, B., Fairaux, N.M., Caldwell, M.K., Picotte, J.J., Howard, S.M., Stitt, S., Dwyer, J.L., 2017. Mapping burned areas using dense time-series of Landsat data. *Remote Sens. Environ.* 198, 504–522. https://doi.org/10.1016/j.rse.2017.06.027

Hawbaker, T.J., Vanderhoof, M.K., Schmidt, G.L., Beal, Y.J., Picotte, J.J., Takacs, J.D., Falgout, J.T., Dwyer, J.L., 2020. The Landsat Burned Area algorithm and products for the conterminous United States. *Remote Sens. Environ.* 244, 111801. https://doi.org/10.1016/j.rse.2020.111801

Hayes, K. (13-08-2021). Wildfire smoke reaches North Pole for 1st time in recorded history. *FOX35 Orlando.* https://www.fox35orlando.com/news/wildfire-smoke-reaches-north-pole-for-1st-time-in-recorded-history

Hu, X., Ban, Y., Nascetti, A., 2021. Uni-Temporal Multispectral Imagery for Burned Area Mapping with Deep Learning. *Remote Sens.* 13, 1509. https://doi.org/10.3390/rs13081509

Hudak, A.T., Brockett, B.H., 2004. Mapping fire scars in a southern African savannah using landsat imagery. *Int. J. Remote Sens.* 25, 3231–3243. https://doi.org/10.1080/01431160310001632666

Jakubauskas, M.E., Lulla, K.P., Mausel, P.W., 1990. Assessment of vegetation change in a fire-altered forest landscape. *Photogramm. Eng. Remote Sens.* 56, 371–377.

Justice, C., Belward, A., Morisette, J., Lewis, P., Privette, J., Baret, F., 2000. Developments in the "validation" of satellite sensor products for the study of the land surface. *Int. J. Remote Sens.* 21, 3383–3390. https://doi.org/10.1080/014311600750020000

Kaufman, Y.J., Remer, L.A., 1994. Detection of Forests Using Mid-IR Reflectance: An Application for Aerosol Studies. *IEEE Trans. Geosci. Remote Sens.* 32, 672–683. https://doi.org/10.1109/36.297984

Key, C.H., Benson, N., 2003. The Normalized Burn Ratio (NBR): A Landsat TM radiometric measure of burn severity. *US Geol. Surv. North. Rocky Mt. Sci. Center.*

Knopp, L., Wieland, M., Rättich, M., Martinis, S., 2020. A Deep Learning Approach for Burned Area Segmentation with Sentinel-2 Data. *Remote Sens.* 12, 2422. https://doi.org/10.3390/rs12152422

Koutsias, N., Mallinis, G., Karteris, M., 2009. A forward/backward principal component analysis of Landsat-7 ETM+ data to enhance the spectral signal of burnt surfaces. *ISPRS J. Photogramm. Remote Sens.* 64, 37–46. https://doi.org/10.1016/j.isprsjprs.2008.06.004

Kramer, M. (30-08-2013). Why Big, Intense Wildfires Are the New Normal. *National Geographic.* https://www.nationalgeographic.com/science/article/130827-wildfires-yosemite-fire-firefighters-vegetation-hotshots-california-drought

Kulkarni, A. (04-10-2021). A look back at the 2021 B.C. wildfire season. *CBC News.* https://www.cbc.ca/news/canada/british-columbia/bc-wildfires-2021-timeline-1.6197751

Lindsay, B. (29-08-2018). 2018 now worst fire season on record as B.C. extends state of emergency. *CBC News.* https://www.cbc.ca/news/canada/british-columbia/state-emergency-bc-wildfires-1.4803546

Liu, J., Heiskanen, J., Maeda, E.E., Pellikka, P.K.E., 2018. Burned area detection based on Landsat time series in savannas of southern Burkina Faso. *Int. J. Appl. Earth Obs. Geoinf.* 64, 210–220. https://doi.org/10.1016/j.jag.2017.09.011

Lizundia-Loiola, J., Otón, G., Ramo, R., Chuvieco, E., 2020. A spatio-temporal active-fire clustering approach for global burned area mapping at 250m from MODIS data. *Remote Sens. Environ.* 236, 111493. https://doi.org/10.1016/j.rse.2019.111493

Lizundia-Loiola, J., Franquesa, M., Boettcher, M., Kirches, G., Pettinari, M.L., Chuvieco, E., 2021. Implementation of the Burned Area Component of the Copernicus Climate Change Service: From MODIS to OLCI Data. *Remote Sens.* 13, 4295. https://doi.org/10.3390/rs13214295

Llorens, R., Sobrino, J.A., Fernández, C., Fernández-Alonso, J.M., Vega, J.A., 2021. A methodology to estimate forest fires burned areas and burn severity degrees using Sentinel-2 data. Application to the October 2017 fires in the Iberian Peninsula. *Int. J. Appl. Earth Obs. Geoinf.* 95, 102243. https://doi.org/10.1016/j.jag.2020.102243

Long, T., Zhang, Z., He, G., Jiao, W., Tang, C., Wu, B., Zhang, X., Wang, G., Yin, R., 2019. 30m resolution global annual burned area mapping based on landsat images and Google Earth Engine. *Remote Sens.* 11, 489. https://doi.org/10.3390/rs11050489

Majdalani, G., Koutsias, N., Faour, G., Adjizian-Gerard, J., Mouillot, F., 2022. Fire Regime Analysis in Lebanon (2001–2020): Combining Remote Sensing Data in a Scarcely Documented Area. *Fire* 5, 141. https://doi.org/10.3390/fire5050141

Marlon, J.R., Bartlein, P.J., Daniau, A.L., Harrison, S.P., Maezumi, S.Y., Power, M.J., Tinner, W., Vanniére, B., 2013. Global biomass burning: A synthesis and review of Holocene paleofire records and their controls. *Quat. Sci. Rev.* 65, 5–25. https://doi.org/10.1016/j.quascirev.2012.11.029

Martins, V.S., Roy, D.P., Huang, H., Boschetti, L., Zhang, H.K., Yan, L., 2022. Deep learning high resolution burned area mapping by transfer learning from Landsat-8 to PlanetScope. *Remote Sens. Environ.* 280, 113203. https://doi.org/10.1016/j.rse.2022.113203

Miller, J.D., Thode, A.E., 2007. Quantifying burn severity in a heterogeneous landscape with a relative version of the delta Normalized Burn Ratio (dNBR). *Remote Sens. Environ.* 109, 66–80. https://doi.org/10.1016/j.rse.2006.12.006

Mouillot, F., Schultz, M.G., Yue, C., Cadule, P., Tansey, K., Ciais, P., Chuvieco, E., 2014. Ten years of global burned area products from spaceborne remote sensing-A review: Analysis of user needs and recommendations for future developments. *Int. J. Appl. Earth Obs. Geoinf.* 26, 64–79. https://doi.org/10.1016/j.jag.2013.05.014

National Aeronautics and Space Administration (NASA), s.f. *CEOS Working Group on Calibration and Validation. Land Product Validation Subgroup.* https://lpvs.gsfc.nasa.gov/index.html

National Geographic (09-08-2018). El peor desastre forestal de Chile. *National Geographic.* https://www.ngenespanol.com/naturaleza/incendios-forestales-en-chile/

Olson, D.M., Dinerstein, E., Wikramanayake, E.D., Burgess, N.D., Powell, G.V.N., Underwood, E.C., D'amico, J.A., Itoua, I., Strand, H.E., Morrison, J.C., Loucks, C.J., Allnutt, T.F., Ricketts, T.H., Kura, Y., Lamoreux, J.F., Wettengel, W.W., Hedao, P., Kassem, K.R., 2001. Terrestrial Ecoregions of the World: A New Map of Life on Earth. *Bioscience* 51, 933–938. https://doi.org/10.1641/0006-3568(2001)051[0933:TEOTWA]2.0.CO;2

Padilla, M., Stehman, S.V., Litago, J., Chuvieco, E., 2014a. Assessing the Temporal Stability of the Accuracy of a Time Series of Burned Area Products. *Remote Sens.* 6, 2050–2068. https://doi.org/10.3390/rs6032050

Padilla, M., Stehman, S. V., Chuvieco, E., 2014b. Validation of the 2008 MODIS-MCD45 global burned area product using stratified random sampling. *Remote Sens. Environ.* 144, 187–196. https://doi.org/10.1016/j.rse.2014.01.008

Padilla, M., Stehman, S. V., Ramo, R., Corti, D., Hantson, S., Oliva, P., Alonso-Canas, I., Bradley, A. V., Tansey, K., Mota, B., Pereira, J.M., Chuvieco, E., 2015. Comparing the accuracies of remote sensing global burned area products using stratified random sampling and estimation. *Remote Sens. Environ.* 160, 114–121. https://doi.org/10.1016/j.rse.2015.01.005

Padilla, M., Olofsson, P., Stehman, S. V., Tansey, K., Chuvieco, E., 2017. Stratification and sample allocation for reference burned area data. *Remote Sens. Environ.* 203, 240–255. https://doi.org/10.1016/j.rse.2017.06.041

Padilla, M., Wheeler, J., Tansey, K., 2018. ESA CCI ECV Fire Disturbance: D4.1.1 Product Validation Report, version 2.1. https://climate.esa.int/media/documents/Fire_cci_D4.1.1_PVR_v2.1.pdf

Paganini, M., Arino, O., Benvenuti, M., Cristaldi, M., Bordin, M., Coretti, C., Musone, A., 2003. ITALSCAR, a Regional Burned Forest Mapping demonstration project in Italy. In: *International Geoscience and Remote Sensing Symposium (IGARSS)*. https://doi.org/10.1109/igarss.2003.1294086

Parmesan, C., Morecroft, M.D., Trisurat, Y., Adrian, R., Anshari, G.Z., Arneth, A., Gao, Q., Gonzalez, P., Harris, R., Price, J., Stevens, N., Talukdarr, G.H., 2022. Terrestrial and Freshwater Ecosystems and Their Services. In: *Climate Change 2022: Impacts, Adaptation and Vulnerability*. Contribution of Working Group II to the Sixth Assessment Report of the Intergovernmental Panel on Climate Change [Pörtner, H.O., Roberts, D.C., Tignor, M., Poloczanska, E.S., Mintenbeck, K., Alegría, A., Craig, M., Langsdorf, S., Löschke, S., Möller, V., Okem, A., Rama, B. (eds.)]. Cambridge University Press, Cambridge, UK and New York, NY, USA, 197–377. https://doi.org/10.1017/9781009325844.004

Pereira, J.M.C., Sá, A.C.L., Sousa, A.M.O., Silva, J.M.N., Santos, T.N., Carreiras, J.M.B., 1999. Spectral characterisation and discrimination of burnt areas. In: Chuvieco, E. (ed.). Remote Sensing of Large Wildfires. *Springer, Berlin, Heidelberg*, 123–138. https://doi.org/10.1007/978-3-642-60164-4_7

Petrakis, R.E., Villarreal, M.L., Wu, Z., Hetzler, R., Middleton, B.R., Norman, L.M., 2018. Evaluating and monitoring forest fuel treatments using remote sensing applications in Arizona, U.S.A. *For. Ecol. Manage.* 413, 48–61. https://doi.org/10.1016/j.foreco.2018.01.036

Pinto, M.M., Trigo, R.M., Trigo, I.F., Dacamara, C.C., 2021. A Practical Method for High-Resolution Burned Area Monitoring Using Sentinel-2 and VIIRS. *Remote Sens.* 13, 1608. https://doi.org/10.3390/rs13091608

Prabowo, Y., Sakti, A.D., Pradono, K.A., Amriyah, Q., Rasyidy, F.H., Bengkulah, I., Ulfa, K., Candra, D.S., Imdad, M.T., Ali, S., 2022. Deep Learning Dataset for Estimating Burned Areas: Case Study, Indonesia. *Data* 7, 78. https://doi.org/10.3390/data7060078

Pyne, S.J., 1997. World fire: the culture of fire on earth. *University of Washington press*, ISBN: 9780295975931

Randerson, J.T., Chen, Y., van der Werf, G.R., Rogers, B.M., Morton, D.C., 2012. Global burned area and biomass burning emissions from small fires. *J. Geophys. Res. Biogeosciences* 117, G04012. https://doi.org/10.1029/2012JG002128

Reid, C.E., Brauer, M., Johnston, F.H., Jerrett, M., Balmes, J.R., Elliott, C.T., 2016. Critical review of health impacts of wildfire smoke exposure. *Environ. Health Perspect.* 124, 1334–1343. https://doi.org/10.1289/ehp.1409277

Roos, C.I., Scott, A.C., Belcher, C.M., Chaloner, W.G., Aylen, J., Bird, R.B., Coughlan, M.R., Johnson, B.R., Johnston, F.H., McMorrow, J., Steelman, T., Archibald, S., Balch, J., Beerling, D., Bond, W., Bowman, D., Carroll, M., Doerr, S., Gazzard, R., Hadden, R., Hudspith, V., Kettridge, N., Millington, J., Page, S., Power, M., Pyne, S., Restuccia, F., Santín, C., Swetnam, T., Walding, N., Wooster, M., 2016. Living on a flammable planet: Interdisciplinary, cross-scalar and varied cultural lessons, prospects and challenges. *Philos. Trans. R. Soc. B Biol. Sci.* 371. https://doi.org/10.1098/rstb.2015.0469

Rouse, J.W., Haas, R.H., Schell, J.A., Deering, D.W., 1973. Monitoring The Vernal Advancement And Retrogradation (Green Wave Effect) Of Natural Vegetation. *NASA Goddard Sp. Flight Cent.* https://ntrs.nasa.gov/citations/19730017588

Roy, D.P., Jin, Y., Lewis, P.E., Justice, C.O., 2005. Prototyping a global algorithm for systematic fire-affected area mapping using MODIS time series data. *Remote Sens. Environ.* 97, 137–162. https://doi.org/10.1016/j.rse.2005.04.007

Roy, D.P., Boschetti, L., Justice, C.O., Ju, J., 2008. The collection 5 MODIS burned area product — Global evaluation by comparison with the MODIS active fire product. *Remote Sens. Environ.* 112, 3690–3707. https://doi.org/10.1016/j.rse.2008.05.013

Roy, D.P., Huang, H., Boschetti, L., Giglio, L., Yan, L., Zhang, H.H., Li, Z., 2019. Landsat-8 and Sentinel-2 burned area mapping - A combined sensor multi-temporal change detection approach. *Remote Sens. Environ.* 231, 111254. https://doi.org/10.1016/j.rse.2019.111254

Schweinsberg, S., Darcy, S., Beirman, D., 2020. 'Climate crisis' and 'bushfire disaster': Implications for tourism from the involvement of social media in the 2019–2020 Australian bushfires. *J. Hosp. Tour. Manag.* 43, 294–297. https://doi.org/10.1016/j.jhtm.2020.03.006

Seydi, S.T., Akhoondzadeh, M., Amani, M., Mahdavi, S., 2021. Wildfire Damage Assessment over Australia Using Sentinel-2 Imagery and MODIS Land Cover Product within the Google Earth Engine Cloud Platform. *Remote Sens.* 13, 220. https://doi.org/10.3390/rs13020220

Simon, M., Plummer, S., Fierens, F., Hoelzemann, J.J., Arino, O., 2004. Burnt area detection at global scale using ATSR-2: The GLOBSCAR products and their qualification. *J. Geophys. Res.* 109, D14S02. https://doi.org/10.1029/2003JD003622

Soulard, C.E., Albano, C.M., Villarreal, M.L., Walker, J.J., 2016. Continuous 1985-2012 Landsat monitoring to assess fire effects on meadows in Yosemite National Park, California. *Remote Sens.* 8, 371. https://doi.org/10.3390/rs8050371

Stephens, S.L., Agee, J.K., Fulé, P.Z., North, M.P., Romme, W.H., Swetnam, T.W., Turner, M.G., 2013. Managing forests and fire in changing climates. Science 342, 41–42. https://doi.org/10.1126/science.1240294

Tansey, K., Grégoire, J., Stroppiana, D., Sousa, A., Silva, J., Pereira, J.M.C., Boschetti, L., Maggi, M., Brivio, P.A., Fraser, R., Flasse, S., Ershov, D., Binaghi, E., Graetz, D., Peduzzi, P., 2004. Vegetation burning in the year 2000: Global burned area estimates from SPOT VEGETATION data. *J. Geophys. Res.* 109, D14S03. https://doi.org/10.1029/2003JD003598

The Local (17-07-2018). What you need to know about Sweden's historic wildfire outbreak. *The Local.* https://www.thelocal.se/20180717/sweden-battles-most-serious-wildfire-situation-of-modern-times-heres-what-you-need-to-know/

Trigg, S., Flasse, S., 2001. An evaluation of different bi-spectral spaces for discriminating burned shrub-savannah. *Int. J. Remote Sens.* 22, 2641–2647. https://doi.org/10.1080/01431160110053185

U.S. Geological Survey (USGS), s.f. *Landsat Missions.* https://www.usgs.gov/landsat-missions

van der Werf, G.R., Randerson, J.T., Giglio, L., Van Leeuwen, T.T., Chen, Y., Rogers, B.M., Mu, M., Van Marle, M.J.E., Morton, D.C., Collatz, G.J., Yokelson, R.J., Kasibhatla, P.S., 2017. Global fire emissions estimates during 1997-2016. *Earth Syst. Sci. Data* 9, 697–720. https://doi.org/10.5194/essd-9-697-2017

van Dijk, D., Shoaie, S., van Leeuwen, T., Veraverbeke, S., 2021. Spectral signature analysis of false positive burned area detection from agricultural harvests using Sentinel-2 data. *Int. J. Appl. Earth Obs. Geoinf.* 97, 102296. https://doi.org/10.1016/j.jag.2021.102296

Vanderhoof, M.K., Fairaux, N., Beal, Y.-J.G.J.G., Hawbaker, T.J., 2017. Validation of the USGS Landsat Burned Area Essential Climate Variable (BAECV) across the conterminous United States. *Remote Sens. Environ.* 198, 393–406. https://doi.org/10.1016/j.rse.2017.06.025

Verhegghen, A., Eva, H., Ceccherini, G., Achard, F., Gond, V., Gourlet-Fleury, S., Cerutti, P., 2016. The Potential of Sentinel Satellites for Burnt Area Mapping and Monitoring in the Congo Basin Forests. *Remote Sens.* 8, 986. https://doi.org/10.3390/rs8120986

Wang, L., Diao, C., Xian, G., Yin, D., Lu, Y., Zou, S., Erickson, T.A., 2020. A summary of the special issue on remote sensing of land change science with Google earth engine. *Remote Sens. Environ.* 248, 112002. https://doi.org/10.1016/j.rse.2020.112002

Wei, M., Zhang, Z., Long, T., He, G., Wang, G., 2021. Monitoring Landsat Based Burned Area as an Indicator of Sustainable Development Goals. *Earth's Futur.* 9, e2020EF001960. https://doi.org/10.1029/2020ef001960

White, J.D., Ryan, K.C., Key, C.C., Running, S.W., 1996. Remote sensing of forest fire severity and vegetation recovery. *Int. J. Wildl. Fire* 6, 125–136. https://doi.org/10.1071/WF9960125

Yu, P., Xu, R., Abramson, M.J., Li, S., Guo, Y., 2020. Bushfires in Australia: a serious health emergency under climate change. *Lancet Planet. Heal.* 4. https://doi.org/10.1016/S2542-5196(19)30267-0

7. Akronimoen zerrenda

Honako hauek dokumentu honetan erabilitako akronimo guztiak dira. Testuan zehar euskara eta gazteleraren arteko hizkuntza-aldaketengatik akronimoa bi modutan azaltzen denean, beste hizkuntzan dagokion forma ere adierazi egin da.

AG1	lehen artikulu gehigarria	es: PA1
AG2	bigarren artikulu gehigarria	es: PA2
AG3	hirugarren artikulu gehigarria	es: PA3
AG4	laugarren artikulu gehigarria	es: PA4
AQ	áreas quemadas	eus: EA
A1	lehen artikulua	es: P1
A2	bigarren artikulua	es: P2
A3	hirugarren artikulua	es: P3
A4	laugarren artikulua	es: P4
BAECV	Burned Area Essential Climate Variable	
BAMS	Burned Area Mapping Software	
BAMT	Burned Area Mapping Tools	
BARD	Burned Area Reference Database	
CE	Commission Error	
CEOS-LPSV Subgroup	Committee on Earth Observing Satellites' Land Product Validation	
CONAF	Corporación Nacional Forestal	
DC	Dice coefficient	
EA	erretako azalerak	es: AQ
ESA	European Space Agency	
ETM+	Enhanced Thematic Mapper Plus	
FIRMS	Fire Information Resource Management System	
GABAM	Global Annual Burned-Area Map	
GEE	Google Earth Engine	
GIS	Geografia-Informazioko Sistemak	
MERIS	Medium Resolution Imaging Spectrometer	
MGRS	Military Grid Reference System	
MIR	Middle Infrared	
MIRBI	Mid-Infrared Burned Index	
MODIS	Moderate Resolution Imaging Spectroradiomater	
MSI	Multispectral Instrument	
MSS	Multispectral Scanner	
NASA	National Aeronautics and Space Administration	
NBR	Normalized Burn Ratio	
NBR2	Normalized Burn Ratio 2	

NDII	Normalized Difference Infrared Index	
NDVI	Normalized Difference Vegetation Index	
NIR	Near Infrared	
OE	Omission error	
OLCI	Ocean and Land Colour Instrument	
OLI	Operational Land Imager	
P1	primera publicación	eus: A1
P2	segunda publicación	eus: A2
P3	tercera publicación	eus: A3
P4	cuarta publicación	eus: A4
PA1	primera publicación	eus: AG1
PA2	segunda publicación	eus: AG2
PA3	tercera publicación	eus: AG3
PA4	cuarta publicación	eus: AG4
RdNBR	relative delta NBR	
relB	relative bias	
SCL	Scene Classification	
SFD	Small Fire Database	
SHA	Saharaz hegoaldeko Afrika	
SWIR	Short Wave Infrared	
S2	Sentinel-2	
S2A	Sentinel-2A	
S2B	Sentinel-2B	
TIR	Thermal Infrared	
TM	Thematic Mapper	
USGS	United States Geological Survey	
UTM	Universal Transverse Mercator	
VIIRS	Visible Infrared Imaging Radiometer Suite	

Eranskinak: argitaratutako artikuluak

I eranskina: A1 – Afrikako EA

Artikulua

Izenburua: Development of a Sentinel-2 burned area algorithm: Generation of a small fire database for sub-Saharan Africa

Egileak: Ekhi Roteta, Aitor Bastarrika, Marc Padilla, Thomas Storm eta Emilio Chuvieco

Argitaratze-data: 2019ko martxoa

DOI: https://doi.org/10.1016/j.rse.2018.12.011

Erreferentzia bibliografikoa:

Roteta, E., Bastarrika, A., Padilla, M., Storm, T., Chuvieco, E., 2019. Development of a Sentinel-2 burned area algorithm: Generation of a small fire database for sub-Saharan Africa. *Remote Sens. Environ.* 222, 1–17. https://doi.org/10.1016/j.rse.2018.12.011

Aldizkaria

Izena: Remote Sensing of Environment

Sortze-urtea: 1969

Argitaratze-urteko inpaktu-faktorea: 9,085

Argitaratze-urteko posizioa *REMOTE SENSING* arloan:

> **Postua**: 2/30
>
> **Pertzentila**: %95
>
> **Kuartila**: Q1
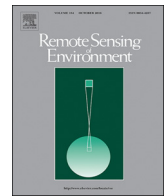
Development of a Sentinel-2 burned area algorithm: Generation of a small fire database for sub-Saharan Africa

E. Roteta[a],[*], A. Bastarrika[a], M. Padilla[b], T. Storm[c], E. Chuvieco[d]

[a] *Department of Mining and Metallurgical Engineering and Materials Science, School of Engineering of Vitoria-Gasteiz, University of the Basque Country UPV/EHU, Nieves Cano 12, 01006 Vitoria-Gasteiz, Spain*
[b] *Centre for Landscape and Climate Research, Department of Geography, University of Leicester, Leicester, United Kingdom*
[c] *Brockmann Consult GmbH, Max-Planck-Straße 2, 21502 Geesthacht, Germany*
[d] *Environmental Remote Sensing Research Group, Department of Geology, Geography and the Environment, University of Alcalá, C/Colegios 2, 28801 Alcalá de Henares, Spain*

ABSTRACT

A locally-adapted multitemporal two-phase burned area (BA) algorithm has been developed using as inputs Sentinel-2 MSI reflectance measurements in the short and near infrared wavebands plus the active fires detected by Terra and Aqua MODIS sensors. An initial burned area map is created in the first step, from which tile dependent statistics are extracted for the second step. The whole Sub-Saharan Africa (around $25 \, M \, km^2$) was processed with this algorithm at a spatial resolution of 20 m, from January to December 2016. This period covers two half fire seasons on the Northern Hemisphere and an entire fire season in the South. The area was selected as existing BA products account it to include around 70% of global BA. Validation of this product was based on a two-stage stratified random sampling of Landsat multitemporal images. Higher accuracy values than existing global BA products were observed, with Dice coefficient of 77% and omission and commission errors of 26.5% and 19.3% respectively. The standard NASA BA product (MCD64A1 c6) showed a similar commission error (20.4%), but much higher omission errors (59.6%), with a lower Dice coefficient (53.6%). The BA algorithm was processed over > 11,000 Sentinel-2 images to create a database that would also include small fires (< 100 ha). This is the first time a continental BA product is generated from medium resolution sensors (spatial resolution = 20 m), showing their operational potential for improving our current understanding of global fire impacts. Total BA estimated from our product was $4.9 \, M \, km^2$, around 80% larger area than what the NASA BA product (MCD64A1 c6) detected in the same period ($2.7 \, M \, km^2$). The main differences between the two products were found in regions where small fires (< 100 ha) account for a significant proportion of total BA, as global products based on coarse pixel sizes (500 m for MCD64A1) unlikely detect them. On the negative side, Sentinel-2 based products have lower temporal resolution and consequently are more affected by cloud/cloud shadows and have less temporal reporting accuracy than global BA products. The product derived from S2 imagery would greatly contribute to better understanding the impacts of small fires in global fire regimes, particularly in tropical regions, where such fires are frequent. This product is named FireCCISFD11 and it is publicly available at: https://www.esa-fire-cci.org/node/262, last accessed on November 2018.

1. Introduction

Biomass burning is a key element of the terrestrial carbon cycle and a significant source of atmospheric trace gases and aerosols (Andreae and Metlet, 2001). Depending on their size, location and timing, fires significantly modify land surface properties, influence atmospheric chemistry and air quality, through aerosol and gas emissions, while modifying albedo by land use transformations (Bowman et al., 2009).

Satellite Earth observation is extensively used to detect burned areas (BA) and active fires. BA detection is commonly based on the effects of fire on vegetation reflectance, while the detection of active fires is mainly based on the thermal contrast between burnings and the background (Giglio et al., 2016; Schroeder et al., 2016, 2014). In recent years, several global burned area (BA) products have been made available to the international community. The first released were the Global Burned Area 2000-GBA2000 (Tansey et al., 2004), and
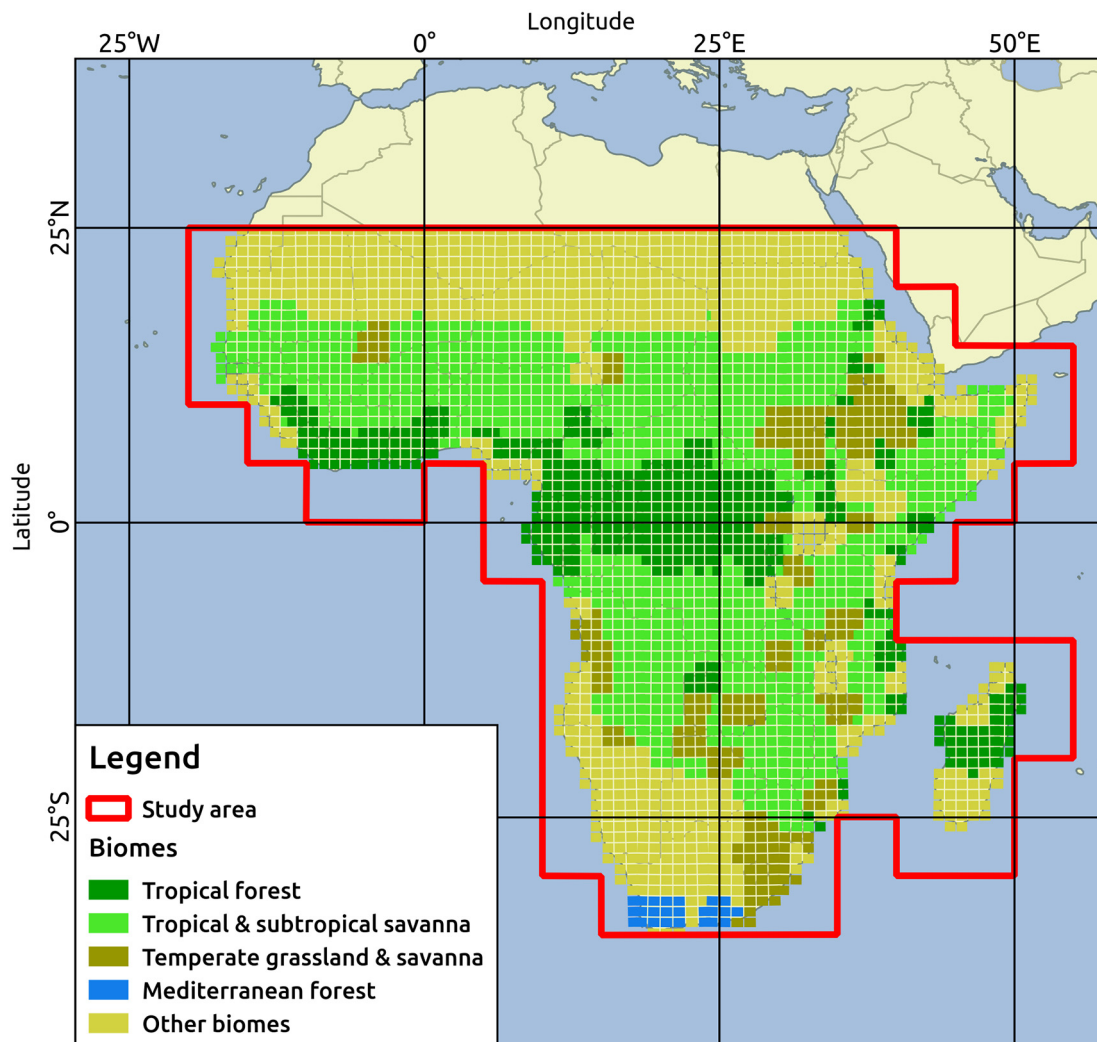
Fig. 1. Biome distribution for the study area according to Olson et al. (2001) for the Copernicus Sentinel-2 tiling system.

GLOBSCAR (Simon et al., 2004), both from European sensors, which were followed by the Globcarbon (Plummer et al., 2006), L3JRC (Tansey et al., 2008), and more recently by the Copernicus Land Burned Area. The first NASA BA product was based on the MODIS sensors: MCD45A1 (Roy et al., 2008) and more recently the MODIS MCD64, which is now the standard NASA BA product (last version released is collection 6: Giglio et al., 2018). From the previous version of this product (c5), the burned component of the Global Fire Emissions Database-GFED was delivered (Giglio et al., 2010). Within the European Space Agency (ESA)'s Climate Change Initiative, several global BA products have been recently releases: FireCCI31 and FireCCI41, based on the MERIS sensor (Alonso-Canas and Chuvieco, 2015), and FireCCI50, based on MODIS 250 m red and near infrared reflectances (Chuvieco et al., 2018).

All currently existing global products are based on coarse spatial-resolution sensors including MERIS (300 m), MODIS (250 m–500 m) and AVHRR or VEGETATION (around 1000 m). With those pixel sizes, detection of small fires (< 100 ha) becomes very challenging. Although small fires are usually less catastrophic than large fires, they still play a significant part in land use transformation and total emissions from fires, particularly in tropical regions, where fires tend to be human driven, either for agricultural expansion, grazing purposes or hunting (Grégoire et al., 2013; Hantson et al., 2015). Extrapolating relations between active fires and small burn patches, Randerson et al. (2012) estimated that 26% of the global BA was the result of small fires, which

would imply increasing total BA area by $1.2\,M\,km^2$/year. The same study estimated that 24% of African BA came from small fires ($0.78\,M\,km^2$/year). However, Hantson et al. (2013) has shown that active fires may have missed up to 80% of all fires in tropical regions, which add up to 50% of the total BA. Additionally, when comparing the accuracy of different global BA products (MCD45A1, MCD64A1 and FireCCI31) with reference perimeters derived manually from Landsat data, omission errors showed to be higher than 65% for the tested products (Padilla et al., 2015). All these omissions cause an underestimation on the greenhouse gas emissions to the atmosphere, which should improve if small burned areas were taken into account.

The increasing availability of medium spatial resolution sensors such as Landsat-OLI (30 m) or Sentinel-2 Multi Spectral Instrument (MSI) (10 m) may soon overcome those limitations to detect smaller fires, making possible a more accurate estimation of global BA. Several local/regional burned area algorithms based on Landsat TM/ETM + images were developed in the last decade (Bastarrika et al., 2011; Goodwin and Collett, 2014; Stroppiana et al., 2015, 2012). Only recent studies have suggested the use of medium resolution sensors to generate global BA products. This was the case of the MODIS-Landsat data fusion product by Boschetti et al. (2015), or the US conus BA product generated from Landsat historical archives (Hawbaker et al., 2017). One of the main limitations of using these sensors for BA mapping is their poor temporal resolution (8 days if both Landsat-7 and 8 are used), which makes BA detection in tropical ecosystems challenging, due to

significant cloud cover and short post-fire signal persistence. With the launch of the two Sentinel-2 missions and a 5-day revisiting frequency (at the equator), this problem will be mitigated, even more if the Landsat-8 and Sentinel-2 data are integrated.

In this paper we present a new BA algorithm adapted to MSI characteristics and its implementation on a very large area and an entire fire season to test the operational potential for producing continental scale BA datasets from S-2 MSI data. This algorithm was developed in the framework of the Climate Change Initiative programme of the ESA. For this reason, we have selected the Sub-Saharan Africa (SSA) region as study case, as it is the most burned continent and produces the larger gas emissions (Chuvieco et al., 2018; Van Der Werf et al., 2017). The whole 2016 year was processed, including the whole fire season in Southern Hemisphere Africa (SHAF), and two half fire seasons in the Northern Hemisphere (NHAF).

2. Methods

2.1. Study area

The BA Algorithm for the MSI sensor has been tested in the SSA (Sub-Saharan Africa) covering the latitudes from 25°N to 35°S (Fig. 1). Although fires affect a variety of ecosystems and locations, the current/ existing global BA products showed that Africa is the most affected continent by biomass burning, comprising up to 70% of all the area burned worldwide (Chuvieco et al., 2016, 2018; Giglio et al., 2013). Fires occur in the corresponding dry season in both the Northern and Southern Hemispheres, being these seasons from October to March north to the Equator and from May to October in the south. Although African fires show a strong variability, particularly in seasonal and daily cycles, most fires detected by Terra and Aqua MODIS (around 90%) were detected during the day (Giglio et al., 2006a). Fires are also affected by land cover changes as the transformation of natural vegetation to croplands, decreasing the total burned area after the conversion (Grégoire et al., 2013).

Most fires in this region are caused by human activities for the management of crops, grazing and hunting (Grégoire et al., 2013; Lewis et al., 2015). This area includes several biomes (Olson et al., 2001): tropical forest (especially around the equator), tropical and subtropical savanna (in subtropical areas), temperate grassland and savanna, Mediterranean forest (in southern Africa), and other residual biomes (mainly arid regions).

2.2. Data

2.2.1. Active fire data

Several BA algorithms combine detection of hotspots and changes in reflectance over time to better discriminate burned pixels, as the thermal contrast of fires is often more noticeable than their impact on reflectance changes (Alonso-Canas and Chuvieco, 2015; Boschetti et al., 2015; Fraser et al., 2000; Giglio et al., 2009; Giglio et al., 2006b; Pereira et al., 2017). Active fire data for development of the BA algorithm were obtained from the Moderate Resolution Imaging Spectroradiometer (MODIS) sensor, comprising 1 km detections from the combined 4 overpasses of the sensor on the Aqua and Terra satellites. The precise coordinates of the hotspots were downloaded from the Fire Information for Resource Management System (FIRMS) (https://firms. modaps.eosdis.nasa.gov/download/, last accessed on November 2018). The data come from the Collection 6 Near Real Time (NRT), extracted from the standard MCD14ML fire product produced at the MODIS Fire Science Computing Facility (SCF). Active fires were not filtered depending on the quality layer.

2.2.2. Copernicus Sentinel-2 MSI

Sentinel-2 (S2) is an Earth observation mission developed by ESA as part of the Copernicus Programme to acquire terrestrial observations in

support of environmental services and natural disaster management (Drusch et al., 2012). The mission includes two identical satellites, S2-A (launched in June 2015) and S2-B (launched in March 2017), providing complementarity for the current SPOT and Landsat missions. The main sensor is the MultiSpectral Instrument (MSI), a pushbroom scanner that provides a wide spectral coverage over the visible, near infrared (NIR) and short-wave infrared (SWIR) domains (amounting to 13 spectral bands), with medium spatial resolution (from 10 m to 60 m depending on the wavelength) and a wide field of view (290 km) (ESA, 2011) (https://earth.esa.int/documents/247904/685211/Sentinel-2_User_Handbook, last accessed on November 2018). This makes possible a global coverage of the Earth's land surface (between 56°S and 83°N latitudes) every 10 days with one satellite and every 5 days with 2 satellites. In this analysis only S2-A data were used because S2-B data were not yet available when we started the processing of the BA product.

The input data for our BA algorithm was the Level-1C product. This product includes Top-Of-Atmosphere (TOA) reflectances with sub-pixel multispectral registration in UTM projection and WGS84 geodetic system in tiles of 100 × 100 km. The data were downloaded from the Sentinel Scientific Data Hub (https://scihub.copernicus.eu, last accessed on November 2018), free of charge. The images were atmospherically corrected using the algorithm 'sen2cor' v2.2.1 issued as part of the standard Sentinel-2 Toolbox (downloadable from http://step.esa. int/main/third-party-plugins-2/sen2cor/, last accessed on November 2018). This algorithm generates Bottom of Atmosphere (BOA) reflectance images, as well as several products such as Aerosol Optical Thickness, Water Vapor and Scene Classification maps (SCL). From these layers, only SCL was used to mask defective pixels and clouds.

2.3. Spectral analysis

A spectral sensitivity analysis was carried out as a first step for the BA algorithm development to determine which bands and/or spectral indices were the most suitable for BA detection. Reference perimeters from 2016 located in 52 S2 tiles systematically distributed through all Africa were visually created using BAMS (Burned Area Mapping Software) methodology (Bastarrika et al., 2014), which consists in a trained classification to detect burned areas between images from two dates.

For each reference location 20,000 random sample points were extracted from burned and unburned categories to analyze their spectral distribution (10,000 samples for each category). The unburned class contains every pixel that could not be classified as burned, water, cloud or cloud shadow: urban areas, bare areas, unburned vegetated areas, and even burned areas that were already burned in the pre-fire date. The spectral sensitivity analysis was computed for 9 MSI bands (all bands processed at 20 m by sen2cor) as well as several common spectral indices used in BA algorithms (Bastarrika et al., 2011; Chuvieco et al., 2002; Huang et al., 2016; Smith et al., 2007; Stroppiana et al., 2012; Veraverbeke et al., 2011), covering the Visible/NIR, the NIR/ Short SWIR and the Short SWIR/Long SWIR spectral spaces:

- Visible/NIR space: Enhanced Vegetation Index (EVI) (Huete et al., 1994), Normalized Difference Vegetation Index (NDVI) (Rouse et al., 1974), Global Environment Monitoring Index (GEMI) (Pinty and Verstraete, 1992), Burned Area Index (BAI) (Martín and Chuvieco, 1998), Soil-Adjusted Vegetation Index (SAVI) (Huete, 1988).
- NIR/SWIR space: Modified Burned Area Index (BAIM) (Martin et al., 2005), Normalized Burn Ratio (NBR) (Key and Benson, 1999).
- Long SWIR/Short SWIR space: Mid-Infrared Burned Index (MIRBI) (Trigg and Flasse, 2001), Normalized Burned Ratio 2 (NBR2) (García and Caselles, 1991).

Spectral sensitivity analyses were performed for both post-fire

values and multitemporal differences (post-fire and pre-fire values subtraction). Both parametric and non-parametric analyses were carried out, as recommended by different authors (Gómez et al., 2016; Huang et al., 2016). The parametric separability index (M) that was defined as follows (Kaufman and Remer, 1994; Lasaponara, 2006; Smith et al., 2007):

$$M = \frac{|\mu_b - \mu_{ub}|}{\sigma_b + \sigma_{ub}} \tag{1}$$

where μ_b and μ_{ub} are the mean values of burned and unburned samples and σ_b and σ_{ub} the corresponding standard deviations. The separability between classes is generally considered poor when the M index is lower than 1, while M higher than 1 indicates a good separability (Kaufman and Remer, 1994).

The non-parametric analysis was based on the Random Forest (RF) Classifier, which provides an importance score for each input variable (https://scikit-learn.org/stable/modules/generated/sklearn.ensemble. RandomForestClassifier.html, last accessed on November 2018). This score measures the total decrease in node impurity averaged over all tress of the ensemble and can be used to rank the importance of that variable in relation to the others in the classification.

The results shown in Fig. 2 are the averages of the values of 52 S2 tiles where reference perimeters were generated.

The Mid-Infrared Burned Index (MIRBI, Eq. (2)) and the Normalized Burned Ratio 2 (NBR2, Eq. (3)) were found to have the highest M value between burned and unburned categories, and this behaviour is also confirmed with the RF importance score.

$$MIRBI = 10 \cdot \rho_{SWIRL} - 9.8 \cdot \rho_{SWIRS} + 2 \tag{2}$$

$$NBR2 = \frac{\rho_{SWIRS} - \rho_{SWIRL}}{\rho_{SWIRS} + \rho_{SWIRL}} \tag{3}$$

where ρ_{SWIRL} and ρ_{SWIRS} are, respectively, Short Wave Infrared Long reflectance and Short Wave Infrared Short reflectance, both adimensional, and corresponding to B12 and B11 bands of MSI sensor.

Both indices were finally selected for the BA algorithm definition, although they rely on the same spectral bands (Short and Long SWIR bands, B11 and B12 for S2 images) because of the different distributions of the burned/unburned category (Fig. 3), being NBR2 much more homogeneous; this different behaviour is important when defining the contextual stage of the algorithm when defining background (not burned)/foreground (burned) cut-off values to maintain low commission errors. The ability of the SWIR bands when emphasizing the burned/unburned in African environments has previously been noted, as they are less influenced than the visible bands by scattering and are well associated to post-fire impacts (Pereira et al., 1999; Smith et al., 2007).

Apart from NBR2 and MIRBI, the NIR variable was also selected (B8A band for MSI images): adding post variables is important to reduce changes not related to fire (specially for differentiate from croplands) and this variable is shown to be one of the most significant with the second M higher value (after MIRBI) and the fourth higher RF score (after the BAI index that it is highly correlated with the NIR). The NIR spectral region is known to play an important role when mapping burned areas and is also the most stable along ecosystems (Huang et al., 2016; Pereira et al., 1999).
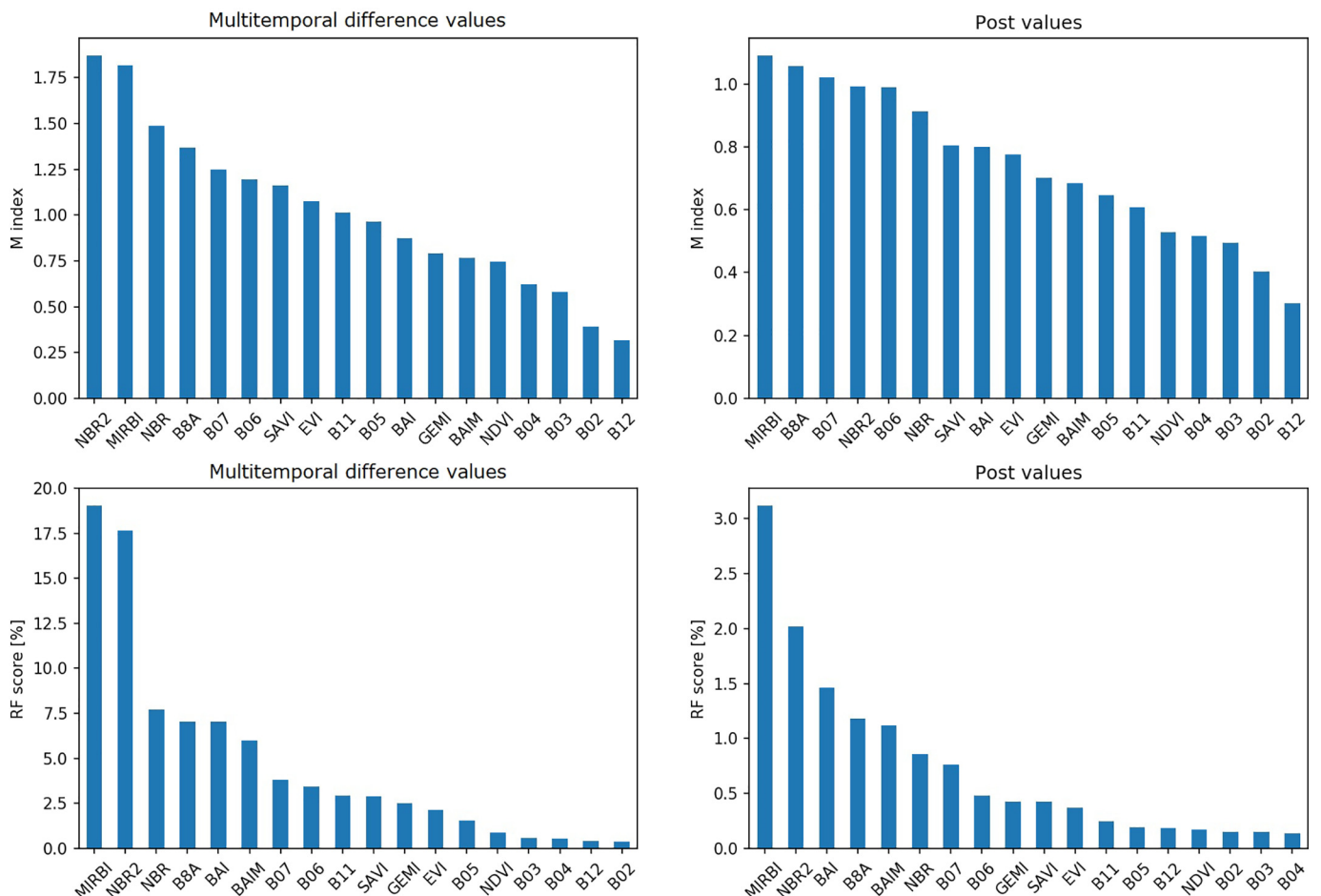

Fig. 2. M separability index (first row) and Random Forest importance score (second row) mean values from 52 reference tiles sorted in descending order. The left column shows the multitemporal difference variables while the right column shows the post-fire values.
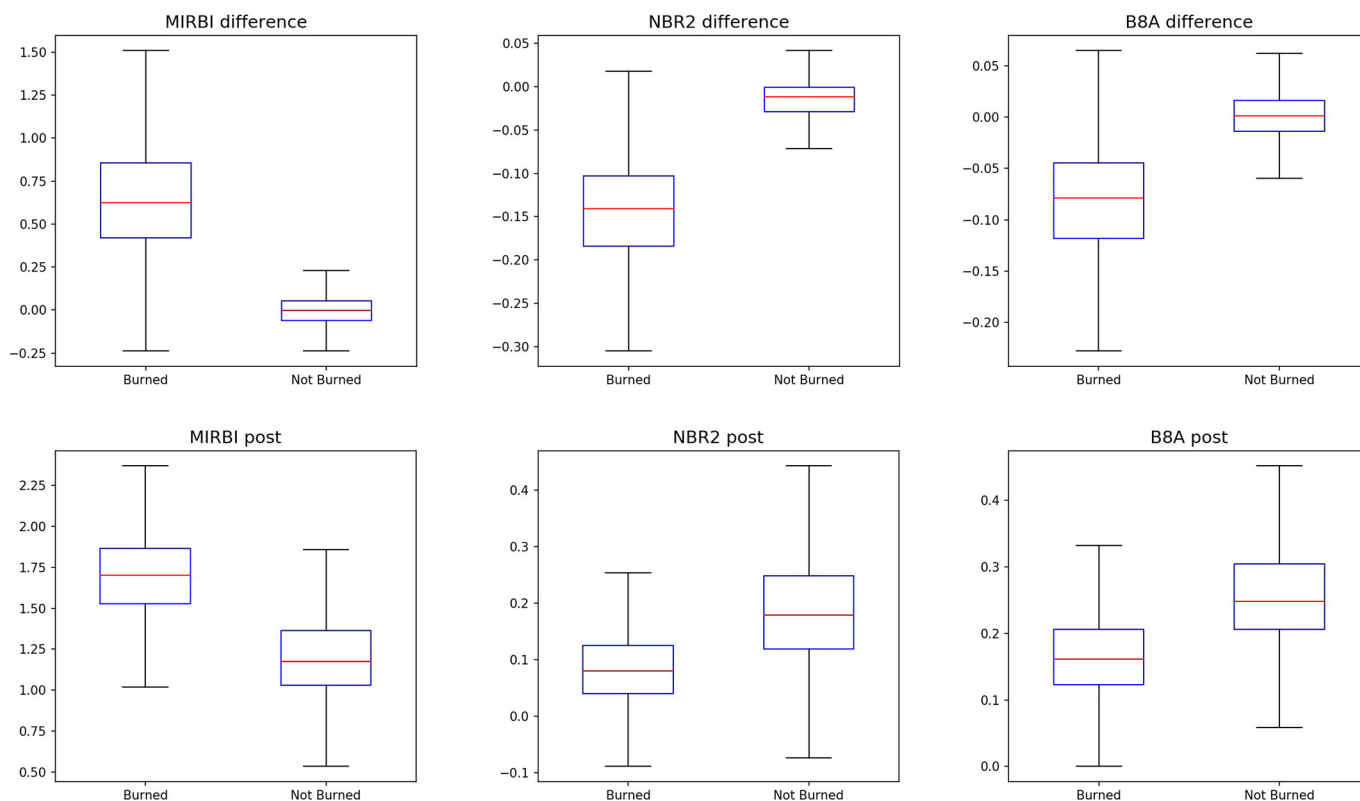
Fig. 3. Spectral distribution of burned and unburned categories for MIRBI, NBR2 and NIR multitemporal difference and post-fire values.

2.4. Algorithm

2.4.1. General overview

The proposed BA algorithm compared two consecutive Sentinel-2 acquisitions by calculating burned probability using MIRBI and NBR2 spectral indices and the NIR band derived from the L2A product (Fig. 4). The algorithm estimated an initial BA based on fixed thresholds, which were overlaid with the MCD14ML hotspots detected between the time-lapse of the two MSI acquisitions in order to define the regions with a very high likelihood of being burned. Those BA areas confirmed by hotspots were used to obtain tile dependent statistical thresholds for each predictive variables in a two-phase burned strategy, following a modified method from Bastarrika et al. (2011).

A mask of 'not burnable' areas was produced using the Scene Classification Layer (SCL) generated by 'sen2cor', corresponding mostly to unobserved areas (clouds and cloud shadows) and water bodies. The pixels that satisfy the following criteria were masked out for further processing:

- No data, saturated pixels, water and snow.
- Medium-high probability clouds and thin cirrus with a dilation of 5 pixels (100 m) were used in order to obtain a more robust cloud mask, to be applied to the image pair under consideration (low probability clouds were not classified as not burnable, since they included a very significant quantity of burned areas).
- Dark area pixels and cloud shadows of the SCL were not used on the mask for the same reason as low probability clouds and because many burned pixels in the savannas fall in these categories. A fixed criterion based on the post-fire [t_2] Long SWIR band (B12) was used instead. Burned areas and shadows were well separated by a reflectance value of 0.07, so pixels where B12 < 0.07 were considered cloud shadows and therefore removed from further processing.

2.4.2. Hotspots confirmed burned pixels (HCBP)

In the first stage of the algorithm a set of burned pixels that satisfied a fixed criteria were selected, whence tile based statistics could be used at the second stage. To ensure initially detected pixels were in fact burned, they had to fulfill certain conditions (described below) and had a MODIS hotspot in the neighborhood. All the hotspots, regardless the detection confidence and sensing angle were selected because they were only used to confirm the spectral change observed in the Sentinel-2 imagery.

Assuming two consecutive Sentinel 2 tiles ([t_1] and [t_2]), a pixel was labeled as Hotspots confirmed burned pixels (HCBP) if it satisfied all the following conditions:

- MIRBI ([t_2]) > tile mean MIRBI ([t_2])
- MIRBI difference ([t_2] − [t_1]) > 0.25
- NBR2 ([t_2]) < tile mean NBR2 ([t_2])
- NBR2 difference ([t_2] − [t_1]) < −0.05
- NIR ([t_2]) < tile mean NIR ([t_2])
- NIR difference ([t_2] − [t_1]) < −0.01
- It had a MODIS hotspot in between ([t_1]) and ([t_2]) in the 1000 m vicinity of that pixel
- It was part of a patch larger than 30 ha (750 pixels), which was observed to be the minimum area necessary to assure that it was actually a burned patch and no other unburned artifacts.

The thresholds for MIRBI, NBR2 and NIR multitemporal difference (0.25, − 0.05 and − 0.01 respectively) were obtained analyzing the cut-off points of the probability distributions of the burned and unburned category at the 52 reference sites cited in Section 2.3. For the post-fire variables, the mean of the whole tile was selected as threshold, obtaining and adaptive thresholds that helped reducing the commission errors of those pixels that fulfilled the multitemporal criteria (for example at croplands).

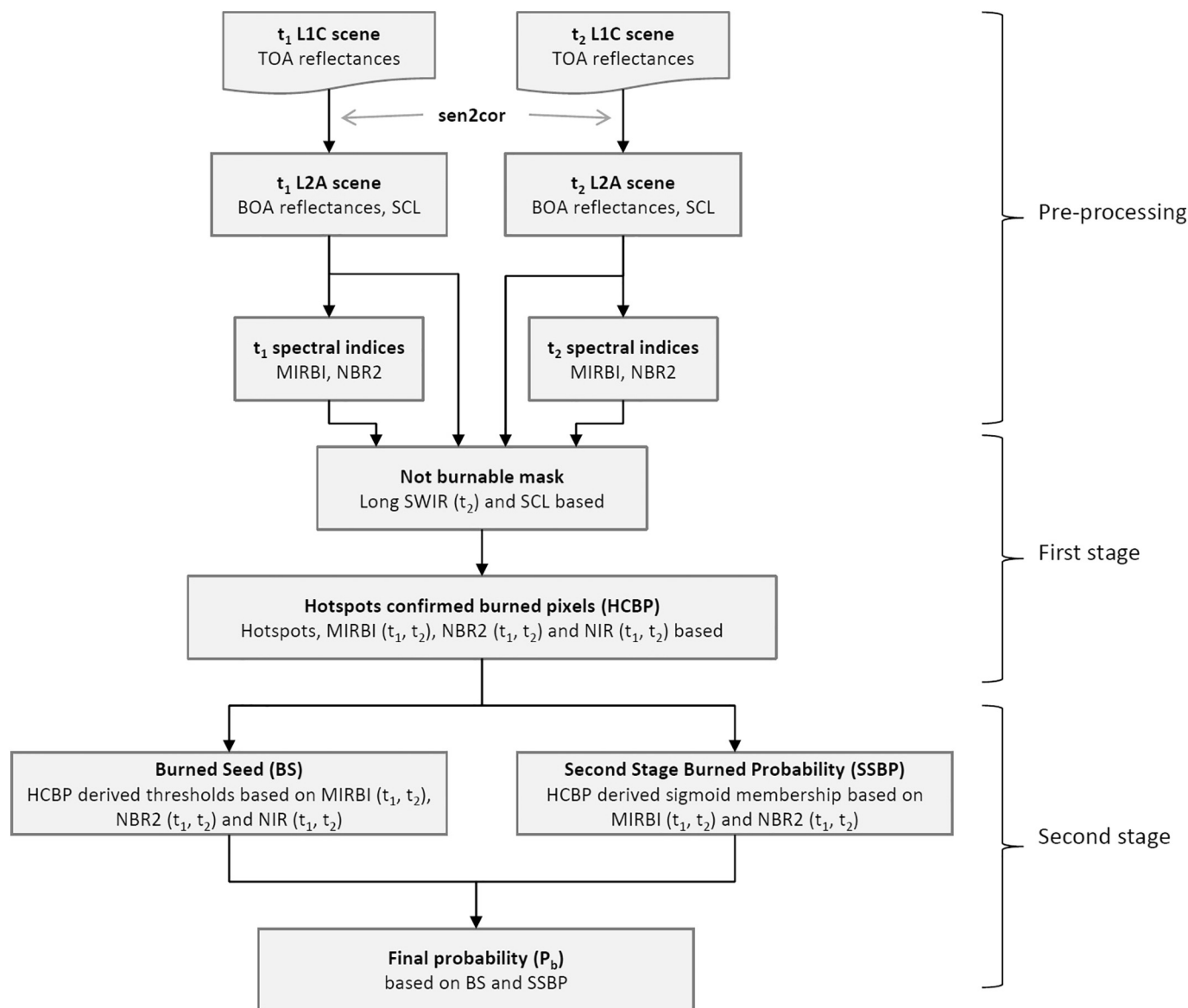The aim behind this first stage of the algorithm was to obtain a set of

Fig. 4. Flowchart of the BA algorithm applied to two time-consecutive S-2 acquisitions.

pixels highly likely to be burned given that an active fire was observed in the vicinity, and a spectral change according to a fire event was shown. The remaining pixels were considered as unburned pixels. This initial classification was used to have foreground (burned) and background (unburned) probability distributions for each tile and period that were used in a following two-stage process.

2.4.3. Burned seeds (BS)

Burned seeds (BS) were obtained assigning as thresholds the 5th and 95th percentiles of HCBP, depending on whether a particular variable higher or lower the values after a fire, respectively. A pixel was identified as a BS if it satisfied all the following rules:

- MIRBI ($[t_2]$) > MIRBI 5th percentile HCBP ($[t_2]$)
- MIRBI difference ($[t_2] - [t_1]$) > MIRBI 5th percentile HCBP ($[t_2]$-$[t_1]$)
- NBR2 ($[t_2]$) < NBR2 95th percentile HCBP ($[t_2]$)
- NBR2 difference ($[t_2] - [t_1]$) < NBR2 95th percentile HCBP ($[t_2]$-$[t_1]$)
- NIR ($[t_2]$) < NIR 95th percentile HCBP ($[t_2]$)
- NIR difference ($[t_2] - [t_1]$) < NIR 95th percentile HCBP ($[t_2]$-$[t_1]$)

2.4.4. Second stage probability of burn (SSPB)

The second stage probability of burn (SSPB) was focused on reducing the omission error (Bastarrika et al., 2011) and it was based exclusively on MIRBI and NBR2 multitemporal difference variables given that they had shown a much higher importance than the post-fire variables according to the RF score. For the same reason the NIR variable was not introduced either to avoid increasing omission errors.

The main purpose in this stage was to define a mathematical function that would make the transition from 0% (unburned pixels) to 100% (burned pixels) probability. A logistic function was used for this purpose, which provided a smooth transition between the two classes. This approach was already used in other BA studies (Bastarrika et al., 2011; Fraser et al., 2002; Koutsias and Karteris, 2000; Pu and Gong, 2004). The logistic functions for MIRBI and NBR2 differences are s-shaped and z-shaped, respectively, to reflect the fact that the former increases its values when an area is burned while the latter decreases (Fig. 5). To calculate the lower and upper boundaries on the logistic curve, corresponding to 0% and 100% probabilities, different percentiles were extracted from the sets of burned and unburned pixels of HCBP. 90th (MIRBI difference) and 10th (NBR2 difference) percentiles of unburned pixels were set as the 0% probability, and the 50th percentile of burned
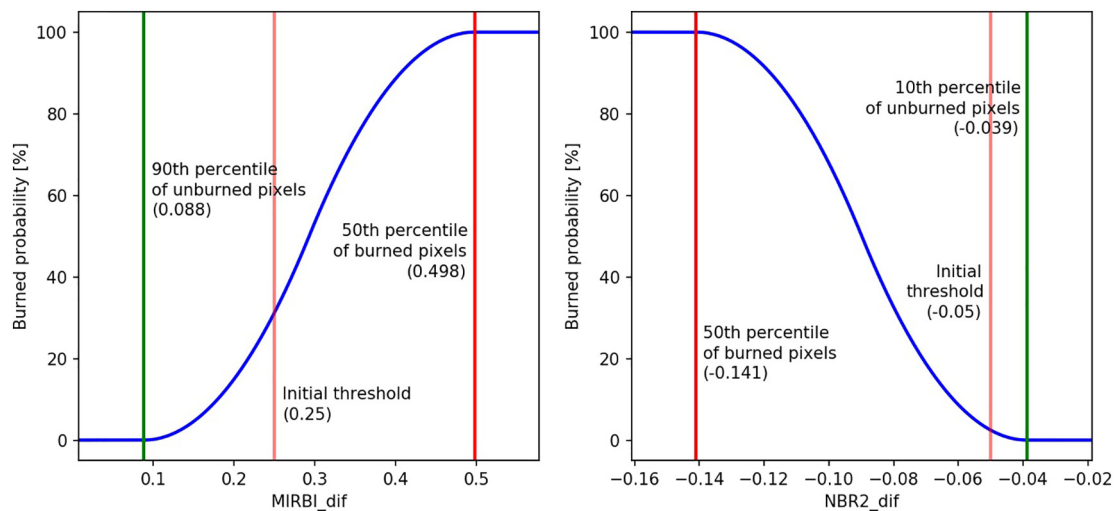
Fig. 5. Two sample logistic curves, with the s-shape for MIRBI difference and z-shape for NBR2 difference, taken from tile 28PET, period December 22, 2015/January 11, 2016. The initial thresholds are those extracted from the spectral analysis and applied to HCBP.

pixels was used for the 100% value. There is no symmetry between the percentiles of both categories; anomalies were found in the set of burned pixels when it was formed by a limited number of pixels, so a more "central" percentile (50th, the median) is used to avoid this effect.

The final second stage probability of burn (SSPB) was obtained by multiplying them, considering MIRBI and NBR2 probabilities were independent.

2.4.5. Final burned probability map

The BS and SSPB image were used to get the Final Burned Probability Map (FBPM) in a two-step focus trying to balance omission and commission errors. Unlike in Bastarrika et al. (2011), the two step process in this algorithm did not use a region growing method but a cost-path based approach as the SSPB image is a continuous space. For each SSPB pixel higher than 0 probability value, the final burned probability was the minimum probability of the route crossing probabilities as high as possible from that pixel towards the BS. If pixel near a seed was considered, the probability was high (the minimum probability that crossed the path between both is high), while when that pixel was far away from the seeds, that probability tended to be low given that crossed low probability burned regions.

2.4.6. Temporal application of the algorithm

Extending the temporal application of the algorithm (the definition until now has been limited to two consecutive scenes named $[t_1]$ and $[t_2]$), the final set of burned pixels was created by comparing each image $[t_n]$ to the preceding four acquisitions $[t_{n-1}, t_{n-2}, t_{n-3}, t_{n-4}]$. The main objective was to fill unobserved areas (masked as detailed in Section 2.4.1) in the previous images. This gap filling process is illustrated in Fig. 6 (although with only 3 pre-fire dates). If the acquisition at $[t_n]$ were compared only with the first preceding image ($[t_{n-1}]$), most burned pixels hidden by clouds in the $[t_{n-1}]$ image would have been masked and they wouldn't be included in the final BA product. Taking into account more preceding images as comparison source the masked areas were filled using the latest pre-fire reference. Only the pair of images with $> 5\,km^2$ (12,500 pixels) of observed (unmasked) areas and at least one active fire between the two dates were processed to improve the computation performance and avoid acquisitions with a higher probability to commit commission errors; otherwise it was assumed that it did not contain any burned pixel within that period.

2.4.7. Processing environment

The described BA algorithm was implemented on Calvalus processing system developed by Brockmann Consult Gmbh, Germany (http://

www.brockmann-consult.de/calvalus, last accessed on November 2018). The pre-processing consisted on running 'sen2cor' processor for 11,054 S2 MSI tiles, amounting for 63 TB of data. This process took about 9 weeks. Additionally, four months were required to run the BA algorithm for the whole 2016 year, totaling additional 87 TB of processed data (including intermediate files). The final product was named FireCCISFD11 (version 10, included a preliminary version covering just the northern hemisphere of Africa, but it was only released to a few climate users).

### 2.4.8. Threshold between burned and unburned areas

The confidence values for each pixel were obtained from the probability distribution functions. Given that the result of the BA algorithm was a continuous image (with confidence levels from 0% to 100%) but reference perimeters were discrete (burned/unburned), a fixed threshold was established to convert the classification outputs into a binary layer. Different values were tested to balance omission and commission estimations based on the 52 tiles that were used for selecting the most sensitive bands for the algorithm (see Section 2.3). Analyzing the distribution of omission, commission and Dice coefficient values in those 52 sites, 5% was found to be the best threshold (see 34PET example in Fig. 7). This low cut-off value was related to the percentiles values used in Section 2.4.4, whose asymmetry caused the logistic curves to be closer to the burned area, and to the multiplication of MIRBI and NBR2 probabilities at the SSPB stage. No cut-off value was used for the MCD64A1 product.

2.5. Validation

BA reference data were generated for a statistically derived sample of validation sites, and compared with the FireCCISFD11 for its assessment. The validation was also carried out with the now standard NASA BA product: the MCD64A1 collection 6, derived from MODIS data (Giglio et al., 2018, 2009), as this product is widely used by atmospheric and carbon modellers. This global product was derived from high temporal resolution data (daily Terra and Aqua acquisitions, compared to 10 days of S-2 acquisitions) but at much lower spatial resolution than the FireCCISFD11 product (500 versus 20 m). Intercomparison of FireCCISFD11 and MCD64A1 products was also carried out, to analyze the seasonal and spatial differences between the two products.

Reference perimeters were generated from multi-temporal comparison of Landsat imagery following standard CEOS CalVal validation protocols (Boschetti et al., 2009). Given the different temporal
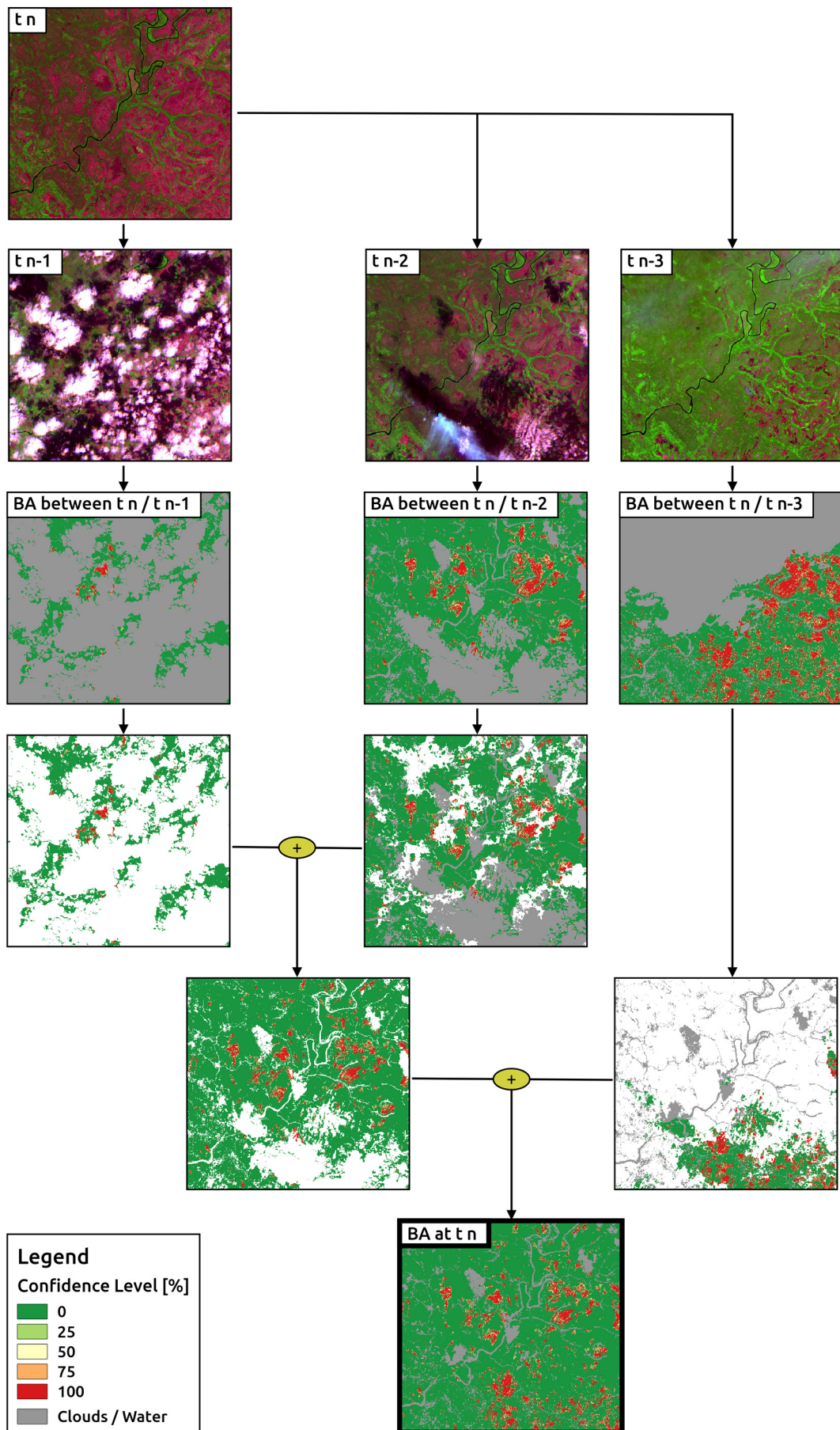
(caption on next page)

Fig. 6. Example of the temporal application of the BA algorithm in a sample area, comparing one post-fire date ([t$_n$]) with 3 previous pre-fire dates ([t$_{n-1}$], [t$_{n-2}$] and [t$_{n-3}$]). The first two rows show SWIR-NIR-Red colour composites for individual dates; the third row shows resulting burned areas using three consecutive precedent pre-fire images. The figure illustrates how cloudy areas are filled with BA detected from previous pre-fire images, being the last aggregation the final BA detected by the algorithm for the post-fire date ([t$_n$]). Even though the post-fire image in this example is compared with 3 pre-fire images, 4 pre-fire dates are used in the algorithm. (For interpretation of the references to colour in this figure legend, the reader is referred to the web version of this article.)
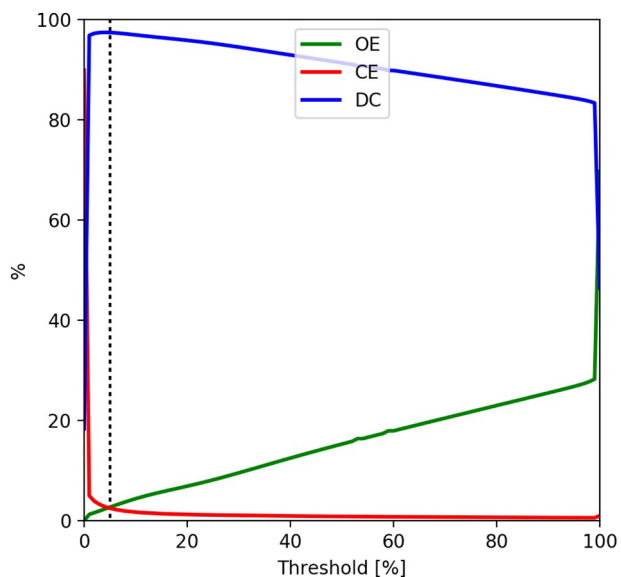

Fig. 7. Evolution of omission and commission errors and the Dice coefficient depending on the threshold applied to the FireCCISFD11, in a sample tile (34PET).

resolutions of both the product and reference perimeters, which cause inevitable differences between dates, temporally *long sampling units* of around 115 days (depending on data availability) were designed to

allow a good overlap of reference perimeters with the product. Validation sites were selected from Landsat 7 and 8 scenes following similar criteria to Padilla et al. (2015, 2014). Olson biomes (Olson et al. (2001) and historical fire occurrence were used as stratification criteria. 45 random *long sampling units* were selected (Fig. 8). Every validation site was subsampled using a 30 × 20 km window located in the centre of the scene to increase sampling efficiency and simplify visual inspections in the reference perimeters generation process.

Reference perimeters were created between all pairs of consecutive images. First training polygons were digitized for burned and unburned classes (plus cloud or cloud shadows when needed), which were used to train a RF Classifier with NBR, SWIR and NIR of both dates and the multitemporal NBR difference as input variables. After this semi-automatic mapping of burns, a systematic quality control was performed through visual inspection and training polygons were modified and classification re-run where necessary. This procedure was iterated until no errors were identified.

The validation of both FireCCISFD11 and MCD64A1 products was carried out by estimating the error matrix for each validation site, obtaining the omission (OE) and commission (CE) error ratios for the burned category. The Dice coefficient (DC), which is a measure of accuracy that has a probabilistic meaning (Dice, 1945; Padilla et al., 2015), was also computed; it is defined as the probability that given that one product (the BA product or the reference perimeters) identifies a pixel as burned, the other product will also identify it as burned (Fleiss, 1981). Relative bias (relB) was also computed, as it indicates if BA are overestimated or underestimated in the product. Since the spatial resolution is different for each product (20 and 500 m) and
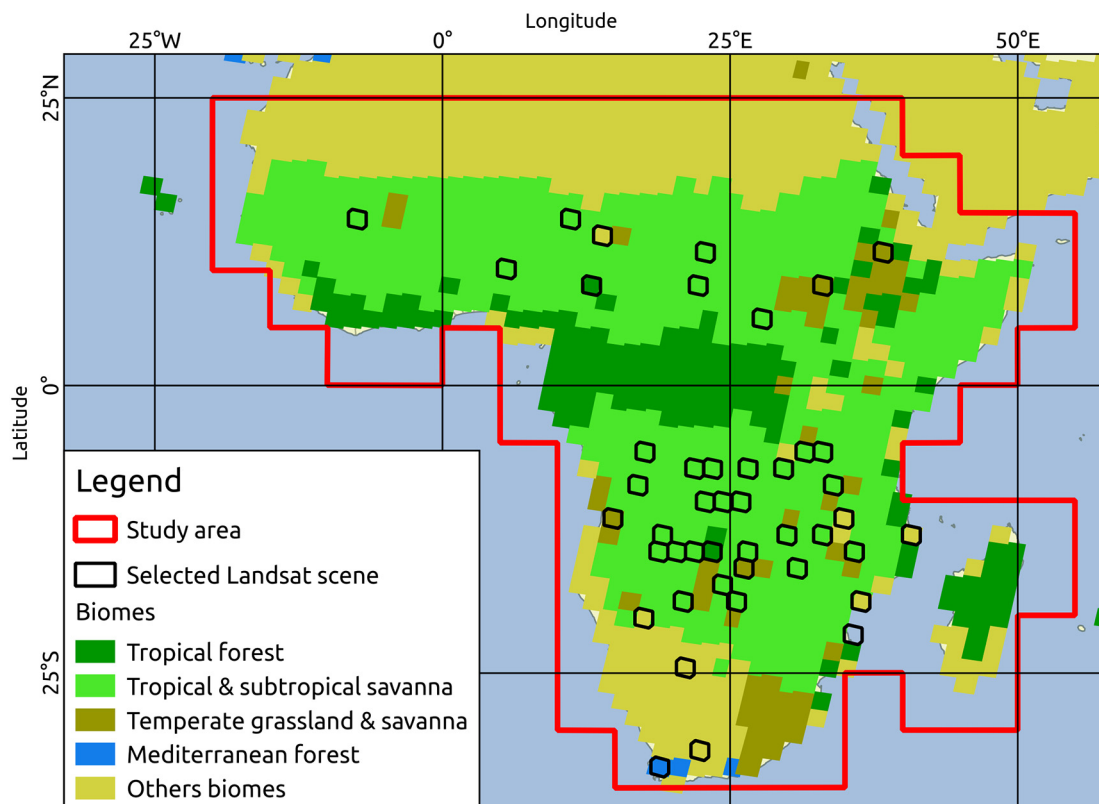
Fig. 8. Location of selected Landsat scenes.

Table 1
Estimated accuracy of the FireCCISFD11 product, in *long* and *short sampling units*. Commission error (CE), omission error (OE), Dice coefficient (DC) and relative bias (relB) are expressed in percentages.

	Commission error (CE)	Omission error (OE)	Dice coefficient (DC)	Relative bias (relB)
Long sampling unit	19.3	26.5	77.0	−9.0
Short sampling unit	64.1	67.4	34.2	−9.0

reference perimeters (30 m), the error matrices were computed by comparing the results as vectors rather than raster images.

All these accuracy measures were computed twice: once for individual pairs of consecutive images (called *short sampling unit*, up to 16 days long), and again for temporal series with consecutive image pairs (called *long sampling unit*, 100 days long at least, 45 in total).

3. Results

3.1. Validation of the FireCCISFD11

The results of the accuracy measures after comparing the FireCCISFD11 product and the validation dataset are shown in Table 1. At *long sampling unit*, omission error (26.5%) is higher than commission error (19.3%), giving a negative relative bias (−9.0%) and a Dice coefficient of 77.0%. At *short sampling unit* both omission and commission sharply increase to over 60%, while DC decreases to 34.2%. The relative bias remains the same, since the total burned surface does not change between a long sampling unit and the sum of corresponding short sampling units. The much lower accuracy of the *short sampling unit* is related to the temporal differences of the acquisitions dates between Landsat (validation source) and Sentinel-2 images.

3.2. Validation of MCD64A1

Table 2 shows the same accuracy measures after comparing the MCD64A1 product and the validation dataset. At *long sampling unit*, omissions (59.6%) were found much higher than commission (20.4%), with a negative relative bias (−49.2%) and Dice coefficient of 53.6%. At *short sampling unit* omission (66.3%) and commission (33.6%) were slightly higher getting 44.7% Dice coefficient.

3.3. Inter-comparison of FireCCISFD11 and MCD64A1

3.3.1. Total BA

Burned area detected by FireCCISFD11 and MCD64A1 were compared in a monthly basis and taking into account the sizes of the burned patches grouped in different fire size classes: < 25 ha, 25–100 ha, 100–250 ha and > 250 ha (Figs. 9 and 10). The total BA detected in the FireCCISFD11 for the whole year 2016 (4.9 M km^2) was 80% larger than the area detected by the MCD64A1 product (2.7 M km^2), being larger on every month (Fig. 9). BA were concentrated between October and March in the Northern Hemisphere (2.3 and 1.3 M km^2 for the FireCCISFD11 and MCD64A1 products, respectively), followed by several months with a reduced fire activity, while in the Southern Hemisphere the highest detection was observed between May and October (2.6 and 1.4 M km^2 for the FireCCISFD11 and MCD64A1 products, respectively).

Both FireCCISFD11 and MCD64A1 products detect a similar BA area

regarding to the largest burned patches (> 250 ha) (Fig. 10), but the differences between products increase gradually as the patch size decreases. The maximum difference was observed for the smallest fire patches (< 25 ha), that were detected by FireCCISFD11 more than thirty times more than by the MCD64A1 for patches equal or < 25 ha. Note that the MODIS minimum detectable area (a pixel) is 25 ha.

3.3.2. Spatial agreement

The fraction of burned area in a 0.05 × 0.05° resolution was aggregated to compare the spatial agreement between FireCCISFD11 and MCD64A1 products (Fig. 11). Both products are shown as well the BA fraction difference between them. Fig. 11d shows the regression between the BA fraction between both products (note FireCCISFD11 is in X axis, and MCD64A1 in Y axis). FireCCISFD11 tends to detect larger burned area than the MCD64A1; the slope of the regression line is lower than 1.0 (0.703) and Fig. 11c shows in general a blue colour that notes the positive fraction difference. Higher burned fractions in the MCD64A1 product were observed when the FireCCISFD11 was not able to detect burned areas because of the high cloud percentage, mostly noticeable at the end of the 2016.

According to Table 3, where correlation is grouped by patch size, very low spatial correlation between the two products was found for patches below 250 ha (R^2 < 0.1), while larger patches showed a much higher correlation (R^2 equal to 0.571), with a regression slope of 0.871 that notes the lower BA fraction values of MCD64A1.

Figs. 12 and 13 illustrate the differences among products in two representative sample sites. The first one (Fig. 12), located in Senegal (tropical and subtropical savanna ecosystems), affects shrublands and tree cover according to the ESA CCI Land Cover map from 2015 (http://maps.elie.ucl.ac.be/CCI/viewer/index.php, last accessed on November 2018). This sample site contains large BA detected with similar shapes by both BA products, though smaller areas were only detected by the FireCCISFD11. Most burned patches were detected later in the FireCCISFD11 than in the MCD64A1 due to its lower temporal resolution, but no significant differences were observed. The second (Fig. 13) sample site, located in Zambia (temperate grassland and savanna ecosystems) affects mostly irrigated croplands and tree covers (ESA CCI Land Cover map). In this case fires tend to be small size, with a very clear underestimation of the MCD64A1; correspondences are only found for largest patches.

3.3.3. Temporal agreement

The temporal accuracy of the BA detection date was analized comparing to de detection dates of the FireCCISFD11 and MCD64A1 against the hotspot MCD14ML acquisition dates. The date of burn chosen in the products was the earliest burned pixel around the hotspot (in a 1 × 1 km^2 window, the spatial accuracy of the active fire product) after the hotspot's date. The overlapping of active fires and FireCCISFD11 showed that 4.2% of the hotspots didn't detect any
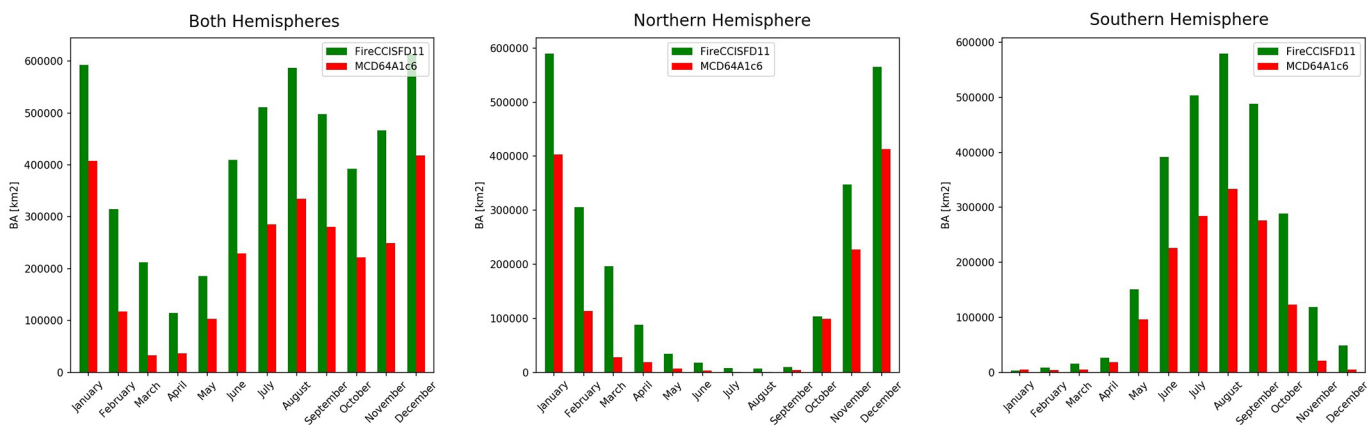
Table 2
Estimated accuracy of the MCD64A1 product, in *long* and *short sampling units*. Commission error (CE), omission error (OE), Dice coefficient (DC) and relative bias (relB) are expressed in percentages.

	Commission error (CE)	Omission error (OE)	Dice coefficient (DC)	Relative bias (relB)
Long sampling unit	20.4	59.6	53.6	−49.2
Short sampling unit	33.6	66.3	44.7	−49.2

Fig. 9. Distribution of burned areas by month in both FireCCISFD11 and MCD64A1 products, depending on the hemisphere.

burned area around them in the FireCCISFD11, while this percentage was significantly higher for MCD64A1 (49.3%). Fig. 14 shows the histogram of the detection delay for both products. For the FireCCISFD11, the 75.5% of the hotspots were detected in the first available image (no > 10 days after the hotspot's date), 88.7% for BA in the second image at the latest (no > 20 days), and almost 95% earlier than the fourth image (no > 40 days). For the MCD64A1 product the detection delay was much lower as due to the higher temporal resolution (1 day), 68.7% of the hotspots were detected within the first acquisition after the fire (no > 1 day), 76.0% in the second image (no > 2 days), and 80.0% in the fourth image (no > 4 days).
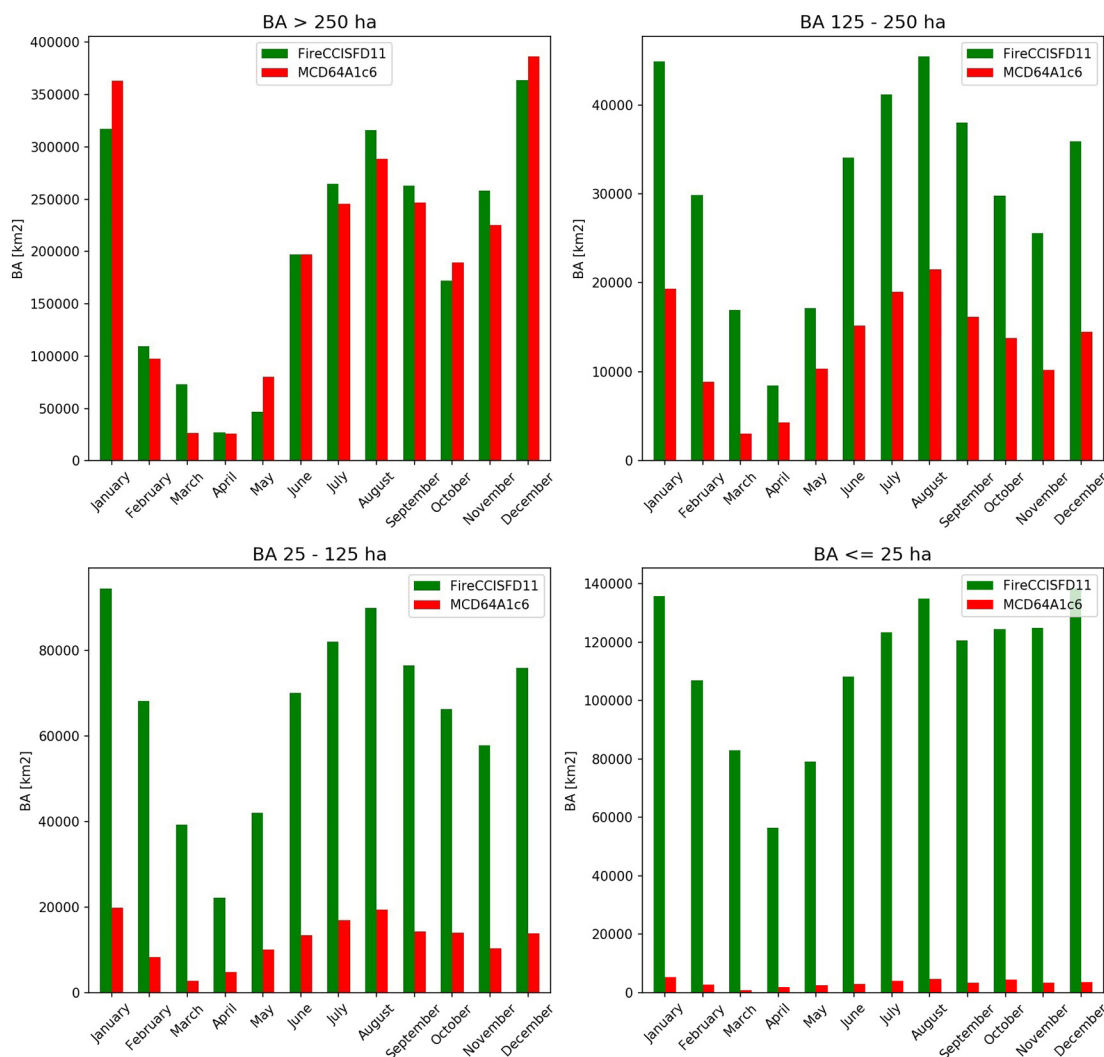

Fig. 10. Distribution of burned area detected in FireCCISFD11 and MCD64A1 grouped by month and patch size.
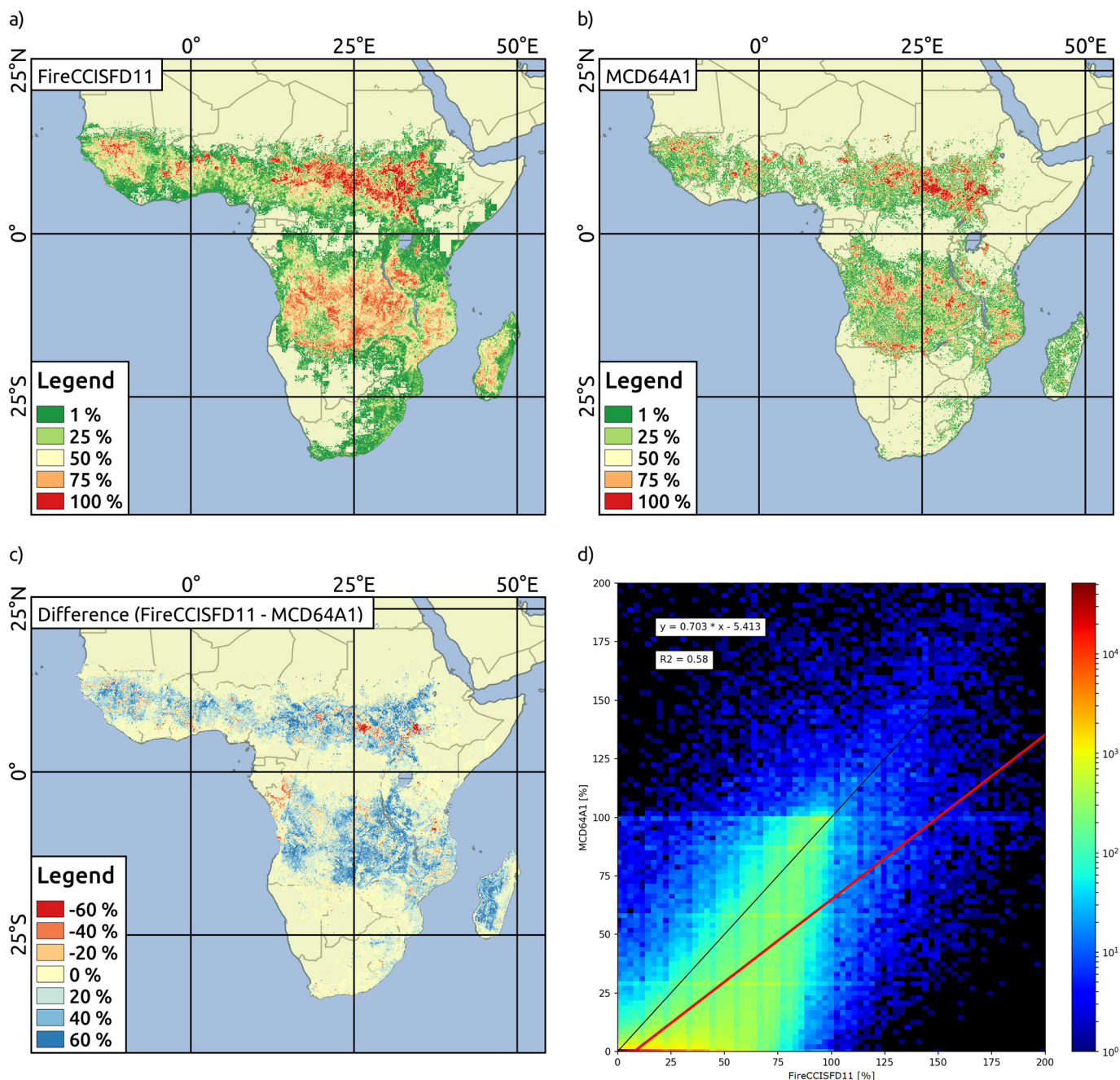
Fig. 11. Aggregated result for the a) FireCCISFD11 and b) MCD64A1 burned areas, representing the fraction of burned surface in a 0.05° grid cell; c) differences between both products, and d) scatter plot and linear regression fitted for the relation between the FireCCISFD11 and MCD64A1 products.

Table 3
Linear regression analysis surface fractions depending on the patch size between FireCCISFD11 and MCD64A1 products.

	Slope	Intercept (%)	R^2
≤ 25 ha	0.015	0.178	0.036
25–125 ha	0.092	0.719	0.072
125–250 ha	0.023	2.343	0.001
> 250 ha	0.835	4.657	0.571
All sizes	0.703	−5.413	0.580

4. Discussion

This paper presents an algorithm to detect burned areas based on Sentinel-2 MSI images and the MCD14ML MODIS active fires product.

The algorithm was implemented operationally and used to generate a new BA product (named FireCCISFD11) that covers the Sub-Saharan Africa for the whole 2016 year, a vast extent of approximately 25 M km^2 covering various biomes (tropical forest, tropical and subtropical savanna, temperate grassland and savanna, and Mediterranean forest, according to Olson et al., 2001). This product involved processing 11 K MSI images in a computation exercise that lasted approximately 6 months.

Even though previous papers have been published using medium resolution data for mapping BA in large regions (such as Hawbaker et al., 2017 and Boschetti et al., 2015 in the US, or Goodwin and Collett, 2014 in Queensland, Australia) this is the first BA continental product generated from medium resolution sensors (in this case Sentinel-2 data) covering a single year. The algorithms by Hawbaker et al., 2017 and Goodwin and Collett, 2014 have some similarities; all of them employ a
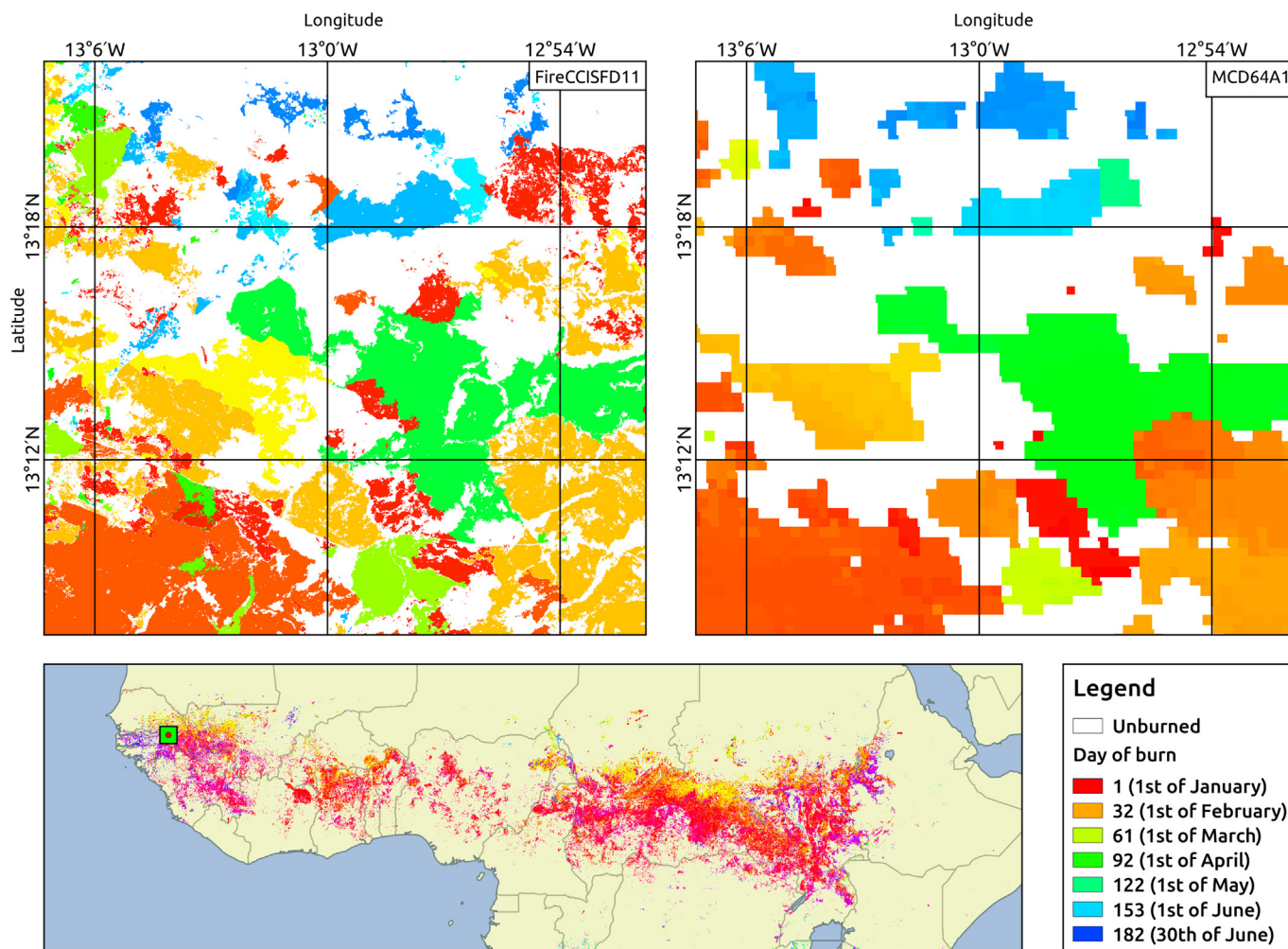
Fig. 12. Sample area of inter-comparison between FireCCISFD11 (left) and MCD64A1 (right) products, located in southeast Senegal.

supervised machine-learning approach based on single or multiple decision trees, adjusted to sample burned data extracted mainly from Landsat images. Both use lagged summaries of Landsat data as a reference against which to measure change, in addition to a region-growing algorithm, although the former used longer lags and also incorporated a wider range of spectral indices as predictors.

The algorithm presented here is more straightforward in this respect: it relies on two very well-known spectral indices—NBR2 and MIRBI- and the NIR spectral region, in a two-phase strategy dependent on MODIS derived active fires. Exploiting the synergy of thermal anomalies detected at the satellite pass and the longer-lasting burned spectral signal is not new (charcoal/ash deposition and removing/alteration of the vegetation) and is the most common strategy used in mapping BA throughout extensive areas globally (Chuvieco et al., 2018; Giglio et al., 2009) as well as continental and regionally (Chen et al., 2017; Merino-De-Miguel et al., 2011; Pereira et al., 2017); however, it has barely been used at a regional/continental scale with higher spatial resolution data (Boschetti et al., 2015). The VIIRS Active fire product was not available at the time the algorithm was designed, but its inclusion can be worthwhile in the future, as it has better spatial resolution than the MODIS product and is likely to provide a greater response over fires of relatively small areas patches (Schroeder et al., 2014, 2008).

A crucial difference of the approach followed here is that after the initialization with fixed thresholds, cut-off values are depending on the individual tile of $100 \times 100\,\text{km}^2$ observed between the burned and unburned categories in each of the six predictive variables (posterior

and multitemporal difference MIRBI, NBR2, and NIR). Consequently, the approach should be more adaptable to the local conditions than the data-mining models grouped by ecosystems (Hawbaker et al., 2017). However, this tile-based focus produces sometimes a grid effect where some tiles showed significantly more burned area detection than their neighbours, or the other way around. This effect is sometimes more pronounced because the criteria that must have at least one hotspot among the pre-fire and post-fire for being processed, resulting in unprocessed tile gaps.

The algorithm mainly relied on two spectral indices (MIRBI, NBR2) as well as the NIR reflectance, with the latter only being used at the seeding process. Although MIRBI and NBR2 were computed from the same two SWIR bands (B11 and B12 on the case of MSI) they have shown to be complementary due to the different frequency distribution that helps reducing the commission errors working together.

The accuracy estimated for the FireCCISFD11 product was quite encouraging, with much lower omission error and commission errors than global products. These errors increase up to 60% for both errors when short periods of time are considered, which reflects the effects of the date discordance between Landsat and Sentinel acquisitions and the low temporal resolution of Sentinel-2 acquisitions. Errors were found similar to those obtained from other authors using medium resolution sensors with relatively small study regions (Bastarrika et al., 2011; Goodwin and Collett, 2014; Mallinis and Koutsias, 2012; Vanderhoof et al., 2017).

Commission errors detected in the FireCCISFD11 are mainly related to an inaccurate masking of clouds, cloud shadows and terrain shadows
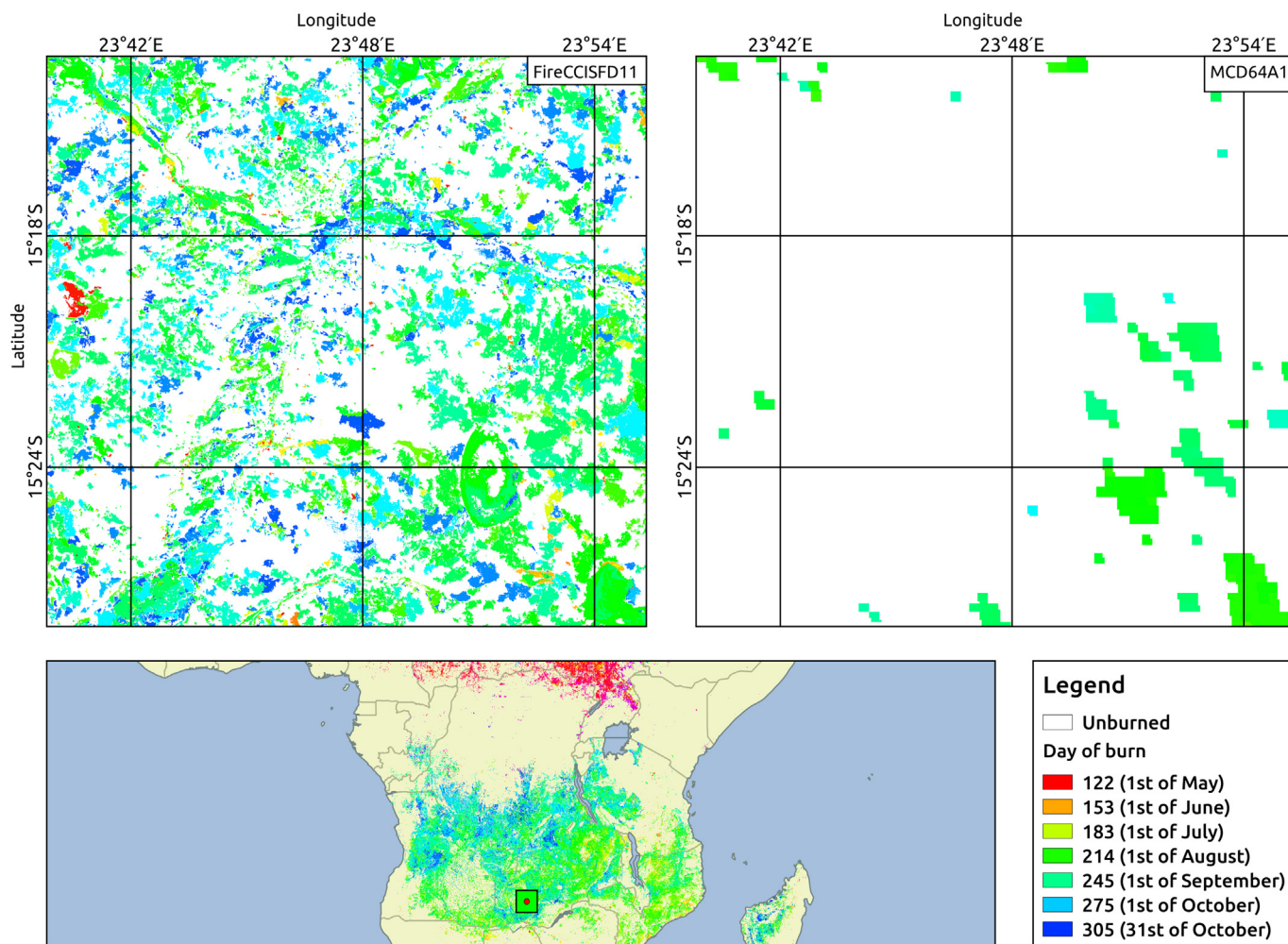
Fig. 13. Sample area of inter-comparison between FireCCISFD11 (left) and MCD64A1 (right) products, located in Zambia.
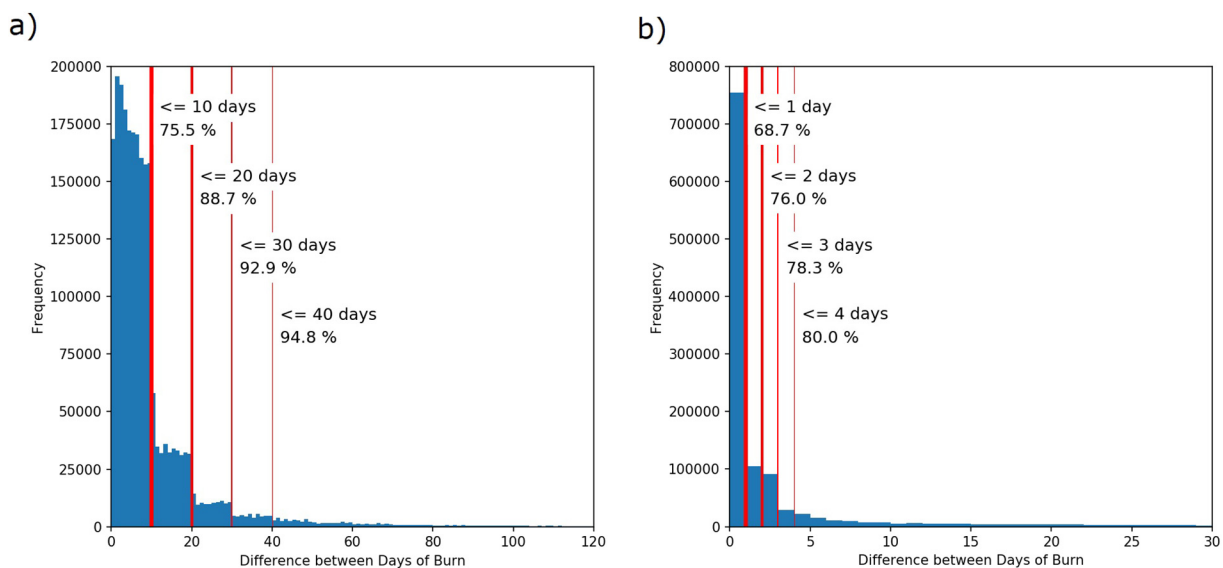

Fig. 14. Detection delay of the a) FireCCISFD11 and b) MCD64A1 comparing to MCD14ML hotspots acquisition date.

that allow locating burned seeds especially in areas where the acquired signal is a mixture of the land surface. The second stage tends to worsen the detection, obtaining many small size burned patches, usually below 25 ha range. The Scene Classification Layer (SCL) derived from the pre-

processing stage, when Level-1C product is converted to Level-2A data, has shown to be complex when using to mask the scenes: *cloud shadows* and *low probability clouds* categories detects many burned areas so they are not used in the mask, while several clouds are still observed in the

masked images, even applying a dilation process to *high probability clouds* and *medium probability cloud* and *thin cirrus* categories. The newer sen2cor version 2.2.1 did not improve either this critical situation. An empirical criterion based on Long SWIR (B12) masked quite efficiently the shadows, but a delay in the detection date of very recently burned areas was observed -especially in the savanna biome- that showed very low Long SWIR reflectance values (these areas are mapped at posterior acquisitions when the burned signal is weaker and high enough to fail the shadow criterion). Another commission source observed, also common in BA algorithms previously published (Bastarrika et al., 2011; Hawbaker et al., 2017; Long et al., 2018) are croplands, whose reflectance changes are often indistinguishable from burning, especially in periods where these changes are coincident with fires (during the harvest, postharvest or preplanting periods) (Korontzi et al., 2006). Omission errors are higher than commission and they are mainly related to burned areas with low contrast with the unburned background, due to low severity fires or the gap of time between the fire and the acquisition where charcoal is removed and vegetation starts recovering. In such situations, the contrast between burned and unburned background is not high enough and omissions happen since the initialization step, and therefore the second stage criteria, consider many burned areas as background making their detection unfeasible.

The comparison analysis between the FireCCISFD11 (20 m spatial resolution) with the widely used MCD64A1 collection 6 (based on 500 m spatial resolution MODIS data) emphasised the importance of the input source spatial resolution to map burned areas accurately. MCD64A1, in the same validation dataset as that used for FireCCISFD11, showed an omission error of approximately 60% for the *long sampling unit*, 30% more than the FireCCISFD11. So the FireCCISFD11 is more accurate in *long sampling units* due to its higher spatial resolution, even if the MCD64A1 product is more accurate for *short sampling units*, because of its higher temporal resolution allows the day of detection to be very close to the day of burn. These omissions are produced mainly in burned patches smaller than 250 ha, showing the higher correlation among products for the larger patches, while commission errors for both products were similar, around 20%. The lower temporal resolution of Sentinel-2 data was reflected in detection date accuracy of the products, with approximately 75% of the burned areas were detected in the first acquisition after the fire (10 days), while in the second acquisition (2 days) for the MCD64A1. This better temporal accuracy of the fire date was also noted on the *short sampling unit* validation with only the 34% of commission error for MCD64A1 but up to 64% for the FireCCISFD11. The future use of both Sentinels 2 (A and B) or the combined use of Sentinel-2 and Landsat-8 images may greatly increase this temporal reporting accuracy for medium resolution sensor BA products.

For the whole study area and period (January–December 2016), FireCCISFD11 detected about 80% more BA than MCD64A1, which underlines the relevance of underestimation of small fires in current global products. This numbers must be qualified in the context of the results obtained in the assessment of the products: commission errors in the FireCCISFD11 are related to clouds/shadows that may impact in a false higher burned detection in cloudy areas that have not been fully validated, while commission errors of MCD64A1 are not common and mainly related to the spatial resolution (Giglio et al., 2018, 2009). The presence of commissions in cloud edges points to the significance of refining clouds masks. Moreover, the validation sites were selected proportionally to the BA in the MCD64A1 product (Section 2.5), so areas where only small fires occur (with low burned area in MCD64A1) may have been missed in the assessment process.

The BA mapping at medium spatial resolution of FireCCISFD11 is crucial to improve the accuracy of the emission of greenhouse gases into the atmosphere, and for many other applications as land management, environmental, climate change adaptation and land cover change applications.

5. Conclusions

An automatic BA mapping algorithm based on Sentinel-2 MSI data is presented in this paper, in order to emphasize the importance of the spatial resolution of this sensor in mapping accurately small burned areas. The FireCCISFD11 product in Sub-Saharan Africa generated by this algorithm is an innovation, since there were very few BA products at high spatial resolution (30 m from Landsat data at best) covering such a large area until now, and none derived from S2 MSI imagery (at 20 m spatial resolution).

The assessment using Landsat data shows that both commissions and omissions are much lower than those measured for global BA products, due to the ability of the FireCCISFD11 to detect small fires that were at a sub-pixel scale in other products. The FireCCISFD11 detects 80% more BA than the global MCD64A1 product in 2016, most of them being burned patches smaller than 250 ha, which signals how much the total BA may have been underestimated in global products. However, the FireCCISFD11 is not so accurate temporally, since the long revisit period of the S2 satellite (10 days) and the presence of clouds delay the detection date; the revisit period will be shorter in the future if a product with S2 data from April 2017 onwards is produced, when both S2-A and S2-B satellites are in orbit with a 5-day revisit.

The next step for the product is to apply the algorithm at a global scale with necessary changes, especially improving the clouds and cloud shadows detection, which is now the main source of commission errors. We also think the product would improve if MODIS hotspots from the MCD14ML were replaced by VIIRS hotspots, which have a better spatial resolution but were not available yet when we designed this algorithm. Creating a global BA product at 20 m would certainly increase the amount of the total burned area. Its implications in different applications (greenhouse gas emissions, land cover changes, land management, etc.) should be analysed in due time.

Acknowledgments

References

Alonso-Canas, I., Chuvieco, E., 2015. Global burned area mapping from ENVISAT-MERIS and MODIS active fire data. Remote Sens. Environ. 163, 140–152. https://doi.org/10.1016/j.rse.2015.03.011.

Andreae, M.O., Metlet, P., 2001. Emission of trace gases and aerosols from biomass burning. Glob. Biogeochem. Cycles 15, 955–966.

Bastarrika, A., Chuvieco, E., Martín, M.P., 2011. Mapping burned areas from Landsat TM/ETM+ data with a two-phase algorithm: balancing omission and commission errors. Remote Sens. Environ. 115, 1003–1012. https://doi.org/10.1016/j.rse.2010.12.005.

Bastarrika, A., Alvarado, M., Artano, K., Martinez, M., Mesanza, A., Torre, L., Ramo, R., Chuvieco, E., 2014. BAMS: a tool for supervised burned area mapping using Landsat data. Remote Sens. 6, 12360–12380. https://doi.org/10.3390/rs61212360.

Boschetti, L., Roy, D., Justice, C., 2009. International global burned area satellite product validation protocol. In: Cal Val, C. (Ed.), Part I - Production and Standardization of Validation Reference Data. Committee on Earth Observation Satellites, USA, pp. 1–11.

Boschetti, L., Roy, D.P., Justice, C.O., Humber, M.L., 2015. MODIS–Landsat fusion for large area 30 m burned area mapping. Remote Sens. Environ. 161, 27–42. https://doi.org/10.1016/j.rse.2015.01.022.

Bowman, D.M.J.S., Balch, J.K., Artaxo, P., Bond, W.J., Carlson, J.M., Cochrane, M.A., D'Antonio, C.M., DeFries, R.S., Doyle, J.C., Harrison, S.P., Johnston, F.H., Keeley, J.E., Krawchuk, M.A., Kull, C.A., Marston, J.B., Moritz, M.A., Prentice, I.C., Roos, C.I., Scott, A.C., Swetnam, T.W., van der Werf, G.R., Pyne, S.J., 2009. Fire in the earth system. Science 324, 481–484.

Chen, D., Pereira, J.M.C., Masiero, A., Pirotti, F., 2017. Mapping fire regimes in China using MODIS active fire and burned area data. Appl. Geogr. 85, 14–26. https://doi.org/10.1016/J.APGEOG.2017.05.013.

Chuvieco, E., Martín, M.P., Palacios, A., 2002. Assessment of different spectral indices in the red-near-infrared spectral domain for burned land discrimination. Int. J. Remote

Sens. 23, 5103–5110. https://doi.org/10.1080/01431160210153129.

Chuvieco, E., Yue, C., Heil, A., Mouillot, F., Alonso-Canas, I., Padilla, M., Pereira, J.M., Oom, D., Tansey, K., 2016. A new global burned area product for climate assessment of fire impacts. Glob. Ecol. Biogeogr. 25, 619–629. https://doi.org/10.1111/geb.12440.

Chuvieco, E., Lizundia-Loiola, J., Pettinari, M.L., Ramo, R., Padilla, M., Tansey, K., Mouillot, F., Laurent, P., Storm, T., Heil, A., Plummer, S., 2018. Generation and analysis of a new global burned area product based on MODIS 250 m reflectance bands and thermal anomalies. Earth Syst. Sci. Data Discuss. 1–24. https://doi.org/10.5194/essd-2018-46.

Dice, L.R., 1945. Measures of the amount of ecologic association between species. Ecology 26, 297–302. https://doi.org/10.2307/1932409.

Drusch, M., Del Bello, U., Carlier, S., Colin, O., Fernandez, V., Gascon, F., Hoersch, B., Isola, C., Laberinti, P., Martimort, P., Meygret, A., Spoto, F., Sy, O., Marchese, F., Bargellini, P., 2012. Sentinel-2: ESA's optical high-resolution mission for GMES operational services. Remote Sens. Environ. 120, 25–36. https://doi.org/10.1016/j.rse.2011.11.026.

ESA, 2011. MSI Instrument – Sentinel-2 MSI Technical Guide – Sentinel Online [WWW Document].

Fleiss, J.L., 1981. Statistical Methods for Rates and Proportions. Wiley.

Fraser, R.H., Li, Z., Cihlar, J., 2000. Hotspot and NDVI differencing synergy (HANDS): a new technique for burned area mapping over boreal forest. Remote Sens. Environ. 74, 362–376. https://doi.org/10.1016/S0034-4257(00)00078-X.

Fraser, R.H., Fernandes, R., Latifovic, R., 2002. Multi-temporal burned area mapping using logistic regression analysis and change metrics. In: IEEE International Geoscience and Remote Sensing Symposium, pp. 1486–1488. https://doi.org/10.1109/IGARSS.2002.1026157.

García, M.J.L., Caselles, V., 1991. Mapping burns and natural reforestation using thematic Mapper data. Geocarto Int. 6, 31–37. https://doi.org/10.1080/10106049109354290.

Giglio, L., Csiszar, I., Justice, C.O., 2006a. Global distribution and seasonality of active fires as observed with the Terra and Aqua Moderate Resolution Imaging Spectroradiometer (MODIS) sensors. J. Geophys. Res. Biogeosci. 111https://doi.org/10.1029/2005JG000142. (n/a-n/a).

Giglio, L., van der Werf, G.R., Randerson, J.T., Collatz, G.J., Kasibhatla, P., 2006b. Global estimation of burned area using MODIS active fire observations. Atmos. Chem. Phys. 6, 957–974. https://doi.org/10.5194/acp-6-957-2006.

Giglio, L., Loboda, T., Roy, D.P., Quayle, B., Justice, C.O., 2009. An active-fire based burned area mapping algorithm for the MODIS sensor. Remote Sens. Environ. 113, 408–420. https://doi.org/10.1016/j.rse.2008.10.006.

Giglio, L., Randerson, J.T., van der Werf, G.R., Kasibhatla, P.S., Collatz, G.J., Morton, D.C., DeFries, R.S., 2010. Assessing variability and long-term trends in burned area by merging multiple satellite fire products. Biogeosciences 7, 1171–1186. https://doi.org/10.5194/bg-7-1171-2010.

Giglio, L., Randerson, J.T., van der Werf, G.R., 2013. Analysis of daily, monthly, and annual burned area using the fourth-generation global fire emissions database (GFED4). J. Geophys. Res. Biogeosci. 118, 317–328. https://doi.org/10.1002/jgrg.20042.

Giglio, L., Schroeder, W., Justice, C.O., 2016. The collection 6 MODIS active fire detection algorithm and fire products. Remote Sens. Environ. 178, 31–41. https://doi.org/10.1016/j.rse.2016.02.054.

Giglio, L., Boschetti, L., Roy, D.P., Humber, M.L., Justice, C.O., 2018. The collection 6 MODIS burned area mapping algorithm and product. Remote Sens. Environ. 217, 72–85. https://doi.org/10.1016/j.rse.2018.08.005.

Gómez, C., White, J.C., Wulder, M.A., 2016. Optical remotely sensed time series data for land cover classification: a review. ISPRS J. Photogramm. Remote Sens. https://doi.org/10.1016/j.isprsjprs.2016.03.008.

Goodwin, N.R., Collett, L.J., 2014. Development of an automated method for mapping fire history captured in Landsat TM and ETM+ time series across Queensland, Australia. Remote Sens. Environ. 148, 206–221. https://doi.org/10.1016/j.rse.2014.03.021.

Grégoire, J.M., Eva, H.D., Belward, A.S., Palumbo, I., Simonetti, D., Brink, A., 2013. Effect of land-cover change on Africa's burnt area. Int. J. Wildland Fire 22, 107–120. https://doi.org/10.1071/WF11142.

Hantson, S., Padilla, M., Corti, D., Chuvieco, E., 2013. Strengths and weaknesses of MODIS hotspots to characterize global fire occurrence. Remote Sens. Environ. 131, 152–159. https://doi.org/10.1016/j.rse.2012.12.004.

Hantson, S., Lasslop, G., Kloster, S., Chuvieco, E., 2015. Anthropogenic effects on global mean fire size. Int. J. Wildland Fire 24, 589–596. https://doi.org/10.1071/WF14208.

Hawbaker, T.J., Vanderhoof, M.K., Beal, Y.-J., Takacs, J.D., Schmidt, G.L., Falgout, J.T., Williams, B., Fairaux, N.M., Caldwell, M.K., Picotte, J.J., Howard, S.M., Stitt, S., Dwyer, J.L., 2017. Mapping burned areas using dense time-series of Landsat data. Remote Sens. Environ. 198, 504–522. https://doi.org/10.1016/j.rse.2017.06.027.

Huang, H., Roy, D.P., Boschetti, L., Zhang, H.K., Yan, L., Kumar, S.S., Gomez-Dans, J., Li, J., 2016. Separability analysis of Sentinel-2A Multi-Spectral Instrument (MSI) data for burned area discrimination. Remote Sens. 8. https://doi.org/10.3390/rs8100873.

Huete, A.R., 1988. A soil-adjusted vegetation index (SAVI). Remote Sens. Environ. 25, 295–309. https://doi.org/10.1016/0034-4257(88)90106-X.

Huete, A.R., Justice, C., Liu, H., 1994. Development of vegetation and soil indexes for Modis-EOS. Remote Sens. Environ. 49, 224–234. https://doi.org/10.1016/0034-4257(94)90018-3.

Kaufman, Y.J., Remer, L.A., 1994. Detection of forests using mid-IR reflectance: an application for aerosol studies. IEEE Trans. Geosci. Remote Sens. 32, 672–683. https://doi.org/10.1109/36.297984.

Key, C.H., Benson, N., 1999. The Normalized Burn Ratio (NBR): A Landsat TM Radiometric Measure of Burn Severity. US Geol. Surv. North. Rocky Mt. Sci. Center.

Korontzi, S., McCarty, J., Loboda, T., Kumar, S., Justice, C., 2006. Global distribution of agricultural fires in croplands from 3 years of Moderate Resolution Imaging Spectroradiometer (MODIS) data. Glob. Biogeochem. Cycles 20. https://doi.org/10.1029/2005GB002529.

Koutsias, N., Karteris, M., 2000. Burned area mapping using logistic regression modeling of a single post-fire Landsat-5 Thematic Mapper image. Int. J. Remote Sens. 21, 673–687. https://doi.org/10.1080/014311600210506.

Lasaponara, R., 2006. Estimating spectral separability of satellite derived parameters for burned areas mapping in the Calabria region by using SPOT-Vegetation data. Ecol. Model. 196, 265–270. https://doi.org/10.1016/j.ecolmodel.2006.02.025.

Lewis, S.L., Edwards, D.P., Galbraith, D., 2015. Increasing human dominance of tropical forests. Science. https://doi.org/10.1126/science.aaa9932.

Long, T., Zhang, Z., He, G., Jiao, W., Tang, C., Wu, B., Zhang, X., Wang, G., Yin, R., 2018. 30 m Resolution Global Annual Burned Area Mapping Based on Landsat Images and Google Earth Engine.

Mallinis, G., Koutsias, N., 2012. Comparing ten classification methods for burned area mapping in a Mediterranean environment using Landsat TM satellite data. Int. J. Remote Sens. 33, 4408–4433. https://doi.org/10.1080/01431161.2011.648284.

Martín, M.P., Chuvieco, E., 1998. Cartografía de grandes insendios forestales en la península Ibérica a partir de imágenes NOAA-AVHRR. In: Teledetección Av. y Apl, pp. 248–251.

Martin, P., Gómez, I., Chuvieco, E., 2005. Performance of a burned-area index (BAIM) for mapping Mediterranean burned scars from MODIS data. In: Proceedings of the 5th International Workshop on Remote Sensing and GIS Application to Forest Fire Management: Fire Effects Assessment, pp. 193–197.

Merino-De-Miguel, S., González-Alonso, F., Huesca, M., Armenteras, D., Franco, C., Topografía, U., 2011. MODIS reflectance and active fire data for burn mapping in Colombia. Earth Interact. 15. https://doi.org/10.1175/2010EI344.1.

Olson, D.M., Dinerstein, E., Wikramanayake, E.D., Burgess, N.D., Powell, G.V.N., Underwood, E.C., D'amico, J.A., Itoua, I., Strand, H.E., Morrison, J.C., Loucks, C.J., Allnutt, T.F., Ricketts, T.H., Kura, Y., Lamoreux, J.F., Wettengel, W.W., Hedao, P., Kassem, K.R., 2001. Terrestrial ecoregions of the world: a new map of life on earth. Bioscience 51, 933. https://doi.org/10.1641/0006-3568(2001)051[0933:TEOTWA]2.0.CO;2.

Padilla, M., Stehman, S.V., Litago, J., Chuvieco, E., 2014. Assessing the temporal stability of the accuracy of a time series of burned area products. Remote Sens. 6, 2050–2068. https://doi.org/10.1207/s15327752jpa4405_22.

Padilla, M., Stehman, S.V., Ramo, R., Corti, D., Hantson, S., Oliva, P., Alonso-Canas, I., Bradley, A.V., Tansey, K., Mota, B., Pereira, J.M., Chuvieco, E., 2015. Comparing the accuracies of remote sensing global burned area products using stratified random sampling and estimation. Remote Sens. Environ. 160, 114–121. https://doi.org/10.1016/j.rse.2015.01.005.

Pereira, J.M.C., Sa, A.C.L., Sousa, A.M.O., Silva, J.M.N., Santos, M.T.N., JMBC, 1999. Spectral characterisation and discrimination of burnt areas. In: Chuvieco, E. (Ed.), Remote Sensing of Large Wildfires in the European Mediterranean Basin, pp. 123–138.

Pereira, A.A., Pereira, J.M.C., Libonati, R., Oom, D., Setzer, A.W., Morelli, F., Machado-Silva, F., de Carvalho, L.M.T., 2017. Burned area mapping in the Brazilian Savanna using a one-class support vector machine trained by active fires. Remote Sens. 9. https://doi.org/10.3390/rs9111161.

Pinty, B., Verstraete, M.M., 1992. GEMI: a non-linear index to monitor global vegetation from satellites. Vegetatio 101, 15–20. https://doi.org/10.1007/BF00031911.

Plummer, S., Arino, O., Simon, M., Steffen, W., 2006. Establishing a earth observation product service for the terrestrial carbon community: the GLOBCARBON Initiative. Mitig. Adapt. Strateg. Glob. Chang. 11, 97–111. https://doi.org/10.1007/s11027-006-1012-8.

Pu, R., Gong, P., 2004. Determination of burnt scars using logistic regression and neural network techniques from a single post-fire Landsat 7 ETM+ image. Photogramm. Eng. Remote. Sens. 70, 841–850. https://doi.org/10.14358/PERS.70.7.841.

Randerson, J.T., Chen, Y., van der Werf, G.R., Rogers, B.M., Morton, D.C., 2012. Global burned area and biomass burning emissions from small fires. J. Geophys. Res. Biogeosci. 117https://doi.org/10.1029/2012JG002128. (n/a-n/a).

Rouse, J.W., Haas, R.H., Schell, J.A., 1974. Monitoring the Vernal Advancement and Retrogradation (Greenwave Effect) of Natural Vegetation. NASA Goddard Sp. Flight Cent (doi:19740008955).

Roy, D.P., Boschetti, L., Justice, C.O., Ju, J., 2008. The collection 5 MODIS burned area product — global evaluation by comparison with the MODIS active fire product. Remote Sens. Environ. 112, 3690–3707. https://doi.org/10.1016/j.rse.2008.05.013.

Schroeder, W., Prins, E., Giglio, L., Csiszar, I., Schmidt, C., Morisette, J., Morton, D., 2008. Validation of GOES and MODIS active fire detection products using ASTER and ETM+ data. Remote Sens. Environ. 112, 2711–2726. https://doi.org/10.1016/j.rse.2008.01.005.

Schroeder, W., Oliva, P., Giglio, L., Csiszar, I.A., 2014. The New VIIRS 375 m active fire detection data product: algorithm description and initial assessment. Remote Sens. Environ. 143, 85–96. https://doi.org/10.1016/j.rse.2013.12.008.

Schroeder, W., Oliva, P., Giglio, L., Quayle, B., Lorenz, E., Morelli, F., 2016. Active fire detection using Landsat-8/OLI data. Remote Sens. Environ. 185, 210–220. https://doi.org/10.1016/j.rse.2015.08.032.

Simon, M., Plummer, S., Fierens, F., Hoelzemann, J.J., Arino, O., 2004. Burnt area detection at global scale using ATSR-2: the GLOBSCAR products and their qualification. J. Geophys. Res. 109, D14S02. https://doi.org/10.1029/2003JD003622.

Smith, A.M.S., Drake, N.A., Wooster, M.J., Hudak, A.T., Holden, Z.A., Gibbons, C.J., 2007. Production of Landsat ETM+ reference imagery of burned areas within Southern African savannahs: comparison of methods and application to MODIS. Int. J. Remote Sens. 28, 2753–2775. https://doi.org/10.1080/01431160600954704.

Stroppiana, D., Bordogna, G., Carrara, P., Boschetti, M., Boschetti, L., Brivio, P.A., 2012. A method for extracting burned areas from Landsat TM/ETM+ images by soft

aggregation of multiple Spectral Indices and a region growing algorithm. ISPRS J. Photogramm. Remote Sens. 69, 88–102. https://doi.org/10.1016/j.isprsjprs.2012. 03.001.

Stroppiana, D., Azar, R., Calò, F., Pepe, A., Imperatore, P., Boschetti, M., Silva, J., Brivio, P., Lanari, R., 2015. Received: 4 May 2014/Accepted: 12 January 2015/Published: 26 January 2015. Remote Sens. 7, 1320–1345. https://doi.org/10.3390/rs70201320.

Tansey, K., Grégoire, J., Stroppiana, D., Sousa, A., Silva, J., Pereira, J.M.C., Boschetti, L., Maggi, M., Brivio, P.A., Fraser, R., Flasse, S., Ershov, D., Binaghi, E., Graetz, D., Peduzzi, P., 2004. Vegetation burning in the year 2000: global burned area estimates from SPOT VEGETATION data. J. Geophys. Res. 109, D14S03. https://doi.org/10. 1029/2003JD003598.

Tansey, K., Beston, J., Hoscilo, A., Page, S.E., Paredes Hernández, C.U., 2008. Relationship between MODIS fire hot spot count and burned area in a degraded tropical peat swamp forest in Central Kalimantan, Indonesia. J. Geophys. Res. 113, D23112. https://doi.org/10.1029/2008JD010717.

Trigg, S., Flasse, S., 2001. An evaluation of different bi-spectral spaces for discriminating burned shrub-savannah. Int. J. Remote Sens. 22, 2641–2647. https://doi.org/10. 1080/01431160110053185.

Van Der Werf, G.R., Randerson, J.T., Giglio, L., Van Leeuwen, T.T., Chen, Y., Rogers, B.M., Mu, M., Van Marle, M.J.E., Morton, D.C., Collatz, G.J., Yokelson, R.J., Kasibhatla, P.S., 2017. Global fire emissions estimates during 1997–2016. Earth Syst. Sci. Data. https://doi.org/10.5194/essd-9-697-2017.

Vanderhoof, M.K., Fairaux, N., Beal, Y.-J.G., Hawbaker, T.J., 2017. Validation of the USGS Landsat Burned Area Essential Climate Variable (BAECV) across the conterminous United States. Remote Sens. Environ. 198, 393–406. https://doi.org/10. 1016/j.rse.2017.06.025.

Veraverbeke, S., Harris, S., Hook, S., 2011. Evaluating spectral indices for burned area discrimination using MODIS/ASTER (MASTER) airborne simulator data. Remote Sens. Environ. 115, 2702–2709. https://doi.org/10.1016/j.rse.2011.06.010.

II eranskina: A2 – BAMT erremintak

Artikulua

Izenburua: Landsat and Sentinel-2 Based Burned Area Mapping Tools in Google Earth Engine

Egileak: Ekhi Roteta, Aitor Bastarrika, Magí Franquesa eta Emilio Chuvieco

Argitaratze-data: 2021eko otsaila

DOI: https://doi.org/10.3390/rs13040816

Erreferentzia bibliografikoa:

Roteta, E., Bastarrika, A., Franquesa, M., Chuvieco, E., 2021. Landsat and Sentinel-2 Based Burned Area Mapping Tools in Google Earth Engine. *Remote Sens.* 13, 816. https://doi.org/10.3390/rs13040816

Aldizkaria

Izena: Remote Sensing

Sortze-urtea: 2009

Argitaratze-urteko inpaktu-faktorea: 5,349

Argitaratze-urteko posizioa *REMOTE SENSING* arloan:

> **Postua**: 11/34
>
> **Pertzentila**: %69
>
> **Kuartila**: Q2

Landsat and Sentinel-2 Based Burned Area Mapping Tools in Google Earth Engine

Ekhi Roteta [1,*] **, Aitor Bastarrika** [1] **, Magí Franquesa** [2] **and Emilio Chuvieco** [2]

1   Department of Mining and Metallurgical Engineering and Materials Science, School of Engineering of Vitoria-Gasteiz, University of the Basque Country UPV/EHU, Nieves Cano 12, 01006 Vitoria-Gasteiz, Spain; aitor.bastarrika@ehu.eus
2   Environmental Remote Sensing Research Group, Department of Geology, Geography and the Environment, Universidad de Alcalá, C/Colegios 2, 28801 Alcalá de Henares, Spain; magin.franquesa@uah.es (M.F.); emilio.chuvieco@uah.es (E.C.)
*   Correspondence: ekhi.roteta@ehu.eus

Abstract: Four burned area tools were implemented in Google Earth Engine (GEE), to obtain regular processes related to burned area (BA) mapping, using medium spatial resolution sensors (Landsat and Sentinel-2). The four tools are (i) the BA Cartography tool for supervised burned area over the user-selected extent and period, (ii) two tools implementing a BA stratified random sampling to select the scenes and dates for validation, and (iii) the BA Reference Perimeter tool to obtain highly accurate BA maps that focus on validating coarser BA products. Burned Area Mapping Tools (BAMTs) go beyond the previously implemented Burned Area Mapping Software (BAMS) because of GEE parallel processing capabilities and preloaded geospatial datasets. BAMT also allows temporal image composites to be exploited in order to obtain BA maps over a larger extent and longer temporal periods. The tools consist of four scripts executable from the GEE Code Editor. The tools' performance was discussed in two case studies: in the 2019/2020 fire season in Southeast Australia, where the BA cartography detected more than 50,000 km^2, using Landsat data with commission and omission errors below 12% when compared to Sentinel-2 imagery; and in the 2018 summer wildfires in Canada, where it was found that around 16,000 km^2 had burned.

Keywords: burned area; Australia; Canada; tools; validation; Landsat; Sentinel-2; Google Earth Engine

1. Introduction

Biomass burning is a significant disturbance that causes soil erosion and land-cover changes and releases greenhouse gas emissions into the atmosphere, also affecting people's lives and properties [1–3]. Fires are present in most types of vegetation in the world, especially grasslands, savannas, and forest, and they occur on all continents, with a significant incidence in Africa, which accounts for 70% of the global burned area [4–6]. Therefore, burned areas (BAs) must be detected accurately both spatially and temporally, for which satellite Earth observation has been much used over the last few decades, especially using coarse spatial resolution [5–14]. Global products at coarse spatial resolutions have significant omission errors [4,15–18], but creating products at medium resolution, although more accurate, is also quite challenging: It implies a heavy data-processing workload, and the temporal resolution is low (typically one image every 5 to 16 days).

Using BA mapping with medium spatial resolution had been operationally quite limited until Landsat historic imagery became freely available in 2008, since the scientific literature on this topic had been mainly limited to single or neighboring scenes [19–21]. In addition, since 2015, the Sentinel-2 imagery has added a large volume of imagery that makes it possible to analyze time series at a medium spatial resolution. A few BA automatic algorithms have been developed, using time series data, especially using Landsat

data [22–25], albeit also using Sentinel-2 [16,26], or a combination of the two [27]. So far, the only example of a global product based on medium-resolution data is Global Annual Burned Area Map (GABAM) [23], obtained for 2015, using Landsat data. At the continental level, it is worth mentioning the Landsat Burned Area Essential Climate Variable (BAECV) covering the Conterminous United States (CONUS) [25,28], the province of Queensland in Australia for the whole Landsat historical database [29] and the sub-Saharan Africa in 2016 [16].

Despite this effort to develop automatic algorithms, supervised multitemporal image analysis is considered to be a superior method for the purpose of mapping burned areas. In fact, it allows for differentiation between old and new burns, and reliably detects small spatially fragmented low-combustion completeness burns. It also enables gross errors that may occur in satellite data to be accommodated, and differentiates between burned and spectrally similar unburned features [30]. For example, supervised analysis of higher spatial resolution imagery is adopted as the validation protocol for BA mapping [31]. Although visual interpretation and delineation are generally recommended [12,30,32,33], these processes usually take the form of a supervised semi-automatic classification that is visually checked and manually refined [15,34]. Compared to the field-based classical methods used to report official statistics on burned areas, remote sensing-based mapping is more objective and efficient, less labor- and time-consuming and more repeatable [35].

In 2014, the University of the Basque Country (UPV/EHU) developed a software for supervised BA mapping, using Landsat data: Burned Area Mapping Software (BAMS). This software was basically designed to process a pair of Landsat images at a time, allowing for BA mapping between the two scenes, using a two-phase mapping strategy, thus obtaining the burned polygons in a vector layer [36]. It provided good cost efficiency, although it relied on the processing capacity of the user's computer and was based on a commercial GIS software. The software was widely used to create validation areas inside the Fire_cci project [15,37,38], as well as for the USGS Burned Product initial validation, and many other fire science-related users, environmental techniques and the commercial community [16,28,37,39–41]. However, several limitations were also detected and discussed with users. Firstly, it was only applicable to Landsat data and was unable to process Sentinel-2 data. Secondly, the software was not easily maintained as metadata and the Landsat data format changed and its proper functioning was interrupted several times. Finally, the BAMS mapping methodology trained only the burned category and saved time for the user, but the user was unable to control the unburned category properly; thus, a manual edition was often necessary to remove commission errors in agricultural areas and cloud shadows.

Google Earth Engine (GEE) is a free cloud-computing platform for satellite data processing, with several data catalogs at different resolutions (notably Landsat, Sentinel-2 and MODIS) and planetary-scale analysis capabilities (https://earthengine.google.com (accessed on 27 January 2021)) [42]. Since the first significant work on the topic was published in 2013 [43], the number of studies using GEE has dramatically increased, with more than 200 papers having been published in 2019 [44], covering all types of applications, such as vegetation mapping and monitoring, land-cover mapping, agricultural applications, and disaster management and Earth sciences [45]. However, there have not been so many published papers on the fire field [23,46–48].

This study presents several tools that we have developed and released in GEE. These tools are referred to as Burned Area Mapping Tools (BAMTs), and they cover the entire BA mapping process: from creating a large extent BA map to creating statistically design samples for validation studies and the actual generation of BA reference perimeters (RPs), using both Landsat and Sentinel-2 images. The study describes these tools and provides two case studies that were applied in the Australian fire season between 2019 and 2020, and in the Canadian wildfires from the summer of 2018. All four tools and the user guide are totally free and can be reached at https://github.com/ekhiroteta/BAMT (accessed on 27 January 2021).

2. BAMT Tools

Four tools have been developed for BA mapping:

1. **BA Cartography**: The user can create a BA product over a large region and a long period of time, from changes between two temporal images via a supervised classification.

2. **VA**: for validation area (VA) selection based on several strata, in accordance with an existing stratified random sampling methodology.

3. **VA Dates**: This tool serves as a bridge between VA and RP tools, providing the user with information about which dates to use to generate RP, after having sampled the best validation areas, i.e., identifying cloud-free dates.

4. **RP**: creates accurate burned areas within a small region, from changes between two dates via a supervised classification. It is mostly oriented towards generating reference perimeters (RPs) for a BA product's assessment.

2.1. Datasets and Preprocessing

BAMT rely on the Landsat and Sentinel-2 datasets that are uploaded to the GEE environment. The Landsat program is a NASA/USGS program for satellite imagery acquisition and Earth observation [49], with a series of satellites that started acquiring images in 1972 with Landsat-1, being the last satellite launched in 2013, and over 8 million scenes of the Earth having been acquired since then. From its seven satellites, only Landsat-4 and -5 Thematic Mapper (TM), Landsat-7 Enhanced Thematic Mapper Plus (ETM +) and Landsat-8 Operational Land Imager (OLI) data are used in BAMT. They provide continuous global coverage since 1982, acquiring images every 16 days (reduced to 8 days in years where two satellites are operational) at 30 m of spatial resolution and covering the visible, near infrared (NIR) and short wavelength infrared (SWIR) spectral regions. From all available Landsat products in GEE, the Landsat Tier 1 Surface Reflectance (SR) [50,51] product was the one selected, which includes atmospherically corrected and orthorectified surface reflectance data for four visible and near-infrared (VNIR) and two short wavelength infrared (SWIR) bands. These products are represented by the following IDs in GEE: 'LANDSAT/LT04/C01/T1_SR' for Landsat-4 TM, 'LANDSAT/LT05/C01/T1_SR' for Landsat-5 TM, 'LANDSAT/LE07/C01/T1_SR' for Landsat-7 ETM + and 'LANDSAT/LC08/C01/T1_SR' for Landsat-8 OLI.

The European Space Agency (ESA) developed the Sentinel-2 mission (S2) as part of the EU Copernicus program [52], with two satellites working simultaneously (Sentinel-2A and Sentinel-2B) since 2017. Both incorporate the Multi-Spectral Instrument (MSI), an optical sensor similar to those aboard the Landsat satellites, albeit with improvements in spectral, spatial and temporal resolutions. MSI covers the globe at 10 or 20 m, depending on the spectral band, with a revisit time of 10 days (from June 2015 onwards, when Sentinel-2 A was launched) and 5 days (from March 2017, after the launch of Sentinel-2B) by combining both satellites, obtaining 2–3 days of revisit time in mid-latitudes, due to the overlap between adjacent orbits. Two Sentinel-2 products are available in GEE: Level-1C (L1C) and Level-2A (L2A), with the corresponding 'COPERNICUS/S2S and 'COPERNICUS/S2_SR' dataset IDs. The bands in the former product contain Top of Atmosphere (TOA) reflectance, although the latter has Bottom of Atmosphere (BOA) reflectance and a scene classification (SCL) including quality indicators such as cloud probabilities and snow [53].

Although BAMT could use L1C and L2A products, there are critical differences between them that make the first-mentioned product preferable. On the one hand, the topographic correction applied in L2A creation [54] gives rise to an overcorrection of mountain shadows and an artificial effect in mountainous regions, even though this does not occur in every image (Figure 1). On the other hand, the L2A product is not globally produced for the completely temporal coverage of Sentinel-2; although 2019 and 2020 have the same number of scenes for both products in GEE, 2015 and 2016 do not have any L2A scenes, and there are only a few for 2017 and 2018 (Figure 2).
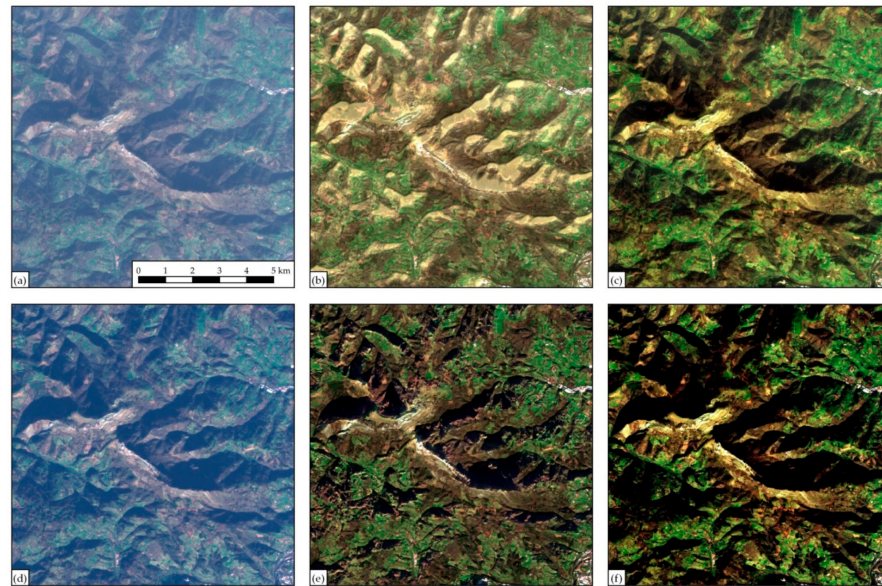
Figure 1. The red/green/blue natural color composition in a sample area in the 30TWN Sentinel-2 (S2) tile. The upper row (**a–c**) is a scene from 2020/02/03, where shadows were overcorrected, while the lower row (**d–f**) is a scene from 2020/01/09 without such that effect. The first column (**a**,**d**) shows the Level-1C (L1C) product with Top of Atmosphere (TOA) reflectances; the second column (**b**,**e**) shows the L2A product with Bottom of Atmosphere (BOA) reflectances as available in Google Earth Engine (GEE); and the third column (**c**,**f**) represents the Level-2A (L2A) product with no topographic correction generated by the authors.
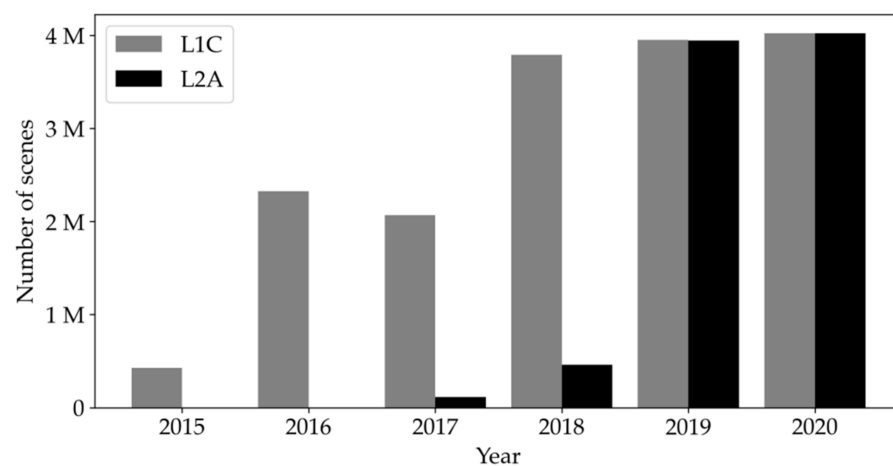
Figure 2. Total number of L1C and L2A scenes available in GEE by year, as of January 2021.

Six reflectance bands common to all four sensors (TM, ETM +, OLI and MSI) are employed: the three visible colors (blue, green and red), the near infrared (NIR) and two short wavelength infrareds (short and long SWIRs). Each of these bands' wavelengths may vary among different sensors, but they cover an equivalent region in the spectrum (Table 1). Landsat bands are available at 30 m spatial resolution. S2 MSI visible bands are at 10 m and both SWIRs at 20 m; there are two NIR bands, each at a different resolution, as indicated in Table 1.

Table 1. Selected bands for every satellite and sensor, and their approximate wavelengths.

Satellite	Landsat-4 and 5	Landsat-7	Landsat-8	Sentinel-2A and B	Approximate Wavelength (μm)
Sensor	TM	ETM +	OLI	MSI	–
Product	LSR	LSR	LSR	L1C	–
Blue	B1	B1	B2	B2	0.45–0.52
Green	B2	B2	B3	B3	0.53–0.59
Red	B3	B3	B4	B4	0.63–0.68
NIR	B4	B4	B5	B8 (20 m)/B8A (30 m)	0.80–0.89
Short SWIR	B5	B5	B6	B11	1.55–1.70
Long SWIR	B7	B7	B7	B12	2.10–2.30
Quality band	pixel_qa	pixel_qa	pixel_qa	QA60	–

SWIR, short wavelength infrared.

The Quality Assessment (QA) band for both sensors has been used to identify pixels that exhibit adverse instrument, atmospheric or superficial conditions (Table 2). The pixel_qa band for Landsat images indicates the presence of cloud shadows and clouds in the 3rd and 5th bits, respectively, while the QA60 band of S2 data contains similar information in its 10th and 11th bits, even though this does not indicate the presence of cloud shadows. In the RP tool, the SCL is used instead of the QA60 quality band if a L2A scene is available since it is more accurate; this SCL includes several cloud probabilities and a cloud shadow category that are crucial for masking purposes. In addition, an empirical threshold based on the B1 band has been employed to avoid the heavily underestimated presence of clouds of the Level-1C product [55]: B1 higher than 1500, or a more relaxed threshold of 2000 if SCL from L2A is used. In our developmental experiments, this band, at 60 m of spatial resolution, has shown the best performance of BA mapping in cloudy areas.

Table 2. Values and conditions applied for masking clouds and cloud shadows, depending on the dataset.

Landsat-4 to 8	Sentinel-2 L1C	Sentinel-2 L2A
pixel_qa: 3rd bit (cloud shadow)5th bit (cloud)	QA60: 10th bit (opaque cloud) 11th bit (cirrus cloud) B1 > 1500	SCL: value 3 (cloud shadow) value 8 (medium probability cloud) value 9 (high probability cloud) value 10 (thin cirrus) B1 > 2000

The normalized difference between the most important spectral spaces for the BA was added to the selected spectral bands described in Table 1, as follows: Normalized Difference Vegetation Index (NDVI) [56] in the red/NIR space, Normalized Burned Ratio (NBR) [57] in the NIR/Long SWIR and Normalized Burned Ratio 2 (NBR2) [19] in the Long SWIR/Short SWIR space. The equations for these indices are as follows:

$$\mathrm{NDVI} = (\rho_{\mathrm{NIR}} - \rho_{\mathrm{Red}})/(\rho_{\mathrm{NIR}} + \rho_{\mathrm{Red}}) \tag{1}$$

$$\mathrm{NBR} = (\rho_{\mathrm{NIR}} - \rho_{\mathrm{LongSWIR}})/(\rho_{\mathrm{NIR}} + \rho_{\mathrm{LongSWIR}}) \tag{2}$$

$$\mathrm{NBR2} = (\rho_{\mathrm{ShortSWIR}} - \rho_{\mathrm{LongSWIR}})/(\rho_{\mathrm{ShortSWIR}} + \rho_{\mathrm{LongSWIR}}) \tag{3}$$

where ρ_{Red} = reflectance in the red band, ρ_{NIR} = reflectance in the NIR band, $\rho_{\mathrm{ShortSWIR}}$ = reflectance in the Short SWIR band, and ρ_{LongSWIR} = reflectance in the Long SWIR band.

2.2. BA Cartography Tool

The purpose of this tool is to generate a BA vector map in a user-defined area and period via a supervised classification of Landsat or Sentinel-2 data, as defined by the 'dataset' parameter. The flowchart of the tool below illustrates its logic (Figure 3).
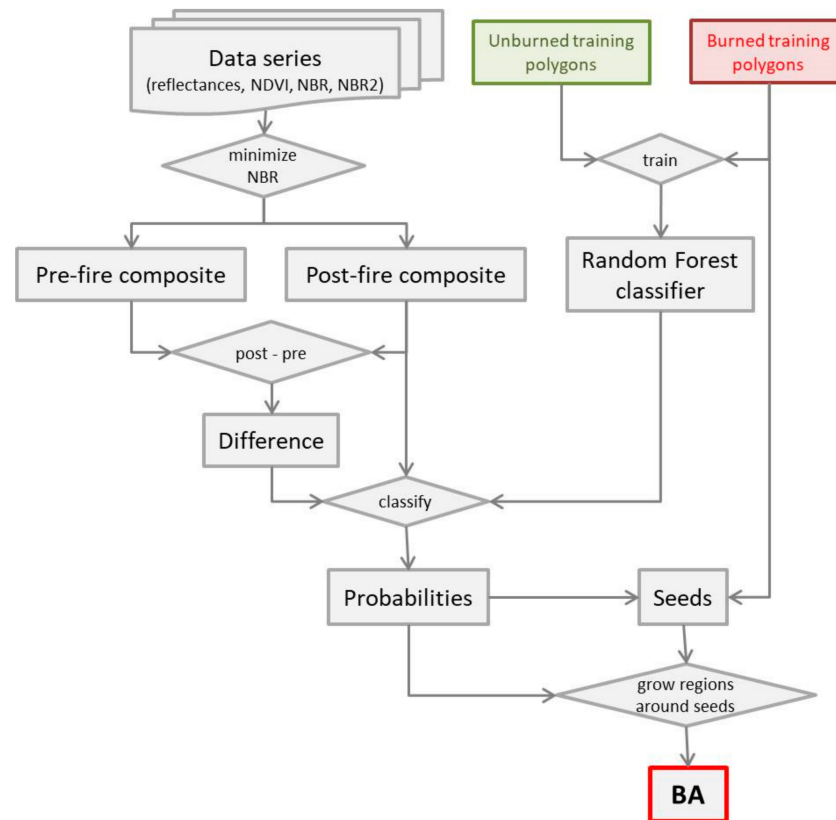
Figure 3. Flowchart of the burned area (BA) Cartography tool's algorithm.

The processing area extent has to be manually digitized in the 'studyArea' predefined geometry layer of the script and could be a region, country or even a continent (the process might lead to an error if the processing area is too large, because the user memory could be exceeded). Two consecutive periods must be defined (by 'date_1', 'date_2a and 'date_3a parameters), namely the pre- and post-fire periods, with the second one beginning the day following the end of the first period. The individual imagery involved in the region, dataset and period defined are masked using the rules described in Table 2 and the NDVI, NBR and NBR2 spectral indices are computed for each scene. Pixel-based temporal composites are computed for both post-fire and pre-fire periods (Figure 4a,b), taking the one with the minimum NBR from the dates available. In our experiments, this band evidenced the best compositing performance, by maximizing or minimizing the individual bands and spectral indices, and retaining the dates' pixel value when the burned signal was considered strongest. Temporal compositing has many advantages in processing frameworks, especially if the analysis covers large areas [58]. Post-fire and pre-fire composites are used to compute the composite subtraction (Figure 4c), and thus another nine bands are obtained over the user-defined extent, six reflectance bands and three spectral indices.
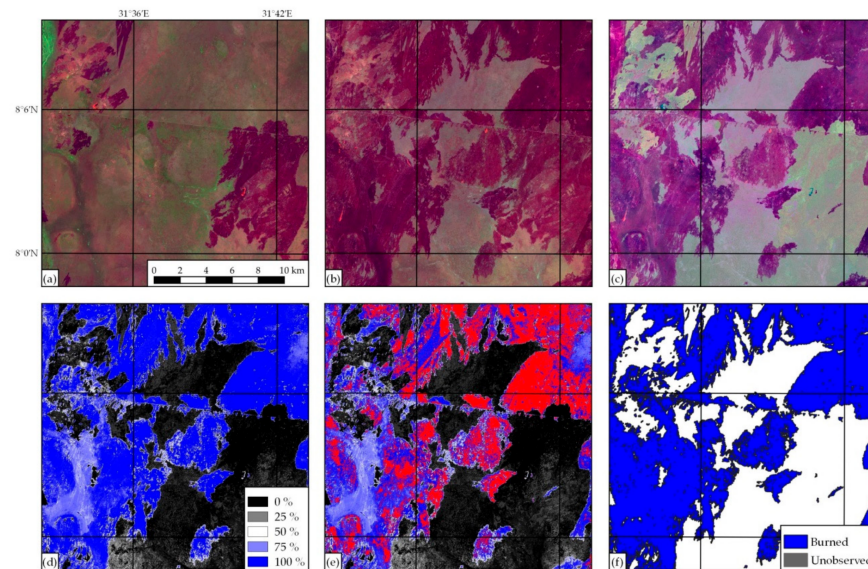
Figure 4. Generation of the BA product from S2 data in a sample area located in South Sudan. (**a**) Pre-fire composite derived from data between 2019/11/01 and 2019/12/31, with a Long SWIR/NIR/red color composition; (**b**) post-fire composite between 2020/01/01 and 2020/02/29 with the same color composition; (**c**) difference between the pre-fire and post-fire composites; (**d**) probability image returned by the Random Forest (RF) classifier; (**e**) burned seeds (in red) shown over the previous image; and (**f**) result exported in an ESRI (Environmental Systems Research Institute) Shapefile.

A Random Forest (RF) classifier is trained, using the burned and unburned samples the user digitized in the 'burned' and 'unburned' layers within the GEE Code Editor environment. These samples are digitized over a Long SWIR/NIR/red color composition of the pre-fire composite, post-fire composite and pre-fire/post-fire difference visualized over the GEE map. Among other data-mining algorithms included in GEE, such as Classification and Regression Tree (CART) [59], Naive Bayes and Support Vector Machine (SVM) [60], RF was selected because of the fast training and prediction involved, unconstrained by the distribution of the predictor variables, reduced overfitting, robustness to outliers and non-linear data. RF classification also handles unbalanced data that are common in BA mapping. Indeed, this technique has become popular within the remote sensing community due to the accuracy of its classifications [61]. A Random Forest classifier is an ensemble classifier that produces multiple decision trees, using a randomly selected subset of training samples and variables [62]. GEE implementation default parameters were maintained for all parameters (the square root of the number of variables as the number of variables, a 0.5 fraction of input to bag per tree, unlimited maximum nodes), except for the number of trees (500), as recommended in a study [61], and the minimum number of elements in each node (10). Each time the user redefines burned and unburned samples and executes the script, a probability image is obtained, with values ranging from 0% (unburned) to 100% (burned) (Figure 4d).

The algorithm ends by applying a two-phased strategy on the output probability image of the RF model in order to map the burned areas, an efficient strategy to balance omission and commission errors [36,63]. Patches of pixels with a probability higher than 50% using a 4-node connection (the only group of pixels that share an edge) are labeled as burned, as long as they contain at least one seed pixel inside. These burned seeds are pixels with higher probability than the average of the mean RF probabilities obtained for the training polygons (Figure 4e). When the algorithm is executed and the results visualized, the user may modify or define more training polygons and re-run the algorithm repeatedly, until the desired visual accuracy is obtained. The end result (only burned or unobserved areas, but not observed and unburned areas) can be exported in ESRI (Environmental

Systems Research Institute) Shapefile format in a 2 × 2-degree grid to the user's Google Drive account (Figure 4f). The grid was fixed to 2-degree tiles because larger tiles were likely to exceed GEE user memory limit, although if the limit is still exceeded, the 2-degree tile can be split into smaller tiles (see user guide). The polygon vector layer assigns the fire detection date from the post-fire composite, computing the mode (most repeated date) for each burned patch.

2.3. VA Tool

The Committee on Earth Observing Satellites (CEOS) Working Group on Calibration and Validation (WGCV) first defined validation as 'the process of assessing by independent means the quality of data products derived from the system outputs' [64]. Satellite product performance information is required to enable users to select and use products appropriately [65,66]. The independent reference data's characteristics influence the reliability and the degree to which validation results are representative of the validated product [33], while the validation sampling design is critical in making the most out of the reference data. Probability sampling designs ensure that accuracy inferences are possible on a global scale [21].

The first inferences of global product accuracies became available a few years ago [15,34]. A great deal of attention was placed on (1) defining the sampling units by attributing them with spatial and temporal dimensions so that accuracy inferences could be made for specific spatial and temporal extents [33], and (2) improving the efficiency of sampling designs to obtain accuracy inferences as precise as possible given a sample size [67]. These methodologies were based on Landsat data, which most global BA validation exercises used. Firstly, two sampling grids were created: a spatial grid, based on Thiessen Scene Areas (TSAs) [68,69], and a temporal grid, consisting of two consecutive image acquisition dates. Two levels of stratification were then applied on the spatial and temporal sampling units: the predominant Olson biome [70], first reduced to seven main categories [33,34], and the fire activity in each sampling unit. Depending on the study, either the BA extent provided by the Global Fire Emissions Database version 3 (GFED3) [71] or the number of hotspots in the MODIS active fire product [72,73] was used as a reference for fire activity, delimited spatially by the extent of the TSA and temporally by its acquisition dates. Sampling units in each biome were split between low and high fire activity strata, resulting in 14 strata in total. Finally, the number of sample sizes for each stratum was computed proportionally to the number of sampling units in the stratum. However, this method assumed that all Landsat acquisitions were available and that the clouds did not affect them, while the ground's observability was not actually secured, as mentioned by Boschetti et al. [33]. In addition, the short temporal length of sampling units (16 days between two consecutive Landsat images) may increase the validated BA product's estimated errors if burning dates are not identified accurately in the global product. To solve these issues, 'long sampling units' have been employed in recent studies [6,14,16]. These units are typically over 100 days long, with a minimum frequency of an available image every 16 days, whereas previous 16-days-long units are referred to as 'short sampling units'.

The VA tool used in this study is an adaptation of this stratified random sampling methodology, not only for sampling validation areas for coarse resolution BA products, but also for the BA maps obtained using medium spatial resolution with the BA Cartography tool in BAMT. Several decisions were taken to adapt the algorithm to this tool:

- Sentinel-2 data were incorporated into the analysis, as these offer better spatial and temporal resolutions than Landsat data and should improve reference data created for the BA validation. The user may thus choose between S2 or Landsat data (with the 'dataset' parameter).
- Landsat or S2 scene extents are considered as sampling units instead of TSAs. Despite using whole TSAs when applying the stratified random sampling methodology, most studies have only created reference data in a central window of about 20–30 km wide and high [6,14,16,37], which the fire activity cover value used in the analysis might not

properly represent. Therefore, the user can define the dimension of a square window ('dimension' parameter), located at the center of the scene, so that the analysis may be carried out in that specific window.

- Either the MCD64A1 [5] or the FireCCI51 [6] can be used to estimate global fire activity to select the samples ('globalBA' parameter). Both products are available in GEE. The latter has a higher spatial resolution (250 m), but was only processed between January 2001 and December 2019, while the MCD64A1 at 500 m has been systematically processed from November 2000 up to the present.
- Optionally, several criteria of data availability are considered when creating long sampling units: minimum length of the unit in days, minimum frequency of available images in days and maximum cloud cover in each available image ('minLength', 'minFreq' and 'maxCloud' parameters, respectively).

The tool samples a number of validation areas ('numberVA' parameter) over a period defined by two dates ('date_pre' and 'date_post') and spatially delimited by a polygon that is manually defined in the 'studyArea' layer. Firstly, it selects the predominant Olson biome and computes the burned surface (according to the BA product, MCD64A1 or FireCCI51) in each sampling unit. Then, it splits the units into 14 strata, consisting of 7 Olson biomes and two low/high BA strata. The validation areas are then sampled from each stratum proportionally to the number of sampling units in it.

If the optional criteria of data availability are applied, long sampling units that do not fulfil these criteria are removed, and the stratified random sampling is then applied to the remaining units. This assures a long data series with frequent cloud-free data from which high-quality reference data will be created.

2.4. VA Dates Tool

The validation areas sampled by the VA tool do not propose the specific images to be used for reference data creation, and only the scene is identified. Since the CEOS Land Product Validation team recommends that reference fire perimeters be obtained from multitemporal pairs of images in order to properly date the validation period, this tool identifies the images available in the specified scene and period. The identified images also meet a cloud cover criterion the user defines to ensure only cloud-free images are shown.

2.5. RP Tool

Validation of remote-sensing-derived products requires independent reference data and must be obtained with minimum error, either by visual interpretation [12,30,32] or by applying a semi-automatic algorithm followed by visual checking and manual refinement [15,34,74]. Coarse spatial resolution BA products have been validated in accordance with the protocol endorsed by the Committee on Earth Observation Satellites (CEOSs), which is based on product comparison with BA maps interpreted from higher spatial resolution satellite multi-date image pairs [32]. Validating medium spatial resolution BA products is more challenging because interpreting multi-date higher spatial resolution data with a temporal resolution high enough to capture the rapidly evolving burning is expensive and often unavailable, and requires a large and representative independent reference dataset collected via a suitable spatiotemporal sampling, in order to obtain statistically rigorous accuracy measures [27].

This tool focuses on easing the BA mapping process between two single Landsat or Sentinel-2 scenes with the highest possible accuracy, so they can then be used as reference perimeters (RPs) for lower spatial resolution BA assessment purposes, in accordance with the CEOS's BA assessment protocol. The BA mapping process is similar to the BA Cartography tool in that it digitizes 'burned' and 'unburned' samples, a RF model with the same parameters is trained, and the user may redefine the training samples until the result is accurate enough, which is then exported in an ESRI Shapefile to the user's Google Drive account. A label is attached for each polygon, indicating whether it was burned or

unobserved accordingly. However, there are some significant differences compared to the BA Cartography tool:

- Spatially, BA detection is limited to a window located at the center of a Landsat or Sentinel-2 scene. The user defines the width and height of the window ('region_dimension' parameter).
- Temporally, two single scenes are used for BA detection instead of temporal composites, defined by two dates. The VA Dates tool can be used to identify the dates with available images.
- For Sentinel-2 derived RP, the SCL image is selected to mask clouds and cloud shadows due to its higher accuracy, if an L2A scene is available on the corresponding date; if there is no L2A scene, QA60 and B1 bands are used. L1C TOA reflectance is used to map BA in both cases.
- A more permissive probability threshold defines the burned seeds because the region of interest is smaller and both burned and unburned areas have greater homogeneity across the image. Instead of the average of mean probabilities used in the BA Cartography tool, the minimum among mean probabilities in each burned training polygon is used as the threshold.
- RP from Landsat data are obtained at 30 m, but Sentinel-2 based RP can be obtained at both 20 and 10 m (depending on the 'resolution' parameter). If a 10 m output resolution is selected, the B8 band is used instead of B8A (at 20 m) in the NIR region, and this is joined to the visible bands at 10 m (blue, red and green) and both SWIR bands at 20 m. If the 20 m output resolution is selected, the B8A is used as the NIR band. Figure 5 shows how bands at different resolution can be combined, where the NBR index at 10 m is significantly more accurate than the same index at 20 m, despite both indices deriving from the same SWIR band at 20 m.
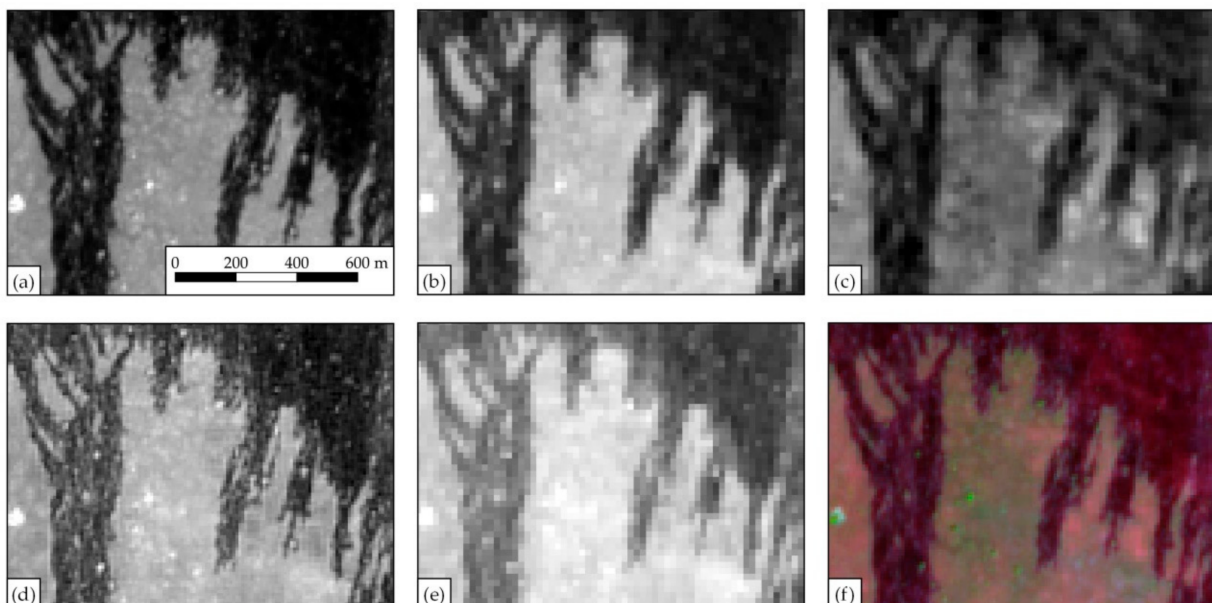
Figure 5. Effect of the NIR band's spatial resolution on the Normalized Burned Ratio (NBR) spectral index, in a sample area from 2020/01/13 located in South Sudan. (**a**) Shows the B8 band (NIR at 10 m); (**b**) the B8A band (NIR at 20 m); (**c**) the B12 band (Long SWIR at 20 m); (**d**) NBR at 10 m (derived from B8 and B12 bands); (**e**) NBR at 20 m (deriving from B8A and B12 bands); and (**f**) the Long SWIR/NIR/red color composition at 10 m. Both NBR indices were computed by using the same B12 band at 20 m.

2.6. Case Studies in Southeast Australia and Canada

We selected two case studies to demonstrate BAMT's applicability for BA mapping at medium spatial resolution data. In the Southeast Australia (SEA) fire season between 2019 and 2020, the set of four BAMT described in this paper were applied by employing Landsat data to map BA and Sentinel-2 for validation purposes. The second case study employed only the BA Cartography tool to map Canada's burned areas in the summer of 2018, using Sentinel-2 data, and the areas were then compared to the Canadian National Fire Database fire polygon data available from the Canadian Wildland Fire Information System (CWFIS).

2.6.1. Southeast Australia

The area selected in the SEA case study comprises four different states and territories, covering an area of 1.05 M km^2: New South Wales (NSW), Victoria (VIC), Australian Capital Territory (ACT) and Jervis Bay Territory (JBT) (Figure 6a). In this area, the selected 2019/2020 fire season was unusually severe, as bushfires were consequently exacerbated by extreme weather conditions and further caused several social impacts [75–77]. A BA product detected between the 1 September 2019 and 30 April 2020 was created, using the BA Cartography tool, employing 2-month-long Landsat composites, both for post- and pre-fire conditions. Therefore, the fire season was divided into 4 bimonthly periods (1 September to 31 October, 1 November to 31 December, 1 January to 29 February, and 1 March to 30 April). Although most fires in SEA were extinguished by the end of February 2020, some were not detected until March 2020 as a result of the gaps caused by clouds in Landsat images. For each post-fire composite, the previous bimonthly composite was used as the pre-fire condition, e.g., the BAs from January to February 2020 were detected by comparing their composite with the November–December 2019 period.

Figure 6. Location maps of the study areas in (**a**) Southeast Australia and (**b**) Canada.

The VA tool sampled 10 validation sites, consisting of 50 × 50 km^2 windows located at the center of the S2 tiles. The sites were sampled by applying the optional criteria of data availability, and thus a minimum length of 100 days, a minimum frequency of 20 days between consecutive images and a maximum cloud cover of 30% were required for each long sampling unit. This way, the sampled validation sites were guaranteed to contain frequently available cloud-free S2 images. The MCD64A1 BA product was used as a reference for fire activity. Reference perimeters for each pair of consecutive images in these validation sites were created at 20 m, using the RP tool, in 50 × 50 km^2 squares at the center of the S2 tiles. Any pixel that was not observed in any single image was

labeled as unobserved for the entire validation period, and only pixels observed through the whole period remained. Among the observed pixels, burned areas were made up of pixels burned in any pair of images. For their part, the accuracy metrics were based on the error matrix approach [78] between the Landsat BA map and the reference perimeters. The commission and omission errors (CEs and OEs, respectively) and the Dice coefficient (DC) were computed for each validation area and also globally. The DC is defined as the probability that one classifier (product or reference data) may identify a pixel as burned, given that the other classifier also identifies it as burned [15,79,80].

The BA product's temporal accuracy was assessed by comparing product detection dates and VIIRS (Visible Infrared Imaging Radiometer Suite) active fire dates [81]; these hotspots were derived at 375 m from the Visible Infrared Imaging Radiometer Suite sensor aboard the Suomi-NPP satellite. For each VIIRS hotspot, the burned pixel temporally closest to the hotspot was chosen within a $375 \times 375 \text{ m}^2$ window around the active fire (the active fire product's spatial accuracy). This closest burned pixel was considered to be part of the burned area whose fire was detected, and its date was compared with that of the hotspot.

2.6.2. Canada

The second case study is located in the 10 provinces of Canada: British Columbia (BC), Alberta (AB), Saskatchewan (SK), Manitoba (MB), Ontario (ON), Québec (QC), Newfoundland and Labrador (NL), Prince Edward Island (PE), Nova Scotia (NS) and New Brunswick (NB) (Figure 6b). This covers the whole of Canada, except for the three territories (Yukon, Northwest Territories and Nunavut), amounting to a total of 6.06 M km^2. The 2018 fire season was quite severe, especially in BC, which experienced its worst fire season on record [82] with more than 2000 fires and 1.35 million hectares burned [83,84]. Fires mostly occurred between May and August [85]. Since a 4-month period could be quite difficult to handle in such a large study area, only fires from July and August were detected in this case. However, since some fires from August were not observed in S2 data until September, the period was extended to include this third month.

The BA product was obtained from Sentinel-2 MSI data at 20 m, using the BA Cartography tool. Reference perimeters were not created by using BAMT tools in this case study, but instead were downloaded from the website of the Canadian Wildland Fire Information System (CWFIS) (https://cwfis.cfs.nrcan.gc.ca/datamart (accessed on 27 January 2021)). These perimeters consisted of polygons with an associated burning date. Since the perimeter accuracy varied among provinces as a result of the different mapping techniques [86,87] and some were observed as having coarser spatial resolution than the BA product, only a visual comparison was made, and commission and omission errors were not computed. The BA map's temporal accuracy was assessed in the same way as in SEA, by comparing burned area dates and VIIRS hotspots.

3. Results

3.1. Southeast Australia

3.1.1. BA Cartography

The BA map for the 2019/2020 fire season in SEA was generated, using the BA Cartography tool, divided into four independent periods. Table 3 shows the number of burned and unburned training polygons digitized in each period, and the number of times (iterations) the script was executed until a visually satisfactory result was obtained throughout the study area. A larger number of burned samples than unburned samples were defined (52 vs. 34 for all four periods), especially in the first period, where finding the balance between removing noise and not omitting burned areas proved difficult. The number of iterations was equal to or lower than 10 in three periods, with the exception of the first period in which double iterations were required. Processing time depended on the number of fires and noise that affected mainly the BA vectorization process: while the November–December period required 29 h, the March–April period completed the process

in just 10.5 h. The number of Landsat scenes processed in each period varied between 869 and 938, amounting to a total of 3653 scenes processed over the whole fire season.

Table 3. The number of training polygons, iterations, exporting time needed and number of images processed over each period in Southeast Australia (SEA) and Canada.

Post-Fire Period	Number of Training Polygons		Iterations	Processing Time (Hours)	Number of Images
	Burned	Unburned			
1 September–31 October 2019	26	15	20	11.0	938
1 November–31 December 2019	9	4	10	29.0	936
1 January–29 February 2020	10	8	9	14.5	910
1 March–30 April 2020	7	7	6	10.5	869
Aggregated period	52	34	45	64.0	3653
1 July–30 September 2018 (Canada)	9	10	11	244.4	254,660

A total burned area of 52,700 km^2 was mapped, most of it in NSW (around 40,000 km^2, 75% of the total BA) (Figure 7). VCT was the next most affected state with 12,400 km^2 (23%), with the ACT with 660 km^2 far behind (1%); no BA was found in the JBT, due to its small surface area (only 67 km^2). The BA map contains some unobserved areas due to high cloud coverage; areas burned during these cloudy dates were not detected on the BA map.
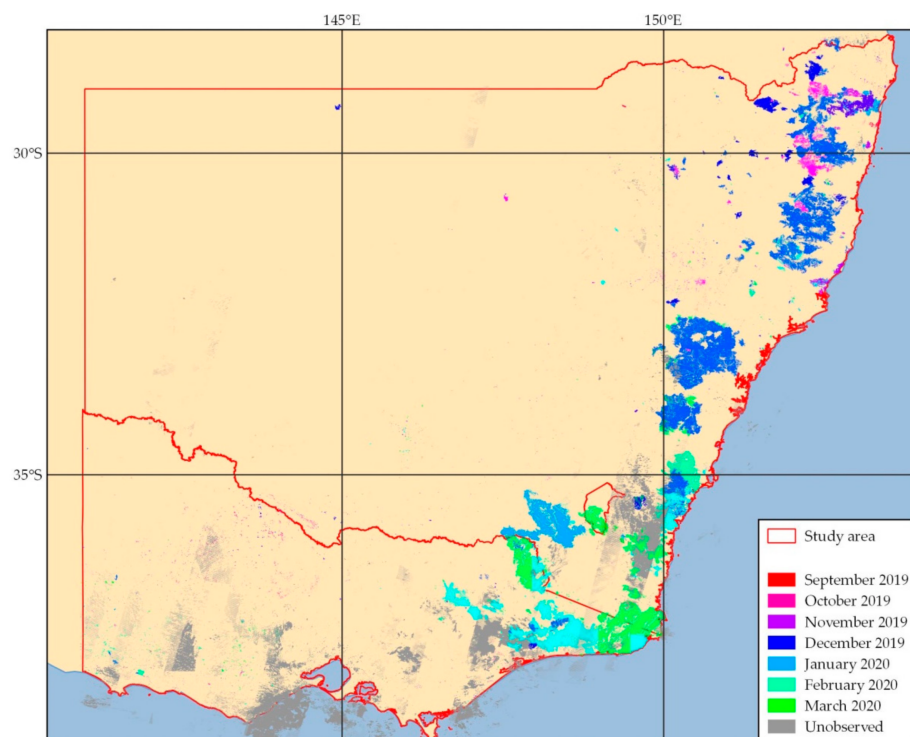
**Figure 7.** BA detected in SEA from Landsat data from September 2019 to March 2020.

3.1.2. Validation

Figure 8 shows the 10 S2 validation areas sampled by the VA tool. Despite the presence of several Olson biomes in SEA (Mediterranean forest, temperate forest, temperate grassland and savanna, and tropical and subtropical savanna), the validation sites were located mainly in the temperate forest biome, which was the most affected biome. Validation periods varied from four to six months long, from the beginning of September

2019 to mid-January or the end of February 2020 (Table 4). Each period contains between 8 and 12 cloud-free images.
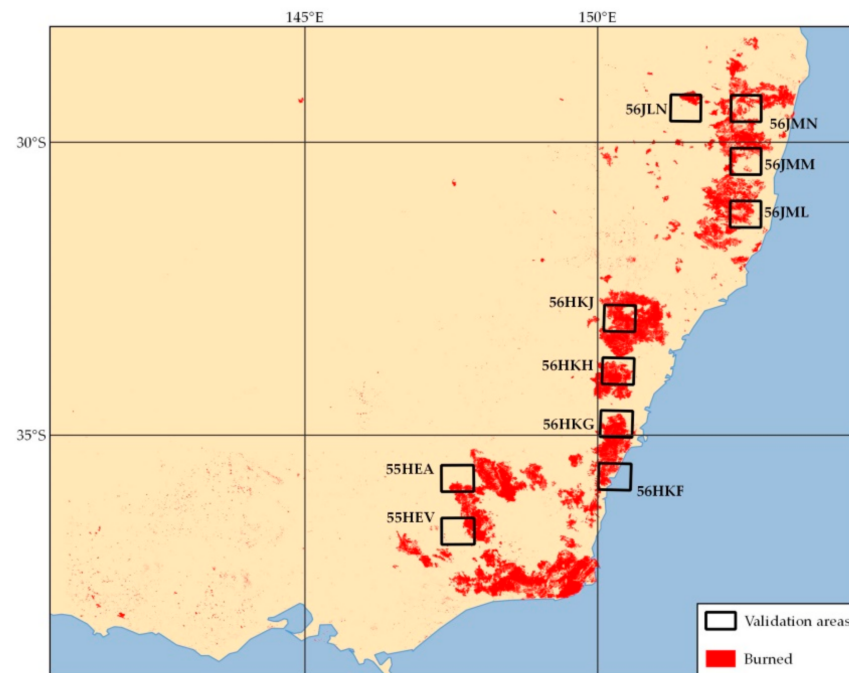
Figure 8. Validation areas of 50 × 50 km^2 that the validation area (VA) tool sampled, based on S2 scenes, and the BA from the map derived from Landsat data.

Table 4. Sampled validation areas, their validation periods and validation results. All accuracy measures (commissions, omissions and Dice coefficients) are expressed in percentages.

Tile	Validation Period				Accuracy		
	Start	End	Length in Days	Number of Images	CE	OE	DC
56HKJ	2019/09/02	2020/02/19	170	10	13.6	10.8	87.8
56HKG	2019/09/22	2020/02/29	160	8	10.6	2.9	93.1
56HKH	2019/09/02	2020/02/19	170	9	11.4	8.0	90.3
56JML	2019/09/03	2020/01/21	140	9	19.2	10.3	85.0
56JMN	2019/09/02	2020/01/10	130	11	7.2	16.4	87.9
56HKF	2019/09/07	2020/02/29	175	8	14.6	7.6	88.8
56JMM	2019/09/02	2020/01/21	140	12	13.9	13.5	86.3
55HEV	2019/09/10	2020/02/22	165	8	7.2	10.5	91.1
55HEA	2019/09/10	2020/01/18	130	9	5.6	6.1	94.1
56JLN	2019/09/02	2020/01/10	130	11	3.3	3.0	96.9
Aggregated	–	–	–	–	11.8	8.9	89.6

CE, commission error; OE, omission error; DC, Dice coefficient.

For each tile, the RPs were created from every pair of consecutive images within the validation period (an illustrative example is shown in Figure 9a–h); results of all image pairs were merged in a final layer (Figure 9i), where only pixels observed over the whole period remained unmasked. Table 4 and Appendix A Figure A1 show the results obtained from the accuracy assessment, with both commission and omission errors being lower than 20% in all 10 validation sites. Omissions for the burned category ranged from 3% to 16%, while commissions varied between 3% and 19%. The largest errors were found in the 56JML S2 tile, where the boundary between burned and unburned forest was difficult to

identify, which increased both CE and OE. The aggregated results for all 10 tiles appeared closely in line, with higher commission (11.8%) than omission (8.9%), and a DC of 89.6%.
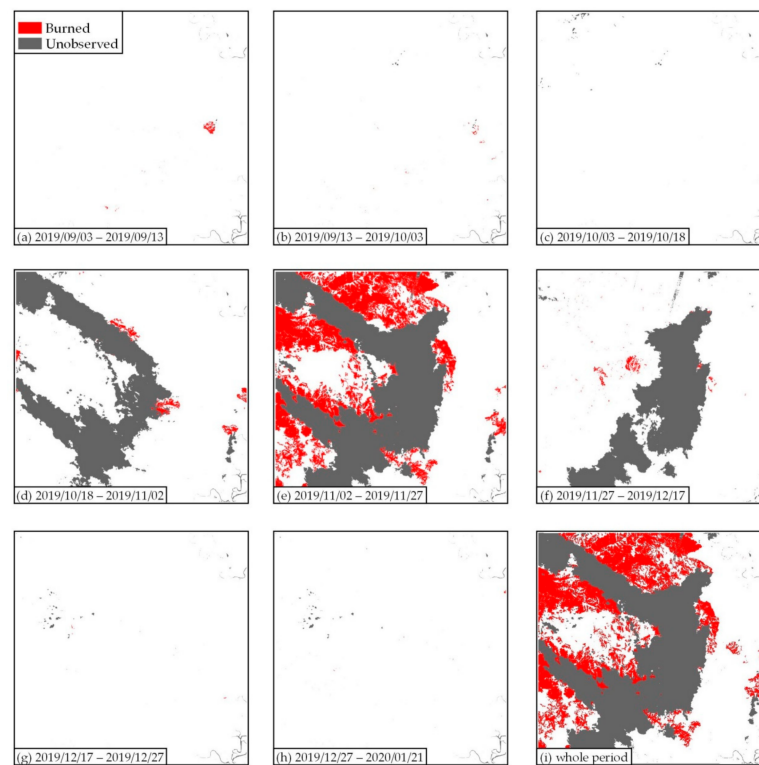

Figure 9. Reference perimeters in tile 56JML. (**a–h**) Perimeters created between consecutive images, from 3 September 2019 to 21 January 2020; (**i**) final merged reference perimeter (RP).

3.1.3. Temporal Accuracy

Despite low commission and omission errors, the BA product's temporal accuracy was not assessed using reference perimeters, since the validation periods were long enough to cover the whole fire season (five to six months), but, rather, by comparing dates from VIIRS hotspots. The distribution of the temporal delay between VIIRS hotspots and the BA detection is shown in Figure 10. Burned pixels were found for 86.5% of the hotspots, while the rest were located either in cloudy areas and croplands where no BA was detected, or close to burned patches but beyond their perimeters, an issue other authors have also mentioned [81]. In most cases (96.0%), the burned pixel was detected later than the hotspot: 55.7% within a temporal window of 30 days after the hotspot's detection, and 95.3% within a window of 60 days after the hotspot.

3.2. *Canada*

Burned areas in Canada were only processed in one unique period, within the second half of the 2018 fire season (July–September). The number of training polygons and iterations required was similar to those for the study area in SEA (Table 3); however, the processing took longer (slightly more than 10 days), because the extent of the study area was almost six times larger (6.06 M km^2 vs. 1.05 M km^2 in SEA). In addition, a larger processing extent implies finding more heterogeneity, which caused the BA detection algorithm to produce more noise than in SEA. This further caused the process to take even longer. More than 250,000 S2 scenes were processed in the course of generating the map.
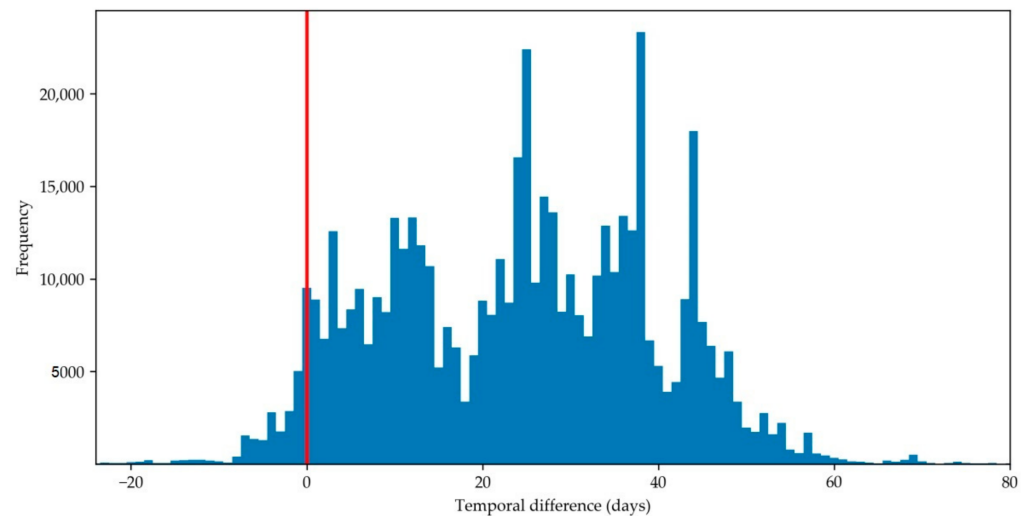
Figure 10. Temporal disagreement between the BA product and VIIRS (Visible Infrared Imaging Radiometer Suite) hotspots in SEA. A positive difference means the BA was detected later than the hotspot.

A total of 16,165 km^2 of burned areas in total were detected in the processed period, with most of the areas being in BC (10,069 km^2), followed by ON, AB, MB, SK and QC, with burned areas ranging between 860 and 1780 km^2 (Table 5). Very few areas were detected in the remaining four provinces, mainly in NB, NS and PE (between 0 and 4 km^2 in each). The total burned surface detected by the CWFIS reference perimeters was practically identical (16,501 km^2) (Figure 11), and more than half of this surface (9986 km^2) was detected by both CWFIS perimeters and the BA S2 product in the same locations. A similar surface was detected in BC, ON and MB, with around 60% of it being common burned areas and the remaining 40% of the areas differing spatially. In AB, SK and QC, the S2 product detected most areas from CWFIS perimeters; however, this contained much larger burned areas. No BA was detected in the CWFIS perimeters in NL, NB, NS and PE, similar to the BA product where few areas were mapped.

Table 5. Total burned surface by province in Canada according to the BA product and Canadian Wildland Fire Information System (CWFIS) perimeters, and the common BA between both, expressed in square kilometers.

| Province	BAMT	CWFIS	Common BA
BC	10,069	12,711	7633
ON	1778	1881	1142
AB	1175	97	83
MB	1146	1309	755
SK	1061	297	222
QC	868	205	151
NL	58	0	0
NB	5	0	0
NS	2	0	0
PE	2	0	0
TOTAL	**16,165**	**16,501**	**9986**

BAMT, Burned Area Mapping Tool; BC, British Columbia; AB, Alberta; SK, Saskatchewan; MB, Manitoba; ON, Ontario; QC, Québec; NL, Newfoundland and Labrador; PE, Prince Edward Island; NS, Nova Scotia; and NB, New Brunswick.
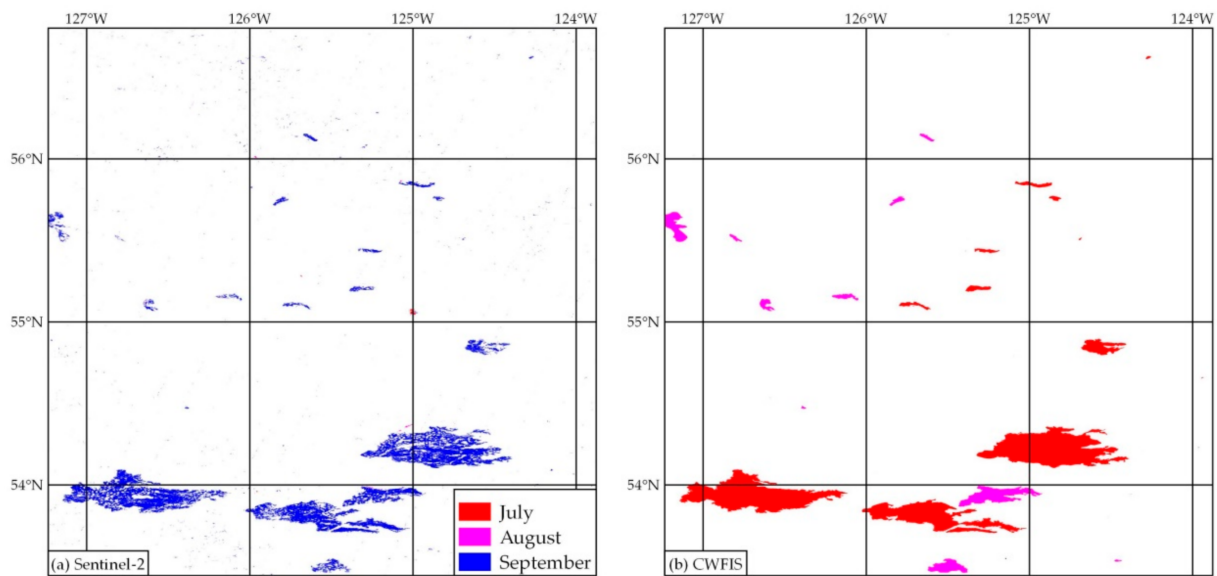
Figure 11. Comparison between BA maps derived from Sentinel-2 data (**a**) and CWFIS (**b**) perimeters, in a sample area located in Central British Columbia.

We found several reasons for these differences. The lower spatial accuracy of the perimeters caused most underestimations of the BA product in comparison to CWFIS perimeters. We observed that these perimeters defined the general boundary of the burned patch, mostly by smoothening limits and including pixels located outside the BA; they also failed to represent unburned islands inside burned patches (the first two rows in Figure 12). The BA product did not omit important BA due to high cloud coverage, since the whole period was observed within the three-month-long period and every pixel was observed at least once. On the other hand, two main sources were found for higher estimations in the BA product than in CWFIS perimeters (mostly in AB, SK and QC). Firstly, many areas burned in June (just before the processed period began) were not observed until July or August; these areas were thus detected as having burned between July and September in the BA map, but not in the CWFIS perimeters for that same period. This is the main reason why larger burned areas were detected in the BA product. Secondly, the algorithm in mountainous regions produced some noise, mainly in BC and AB, where different mountain shadow shapes throughout the year were confused with burned areas (the third row in Figure 12).

The distribution of temporal delay between VIIRS hotspots and the BA detection is shown in Figure 13. Burned pixels were found for 93.4% of the hotspots; in most cases (99.1%), the burned pixel was detected after the hotspot, 30.4% within a temporal window of 30 days after the hotspot was detected, and 97.0% within a window of 60 days after the hotspot. Differences of more than two months were found only for 2.1% of the hotspots.
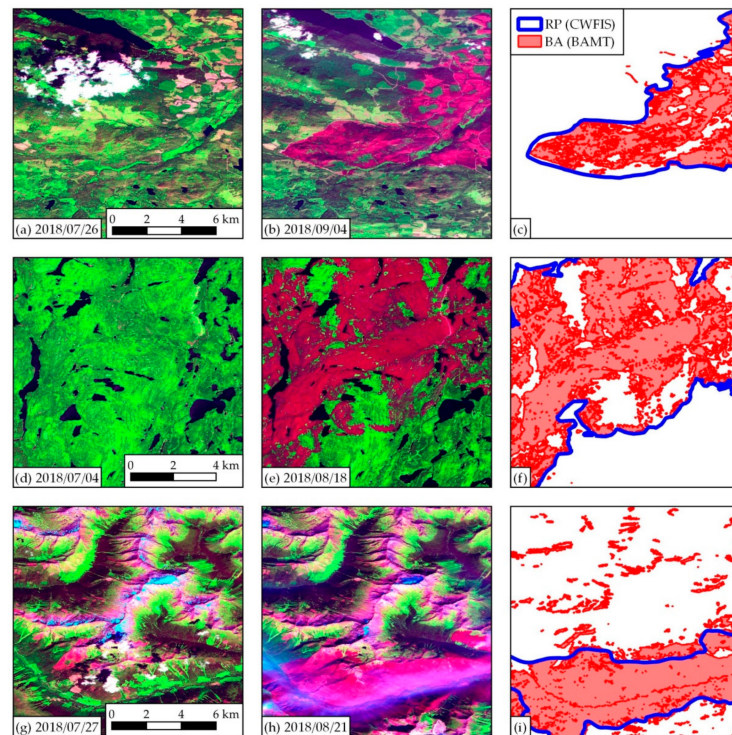
Figure 12. Comparison between the BA Sentinel-2 product generated by BAMT and CWFIS perimeters in three sample areas in Canada: the first row (**a**–**c**) is located in S2 tile 10UCF, west of Prince George (BC); the second row (**d**–**f**) in tile 17TNN, north of Gran Sudbury (ON); and the third row (**g**–**i**) in tile 10UGD, near Valemount (BC) in the Rocky Mountains. The first (**a**,**d**,**g**) and second (**b**,**e**,**h**) columns show the pre- and post-fire conditions, respectively, and the third column (**c**,**f**,**i**) represents the BA from the S2 product and CWFIS perimeters.
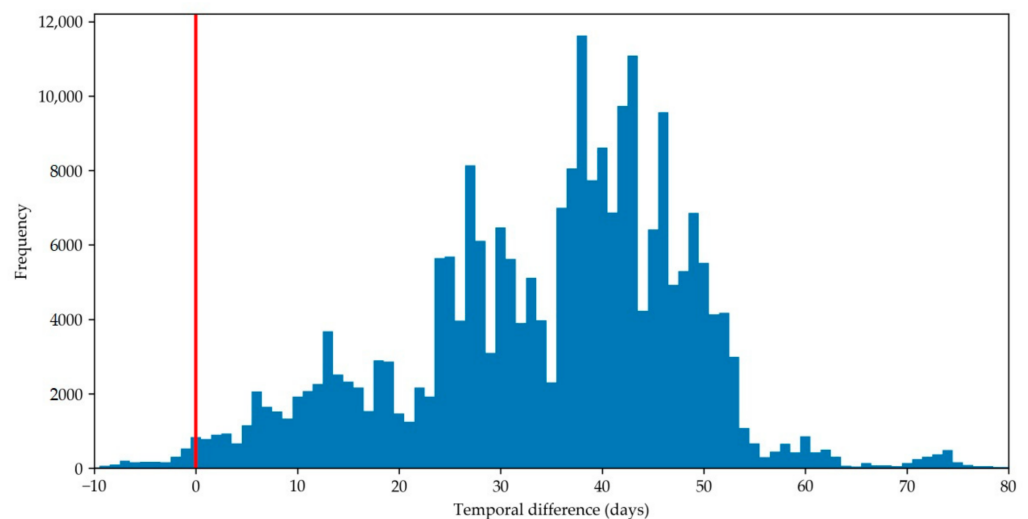
Figure 13. Temporal disagreement between the BA product and VIIRS hotspots in Canada, measured in days. A positive difference means the BA was detected after the hotspot.

4. Discussion

This manuscript presents the Burned Area Mapping Tools (BAMTs), a set of tools developed under the Google Earth Engine (GEE) platform [42] for BA analysis with medium spatial resolution data (Landsat and Sentinel-2) that covers the BA mapping, the selection of statistically significant validation sites and imagery [33], and the genera-

tion of reference perimeters. The tools consist of four scripts using the JavaScript Earth Engine API that are executed from the GEE Code Editor, and these can be reached at https://github.com/ekhiroteta/BAMT (last accessed January 2021). The new tools exploit the cloud computing capabilities of the GEE platform (https://earthengine.google.com/, (accessed on 27 January 2021)) and take advantage of the Landsat and Sentinel-2 analysis-ready datasets, in addition to other BA-related products such as the MCD64A1 [5] and ESA FireCCI51 [6] products that have already been uploaded to the platform. Publishing BAMT as open-source code and using the GEE Code Editor allow the code to be easily maintained and improved for both the authors and the community. These tools came into being as a natural evolution of the BAMS software [36], which had hitherto been confined to Landsat data and processed under a commercial GIS software limited to the local server's processing capability.

Both BA Cartography and RP tools included in BAMT make BA detection easier by using a supervised classification, via change detection by a Random Forest classifier, followed by a two-stage mapping approach [63]. While BA Cartography is designed to generate a BA map at a regional or country scale, by identifying BA during a relatively long period (one to a few months), using two temporal composites that represent the pre- and post-fire spectral conditions, the RP tool creates high-quality reference data for BA validation by analyzing the spectral changes between two single dates over a single scene extent. The main process in both cases consists of a supervised classification based on an RF model, whose predicted burned probabilities are used for BA mapping in a two-stage approach [63]. The user must define several training sample polygons (both burned and unburned) and visually analyze the results iteratively, until an acceptable result is obtained. RF is an ensemble learning-method classification that constructs a multitude of decision trees and outputs the class represented by the mode of the individual trees' classes [88]. This classifier has become popular within the remote-sensing community, due to the accuracy of the classification [61] and particularly in those researches related to BA mapping, both at medium [23,37,89,90] and coarse resolution data [91,92]. RF is essentially based on several binary trees whose predictions are combined into a single model, adapting well to the BA signal variability [93] and in accordance with the recommendations that involve using several spectral indices and bands to ensure accurate BA mapping [94,95]. In comparison to BAMS, where the user has to select the spectral indices to be used, RF naturally ranks the features according to how well they improve the purity of the node, and nodes with the largest decrease in impurity form at the start of the trees, offering a less subjective and straightforward method for selecting the variables with greater contribution in the classification. Another difference, when compared to BAMS that only trained the burned category, is that using a RF model implies identifying both burned and unburned samples. The ability to train the unburned category has improved the ability to reduce commission errors, and reduces the manual edition of the obtained BA Cartography, especially in areas spectrally similar to burned areas, such as croplands and cloud shadows [16,23,28,63].

BAMT applicability within the GEE environment has been demonstrated as a means for mapping fires at medium spatial resolution over large areas. In the devastating fire season between 2019 and 2020 in Southeast Australia (SEA), a region larger than 1 M km^2 was processed with a minimum user-dedication (around 90 training samples were collected) and three days' processing time (64 h involving more than 3500 Landsat scenes), obtaining a BA vector map of around 56,000 km^2 for the eight-month period covering the fire season. For the case study of Canada, a larger area was processed (6 M km^2), and the BA map was obtained by using a higher spatial resolution (20 m) and a shorter re-visit period (five days) imagery. More than 250,000 Sentinel-2 images were involved in a single three-month-long period analysis in a process that took only 10 days. The BAMT have shown to be not only cost-effective, but also reliable, and the results in SEA, where the BA map was validated using Sentinel-2 data, achieved a 'reasonable' categorized accuracy requirement below a 15% error rate [96]. This error is standing as similar or slightly more

accurate than automatic BA mapping processes with medium spatial resolution published in literature on the topic, which are within the 20–50% range [16,22,23,26,28,29,41,95].

High cloud coverage can cause omissions in some areas in the BA map when using the BA Cartography tool. This effect was detected in SEA, mainly east of the Australian Capital Territory next to the sea (Figure 7); this area had not been observed on a single date during either the pre- or post-fire period, and so was exported as an unobserved area. Users can solve this problem by defining longer periods of time, thus including more cloud-free images. We also found some residual commissions, mostly located west of longitude 145°E and deriving from croplands, since their spectral signal following harvesting is often indistinguishable from burned areas. However, they accounted for very small portions of the total BA. In Canada, when the BA map generated by BAMT was compared to the reference perimeters downloaded from the Canadian Wildland Fire Information System's (CWFIS) website, 40% omissions of BA were obtained. A visual analysis of both maps showed that the undetected areas of the BAMT-derived product were not real omissions, but rather overestimations in CWFIS perimeters related to various sources used at different spatial resolutions [86,87]. In addition, the positive difference in BAMT mapped BA was related to a delay in detection due to clouds and commission errors in mountainous regions.

The total burned area detected by the BAMT coincided with what has been detected in different global BA products or by other studies (Figure 14). In SEA, the MCD64A1 [5] product detected 55,800 km^2 from September 2019 to April 2020 (as opposed to 52,700 km^2 in the case of our Landsat product), with similar amounts in NSW, VIC and ACT. Significantly larger burned areas were also observed within the same period: 71,600 km^2 [97] (Filkov in Figure 14). In Canada, the global products MCD64A1 and FireCCI51 [6] detected less burned areas than the BA S2 product: 14,153 and 10,610 km^2, respectively (16,165 km^2 in the case of our product). However, MCD64A1 was very similar to the S2 product in BC, ON and MB; larger differences were found in AB, SK and QC, mainly due to areas burned in June before the S2 product's period began. FireCCI51 differed the most from our product, especially in BC, where the global product omitted more than 30% of the burned areas.
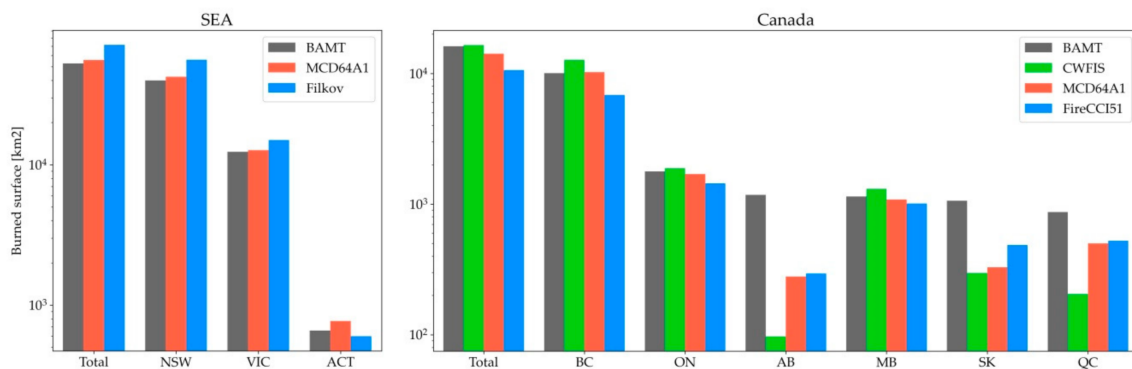
Figure 14. Comparison of burned surfaces by several studies, in SEA and Canada. Note that the vertical axis is logarithmic, and that several regions are not represented because of insignificant BA: Jervis Bay Territory (JBT) in SEA, and NL, NB, NS and PE in Canada.

The BA maps obtained using BAMT evidenced a significant detection delay when compared to VIIRS active fires. This delay is related to the lower temporal resolution of Sentinel-2 or Landsat data that worsens in cloudy areas. For example, in SEA, 40.3% of pixels were detected at least one month after the hotspot's date, with the largest differences being found in the south of the study area, around the border between New South Wales and Victoria. In this area, fires burning in January were not detected until March because of cloud cover persistence. In Canada, the delay was even more severe and 70% of pixels were detected at least one month later, even though Sentinel-2 data (with a higher temporal resolution) were used. Another source for the delay was the temporal compositing criteria

that minimize the NBR index of the time series subject to consideration in creating a temporal composite. The minimum NBR does not always correspond to the first observable burned date, due to atmospheric effects of the acquisitions, smoke, sun angle or delayed mortality [98]. In addition, BA pixels that are members of the same polygon record only a unique date (the most frequent one): For example, if the largest section of the polygon was observed later than the other sections of the fire because of clouds, these later date would be assigned to the whole polygon. Moreover, creating BA maps over longer periods to reduce unobserved areas, as mentioned previously, may affect the product's temporal accuracy, as unrelated but adjacent burned areas could be merged into a single polygon and assigned the same date.

BA tools are complemented by the VA tool that selects the locations and periods representing the full range of conditions present in a statistically robust way [15,33]. This tool conforms to Stage 3 Validation, as defined by the Committee on Earth Observation Satellites (CEOS) Land Product Validation subgroup. Initially developed for global BA product validation, the tool has been adapted to medium spatial resolution, taking advantage of the Landsat and Sentinel-2 GEE catalogs for the data-availability criteria, and overcoming the major difficulties attached to handling the dataset calendar [33] and the MCD64A1 and FireCCI51 BA products that have already been uploaded to the system. Unfortunately, both global products have been reported to as underestimating small fires [4,6,15], which may alter the real distribution of low and high fire activity strata. A good alternative could be a combination of previous BA products with VIIRS active fire dataset that provides a greater response to fires over relatively small areas [81,99], but this dataset is not systematically available within the GEE environment.

Known Limitations

Several limitations have been identified for these BAMT tools, both in their development and their implementation. Here we would like to address the most important of these limitations.

We are aware that the most time-consuming task in mapping BA is vectorizing the RF probability raster to ensure the two-phase focus strategy (getting the areas with a probability higher than 50% that have at least one seed inside). This process, especially when large areas are processed by using the BA Cartography tool, and despite the process being split in chunks of $2° × 2°$ rectangles, may exceed the GEE user memory limit, depending on the number and geometrical complexity of the polygons, which prevent the successful conclusion of the mapping process. Other GEE raster methods used in segmentation, such as Simple Non-Iterative Clustering (SNIC) [100] or connected component grouping algorithms, have also been tested, but discarded due to their not being able to implement a rigorous two-stage focus. In addition, processing very large areas (at a country or continent level) could considerably slow down the iterative supervision of both the training and assessment process.

Critical omission errors can occur when cloud coverage is persistent throughout the processed period. Our initial recommendation in such cases is to extend the period subject to analysis, thus increasing the probability of finding cloud-free scenes that still maintain the burned signal [93]. However, we should advise being careful to define a processing period longer than the fire recurrence, since the BA mapping process can only detect one burning per analyzed period (with a burning date coinciding with the minimum NBR value of the time series). This interval depends on the fire regime and biome, and it may vary from a couple of months in tropical regions to several years at high latitudes [21,101,102].

When working with Sentinel-2 data, some adopted decisions must be clarified. Firstly, the 10 m output is solely applied to the RP tool, taking advantage of the Sentinel-2 bands at the highest spatial resolution. In the case of the BA Cartography tool, a heavy noise was observed in the RF probability that prevented a good accuracy when working at 10 m of resolution over large extents. Similarly, both tools exclusively use the L1C product, due to artifacts detected in the topographic correction in the Level-2A creation by the ESA Sen2cor

processor [54]; the SCL, contained in the L2A product, is limited in terms of masking cloud probabilities and shadows exclusively in the RP tool.

We should also clarify the fact that the dates obtained for the BA Cartography tool have to be considered with caution, as the burning date depends on native medium temporal resolution of the data (5–10 days for Sentinel-2 and 8–16 days for Landsat), that may still be delayed because of cloud cover and the use of temporal NBR composites. In addition, the dissolution process of fires burned on different dates in a unique polygon increases this delay.

Finally, users should note that, although commission errors in croplands and shadows have improved from the previous BAMS software [36], they may still persist to a minimal extent. We recommend paying attention to increasing omission errors when defining suitable unburned samples to avoid detecting these land-cover classes.

The VA tool may serve for a wide section of the scientific community as a way of implementing the stratified random sampling methodology for assessment purposes. Implementation was challenging due to the complex design of the algorithm [15,33], and it is quite dependent on the GEE user memory limit and periods and extents where the analysis is carried out. We should warn that the GEE user memory limit is easily exceeded when using the optional data availability criteria, since the tool analyzes the availability, frequency and cloud coverage of several long temporal series. However, not applying these optional criteria could result in sampling long units with images that are too cloudy. We should also note that the central subset sample selected by the VA tool might contain more clouds than desired, because the cloud cover information is taken from the metadata of the whole scene, rather than being computed from the central subset.

5. Conclusions

This paper describes the Burned Area Mapping Tools (BAMTs) as a continuation and improvement on the previous BAMS software [36]. The tools take advantage of the huge cloud-computing and processing capacities of Google Earth Engine (GEE), and the Landsat and Sentinel-2 preloaded datasets to obtain a very cost- and time-effective system for mapping and validating burned areas (BA), using medium spatial resolution data.

The tools' performance was demonstrated in two different case studies, the first in the catastrophic 2019/2020 fire season in Southeast Australia, covering a region of 1 M km^2 over eight months, and the second in Canada over the summer of 2018, covering a larger extent (6 M km^2). In the first study, a BA map was obtained by using Landsat data and was validated in 10 Sentinel-2 validation sites selected by a stratified random sampling methodology. More than 52,700 km^2 of burned areas was mapped, and validation results showed omission and commission errors below 12%, according to Sentinel-2 data. Similarly, a burned surface of more than 16,000 km^2 was mapped by using Sentinel-2 data in Canada, and several discrepancies were detected in comparison to the National Fire Database downloaded from the CWFIS Datamart.

BAMT proved to be a cost-effective methodology for BA mapping; in Canada, the BA vector map involved more than 250,000 Sentinel-2 scenes and was produced with minimum user-intervention (19 training polygons and 11 iterations in total) in 10 days. In Australia, more than 3500 Landsat scenes were involved in the process, with the algorithm being trained with 130 samples in total (over four different periods) and the BA vector map being obtained in less than three days. The validation tools completed the suite in embracing the BA mapping tools.

The tools consist of four JavaScript API scripts executable from the Google Earth Engine Code Editor that can be reached at https://github.com/ekhiroteta/BAMT (accessed on 27 January 2021). Data created for this study are available at the same repository.

Author Contributions: E.R. developed the tools and applied them on the case study. A.B. and M.F. helped design and improve the tools. E.R., A.B., M.F. and E.C. wrote the manuscript. All authors have read and agreed to the published version of the manuscript.

Institutional Review Board Statement: Not applicable.

Informed Consent Statement: Not applicable.

Data Availability Statement: Publicly available datasets were analyzed in this study. These data can be found here: https://github.com/ekhiroteta/BAMT (accessed on 27 January 2021).

Conflicts of Interest: The authors declare no conflict of interest.
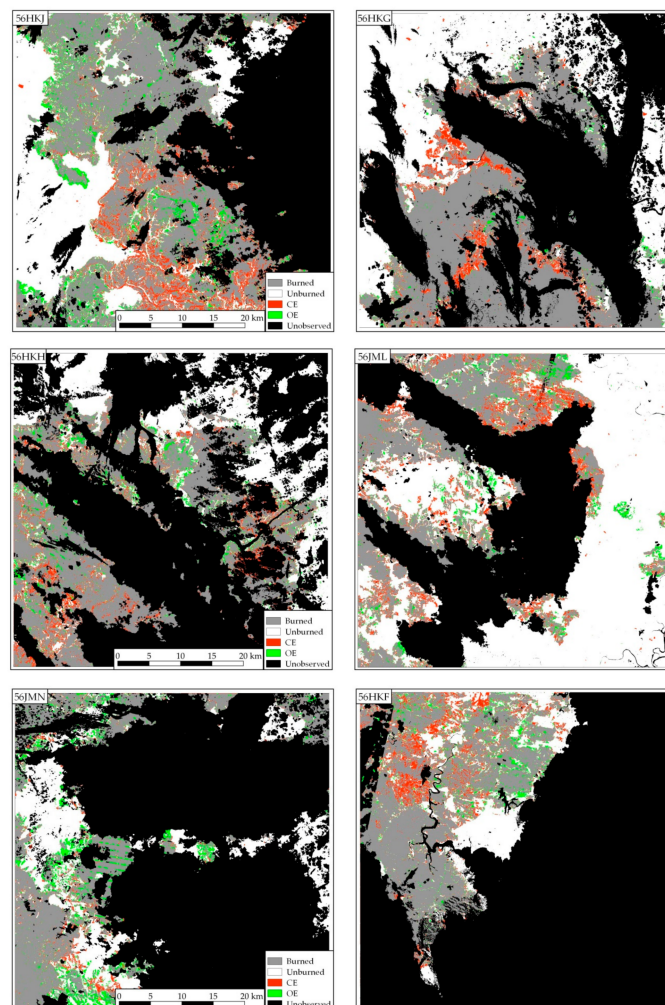
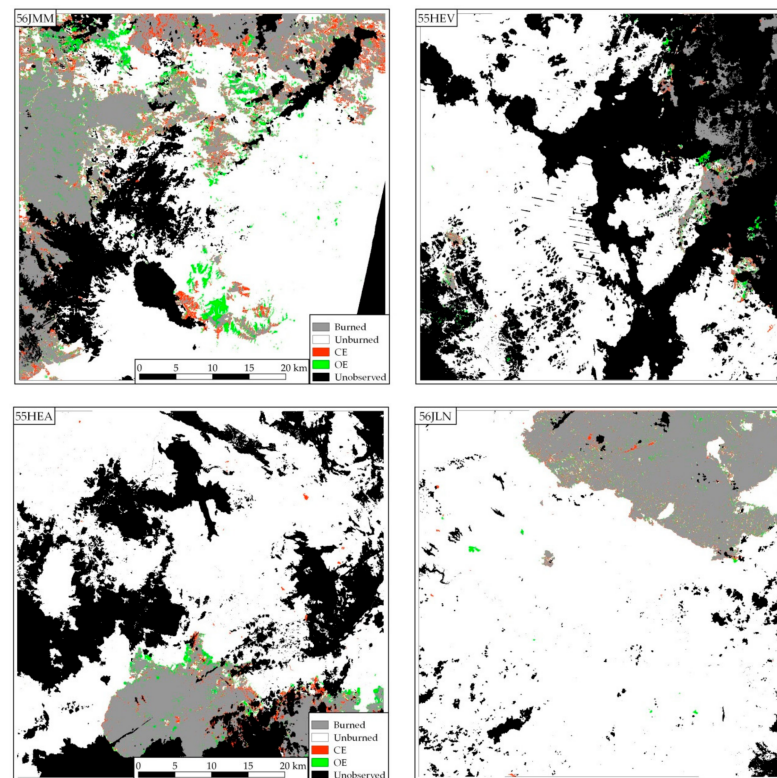## Appendix A

Figure A1. *Cont.*

Figure A1. Committed and omitted errors in the 10 validation areas in SEA.

References

1. Van Der Werf, G.R.; Randerson, J.T.; Giglio, L.; Van Leeuwen, T.T.; Chen, Y.; Rogers, B.M.; Mu, M.; Van Marle, M.J.E.; Morton, D.C.; Collatz, G.J.; et al. Global fire emissions estimates during 1997–2016. *Earth Syst. Sci. Data* **2017**, *9*, 697–720. [CrossRef]
2. Goldammer, J.G.; Statheropoulos, M.; Andreae, M.O. Impacts of Vegetation Fire Emissions on the Environment, Human Health, and Security: A Global Perspective. In *Wildland Fires and Air Pollution*; Bytnerowicz, A., Arbaugh, M.J., Riebau, A.R., Andersen, C.B.T.-D., Eds.; Elsevier: Amsterdam, The Netherlands, 2008; Volume 8, pp. 3–36. ISBN 1474–8177.
3. Roos, C.I.; Scott, A.C.; Belcher, C.M.; Chaloner, W.G.; Aylen, J.; Bird, R.B.; Coughlan, M.R.; Johnson, B.R.; Johnston, F.H.; McMorrow, J.; et al. Living on a flammable planet: Interdisciplinary, cross-scalar and varied cultural lessons, prospects and challenges. *Philos. Trans. R. Soc. B Biol. Sci.* **2016**, *371*, 20150469. [CrossRef] [PubMed]
4. Randerson, J.T.; Chen, Y.; Van Der Werf, G.R.; Rogers, B.M.; Morton, D.C. Global burned area and biomass burning emissions from small fires. *J. Geophys. Res. Space Phys.* **2012**, *117*. [CrossRef]
5. Giglio, L.; Boschetti, L.; Roy, D.P.; Humber, M.L.; Justice, C.O. The Collection 6 MODIS burned area mapping algorithm and product. *Remote Sens. Environ.* **2018**, *217*, 72–85. [CrossRef] [PubMed]
6. Lizundia-Loiola, J.; Otón, G.; Ramo, R.; Chuvieco, E. A spatio-temporal active-fire clustering approach for global burned area mapping at 250 m from MODIS data. *Remote Sens. Environ.* **2020**, *236*, 111493. [CrossRef]
7. Tansey, K.; Grégoire, J.; Stroppiana, D.; Sousa, A.; Silva, J.; Pereira, J.M.C.; Boschetti, L.; Maggi, M.; Brivio, P.A.; Fraser, R.; et al. Vegetation burning in the year 2000: Global burned area estimates from SPOT VEGETATION data. *J. Geophys. Res. Space Phys.* **2004**, *109*, D14S03. [CrossRef]
8. Simon, M.; Plummer, S.; Fierens, F.; Hoelzemann, J.J.; Arino, O. Burnt area detection at global scale using ATSR-2: The GLOBSCAR products and their qualification. *J. Geophys. Res. Space Phys.* **2004**, *109*, D14S02. [CrossRef]
9. Tansey, K.; Grégoire, J.-M.; Defourny, P.; Leigh, R.; Pekel, J.-F.; Van Bogaert, E.; Bartholomé, E. A new, global, multi-annual (2000–2007) burnt area product at 1 km resolution. *Geophys. Res. Lett.* **2008**, *35*, 35. [CrossRef]
10. Tansey, K.; Bradley, A.; Smets, B.; van Best, C.; Lacaze, R. The Geoland2 BioPar Burned Area Product. In Proceedings of the EGU General Assembly Conference Abstracts, Vienna, Austria, 22–27 April 2012; p. 4727.
11. Roy, D.; Boschetti, L.; Justice, C.; Ju, J. The collection 5 MODIS burned area product—Global evaluation by comparison with the MODIS active fire product. *Remote Sens. Environ.* **2008**, *112*, 3690–3707. [CrossRef]
12. Giglio, L.; Loboda, T.; Roy, D.P.; Quayle, B.; Justice, C.O. An active-fire based burned area mapping algorithm for the MODIS sensor. *Remote Sens. Environ.* **2009**, *113*, 408–420. [CrossRef]
13. Alonso-Canas, I.; Chuvieco, E. Global burned area mapping from ENVISAT-MERIS and MODIS active fire data. *Remote Sens. Environ.* **2015**, *163*, 140–152. [CrossRef]

14. Chuvieco, E.; Lizundia-Loiola, J.; Pettinari, M.L.; Ramo, R.; Padilla, M.; Tansey, K.; Mouillot, F.; Laurent, P.; Storm, T.; Heil, A.; et al. Generation and analysis of a new global burned area product based on MODIS 250 m reflectance bands and thermal anomalies. *Earth Syst. Sci. Data* **2018**, *10*, 2015–2031. [CrossRef]

15. Padilla, M.; Stehman, S.V.; Ramo, R.; Corti, D.; Hantson, S.; Oliva, P.; Alonso-Canas, I.; Bradley, A.V.; Tansey, K.; Mota, B.; et al. Comparing the accuracies of remote sensing global burned area products using stratified random sampling and estimation. *Remote Sens. Environ.* **2015**, *160*, 114–121. [CrossRef]

16. Roteta, E.; Bastarrika, A.; Padilla, M.; Storm, T.; Chuvieco, E. Development of a Sentinel-2 burned area algorithm: Generation of a small fire database for sub-Saharan Africa. *Remote Sens. Environ.* **2019**, *222*, 1–17. [CrossRef]

17. Hantson, S.; Padilla, M.; Corti, D.; Chuvieco, E. Strengths and weaknesses of MODIS hotspots to characterize global fire occurrence. *Remote Sens. Environ.* **2013**, *131*, 152–159. [CrossRef]

18. Boschetti, L.; Roy, D.P.; Giglio, L.; Huang, H.; Zubkova, M.; Humber, M.L. Global validation of the collection 6 MODIS burned area product. *Remote Sens. Environ.* **2019**, *235*, 111490. [CrossRef]

19. Garcia, M.J.L.; Caselles, V. Mapping burns and natural reforestation using thematic Mapper data. *Geocarto Int.* **1991**, *6*, 31–37. [CrossRef]

20. Koutsias, N.; Karteris, M. Burned area mapping using logistic regression modeling of a single post-fire Landsat-5 Thematic Mapper image. *Int. J. Remote Sens.* **2000**, *21*, 673–687. [CrossRef]

21. Chuvieco, E.; Mouillot, F.; van der Werf, G.R.; Miguel, J.S.; Tanase, M.; Koutsias, N.; García, M.; Yebra, M.; Padilla, M.; Gitas, I.; et al. Historical background and current developments for mapping burned area from satellite Earth observation. *Remote Sens. Environ.* **2019**, *225*, 45–64. [CrossRef]

22. Boschetti, L.; Roy, D.P.; Justice, C.O.; Humber, M.L. MODIS–Landsat fusion for large area 30 m burned area mapping. *Remote Sens. Environ.* **2015**, *161*, 27–42. [CrossRef]

23. Long, T.; Zhang, Z.; He, G.; Jiao, W.; Tang, C.; Wu, B.; Zhang, X.; Wang, G.; Yin, R. 30 m Resolution Global Annual Burned Area Mapping Based on Landsat Images and Google Earth Engine. *Remote Sens.* **2019**, *11*, 489. [CrossRef]

24. Liu, J.; Heiskanen, J.; Maeda, E.E.; Pellikka, P.K. Burned area detection based on Landsat time series in savannas of southern Burkina Faso. *Int. J. Appl. Earth Obs. Geoinf.* **2018**, *64*, 210–220. [CrossRef]

25. Hawbaker, T.J.; Vanderhoof, M.K.; Beal, Y.-J.; Takacs, J.D.; Schmidt, G.L.; Falgout, J.T.; Williams, B.; Fairaux, N.M.; Caldwell, M.K.; Picotte, J.J.; et al. Mapping burned areas using dense time-series of Landsat data. *Remote Sens. Environ.* **2017**, *198*, 504–522. [CrossRef]

26. Filipponi, F. Exploitation of Sentinel-2 Time Series to Map Burned Areas at the National Level: A Case Study on the 2017 Italy Wildfires. *Remote Sens.* **2019**, *11*, 622. [CrossRef]

27. Roy, D.P.; Huang, H.; Boschetti, L.; Giglio, L.; Yan, L.; Zhang, H.H.; Li, Z. Landsat-8 and Sentinel-2 burned area mapping—A combined sensor multi-temporal change detection approach. *Remote Sens. Environ.* **2019**, *231*. [CrossRef]

28. Hawbaker, T.J.; Vanderhoof, M.K.; Schmidt, G.L.; Beal, Y.-J.; Picotte, J.J.; Takacs, J.D.; Falgout, J.T.; Dwyer, J.L. The Landsat Burned Area algorithm and products for the conterminous United States. *Remote Sens. Environ.* **2020**, *244*, 111801. [CrossRef]

29. Goodwin, N.R.; Collett, L.J. Development of an automated method for mapping fire history captured in Landsat TM and ETM+ time series across Queensland, Australia. *Remote Sens. Environ.* **2014**, *148*, 206–221. [CrossRef]

30. Roy, D.P.; Frost, P.G.H.; Justice, C.O.; Landmann, T.; Le Roux, J.L.; Gumbo, K.; Makungwa, S.; Dunham, K.; Du Toit, R.; Mhwandagaraii, K.; et al. The Southern Africa Fire Network (SAFNet) regional burned-area product-validation protocol. *Int. J. Remote Sens.* **2005**, *26*, 4265–4292. [CrossRef]

31. Boschetti, L.; Roy, D.P.; Justice, C.O. *International Global Burned Area Satellite Product Validation Protocol Part I-Production and Standardization of Validation Reference Data (to be Followed by Part II-Accuracy Reporting)*; Committee on Earth Observation Satellites: Silver Spring, MD, USA, 2009.

32. Roy, D.; Boschetti, L. Southern Africa Validation of the MODIS, L3JRC, and GlobCarbon Burned-Area Products. *IEEE Trans. Geosci. Remote Sens.* **2009**, *47*, 1032–1044. [CrossRef]

33. Boschetti, L.; Stehman, S.V.; Roy, D.P. A stratified random sampling design in space and time for regional to global scale burned area product validation. *Remote Sens. Environ.* **2016**, *186*, 465–478. [CrossRef]

34. Padilla, M.; Stehman, S.V.; Chuvieco, E. Validation of the 2008 MODIS-MCD45 global burned area product using stratified random sampling. *Remote Sens. Environ.* **2014**, *144*, 187–196. [CrossRef]

35. Chen, D.; Pereira, J.M.; Masiero, A.; Pirotti, F. Mapping fire regimes in China using MODIS active fire and burned area data. *Appl. Geogr.* **2017**, *85*, 14–26. [CrossRef]

36. Bastarrika, A.; Alvarado, M.; Artano, K.; Martinez, M.P.; Mesanza, A.; Torre, L.; Ramo, R.; Chuvieco, E. BAMS: A Tool for Supervised Burned Area Mapping Using Landsat Data. *Remote Sens.* **2014**, *6*, 12360–12380. [CrossRef]

37. Franquesa, M.; Vanderhoof, M.K.; Stavrakoudis, D.; Gitas, I.Z.; Roteta, E.; Padilla, M.; Chuvieco, E. Development of a standard database of reference sites for validating global burned area products. *Earth Syst. Sci. Data* **2020**, *12*, 3229–3246. [CrossRef]

38. Padilla, M.; Stehman, S.V.; Litago, J.; Chuvieco, E. Assessing the Temporal Stability of the Accuracy of a Time Series of Burned Area Products. *Remote Sens.* **2014**, *6*, 2050–2068. [CrossRef]

39. Valencia, G.M.; Anaya, J.A.; Velásquez, É.A.; Ramo, R.; Caro-Lopera, F.J. About Validation-Comparison of Burned Area Products. *Remote Sens.* **2020**, *12*, 3972. [CrossRef]

40. Alva-Álvarez, G.I.; Reyes-Hernández, H.; Palacio-Aponte, Á.G.; Núñez-López, D.; Muñoz-Robles, C. Cambios en el paisaje ocasionados por incendios forestales en la región de Madera, Chihuahua. *Madera Bosques* **2018**, *24*. [CrossRef]

41. Vanderhoof, M.K.; Fairaux, N.; Beal, Y.-J.G.; Hawbaker, T.J. Validation of the USGS Landsat Burned Area Essential Climate Variable (BAECV) across the conterminous United States. *Remote Sens. Environ.* **2017**, *198*, 393–406. [CrossRef]

42. Gorelick, N.; Hancher, M.; Dixon, M.; Ilyushchenko, S.; Thau, D.; Moore, R. Google Earth Engine: Planetary-scale geospatial analysis for everyone. *Remote Sens. Environ.* **2017**, *202*, 18–27. [CrossRef]

43. Hansen, M.C.; Potapov, P.V.; Moore, R.; Hancher, M.; Turubanova, S.A.; Tyukavina, A.; Thau, D.; Stehman, S.V.; Goetz, S.J.; Loveland, T.R.; et al. High resolution global maps of 21st-century forest cover change. *Science* **2013**, *342*, 850–853. [CrossRef] [PubMed]

44. Wang, L.; Diao, C.; Xian, G.; Yin, D.; Lu, Y.; Zou, S.; Erickson, T.A. A summary of the special issue on remote sensing of land change science with Google earth engine. *Remote Sens. Environ.* **2020**, *248*, 112002. [CrossRef]

45. Mutanga, O.; Kumar, L. Google earth engine applications. *Remote Sens.* **2019**, *11*, 591. [CrossRef]

46. Daldegan, G.A.; Roberts, D.A.; Ribeiro, F.D.F. Spectral mixture analysis in Google Earth Engine to model and delineate fire scars over a large extent and a long time-series in a rainforest-savanna transition zone. *Remote Sens. Environ.* **2019**, *232*. [CrossRef]

47. Seydi, S.T.; Akhoondzadeh, M.; Amani, M.; Mahdavi, S. Wildfire Damage Assessment over Australia Using Sentinel-2 Imagery and MODIS Land Cover Product within the Google Earth Engine Cloud Platform. *Remote Sens.* **2021**, *13*, 220. [CrossRef]

48. Roteta, E.; Oliva, P. Optimization of a Random Forest Classifier for Burned Area Detection in Chile Using Sentinel-2 Data. In Proceedings of the 2020 IEEE Latin American GRSS and ISPRS Remote Sensing Conference, LAGIRS 2020-Proceedings, Santiago, Chile, 21–26 March 2020.

49. Landsat Missions. Available online: https://www.usgs.gov/core-science-systems/nli/landsat (accessed on 24 January 2021).

50. Masek, J.; Vermote, E.; Saleous, N.; Wolfe, R.; Hall, F.; Huemmrich, K.; Gao, F.; Kutler, J.; Lim, T.-K. A Landsat Surface Reflectance Dataset for North America, 1990–2000. *IEEE Geosci. Remote Sens. Lett.* **2006**, *3*, 68–72. [CrossRef]

51. Vermote, E.; Justice, C.; Claverie, M.; Franch, B. Preliminary analysis of the performance of the Landsat 8/OLI land surface reflectance product. *Remote Sens. Environ.* **2016**, *185*, 46–56. [CrossRef] [PubMed]

52. ESA-Sentinel-2. Available online: http://www.esa.int/Applications/Observing_the_Earth/Copernicus/Sentinel-2 (accessed on 24 January 2021).

53. Gascon, F.; Bouzinac, C.; Thépaut, O.; Jung, M.; Francesconi, B.; Louis, J.; Lonjou, V.; Lafrance, B.; Massera, S.; Gaudel-Vacaresse, A.; et al. Copernicus Sentinel-2A Calibration and Products Validation Status. *Remote Sens.* **2017**, *9*, 584. [CrossRef]

54. Level-2A Algorithm-Sentinel-2 MSI Technical Guide-Sentinel Online-Sentinel. Available online: https://sentinel.esa.int/web/sentinel/technical-guides/sentinel-2-msi/level-2a/algorithm (accessed on 24 January 2021).

55. Coluzzi, R.; Imbrenda, V.; Lanfredi, M.; Simoniello, T. A first assessment of the Sentinel-2 Level 1-C cloud mask product to support informed surface analyses. *Remote Sens. Environ.* **2018**, *217*, 426–443. [CrossRef]

56. Rouse, J.W.; Haas, R.H.; Schell, J.A. *Monitoring the Vernal Advancement and Retrogradation (Greenwave Effect) of Natural Vegetation*; NASA/GSFC Type III Final Report; Goddard Space Flight Center: Greenbelt, MD, USA, 1974; pp. 1–8.

57. Key, C.H.; Benson, N. *The Normalized Burn Ratio (NBR): A Landsat TM Radiometric Measure of Burn Severity*; US Geological Survey, Northern Rocky Mountain Science Center: Bozeman, MT, USA, 1999.

58. Griffiths, P.; Nendel, C.; Hostert, P. Intra-annual reflectance composites from Sentinel-2 and Landsat for national-scale crop and land cover mapping. *Remote Sens. Environ.* **2019**, *220*, 135–151. [CrossRef]

59. Breiman, L.; Friedman, J.H.; Olshen, R.A.; Stone, C.J. *Classification and Regression Trees*; Wadsworth International Group: Belmont, CA, USA, 1984; ISBN 9780534980535.

60. Vapnik, V. Pattern recognition using generalized portrait method. *Autom. Remote Control* **1963**, *24*, 774–780.

61. Belgiu, M.; Drăgu, L. Random forest in remote sensing: A review of applications and future directions. *ISPRS J. Photogramm. Remote Sens.* **2016**, *114*, 24–31. [CrossRef]

62. Breiman, L. Random forests. *Mach. Learn.* **2001**, *45*, 5–32. [CrossRef]

63. Bastarrika, A.; Chuvieco, E.; Martín, M.P. Mapping burned areas from Landsat TM/ETM+ data with a two-phase algorithm: Balancing omission and commission errors. *Remote Sens. Environ.* **2011**, *115*, 1003–1012. [CrossRef]

64. Justice, C.; Belward, A.; Morisette, J.; Lewis, P.; Privette, J.; Baret, F. Developments in the 'validation' of satellite sensor products for the study of the land surface. *Int. J. Remote Sens.* **2000**, *21*, 3383–3390. [CrossRef]

65. Roy, D.P.; Borak, J.S.; Devadiga, S.; Wolfe, R.E.; Zheng, M.; Descloitres, J. The MODIS Land product quality assessment approach. *Remote Sens. Environ.* **2002**, *83*, 62–76. [CrossRef]

66. Morisette, J.T.; Privette, J.L.; Justice, C.O. A framework for the validation of MODIS Land products. *Remote Sens. Environ.* **2002**, *83*, 77–96. [CrossRef]

67. Padilla, M.; Olofsson, P.; Stehman, S.V.; Tansey, K.; Chuvieco, E. Stratification and sample allocation for reference burned area data. *Remote Sens. Environ.* **2017**, *203*, 240–255. [CrossRef]

68. Kennedy, R.E.; Yang, Z.G.; Cohen, W.B. Detecting trends in forest disturbance and recovery using yearly Landsat time series: 1. LandTrendr—Temporal segmentation algorithms. *Remote Sens. Environ.* **2010**, *114*, 2897–2910. [CrossRef]

69. Cohen, W.B.; Yang, Z.G.; Kennedy, R. Detecting trends in forest disturbance and recovery using yearly Landsat time series: 2. TimeSync—Tools for calibration and validation. *Remote Sens. Environ.* **2010**, *114*, 2911–2924. [CrossRef]

70. Olson, D.M.; Dinerstein, E.; Wikramanayake, E.D.; Burgess, N.D.; Powell, G.V.N.; Underwood, E.C.; D'amico, J.A.; Itoua, I.; Strand, H.E.; Morrison, J.C.; et al. Terrestrial Ecoregions of the World: A New Map of Life on Earth. *Bioscience* **2001**, *51*, 933. [CrossRef]

71. Giglio, L.; Randerson, J.T.; Van Der Werf, G.R.; Kasibhatla, P.S.; Collatz, G.J.; Morton, D.C.; DeFries, R.S. Assessing variability and long-term trends in burned area by merging multiple satellite fire products. *Biogeosciences* **2010**, *7*, 1171–1186. [CrossRef]

72. Giglio, L.; Descloitres, J.; Justice, C.O.; Kaufman, Y.J. An Enhanced Contextual Fire Detection Algorithm for MODIS. *Remote Sens. Environ.* **2003**, *87*, 273–282. [CrossRef]

73. Giglio, L. Characterization of the tropical diurnal fire cycle using VIRS and MODIS observations. *Remote Sens. Environ.* **2007**, *108*, 407–421. [CrossRef]

74. Boschetti, L.; Brivio, P.A.; Eva, H.; Gallego, J.; Baraldi, A.; Gregoire, J.-M. A sampling method for the retrospective validation of global burned area products. *IEEE Trans. Geosci. Remote Sens.* **2006**, *44*, 1765–1773. [CrossRef]

75. Yu, P.; Xu, R.; Abramson, M.J.; Li, S.; Guo, Y. Bushfires in Australia: A serious health emergency under climate change. *Lancet Planet. Health* **2020**, *4*, e7–e8. [CrossRef]

76. Schweinsberg, S.; Darcy, S.; Beirman, D. 'Climate crisis' and 'bushfire disaster': Implications for tourism from the involvement of social media in the 2019–2020 Australian bushfires. *J. Hosp. Tour. Manag.* **2020**, *43*, 294–297. [CrossRef]

77. Bowman, D.; Williamson, G.; Yebra, M.; Lizundia-Loiola, J.; Pettinari, M.L.; Shah, S.; Bradstock, R.; Chuvieco, E. Wildfires: Australia needs national monitoring agency. *Nat. Cell Biol.* **2020**, *584*, 188–191. [CrossRef]

78. Congalton, R.G.; Green, K. *Assessing the Accuracy of Remotely Sensed Data: Principles and Practices*; CRC Press: Boca Raton, FL, USA, 2008.

79. Dice, L.R. Measures of the Amount of Ecologic Association between Species. *Ecology* **1945**, *26*, 297–302. [CrossRef]

80. Fleiss, J.L. *Statistical Methods for Rates and Proportions*; Wiley: New York, NY, USA, 1981; ISBN 0471064289.

81. Schroeder, W.; Oliva, P.; Giglio, L.; Csiszar, I.A. The New VIIRS 375 m active fire detection data product: Algorithm description and initial assessment. *Remote Sens. Environ.* **2014**, *143*, 85–96. [CrossRef]

82. Now Worst Fire Season on Record as, B.C. Extends State of Emergency | CBC News. 2018. Available online: https://www.cbc.ca/news/canada/british-columbia/state-emergency-bc-wildfires-1.4803546 (accessed on 24 January 2021).

83. Fire Perimeters-Historical-Datasets-Data Catalogue. Available online: https://catalogue.data.gov.bc.ca/dataset/fire-perimeters-historical (accessed on 23 January 2021).

84. Fire Incident Locations-Historical-Datasets-Data Catalogue. Available online: https://catalogue.data.gov.bc.ca/dataset/fire-incident-locations-historical (accessed on 23 January 2021).

85. Canadian Interagency Forest Fire Centre Inc. Canada Report. 2018. Available online: https://www.ciffc.ca/sites/default/files/2019--06/2018CanadaReport2019_05_28R1.pdf (accessed on 23 January 2021).

86. Canadian Wildland Fire Information System | Data Sources and Methods for Daily Maps. Available online: https://cwfis.cfs.nrcan.gc.ca/background/dsm/fm3 (accessed on 24 January 2021).

87. Fraser, R.; Li, Z.; Cihlar, J. Hotspot and NDVI Differencing Synergy (HANDS) a New Technique for Burned Area Mapping over Boreal Forest. *Remote Sens. Environ.* **2000**, *74*, 362–376. [CrossRef]

88. Ho, T.K. The random subspace method for constructing decision forests. *IEEE Trans. Pattern Anal. Mach. Intell.* **1998**, *20*, 832–844.

89. Çömert, R.; Matci, D.K.; Avdan, U. Object Based Burned Area Mapping with Random Forest Algorithm. *Int. J. Eng. Geosci.* **2019**, *4*, 78–87. [CrossRef]

90. Sulova, A.; Arsanjani, J.J. Exploratory Analysis of Driving Force of Wildfires in Australia: An Application of Machine Learning within Google Earth Engine. *Remote Sens.* **2021**, *13*, 10. [CrossRef]

91. Ramo, R.; Chuvieco, E. Developing a Random Forest Algorithm for MODIS Global Burned Area Classification. *Remote Sens.* **2017**, *9*, 1193. [CrossRef]

92. Ramo, R.; García, M.; Rodríguez, D.; Chuvieco, E. A data mining approach for global burned area mapping. *Int. J. Appl. Earth Obs. Geoinf.* **2018**, *73*, 39–51. [CrossRef]

93. Pereira, J.M.; Sá, A.C.; Sousa, A.M.; Silva, J.M.; Santos, T.N.; Carreiras, J.M. Spectral characterisation and discrimination of burnt areas. In *Remote Sensing of Large Wildfires*; Chuvieco, E., Ed.; Springer: Berlin/Heidelberg, Germany, 1999; pp. 123–138.

94. Smiraglia, D.; Filipponi, F.; Mandrone, S.; Tornato, A.; Taramelli, A. Agreement Index for Burned Area Mapping: Integration of Multiple Spectral Indices Using Sentinel-2 Satellite Images. *Remote Sens.* **2020**, *12*, 1862. [CrossRef]

95. Stroppiana, D.; Bordogna, G.; Carrara, P.; Boschetti, M.; Brivio, P. A method for extracting burned areas from Landsat TM/ETM+ images by soft aggregation of multiple Spectral Indices and a region growing algorithm. *ISPRS J. Photogramm. Remote Sens.* **2012**, *69*, 88–102. [CrossRef]

96. Mouillot, F.; Schultz, M.G.; Yue, C.; Cadule, P.; Tansey, K.; Ciais, P.; Chuvieco, E. Ten years of global burned area products from spaceborne remote sensing—A review: Analysis of user needs and recommendations for future developments. *Int. J. Appl. Earth Obs. Geoinf.* **2014**, *26*, 64–79. [CrossRef]

97. Filkov, A.I.; Ngo, T.; Matthews, S.; Telfer, S.; Penman, T.D. Impact of Australia's catastrophic 2019/20 bushfire season on communities and environment. Retrospective analysis and current trends. *J. Saf. Sci. Resil.* **2020**, *1*, 44–56. [CrossRef]

98. Key, C.H. Ecological and Sampling Constraints on Defining Landscape Fire Severity. *Fire Ecol.* **2006**, *2*, 34–59. [CrossRef]

99. Oliva, P.; Schroeder, W. Assessment of VIIRS 375 m active fire detection product for direct burned area mapping. *Remote Sens. Environ.* **2015**, *160*, 144–155. [CrossRef]

100. Achanta, R.; Süsstrunk, S. Superpixels and Polygons Using Simple Non-Iterative Clustering. In Proceedings of the IEEE Conference on Computer Vision and Pattern Recognition (CVPR), Honolulu, HI, USA, 21–26 July 2017.

101. Cuevas-González, M.; Gerard, F.; Balzter, H.; Riaño, D. Analysing forest recovery after wildfire disturbance in boreal Siberia using remotely sensed vegetation indices. *Glob. Chang. Biol.* **2009**, *15*, 561–577. [CrossRef]

102. Sader, S.A.; Stone, T.A.; Joyce, A.T. Remote sensing of tropical forests: An overview of research and applications using non-photographic sensors. *Photogramm. Eng. Remote Sens.* **1990**, *56*, 1343–1351.

III eranskina: A3 – Txileko EA

Kongresu-artikulua

Izenburua: Optimization of A Random Forest Classifier for Burned Area Detection in Chile Using Sentinel-2 Data

Egileak: Ekhi Roteta eta Patricia Oliva

Argitaratze-data: 2020ko martxoa

DOI: https://doi.org/10.1109/LAGIRS48042.2020.9165585

Erreferentzia bibliografikoa:

Roteta, E., Oliva, P., 2020. Optimization of A Random Forest Classifier for Burned Area Detection in Chile Using Sentinel-2 Data, in: *2020 IEEE Latin American GRSS and ISPRS Remote Sensing Conference, LAGIRS 2020 - Proceedings.* https://doi.org/10.1109/LAGIRS48042.2020.9165585

Kongresua

Izena: LAGIRS 2020: 2020 Latin American GRSS & ISPRS Remote Sensing Conference

Data: 2020ko martxoaren 22-26

Lekua: Santiago (Txile)

OPTIMIZATION OF A RANDOM FOREST CLASSIFIER FOR BURNED AREA DETECTION IN CHILE USING SENTINEL-2 DATA

E. Roteta [1, *], P. Oliva [2]

[1] Deparment of Geography, Prehistory and Archaeology, University of the Basque Country, Spain – ekhi.roteta@ehu.eus
[2] Hémera Centro de Observación de la Tierra, Universidad Mayor, Chile – patricia.oliva@umayor.cl

KEY WORDS: fires, South America, Sentinel-2, GEE, machine learning, satellite imagery

ABSTRACT:

Due to the high variability of biomes throughout the country, the classification of burned areas is a challenge. We calibrated a random forest classifier to account for all this variability and ensure an accurate classification of burned areas. The classifier was optimized in three steps, generating a version of the burned area product in each step. According to the visual assessment, the final version of the BA product is more accurate than the perimeters created by the Chilean National Forest Corporation, which overestimate large burned areas because it does not consider the inner unburned areas and, it omits some small burned areas. The total burned surface from January to March 2017 was 5,000 km^2 in Chile, 20 % of it belonging to a single burned area in the Maule Region, and with 91 % of the total burned surface distributed in 6 adjacent regions of Central Chile.

1. INTRODUCTION

Fires are a tremendous hazard to both natural resources and human activities. Every year, more than 4 Mkm^2 (Chuvieco et al., 2019) of land burn globally, causing significant ecological and economic consequences, and associated climatological and health effects as a result of fire emissions (O'Donnell et al., 2011; Thelen et al., 2013; Van Der Werf et al., 2017). In Chile, there has been a continuous increase in the number of fires occurred in the country since 1975. The average annual reported burned area was around 100.000 ha with an average fire size of 10 ha. However, the devastating fires that affected the Central region of Chile in 2017 marked a breaking point and possibly signalled a change in the fire regime of the country. More than 500.000 ha were burned, more than 1.000 homes were consumed by the fire and 11 deaths were the tragic result of Chile 2017 fire season.

It is expected that due to climate change Central Chile will experience longer drought periods and higher temperatures, which will result in dryer fuels available for burning favouring longer and more intense fire seasons with larger and more severe forest fires (Rogers et al., 2011). These conditions highlight the importance of the implementation of a system to report the area affected by forest fires accurately and in a timely manner, so the proper forest management decisions could be making efficiently.

In recent decades, remote sensing products have positioned as a valuable resource to monitor Earth dynamics. In particular, burned area estimates generated from satellite data have provided systematic global information for ecological analysis of fire impacts, climate, and carbon cycle models, and fire regime studies, among many others (Beverly et al., 2011; Canadell et al., 2010; Mouillot et al., 2014; Van Der Werf et al., 2017). Burned area mapping from satellite images has been performed using a broad set of methods and sensors, from coarse to very high spatial resolution, such as Advance Very High Resolution Radiometer (AVHRR), SPOT-VEGETATION, MODIS, or MERIS (Alonso-Canas and Chuvieco, 2015; Oliva et al., 2011; Roy et al., 2005; Silva et al., 2005; Tansey et al., 2008; Zhang et al., 2003), Landsat TM, ETM and OLI

(Bastarrika et al., 2011; Hawbaker et al., 2017; Koutsias and Karteris, 2000), Worldview or Ikonos (Dragozi et al., 2014; Wu et al., 2015).

The recent successful launches of Sentinel-2A (2015) and Sentinel-2B (2016) marked the beginning of a new era in the development of remotely sensed products, as the combined detections of both satellites reduced the revisit time to 5 days. In addition, Sentinel-2 Multispectral Imager (MSI) sensor improve upon their predecessors by providing information at 10 and 20 m and including a wider range of spectral bands (Drusch et al., 2012). The enhanced characteristics of Sentinel-2 MSI make the sensor specially indicated to fill current gaps in knowledge and improve current products. The enhanced spatial resolution of Sentinel-2 allows a more detailed analysis of fire perimeters, as well as a better definition of small fires (<25 ha) which will be most likely missed in coarser resolution products (Roteta et al., 2019).

The design of a burned area algorithm requires considering the vast diversity of ecosystems affected by fires, since the spectral response and the burn severity of the burned areas differ greatly among ecosystems. That is why novel studies have explore the use of machine learning techniques, such as Random Forest (Ramo and Chuvieco, 2017), neural networks (Ba et al., 2019), support vector machines (Dragozi et al., 2014) or genetic programming (Cabral et al., 2018), or the application of object-based analysis (Dragozi et al., 2014; Shimabukuro et al., 2015). The most extended approaches are based on (i) using active fire detections to guide the sample selection used to compute the burned area statistics introduced in the algorithm (Alonso-Canas and Chuvieco, 2015; Fraser et al., 2000; Giglio et al., 2009; Pu et al., 2007), or (ii) applying the two-phase strategy method which in a first instance identifies the strong burned spectral response and in a second phase delineates the rest of the burned area by applying contextual classifiers (Alonso-Canas and Chuvieco, 2015; Bastarrika et al., 2011; Oliva et al., 2011).

Due to the diverse climatic conditions, Chile has a vast diversity of ecosystems expanding from North to South, which produces an important variety of spectra representing burned areas and

---

* Corresponding author

many other land cover classes. This creates particular conditions for burned area algorithm generalization, making the process very challenging. Due to the complexity in the spectral responses of burned area we selected the Random forest method (Breiman, 2001) to develop an automatic burned area classification algorithm. We use random forest because of its ability to integrate data from different sources, being insensitive to outliers and non-normal distributions, and its efficient computing performance. Random forest has also been used in different areas of forest fire research, particularly for fire regimes characterization (Archibald et al., 2009), fire occurrence prediction (Oliveira et al., 2012), and burned area discrimination (Ramo and Chuvieco, 2017).

In this study we analyse the application of the random forest method for burned area discrimination in Chile. The classification model is applied to the whole Chilean territory. Therefore, we aim to accurately map the area affected by both forest and agricultural fires. We explore the optimization of the classifier calibration and analyse the effects of increasing the variability included in the training sample to obtain the most accurate results.

2. METHODOLOGY

2.1 Study area

Chile is a South American country located in the south-west of the continent, between the Andes and the Pacific Ocean. It is 350 km wide from west to east in its widest point, but more than 4000 km long from north to south. Due to its length, several biomes can be found in this country, from deserts in the north, to Mediterranean and temperate forests in the center and subpolar forests in the south (Olson et al., 2001). Fires are most common in Central Chile, between latitudes 30°S and 40°S since the Atacama Desert in the north does not contain enough vegetation to be affected by fires, and the forests in the south are too cold and moist to burn. In this study, only areas burned from January to March 2017 were detected and analysed.

2.2 Sentinel-2 MSI data

In June 2015, the first of the Sentinel-2 mission satellites was launch. The Sentinel-2A satellite provides data at 10, 20 and 60 m of spatial resolution. This satellite provided a temporal resolution of 10 days, which was reduced to 5 days after the launching of Sentinel-2B satellite on March 2017 established at an complimentary orbit. However, since the period from January to March 2017 was analysed in this study, Sentinel-2B images were not available for most fires yet.

Input data for this BA detection was the Level-1C product, which includes Top-Of-Atmosphere (TOA) reflectances. The Level-2A product with Bottom-Of-Atmosphere (BOA) reflectances is preferable, but in the moment of processing the data for this study L2A products were not uploaded to GEE. The L1C product contains 13 bands ranging from the visible region of the spectrum to the red edge, Near Infrared (NIR) and Short-Wavelength Infrared (SWIR) (Drusch et al., 2012). In this study we work at 20 m spatial resolution.

2.3 Google Earth Engine

Google Earth Engine (GEE, https://earthengine.google.com/) is a cloud-computing platform to process satellite data, developed by Google. The platform includes access to a large database of various satellite imagery datasets and a powerful ability of data processing, which makes it suitable for processing large amounts of data (otherwise too heavy to process) or for

implementing and publishing various applications to the public. To operate efficiently with GEE the only requirement is a good internet connexion. The GEE API is available with the JavaScript programming language, a code editor where algorithms are developed and a map to visualize results.

2.4 Temporal composites

Burned areas were detected analysing the spectral differences observe on land covers after the fire, so two dates were required: pre-fire and post-fire dates. Only areas burned in the post-fire date that were unburned in the pre-fire date were detected as burned. We decided to compute temporal composites to avoid the low data availability found in South Chile due to the frequent cloud coverage. Therefore, the pre- and post-fire dates are not images acquired on a single date, but temporal combination of images acquired over several months.

The post-fire composite was generated by minimizing the Normalized Burn Ratio spectral index (NBR) (Key and Benson, 1999) over the images acquired from January 1st to March 31st 2017, covering most of the fire season. This minimization selects burned pixels while dismissing most clouds, cloud shadows and snow. The same minimization was applied over the pre-fire period, corresponding to October-December 2016.

2.5 Development of the generalized Random Forest model

2.5.1 Workflow: The BA detection in this study was carried out in three steps: 1) selecting sample dataset from different study areas, 2) training a Generalized Random Forest (GRF) model with these data, and 3) applying the GRF to classify BA for all the Chilean territory. After generating a BA product, we inspected it visually. Based on the classification errors observed, new training sites were to improve the resulting BA product. Three iterations were needed to optimize the final product, thus generating three different versions, each more accurate than the previous.

2.5.2 Training data: In each training site, burned and unburned polygons were defined manually to train a Random Forest model specific of each training site. A two-phase strategy was then applied over the burn probability image obtained for each study area. First identifying seeds with a strong burned signal (using as threshold the minimum among the mean burn probabilities from all training polygons) and then extending the burned areas by applying a less strict threshold (50% burn probability). This way, we produced reference perimeters for every training site. From the classification of the training sites, we randomly selected the training dataset (burned and unburned samples) used to obtain the GRF.

Ten study areas were used for the first version (v1), located between latitudes 33°S and 37°S where most of the 2017 fires occurred. We sampled 1000 random points from each category (burned and unburned) and study area, with a total of 20,000 training points for introduced in the GRF-v1 model.

In the second version (v2), we added four new training sites. Two around latitudes 38 and 39°S, where agricultural fires are most common and where overestimation of BA was observed. Another around latitude 47°S to include sample points representing the subpolar biome in the south. The last one located between latitudes 31-32°S represented the desert from northern Chile where we observed commission errors. More than 27,000 points were used to train the GRF-v2 model.
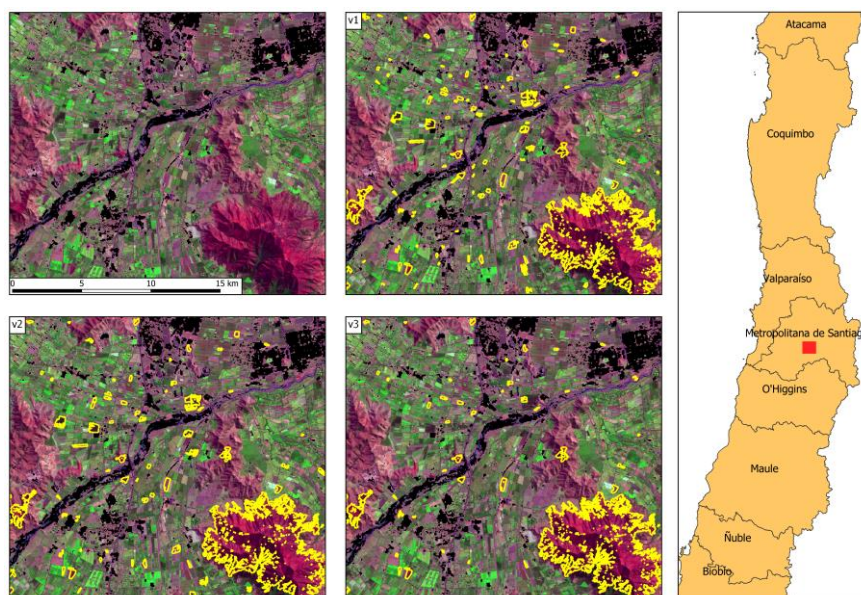
Figure 1. Comparison of different versions of the BA product (yellow line) in a sample area located in the Santiago Metropolitan Region. The background image is the postfire image composite resulting from the combination of the available images from January 1st to March 31st.

In the third and final version (v3), eight additional training sites were used. We distributed them throughout Chile (latitudes 30 and 50°S). The training sites were located where we observed a higher presence of errors. Therefore, some of them did not contain any burned area, in which case only training points for the unburned class were sampled. With a total of 22 study areas, the GRF model was trained with almost 40,000 sample points.

2.5.3 The generalized Random Forest model: The Random Forest model (RF) (Breiman, 2001) for each version was created considering 100 decision trees and a minimum of 10 leaves in every branch or node. The model was then trained with the corresponding sampled points and a total of 27 variables:

- 9 original post-fire bands from product L1C: Blue (B2), Green (B3), Red (B4), red edge (B5, B6, B7), NIR (B8A), and Short and Long SWIR (B11, B12).
- 4 post-fire spectral indices: Normalized Difference Vegetation Index (NDVI) (Rouse et al., 1974), Normalized Burn Ratio (NBR) (Key and Benson, 1999), Normalized Burn Ratio 2 (NBR2) (García and Caselles, 1991), and Mid-Infrared Burned Index (MIRBI) (Trigg and Flasse, 2001).
- 13 variables representing the temporal difference between pre- to post-fire composites of the bands and indexes exposed above.
- Relative difference NBR (RdNBR) (Miller and Thode, 2007).

Finally, the GRF classifier was applied on pre- and post-fire composites, resulting in a probability image with values from 0 % (unburned) to 100 % (burned). To obtain the last BA map, a two-phase strategy was used on this image, resulting in a binary layer of burned and unburned areas; a 100% threshold was used for identifying seeds, and 50% to extend burned areas around seeds.

2.6 Validation strategy

All three versions of the BA product were visually inspected after their generation, comparing them with pre-fire and post-fire temporal composites. These composites were first assigned

a SWIR-NIR-Red colour composition, as shown in Figure 1. BA products were also compared with perimeters conceded by the National Forest Corporation (CONAF). By this comparison, we evaluated the goodness of the classification, identified the errors and decided whether more study areas should be included, and where.

3. RESULTS AND DISCUSSION

3.1 Version comparison

The classification errors observed throughout Chile were mainly due to cloud or relief shadow, and harvested croplands classified as burned. Figure 1 and 2 compare all three BA versions produced for two training sites. Burned areas are detected with very similar shapes in all of them, but small BA corresponding to croplands misclassified as BA are filtered out in later versions. Only the largest agricultural fields remain in GRF-v3, which have a higher burn probability.

In Figure 2, most BA correspond to agricultural fires, but there are many pixel groups belonging to cloud shadows. These shadows are detected as burned in GRF-v1 but are mostly removed in GRF-v3 due to the inclusion of new training sites with this kind of noise. After visual validation of GRF-v3, we decided that the result was the most accurate product that we could produce.

3.2 Separability analysis

After a Random Forest model has been trained, it is possible to know the importance that each variable had when creating the decision trees. In , the three most important variables are shown, along with their cumulative importance, for every version of the BA product. According to this Table, the RdNBR is always the most important or second most important variable in these RF models, followed by the temporal differences of NBR and NBR2. Differences of the MIRBI index and post-fire values of the B7 band appear only once.

According to the cumulative importance, the three most important variables are sufficient to approach 50 % of importance in the decision trees. Nevertheless, the cumulative importance of these variables decreases slightly in later
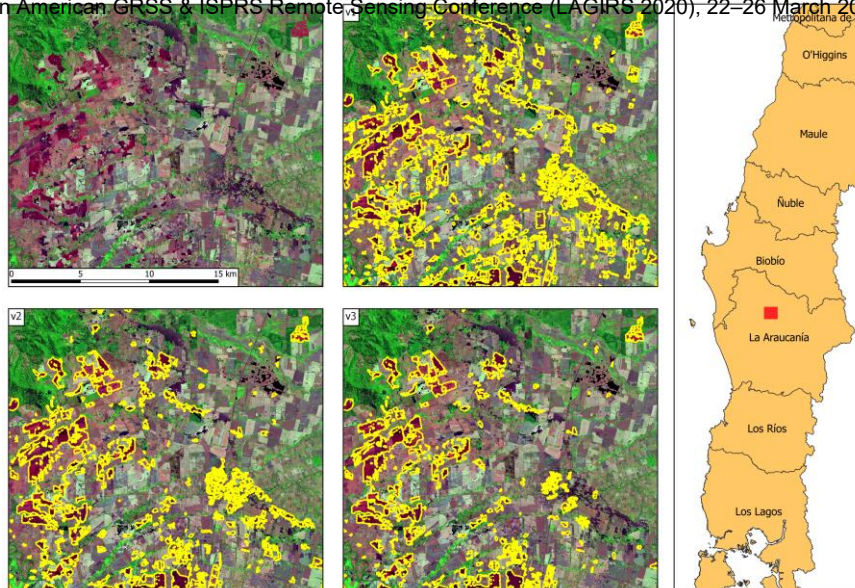
Figure 2. Comparison of different versions of the BA product in a sample area located in the Araucanía Region.

versions, since more study areas were included and sample points became more heterogeneous, indicating that more variables were needed to decide whether a pixel was burned or unburned.

Table 1. The most important variables of the RF model and their cumulative importance in all three versions.

BA Product version	1st position	2nd position	3rd position	Cumulative importance
GRF-v1	RdNBR	dNBR	dNBR2	46.6 %
GRF-v2	dNBR	RdNBR	B7	43.7 %
GRF-v3	RdNBR	dNBR2	dMIRBI	41.5 %

3.3 Comparison with reference data

The BA product was compared with the official BA perimeters produced by CONAF. A quick view to both perimeters in Figure 3 was enough to see that the BA detected in this study were more accurate than those by CONAF, since the later did not account for the unburned islands inside the BA perimeter. The mismatch between BA perimeters due to inclusion of unburned island has also been reported in previous studies (Ramo and Chuvieco, 2017).

While our BA product works at 20 m, CONAF perimeters seem to have a lower spatial resolution, since the border of the polygons are smoother.

We also observed that some pixels without a strong burned signal were classified as unburned by the GRF-v3 BA product. It is difficult to decide which BA delineation is correct in this case based only on the colour composition from Figure 3.

Vegetation under the canopy might be burned, which is difficult to distinguish from satellite imagery if the upper canopy remains unburned and green.

Overall, the CONAF perimeters seem to generally overestimate burned areas when compared to the GRF-v3 BA product. There are also some small BA that are not identified by CONAF.

3.4 Product assessment

According to GRF-v3 BA product, around 5,460 km^2 were burned in Chile in January, February and March 2017, a considerable increase compared to the average annual 1,000 km^2. From this total surface, 20 % corresponds with burned areas larger than 1,000 km^2 (Figure 4). In fact, this corresponds to a single burned area located in the Maule Region. 47 % of the burned surface was divided in BA between 10 and 1000 km^2, and 67 % of the total burned surface (3,660 km^2) was represented in burned patches larger than 10 km^2. Only 33 % of the burned surface (1,800 km^2) corresponds to BA smaller than 10 km^2.

When analysing the burned surfaces by region, we found that most of the BA is in Central Chile (Figure 5), as expected. The Maule Region contains 2240 km^2 of burned surface, 41 % of the total. Following by O'Higgins (735 km^2, 13.4 %), Biobío (640 km^2, 11.7 %), Araucanía (550 km^2, 10 %), Ñuble (470 km^2, 8.6 %) and Santiago Metropolitan Region (320 km^2, 5.9 %). All these 6 regions amount to 91 % of the total burned surface in Chile. In the four northern regions we accounted only 2 km^2 of burned surface. Even though there are some small BA areas in these regions, most of the detected BA are commission errors due to relief shadows.
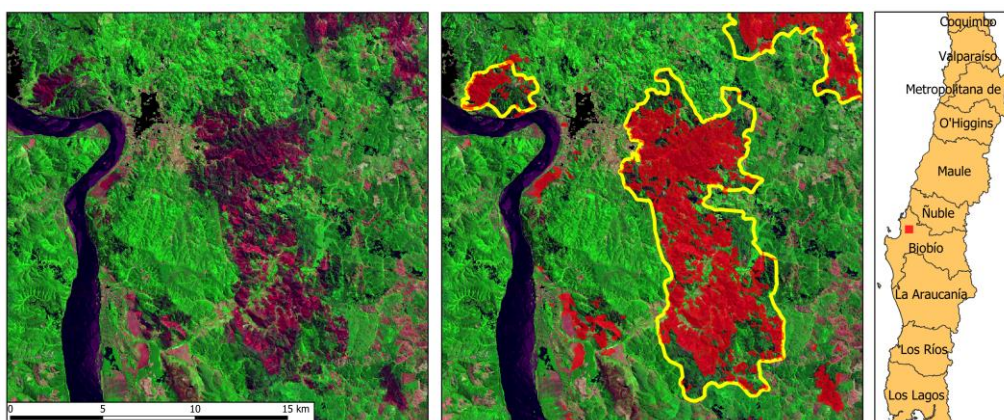

Figure 3. Comparison between BA product (red) and CONAF perimeters (yellow) in a sample area located in the Biobío Region.
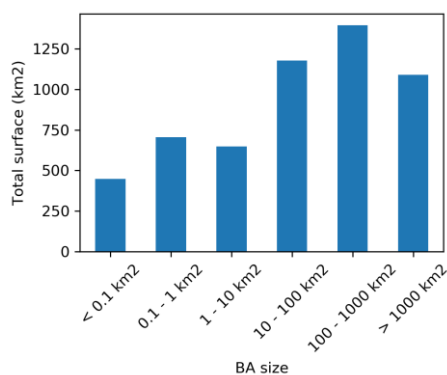
Figure 4. Distribution of burned surface by BA sizes.

4. CONCLUSIONS

This study presents the optimized calibration of a generalized random forest model which could be applied to classify burned area in Chile automatically. We showed the importance of the training sample in the classification result and the need to include a diverse set of land covers and burned area conditions to unsure the accuracy of the fil product, supporting previous studies (Colditz, 2015). We produced a BA classification which improved current BA perimeters offered by CONAF, since our product considers unburned patches inside burned areas, detects more small BA areas and includes agricultural fires. In addition, it is implemented in GEE ensuring the operational efficiency of the methodology.
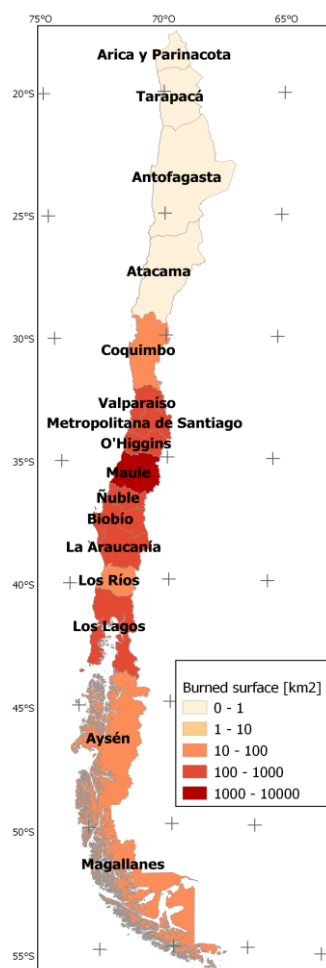

Figure 5. Total burned surface by region.

REFERENCES

Alonso-Canas, I., Chuvieco, E., 2015. Global burned area mapping from ENVISAT-MERIS and MODIS active fire data. *Remote Sens. Environ.* 163, 140–152. https://doi.org/10.1016/j.rse.2015.03.011

Archibald, S., Roy, D.P., WILGEN, V., Brian, W., SCHOLES, R.J., 2009. What limits fire? An examination of drivers of burnt area in Southern Africa. *Glob. Chang. Biol.* 15, 613–630.

Ba, R., Song, W.G., Li, X.L., Xie, Z.X., Lo, S.M., 2019. Integration of Multiple Spectral Indices and a Neural Network for Burned Area Mapping Based on MODIS Data. *Remote Sens.* 11. https://doi.org/32610.3390/rs11030326

Bastarrika, A., Chuvieco, E., Martín, M.P., 2011. Mapping burned areas from Landsat TM/ETM+ data with a two-phase algorithm: Balancing omission and commission errors. *Remote Sens. Environ.* 115, 1003–1012. https://doi.org/10.1016/j.rse.2010.12.005

Beverly, J.L., Flannigan, M.D., Stocks, B.J., Bothwell, P., 2011. The association between Northern Hemisphere climate patterns and interannual variability in Canadian wildfire activity. *Can. J. For. Res*. 41, 2193–2201.

Breiman, L., 2001. Random forests. *Mach. Learn.* 45, 5–32. https://doi.org/10.1023/A:1010933404324

Cabral, A.I.R., Silva, S., Silva, P.C., Vanneschi, L., Vasconcelos, M.J., 2018. Burned area estimations derived from Landsat ETM plus and OLI data: Comparing Genetic Programming with Maximum Likelihood and Classification and Regression Trees. *Isprs J. Photogramm. Remote Sens.* 142, 94–105. https://doi.org/10.1016/j.isprsjprs.2018.05.007

Canadell, J.G., Ciais, P., Dhakal, S., Dolman, H., Friedlingstein, P., Gurney, K.R., Held, A., Jackson, R.B., Le Quere, C., Malone, E.L., 2010. Interactions of the carbon cycle, human activity, and the climate system: a research portfolio. *Curr. Opin. Environ. Sustain.* 2, 301–311.

Chuvieco, E., Mouillot, F., van der Werf, G.R., San Miguel, J., Tanase, M., Koutsias, N., Garcia, M., Yebra, M., Padilla, M., Gitas, I., Heil, A., Hawbaker, T.J., Giglio, L., 2019. Historical background and current developments for mapping burned area from satellite Earth observation. *Remote Sens. Environ*. 225, 45–64. https://doi.org/10.1016/j.rse.2019.02.013

Colditz, R.R., 2015. An Evaluation of Different Training Sample Allocation Schemes for Discrete and Continuous Land Cover Classification Using Decision Tree-Based Algorithms 9655–9681. https://doi.org/10.3390/rs70809655

Dragozi, E., Gitas, I.Z., Stavrakoudis, D.G., Theocharis, J.B., 2014. Burned area mapping using support vector machines and the FuzCoC feature selection method on VHR IKONOS imagery. *Remote Sens.* 6, 12005–12036.

Drusch, M., Del Bello, U., Carlier, S., Colin, O., Fernandez, V., Gascon, F., Hoersch, B., Isola, C., Laberinti, P., Martimort, P., Meygret, A., Spoto, F., Sy, O., Marchese, F., Bargellini, P., 2012. Sentinel-2: ESA's Optical High-Resolution Mission for GMES Operational Services. *Remote Sens. Environ.* 120, 25–36. https://doi.org/10.1016/j.rse.2011.11.026

Fraser, R.H., Li, Z., Cihlar, J., 2000. Hotspot and NDVI differencing synergy (HANDS): A new technique for

burned area mapping over boreal forest. *Remote Sens. Environ*. 74, 362–376. https://doi.org/10.1016/S0034-4257(00)00078-X

García, M.J.L., Caselles, V., 1991. Mapping burns and natural reforestation using thematic Mapper data. *Geocarto Int*. 6, 31–37. https://doi.org/10.1080/10106049109354290

Giglio, L., Loboda, T., Roy, D.P., Quayle, B., Justice, C.O., 2009. An active-fire based burned area mapping algorithm for the MODIS sensor. *Remote Sens. Environ*. 113, 408–420. https://doi.org/10.1016/j.rse.2008.10.006

Hawbaker, T.J., Vanderhoof, M.K., Beal, Y.-J., Takacs, J.D., Schmidt, G.L., Falgout, J.T., Williams, B., Fairaux, N.M., Caldwell, M.K., Picotte, J.J., Howard, S.M., Stitt, S., Dwyer, J.L., 2017. Mapping burned areas using dense time-series of Landsat data. *Remote Sens. Environ*. 198, 504–522. https://doi.org/10.1016/j.rse.2017.06.027

Key, C.H., Benson, N., 1999. The Normalized Burn Ratio (NBR): a Landsat TM radiometric measure of burn severity. *US Geol. Surv. North. Rocky Mt. Sci. Center*.

Koutsias, N., Karteris, M., 2000. Burned area mapping using logistic regression modeling of a single post-fire Landsat-5 Thematic Mapper image. *Int. J. Remote Sens*. 21, 673–687. https://doi.org/10.1080/014311600210506

Miller, J.D., Thode, A.E., 2007. Quantifying burn severity in a heterogeneous landscape with a relative version of the delta Normalized Burn Ratio (dNBR). *Remote Sens. Environ*. 109, 66–80. https://doi.org/10.1016/j.rse.2006.12.006

Mouillot, F., Schultz, M.G., Yue, C., Cadule, P., Tansey, K., Ciais, P., Chuvieco, E., 2014. Ten years of global burned area products from spaceborne remote sensing-A review: Analysis of user needs and recommendations for future developments. *Int. J. Appl. Earth Obs. Geoinf*. 26, 64–79. https://doi.org/10.1016/j.jag.2013.05.014

O'Donnell, M.J., Fang, J., Mittleman, M.A., Kapral, M.K., Wellenius, G.A., 2011. Fine particulate air pollution (PM2.5) and the risk of acute ischemic stroke. *Epidemiology* 22, 422–431. https://doi.org/10.1097/EDE.0b013e3182126580

Oliva, P., Martín, P., Chuvieco, E., 2011. Burned area mapping with MERIS post-fire image. *Int. J. Remote Sens*. 32. https://doi.org/10.1080/01431161.2010.489062

Oliveira, S., Oehler, F., San-Miguel-Ayanz, J., Camia, A., Pereira, J.M.C., 2012. Modeling spatial patterns of fire occurrence in Mediterranean Europe using Multiple *Regression and Random Forest. For. Ecol. Manage*. 275, 117–129.

Olson, D.M., Dinerstein, E., Wikramanayake, E.D., Burgess, N.D., Powell, G.V.N., Underwood, E.C., D'amico, J.A., Itoua, I., Strand, H.E., Morrison, J.C., Loucks, C.J., Allnutt, T.F., Ricketts, T.H., Kura, Y., Lamoreux, J.F., Wettengel, W.W., Hedao, P., Kassem, K.R., 2001. Terrestrial Ecoregions of the World: A New Map of Life on Earth. *Bioscience* 51, 933. https://doi.org/10.1641/0006-3568(2001)051[0933:TEOTWA]2.0.CO;2

Pu, R., Li, Z., Gong, P., Csiszar, I., Fraser, R., Hao, W.-M., Kondragunta, S., Weng, F., 2007. Development and analysis of a 12-year daily 1-km forest fire dataset across North America from NOAA/AVHRR data. *Remote Sens.* Environ. 108, 198–208.

Ramo, R., Chuvieco, E., 2017. Developing a Random Forest algorithm for MODIS global burned area classification. *Remote Sens.* 9. https://doi.org/10.3390/rs9111193

Rogers, B.M., Neilson, R.P., Drapek, R., Lenihan, J.M., Wells, J.R., Bachelet, D., Law, B.E., 2011. Impacts of climate change on fire regimes and carbon stocks of the US Pacific Northwest. *J. Geophys. Res. Biogeosciences* 116.

Roteta, E., Bastarrika, A., Padilla, M., Storm, T., Chuvieco, E., 2019. Development of a Sentinel-2 burned area algorithm: Generation of a small fire database for sub-Saharan Africa. *Remote Sens. Environ.* 222, 1–17. https://doi.org/10.1016/j.rse.2018.12.011

Rouse, J.W., Haas, R.H., Schell, J.A., 1974. Monitoring the vernal advancement and retrogradation (greenwave effect) of natural vegetation. *NASA Goddard Sp. Flight Cent.* https://doi.org/19740008955

Roy, D.P., Jin, Y., Lewis, P.E., Justice, C.O., 2005. Prototyping a global algorithm for systematic fire-affected area mapping using MODIS time series data. *Remote Sens. Environ.* 97, 137–162. https://doi.org/10.1016/j.rse.2005.04.007

Shimabukuro, Y.E., Miettinen, J., Beuchle, R., Grecchi, R.C., Simonetti, D., Achard, F., 2015. Estimating Burned Area in Mato Grosso, Brazil, Using an Object-Based Classification Method on a Systematic Sample of Medium Resolution Satellite Images. *Ieee J. Sel. Top. Appl. Earth Obs. Remote Sens.* 8, 4502–4508. https://doi.org/10.1109/jstars.2015.2464097

Silva, J.M.N., Sá, A.C.L., Pereira, J.M.C., 2005. Comparison of burned area estimates derived from SPOT-VEGETATION and Landsat ETM+ data in Africa: Influence of spatial pattern and vegetation type. *Remote Sens. Environ.* 96, 188–201.

Tansey, K., Grégoire, J., Defourny, P., Leigh, R., Pekel, J., Van Bogaert, E., Bartholomé, E., 2008. A new, global, multi-annual (2000–2007) burnt area product at 1 km resolution. *Geophys. Res. Lett.* 35.

Thelen, B., French, N.H., Koziol, B.W., Billmire, M., Owen, R.C., Johnson, J., Ginsberg, M., Loboda, T., Wu, S., 2013. Modeling acute respiratory illness during the 2007 San Diego wildland fires using a coupled emissions-transport system and generalized additive modeling. *Environ. Heal. A Glob. Access Sci. Source* 12. https://doi.org/10.1186/1476-069X-12-94

Trigg, S., Flasse, S., 2001. An evaluation of different bi-spectral spaces for discriminating burned shrub-savannah. Int. J. *Remote Sens.* 22, 2641–2647. https://doi.org/10.1080/01431160110053185

Van Der Werf, G.R., Randerson, J.T., Giglio, L., Van Leeuwen, T.T., Chen, Y., Rogers, B.M., Mu, M., Van Marle, M.J.E., Morton, D.C., Collatz, G.J., Yokelson, R.J., Kasibhatla, P.S., 2017. Global fire emissions estimates during 1997-2016. *Earth Syst. Sci. Data.* https://doi.org/10.5194/essd-9-697-2017

Wu, Z., Middleton, B., Hetzler, R., Vogel, J., Dye, D., 2015. Vegetation burn severity mapping using Landsat-8 and WorldView-2. *Photogramm. Eng. Remote Sens.* 81, 143–154.

Zhang, Y.H., Wooster, M.J., Tutubalina, O., Perry, G.L.W., 2003. Monthly burned area and forest fire carbon emission estimates for the Russian Federation from SPOT VGT. *Remote Sens. Environ.* 87, 1–15. https://doi.org/10.1016/S0034-4257(03)00141-X

.

IV eranskina: A4 – EAen algoritmoa mundu-mailan

Artikulua

Izenburua: A Preliminary Global Automatic Burned-Area Algorithm at Medium Resolution in Google Earth Engine

Egileak: Ekhi Roteta, Aitor Bastarrika, Askoa Ibisate eta Emilio Chuvieco

Argitaratze-data: 2021eko urria

DOI: https://doi.org/10.3390/rs13214298

Erreferentzia bibliografikoa:

Roteta, E., Bastarrika, A., Ibisate, A., Chuvieco, E., 2021. A Preliminary Global Automatic Burned-Area Algorithm at Medium Resolution in Google Earth Engine. *Remote Sens.* 13, 4298. https://doi.org/10.3390/rs13214298

Aldizkaria

Izena: Remote Sensing

Sortze-urtea: 2009

Argitaratze-urteko inpaktu-faktorea: 5,349

Argitaratze-urteko posizioa *REMOTE SENSING* **arloan**:

      Postua: 11/34

      Pertzentila: %69

      Kuartila: Q2

A Preliminary Global Automatic Burned-Area Algorithm at Medium Resolution in Google Earth Engine

Ekhi Roteta [1,2,*], Aitor Bastarrika [2], Askoa Ibisate [1] and Emilio Chuvieco [3]

1   Department of Geography, Prehistory and Archaeology, University of the Basque Country UPV/EHU, Tomás y Valiente s/n, 01006 Vitoria-Gasteiz, Spain; askoa.ibisate@ehu.eus
2   Department of Mining and Metallurgical Engineering and Materials Science, School of Engineering of Vitoria-Gasteiz, University of the Basque Country UPV/EHU, Nieves Cano 12, 01006 Vitoria-Gasteiz, Spain; aitor.bastarrika@ehu.eus
3   Environmental Remote Sensing Research Group, Department of Geology, Geography and the Environment, University of Alcalá UAH, C/Colegios 2, 28801 Alcalá de Henares, Spain; emilio.chuvieco@uah.es
*   Correspondence: ekhi.roteta@ehu.eus

Abstract: A preliminary version of a global automatic burned-area (BA) algorithm at medium spatial resolution was developed in Google Earth Engine (GEE), based on Landsat or Sentinel-2 reflectance images. The algorithm involves two main steps: initial burned candidates are identified by analyzing spectral changes around MODIS hotspots, and those candidates are then used to estimate the burn probability for each scene. The burning dates are identified by analyzing the temporal evolution of burn probabilities. The algorithm was processed, and its quality assessed globally using reference data from 2019 derived from Sentinel-2 data at 10 m, which involved 369 pairs of consecutive images in total located in 50 20×20 km^2 areas selected by stratified random sampling. Commissions were around 10% with both satellites, although omissions ranged between 27 (Sentinel-2) and 35% (Landsat), depending on the selected resolution and dataset, with highest omissions being in croplands and forests; for their part, BA from Sentinel-2 data at 20 m were the most accurate and fastest to process. In addition, three 5×5 degree regions were randomly selected from the biomes where most fires occur, and BA were detected from Sentinel-2 images at 20 m. Comparison with global products at coarse resolution FireCCI51 and MCD64A1 would seem to show to a reliable extent that the algorithm is procuring spatially and temporally coherent results, improving detection of smaller fires as a consequence of higher-spatial-resolution data. The proposed automatic algorithm has shown the potential to map BA globally using medium-spatial-resolution data (Sentinel-2 and Landsat) from 2000 onwards, when MODIS satellites were launched.

Keywords: burned-area mapping; Landsat; Sentinel-2; active fires; global; Google Earth Engine

1. Introduction

Fire disturbance is one of the Essential Climate Variables (ECV) defined by the Global Climate Observing System (GCOS) program [1], since it affects land-cover changes, soil erosion, emissions of gases and aerosols into the atmosphere, and people's lives [2–4]. Burned areas (BA) and active fires have been detected by satellite Earth observation, the main purpose of which is to obtain a better understanding of fire regimes to analyze their effect on climate change, since both fires and climate have a mutual effect on the fact that fire can be affected by droughts and high temperatures [5], and climate change is impacted by biomass burning and greenhouse gas emissions into the atmosphere [3], among many other factors.

The first global BA products were released almost two decades ago based on data at coarse spatial resolution (>100 m): GBA2000 and GLOBSCAR, derived from SPOT-Vegetation and ATSR-2 sensors respectively, both at 1 km resolution [6,7]. GLOBSCAR was later modified and released again as Geoland2 [8,9]. NASA released two BA products,

MCD45A1 [10] and MCD64A1 [11], both derived from MODIS data at 500 m. MCD64A1 is now NASA's standard BA product, and its collection 6 is the latest version, released in 2018 [12]. On the other hand, the Fire_cci project, which is part of the Climate Change Initiative program of the European Space Agency (ESA), has released several global BA products at coarse resolution: first FireCCI31 and FireCCI41 based on MERIS at 300 m [13,14], and then FireCCI50 and FireCCI51 from MODIS data at 250 m [15,16]. The FireCCI51 is currently the most accurate among existing global BA products at coarse spatial resolution, according to recent assessments [16].

However, these global products omit many burned areas, especially those smaller than the product's spatial resolution. It was estimated, based on the MCD64A1 product and distribution of thermal anomalies, that around 25% of the actual global burned area corresponds to small fires, and that they are being omitted [17], but later studies comparing the same global product at coarse resolution and regional products based on Sentinel-2 data at 20 m in Africa have shown that up to 55% of the total BA is missed, mainly because of the almost total absence of small fire patches (<100 ha) by MODIS products [18,19]. Accuracy reports of global BA products show the same trends. Most global products have higher omissions than commissions, with the former being around 70% for MCD64A1 and FireCCI51 products [16,20,21]. Small fire patches should thus be detected from higher-spatial-resolution data to reduce these omissions and better estimate the actual burned areas.

Global or continental BA products at medium resolution (<100 m) have not been released until recently. The only up-to-date global BA product at this resolution is the Global Annual Burned-Area Map (GABAM), which was obtained from Landsat-8 OLI data, and initially contained BA from 2015 at 30 m [22]; recently, the whole temporal series from 1985 to 2020 has also been processed and released [23,24]. Unfortunately, this global product indicates whether a pixel has been burned in the corresponding year, but not the burning date. ESA's Fire_cci project released a continental product at medium resolution for one year, obtained from Sentinel-2 MSI imagery at 20 m: FireCCISFD11 [18], containing areas burned in 2016 in Sub-Saharan Africa, where 70% of the global BA are reported to occur [12,17]. Some BA products and algorithms at a national and regional level are the Landsat Burned-Area Essential Climate Variable (BAECV) in the Conterminous United States (CONUS) [25,26], BA detected in the Australian province of Queensland [27] and savannas in southern Burkina Faso [28], all of them using Landsat images as main input data, and also 2017 fires in Italy [29] and the Iberian Peninsula [30] from Sentinel-2 data. There has also been some attempts to merge Landsat and Sentinel-2 datasets in one algorithm [31], MODIS and Landsat data [32], as well as integrating data from optical and SAR sensors [33,34]. However, despite multiple approaches to detect BA automatically at medium spatial resolution, most of them have been adapted and limited to the corresponding region's specific spectral characteristics, with the algorithm developed for GABAM being the only one applied at a global scale.

Processing BA at medium spatial resolution requires enormous capacities for data storage and processing, which proves challenging when working at a global scale. This has been made possible by Google Earth Engine (GEE), a free cloud-computing platform with several satellite data catalogs at different spatial resolutions (mainly MODIS, Landsat and Sentinel-2) and global-scale analysis capabilities [35]. Even though the first significant work on the topic was published almost a decade ago [36] and a significant number of studies has used GEE since then [37], there are still few published works on the field of burned areas [38–42], especially at a global scale [22].

In this study, we present a preliminary locally adapted automatic BA algorithm designed for global application at medium spatial resolution implemented in the GEE environment, based on Landsat or Sentinel-2 reflectance images and MODIS active fires. An initial quality assurance was carried out on 50 sites covering several biomes and land covers. Existing global BA products obtained from coarse-resolution data (MCD64A1 and FireCCI51) were also assessed in the same dataset and the impact of employing medium

spatial resolutions data was evaluated. In addition, three large sites (5 × 5 degrees) were also processed and compared with existing global BA products to assess detection confidence both temporally and spatially.

2. Methodology

2.1. Input Data

The BA algorithm proposed in this manuscript focuses on Landsat and Sentinel-2 as imagery source. The Landsat program was developed by NASA and USGS for satellite image acquisition and Earth observation [43]. A total of 7 satellites in total have been launched successfully over several years, of which two are currently operational. Short wavelength infrared (SWIR) bands, required by our algorithm, are only acquired by three sensors: Thematic Mapper (TM) aboard Landsat-4 and Landsat-5 satellites, Enhanced Thematic Mapper Plus (ETM+) on Landsat-7, and Operational Land Imager (OLI) on Landsat-8. Data from the Landsat-4 satellite cannot be used by the algorithm explained in this study, since the TM sensor aboard ceased to transmit data in 1993, which only leaves three Landsat satellites. Each satellite has a revisit period of 16 days, which is reduced to 8 days if images from different satellites are combined; there is, however, a short period with a revisit period of 16 days, between the last images from May 2012 of the TM on Landsat-5 and Landsat-8's first data from April 2013. Landsat images are delivered in scenes about 185 km wide and 170 km high, in accordance with the Worldwide Reference System (WRS) [44,45], and all bands required by the algorithm are acquired at 30 m of spatial resolution. This study uses the Landsat Surface Reflectance (LSR) Tier 1 product, with Bottom-of-Atmosphere (BOA) reflectance [46,47]; the IDs of the datasets in GEE are 'LANDSAT/LT05/C01/T1_SR' (Landsat-5 TM), 'LANDSAT/LE07/C01/T1_SR' (Landsat-7 ETM+) and 'LANDSAT/LC08/C01/T1_SR' (Landsat-8 OLI).

Similar to the Landsat program, the European Space Agency (ESA) has developed the Sentinel-2 mission (S2) for Earth observation, which is part of the Copernicus program [48]. It consists of a constellation with two satellites—Sentinel-2A and Sentinel-2B—each with a revisit period of 10 days, or 5 days by combining both satellites; the first satellite was launched in June 2015, and the second in March 2017. Each scene covers 110 × 110 km^2, in accordance with the Military Grid Reference System (MGRS) [49]. Bands acquired by the MultiSpectral Instrument (MSI) have different spatial resolutions ranging from 10 to 20 and 60 m; the main bands of the algorithm (NIR and two SWIRs) are at 20 m, although there is also a second NIR band at 10 m. Both Level-1C (L1C) and Level-2A (L2A) products are available in GEE; L1C contains Top-of-Atmosphere reflectance, while L2A has Bottom-of-Atmosphere reflectance after the atmospheric correction is applied. A Scene Classification (SCL) is also generated in the L2A product, which labels the presence of clouds, cloud shadows, water and snow on the scene [50]. Unfortunately, the L2A product is not consistently processed for the complete S2 temporal series, and while all L1C scenes from 2019 up to the present have been processed to obtain L2A scenes, there are only a few L2A scenes available for 2017 and 2018, and none at all for 2015 and 2016 (Figure 1). Therefore, the algorithm uses either L1C or L2A scenes depending on L2A availability. Their IDs in GEE are 'COPERNICUS/S2' and 'COPERNICUS/S2_SR', respectively.

Three bands are required for BA detection in total, namely the Near Infrared (NIR) and two Short Wavelength Infrared (SWIR) bands, all of which are commonly used for BA detection [6,7,12,16,18,22,51]. Another band on the visible blue color and the quality band are used to mask clouds, and the visible red color band to reduce confusions with croplands. The exact width and location of these bands in the spectrum may vary slightly depending on the sensor, but they cover a similar spectral region (Table 1). For S2 data, the B8A and B8 bands have 20 and 10 m of spatial resolution, respectively, and are selected depending on the resolution at which BA are detected. Similarly, selection of the quality band depends on the product employed; for L2A scenes the SCL is used, and QA60 for L1C.
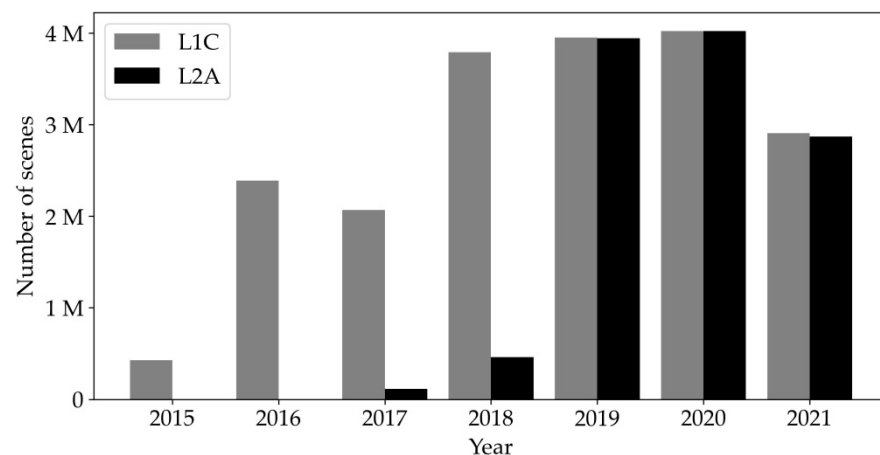
Figure 1. Number of L1C and L2A scenes available globally in GEE, for every year, as of September 2021.

Table 1. Bands and approximate wavelengths used by the algorithm.

Band	Landsat-5 TM	Landsat-7 ETM+	Landsat-8 OLI	Sentinel-2A&B MSI	Approximate Wavelength (µm)
Blue	B1	B1	B2	B2	0.45–0.52
Red	B3	B3	B4	B4	0.64–0.68
NIR	B4	B4	B5	B8A (20m)/B8 (10m)	0.80–0.89
Short SWIR	B5	B5	B6	B11	1.55–1.70
Long SWIR	B7	B7	B7	B12	2.10–2.30
Quality band	pixel_qa	pixel_qa	pixel_qa	QA60 (L1C)/SCL (L2A)	-

The BA algorithm relies on hotspots, for which there is only one product in GEE: MCD14DL, consisting of MODIS Collection 6 Near-Real-Time active fires, at 1000 m of spatial resolution [52]. The product is already rasterized by defining a 1-km-wide bounding box around the hotspot, and a confidence level from 0 to 100% is provided. The dataset is presented as a daily product, and so the detection date is known for each hotspot, but not the exact burning time. The dataset's ID in GEE is 'FIRMS'.

Finally, two additional products are used to identify different land covers (LC). On the one hand, the International Geosphere-Biosphere Program (IGBP) classification in the MCD12Q1 product [53], derived from MODIS data at 500 m, was used to reduce confusions at croplands and urban areas. The Copernicus Land-Cover map [54] developed at a higher spatial resolution (100 m) is also available in GEE but only for the period between 2015 and 2019, and MODIS LC map was preferred due to its longer covered period (from 2001 to 2019). On the other hand, the Global Surface Water (GSW) mask at 30 m obtained from Landsat data [55] is used to mask water bodies. This water mask contains an 'occurrence' band, which indicates the frequency of water presence in each pixel between 1984 and 2019, with values from 0 to 100%. The respective GEE IDs of these two datasets are 'MODIS/006/MCD12Q1' and 'JRC/GSW1_2/GlobalSurfaceWater'.

2.2. Algorithm

The algorithm may be run separately on both S2 and Landsat data. The former have better spatial and temporal resolutions and thus are more accurate for BA detection, although Landsat data cover a much longer period, since the corresponding satellites have been operable since the mid-1970s. However, this algorithm is not operable for data before November 2000, as it relies on MODIS hotspots that are only available from that date onwards. The BA algorithm proposed creates one monthly BA map at a time, and so it should be run 12 times to cover the whole year. The area processed by the algorithm is bounded by a tile of the Military Grid Reference System (MGRS), irrespective of whether BA derive from S2 data (already delivered in the MGRS grid) or from Landsat images (in

the WRS). BA can be detected at 10 or 20 m of spatial resolution with S2 data, or at 30 m with Landsat data.

The flowchart of the BA algorithm is shown in Figure 2. It relies on one reflectance band, the Near Infrared (NIR), and three spectral indices, NBR, NBR2, and MIRBI, covering the most significant spectral areas in BA mapping; the Blue, Red and Long SWIR reflectance bands are also used to remove clouds, croplands, and cloud shadows, respectively. For every month, the spectral changes around hotspots are analyzed to identify burned candidate pixels (BC), from which burned and unburned samples are extracted. Locally adapted probability functions are defined based on those samples, and images from the data series are then classified, with each pixel being assigned a static burned probability value (P_{st}); depending on the temporal evolution of P_{st} for each pixel, a dynamic probability (P_{dy}) is computed. The final BA map is obtained by retaining the pixels with the maximum dynamic probability and segmenting the result to remove noise and reduce commissions. Since the algorithm is implemented in GEE, its design is restricted by the platform's memory and processing limitations.
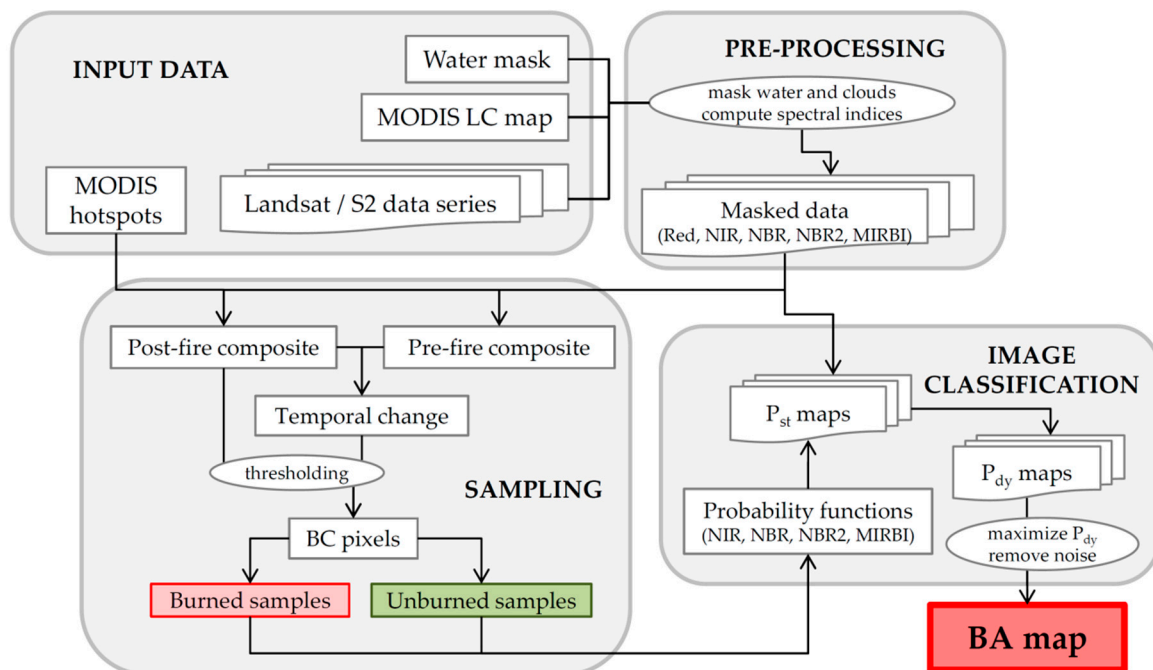
Figure 2. Flowchart of the BA algorithm applied to each monthly BA map.

2.2.1. Pre-Processing

The first step involved with the BA algorithm prepares the data for BA detection, mainly by obtaining the required images, reducing the amount of data, masking clouds, cloud shadows and water bodies, and computing spectral indices.

The algorithm creates a monthly map located in one MGRS tile at a time. For every month (henceforth referred to as 'processing month'), images from 5 consecutive months are selected (called 'processing period'), including two previous ones and a further two subsequent months (Figure 3). S2 data are already delivered in the MGRS grid, and so S2 scenes are simply selected by metadata filtering. However, Landsat data are originally in the WRS, and must be filtered and clipped by the extent of the MGRS tile, and the scenes acquired on the same day are then merged. Processing BA from Landsat data using the native WRS scenes was previously considered, but combining images from adjacent orbit swaths in overlapping areas was not plausible and prevented the full potential of the data catalog from being exploited properly; moreover, at high latitudes, this meant that every region would be processed several times—once per each orbit swath covering the region, which would prolong the process considerably. The selection of L1C or L2A scenes for S2

data depends on L2A availability in GEE, as mentioned previously. When both options are available, L2A scenes are preferred and used by the algorithm, but if the number of available L2A images is less than 90% of the number of L1C scenes in the same area and period, then L1C scenes are used instead.
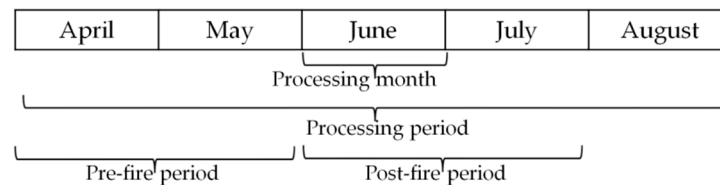
Figure 3. The temporal location of different periods, in relation to the sample processing month in June. All three periods may ultimately be shorter than indicated here, depending on the filters applied in the pre-processing to reduce the data series.

A 5-month-long processing period in a MGRS tile near the Equator may contain 30 S2 scenes, with one image every 5 days (if both S2A and S2B satellites were already operable at the time), or 60 scenes if the tile is in the overlapping area between two orbit swaths. Similarly, an MGRS tile at the Equator may contain Landsat scenes from up to 38 different dates if located between two orbit swaths and with two operable satellites (Landsat-5 and 7 between 2000 and 2012, or Landsat-7 and 8 from 2013 forwards). However, the number of scenes can increase considerably at higher latitudes, where multiple orbit swaths overlapping each other may result in one image every day or around 180 images in the 5-month-long period. Since the implementation of the algorithm in such a large data series exceeds GEE's user memory limit, several filters are applied to reduce the amount of data while maintaining the most meaningful scenes. In each step, if the data series resulting from the previous step contains more than 50 images, the following are removed:

1. Images with a cloud percentage over 90%
2. Images with a cloud percentage over 80%
3. Images with a cloud percentage over 70%
4. Images with a cloud percentage over 60%
5. Images with a cloud percentage over 50%
6. Images from the first and last months of the original 5-month-long period
7. Images from the first half of originally the second month, and from the last half of originally the fourth month

If all filters need to be applied, 1.5 months will have been removed from the beginning and end of the original processing period, and the data series will only be 2 months long.

Once the number of images is reduced, undesired artifacts are then masked. The quality bands are used to mask clouds and cloud shadows, which are indicated in the 3rd and 5th bits in Landsat images, and in the 10th and 11th bits in L1C scenes of S2 images; since the SCL image in S2 L2A scenes have several categories, 7 different values are masked in total (Table 2). Residual clouds and snow not represented in the quality bands are masked in all three datasets by applying an empirical threshold of 0.2 in the visible blue band, where both burned and unburned areas have lower values than clouds and snow. Water bodies are not represented in the S2 L1C quality band, and so a mask obtained from the GSW product is used for both S2 and Landsat data. A conservative threshold is chosen here, masking every pixel with a frequency over 10% in the 'occurrence' band.

Finally, three spectral indices are computed for every image in the series: the Normalized Burn Ratio or NBR [56], the Normalized Burn Ratio 2 or NBR2 [57], and the Mid-Infrared Burned Index or MIRBI [58]. Their formulas are listed below:

$$NBR = (\rho_{NIR} - \rho_{LongSWIR}) / (\rho_{NIR} + \rho_{LongSWIR}), \tag{1}$$

$$NBR2 = (\rho_{ShortSWIR} - \rho_{LongSWIR}) / (\rho_{ShortSWIR} + \rho_{LongSWIR}), \tag{2}$$

$$\text{MIRBI} = 10\,\rho_{\text{LongSWIR}} - 9.8\,\rho_{\text{ShortSWIR}} + 2 \tag{3}$$

where ρ_{NIR}, $\rho_{\text{ShortSWIR}}$ and ρ_{LongSWIR} refer to reflectance in the NIR, Short SWIR, and Long SWIR bands, respectively.

Table 2. Values from the quality bands masked as clouds and cloud shadows, depending on the dataset.

Landsat-5 to 8 pixel_qa	S2 L1C QA60	S2 L2A SCL
3rd bit (cloud shadow) 5th bit (cloud)	10th bit (cloud) 11th bit (cirrus)	1 (saturated or defective) 3 (cloud shadows) 6 (water) 8 (medium prob. clouds) 9 (high prob. clouds) 10 (thin cirrus) 11 (snow)

Henceforth, the algorithm is mainly based on the NIR band and the NBR, NBR2, and MIRBI indices. The importance of these bands and indices in discriminating BA has already been analyzed and observed [18,22,59–61], and they ensure coverage of three different areas of the spectrum commonly used for BA detection (NIR, Short SWIR and Long SWIR) [11,13,16,18,26,27,29,31]. The NIR band selected for S2 data depends on the spatial resolution at which BA are to be detected: B8A at 20 m, and B8 at 10 m.

2.2.2. Sampling

After the algorithm's pre-processing step, burned candidate pixels (BC) between two dates are detected based on spectral changes around hotspots, and samples for burned and unburned categories are extracted from these burned pixels, which correspond to the values observed before and after the burning of the pixel; these samples will later be used to classify images and detect BA. This identification of BC pixels is loosely based on the way burned seed pixels were identified in another study conducted for BA detection in Italy [29].

Before selecting BC pixels, clouds and cloud shadows that may have remained after the pre-processing step are further masked with two conservative thresholds, removing pixels with the following reflectance: Blue > 0.15 OR LongSWIR < 0.05. Pixels belonging to urban areas in the LC map obtained from MODIS data are likewise masked. This further masking is only applied in this sampling step of the algorithm, but not in the classification step described in the next section. Hotspots from the MCD14DL product at 1000 m, obtained from MODIS data, are filtered according to their confidence level, with those with a value lower than 80% being removed.

The possibility of being burned is considered for every pixel in the MGRS tile by comparing the temporal evolution of the NBR spectral index and the location and timing of active fires. For every pixel and by analyzing every pair of consecutive images in the processing month, if the pixel is covered by a hotspot between two consecutive dates, it is considered to have burned between these dates; if hotspots are found between several pairs of images, the one with the largest drop in NBR values is chosen (Figure 4). The dates between which the pixel is considered to have burned are labeled as t_{pre} and t_{post}.

As a result, two acquisition dates with an active fire in between are obtained for every pixel in the MGRS tile (t_{pre} and t_{post}), except for those where no MODIS hotspot was found. Two composite images are formed with values for every pixel from the corresponding pre- and post-fire dates (Figure 5a,b). A third temporal change image is created by a simple subtraction between t_{post} and t_{pre} composites (dt, Figure 5c).
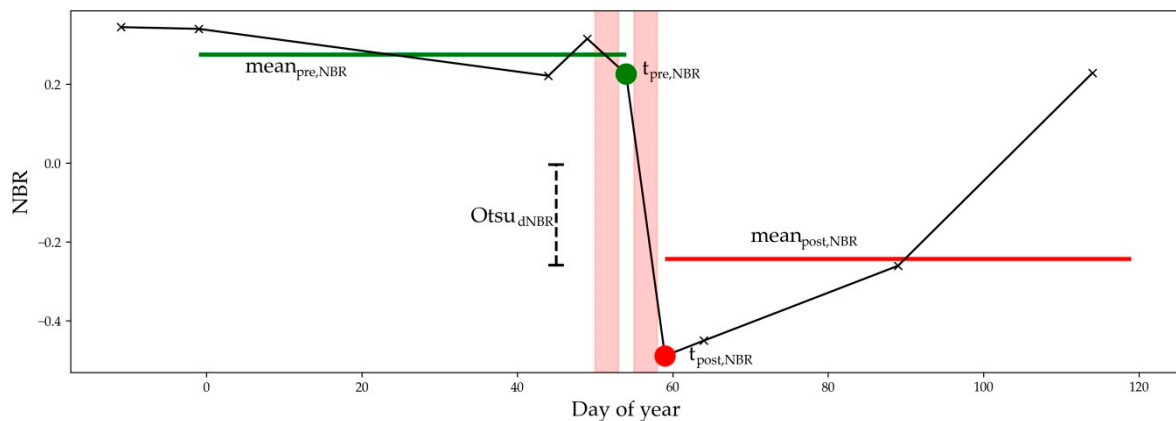
Figure 4. The NBR temporal evolution in a sample pixel at 20 m (S2 data) located in southern France, tile 30TXN, at 43°7′17.5″N 1°19′19.1″W, burned on 28 February 2019, and the four measurements computed for that pixel. Vertical red strips represent active fires; the dates around the second hotspot were chosen in this case due to the larger NBR decrease. The Otsu threshold for the NBR temporal change (Otsu$_{dNBR}$) was −0.25 in this case.
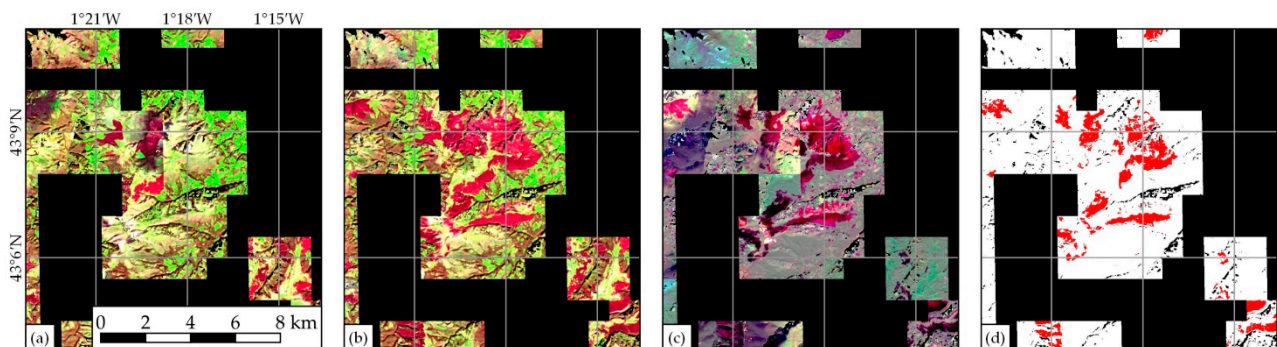
Figure 5. Resulting composites and selected BC pixels, in the same sample area where the pixel from Figure 4 was located. (**a**) shows the composite image with values from the t$_{pre}$ dates, with the LongSWIR/NIR/Red color composition; (**b**) composite image from t$_{post}$ dates, with the same color composition; (**c**) dt, temporal change between t$_{pre}$ and t$_{post}$ dates; and (**d**) BC pixels in red. Black areas correspond to pixels for which no corresponding MODIS hotspot was found in the processing month.

BC pixels, from which burned and unburned samples will later be extracted, are detected by analyzing the spectral signal in the t$_{post}$ composite and temporal change between composites. Three groups of bands must be defined for such purpose, from which candidate pixels will later be identified. These groups of bands are:

1. Temporal change of NBR, NBR2, and MIRBI spectral indices and NIR reflectance: dNBR, dNBR2, dMIRBI, and dNIR
2. NBR, NBR2, and MIRBI spectral indices at t$_{post}$
3. Red reflectance at t$_{post}$

The first group of bands corresponds to temporal changes. First, the Otsu threshold is computed (Otsu$_i$) for each band i, this threshold being the optimum value that separates the image in two classes by minimizing the inter-class variance, considering that pixels have a bimodal distribution [62]. At the same time, two additional values are computed for each pixel: the mean value of the band over the two months prior to the pre-fire date (mean$_{pre,i}$), and the mean value over two months following the post-fire date (mean$_{post,i}$) (Figure 4). In any band i (NBR, NBR2, MIRBI and NIR), pixels are labeled as BC pixels in that band if they meet two conditions, as shown in this formula for band NIR:

$$BC_{dNIR} = (dNIR < Otsu_{NIR}) \text{ AND } (mean_{post,NIR} - mean_{pre,NIR} < Otsu_{NIR}/2), \quad (4)$$

The temporal change being larger than the Otsu threshold ensures that there was some significant spectral change in the BC pixel that might be caused by a fire. Meanwhile, the difference between mean values from both periods also denotes that this change was prolonged over time, even though this requirement is not so strict (only half the Otsu threshold), because the vegetation may recover during the post-fire period (Figure 4). Please note that the conditions above are suitable for spectral indices and reflectance that decrease when burned (NBR, NBR2 and NIR), while the MIRBI index increases its values in burned areas, and so opposite signs should be used in such case. Additionally, the presence of hotspots does not necessarily mean the presence of burned areas, and so some empirically obtained minimum values for Otsu thresholds are required to reject false detections: -0.05, -0.05, 0.25 and -0.02 for dNBR, dNBR2, dMIRBI, and dNIR bands, respectively. If the threshold computed initially in any band is closer to 0 than this minimum, then it is replaced by this value.

The second group of bands is based on post-fire values (NBR, NBR2, and MIRBI at t_{post}). The Otsu threshold is also computed for each band among the pixels in the composite. The BC pixels in each band ($BC_{post,NBR}$, $BC_{post,NBR2}$ and $BC_{post,MIRBI}$) are simply those with a value lower than the threshold (higher in the case of MIRBI). This makes sure that BC pixels, in addition to the drop observed in the first group of bands, evidence the strongest burned signals in the image, since some events unrelated to fires (such as deforestation and floods) could exhibit a sudden decrease similar to burned areas even if they did not show such a strong-burned signal on the post-fire date. The NIR reflectance band was not included in this case, because its post-fire reflectance was found to be too variable in some biomes.

Finally, the third group is based on only one band: t_{post} reflectance in the visible red band, with pixels with a reflectance below Otsu threshold being labeled as burned candidates ($BC_{post,Red}$). This band was primarily included because according to literature on the subject it is the best band to discriminate between burned areas and agricultural false positives [60], since croplands are a well-known source of commission errors in BA mapping due to their spectral similarity to burned areas [18,22,26,27].

Final BC pixels are selected by combining BC pixels from the three previous groups of bands:

- In the first group of bands, pixels must be labeled as BC in at least 3 out of 4 bands (BC_{dNBR}, BC_{dNBR2}, BC_{dMIRBI}, and BC_{dNIR})
- In the second group, they must be labeled as BC in at least 2 out of 3 bands ($BC_{post,NBR}$, $BC_{post,NBR2}$ and $BC_{post,MIRBI}$)
- In the third group, being labeled as BC in the Red reflectance band at t_{post} ($BC_{post,Red}$) is mandatory

The result is a group of pixels with a strong-burned signal, located both spatially and temporally around a MODIS hotspot (Figure 5d).

Even though the criterion for the red reflectance band at t_{post} removes many false positives from croplands, further restrictions are applied in the first group of bands. For pixels identified as crops in the IGBP classification of the MCD12Q1 product at 500 m, the thresholds used in both conditions are multiplied by 2:

$$BC_{dNIRcrops} = (dNIR < 2 \cdot Otsu_{dNIR}) \text{ AND } (mean_{post,NIR} - mean_{pre,NIR} < Otsu_{dNIR}), \quad (5)$$

The criteria for detecting BC pixels are quite strict to avoid commissions, and selected pixels represent burned areas with a high severity, frequently omitting pixels with a lower severity. Next, 1000 samples are extracted in total from the BC pixels. The unburned category is composed by NIR, NBR, NBR2, and MIRBI values of BC pixels in the pre-fire composite (t_{pre}), while the same values in the post-fire composite (t_{post}) form the burned category. Thus, all samples are in the same pixels, although unburned values were observed before the BC pixels were burned, with burned values being observed after the burning.

These unburned and burned samples will then be used as training samples for image classification.

Finally, to avoid false detections as a consequence of hotspots not pointing to actual burned areas, two criteria must be met along the sampling step of the algorithm:

- Hotspots filtered temporally between composites' dates must cover a minimum surface of 5 km^2 in the whole MGRS tile
- Burned candidate pixels must cover a minimum surface of 1 km^2

If either criterion fails, the algorithm assumes that no area was burned in the region or that the available data are insufficient for the purpose of detecting any BA. In such case, the algorithm skips the following image classification step and returns an output image with no BA.

2.2.3. Image Classification

Samples extracted in the previous section are employed to classify the individual scenes from the pre-processed series. The strict masking used at the beginning of the sampling step is not applied here; the data series resulting from the pre-processing is used instead. For each band (NIR, NBR, NBR2, and MIRBI), a probability function is defined based on a logistic function, which is a smooth transition between two classes, this having already been used for BA detection in several studies [18,63–66]. The function is s-shaped for the MIRBI index, but z-shaped for the rest of the bands (Figure 6). To define the boundaries of the logistic curve, the 95th percentile of the burned samples and the 5th percentile of the unburned samples are computed, with the objective being to adjust the logistic curve between these two percentiles. However, the strict criteria for BC pixel detection may have omitted pixels with lowest burn severity, and so the logistic curve is shifted closer to the unburned distribution. Therefore, a midpoint between both percentiles, located halfway between both values, and the 5th unburned percentile are used as boundaries of the curve, which correspond to 100% and 0% of probability values, respectively. If the distributions of both categories overlap each other, the 95th burned percentile may be higher than the 5th unburned percentile; in this case, the logistic curve is adjusted between the midpoint and the 95th burned percentile (NIR in Figure 6). Additionally, note the reverse order of all parameters for the MIRBI spectral index. BA detection in croplands is more restricted than in other LC categories: the upper boundary of the logistic curve, corresponding to a 100% probability, is placed at the 50th percentile or median of the burned distribution.

Along with the probability function, the discriminability of burned areas is also measured for each band. This is computed using the M separability index (Equation (4)) [67], which has been employed in several studies for BA detection [18,30,68–70].

$$M = |\mu_b - \mu_{ub}| / (\sigma_b + \sigma_{ub}), \tag{6}$$

where μ_b and μ_{ub} are the mean values of burned and unburned samples, respectively, and σ_b and σ_{ub} the standard deviations of the same categories.

The four probability functions are applied on every image of the data series, each on the corresponding band, which results in four probability images for every date in the series (Figure 7a–d), with values ranging from 0% (unburned) to 100% (burned). These are aggregated into one probability image by computing a weighted average, with the weight being equal to the square of the separability index, using the following formula:

$$P_{st} = \sum P_i M_i{}^2 / \sum M_i{}^2, \tag{7}$$

where P_i and M_i are the probability and the separability index of the band i (NIR, NBR, NBR2, or MIRBI). This P_{st} value, referred to as static probability, indicates the probability of being burned on that date (Figure 7e), regardless of whether the pixel was already burned on a previous date in the series.
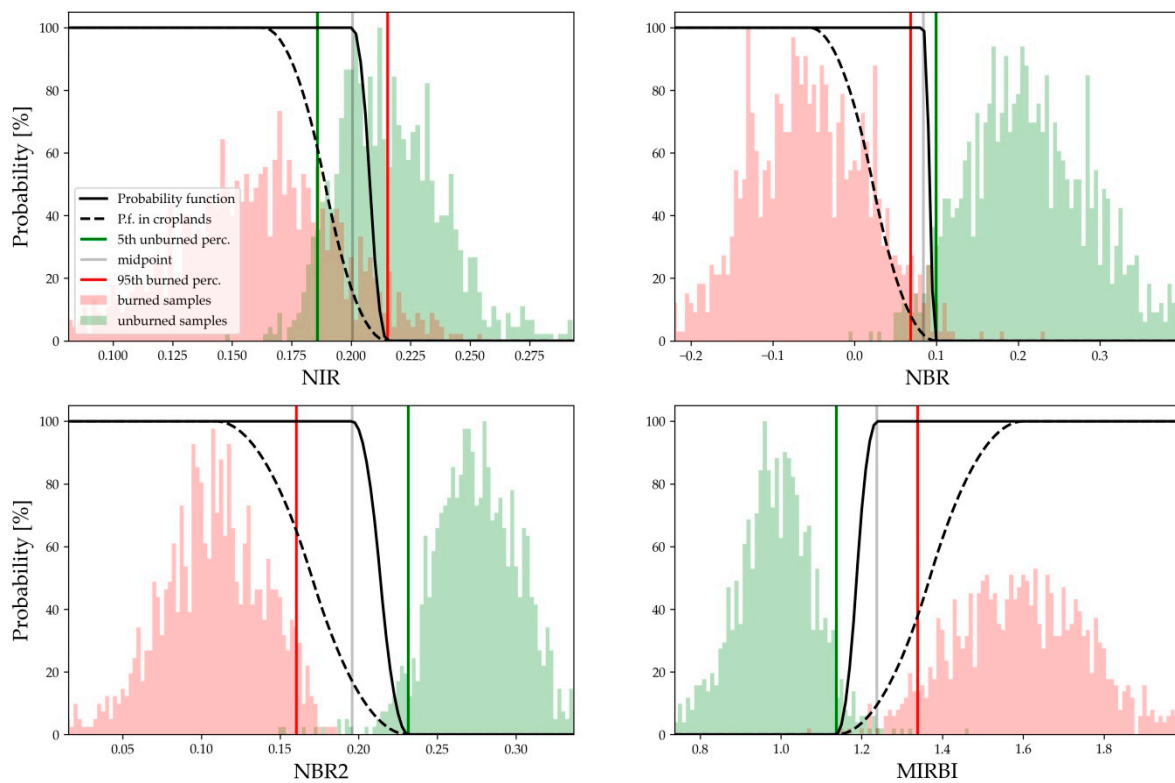
Figure 6. Distribution of burned and unburned samples and the probability function between both categories in each band, in the monthly product from July 2018 in tile 53LME (S2 data).
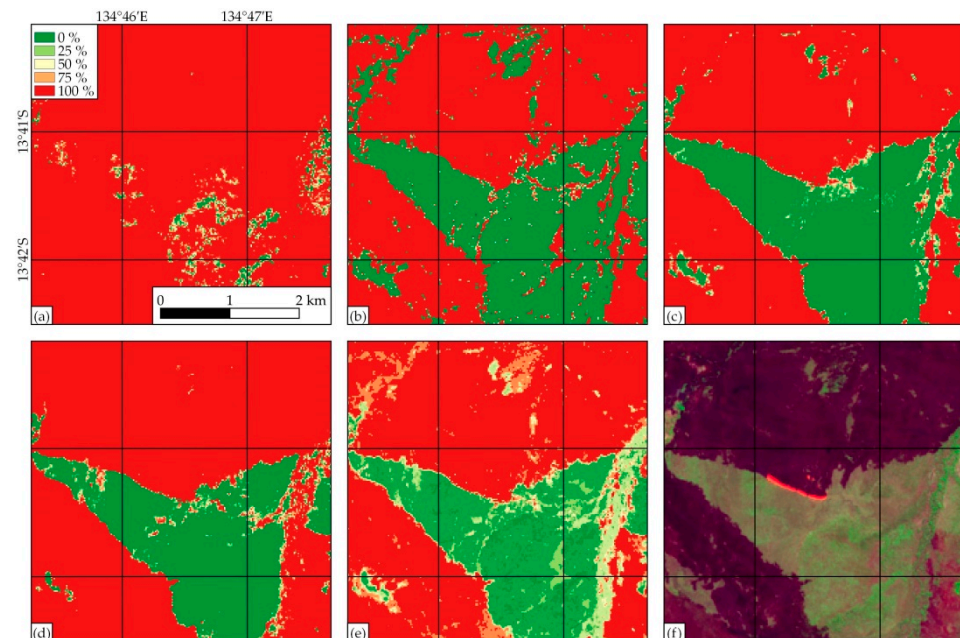
Figure 7. The probability of burn in a sample area from 13th July 2018, in tile 53LME, at 20 m (S2 data), according to: (**a**) the NIR reflectance band; (**b**) the NBR spectral index; (**c**) the NBR2 index; (**d**) the MIRBI index; and (**e**) the aggregated result (weighted average), P_{st}. The image in (**f**) is a LongSWIR/NIR/Red color composition. The M separability indices for NIR, NBR, NBR2, and MIRBI were 1.0, 1.8, 2.7 and 2.3, respectively.

Once every image in the data series has been assigned the static probability (P_{st}), the temporal evolution of this P_{st} is analyzed to detect the date immediately after the

pixel was burned. For this purpose, a second probability, called dynamic probability (P_{dy}), is computed for every pixel from every date in the data series based on three measures:

1. P_{pre}: mean P_{st} during previous two months, up to the corresponding date
2. P_t: P_{st} on the corresponding date
3. P_{post}: mean P_{st} during next two months, immediately after the corresponding date

The mean probabilities from the previous and following months (P_{pre} and P_{post}) are weighted averages, with highest weights for dates closer to the day for which P_{dy} is being computed. A logistic function is used to estimate these weights based on the distance from the central day; this function is adjusted to fit in the over-4-month-long period, with weights reaching the 0 value after a distance of two months (Figure 8). This weighted average enables burned pixels to be detected in biomes where the vegetation is regenerated in a few weeks, such as in tropical regions [71–73].
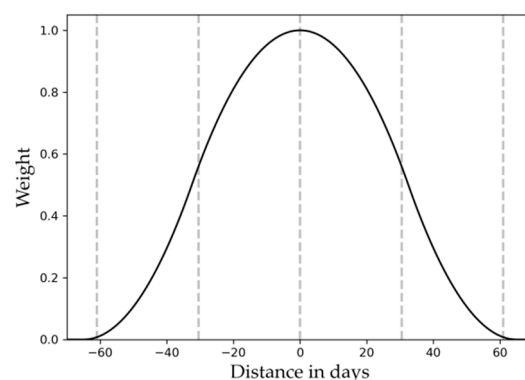
Figure 8. Weight of every date when computing P_{pre} and P_{post}, depending on the distance from the central day for which the P_{dy} is estimated.

High values of P_{dy} should only be found when pixels are observed as having burned for the first time, which should correspond to the first available image after the actual burning date. These fires appear as sudden increases in static probabilities and are maintained high over several consecutive acquisitions: a low probability on previous dates (P_{pre}) and high values on the corresponding date and following ones (P_t and P_{post}) are required. The following formula is used to compute this dynamic probability:

$$P_{dy} = (100\% - P_{pre}) \cdot P_t \cdot P_{post}, \tag{8}$$

A low P_{dy} will be computed for pixels already burned on previous dates, since those pixels will show a high P_{pre} (Figure 9). Similarly, sudden increases in P_{st} values that decrease again in the next image, usually belonging to clouds and cloud shadows unmasked in the pre-processing step, will have a low P_{dy}, because the P_{post} from the following dates will be low. However, clouds and shadows, despite having a low P_{dy}, may cause a decrease in dynamic probability on a nearby date that corresponded to an actual burning (Figure 9b).

Therefore, for every image in the data series (Figure 10a–d), two series of probabilities are obtained. The P_{st} maps indicate the probability of being burned on each date, even if they have been already observed as burned in previous images (Figure 10e–h); meanwhile, the P_{dy} maps show the probability of having burned on the considered date for each pixel (Figure 10i–l), showing a high value on the first date after burning but lower probabilities on the following dates. The BA algorithm then creates a temporal composite from this P_{dy} map series, by selecting the date with highest dynamic probability for each pixel (Figure 11a).
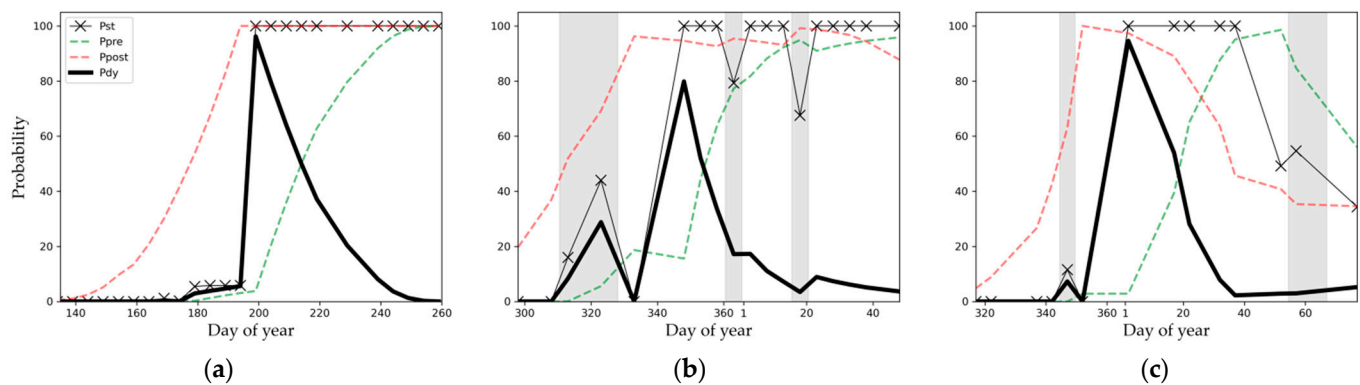
Figure 9. Temporal evolution of different probabilities throughout the processing period, in three sample pixels. (**a**) A pixel located in Australia, tile 53LME, at 13°41′38.3″S 134°46′24.8″E, in the same area as in Figure 7, which burned on 18 July 2018; (**b**) in South Sudan, tile 36NVP, at 8°6′35.1″N 32°7′43.3″E, burned on December 14th, 2018; and (**c**) in Brazil, tile 21KVV, at 18°55′7.0″S 57°18′0.8″W, on 2 January 2019. All three pixels were detected from S2 data at 20 m. Grey stripes indicate dates with cloud shadows unmasked in the pre-processing.
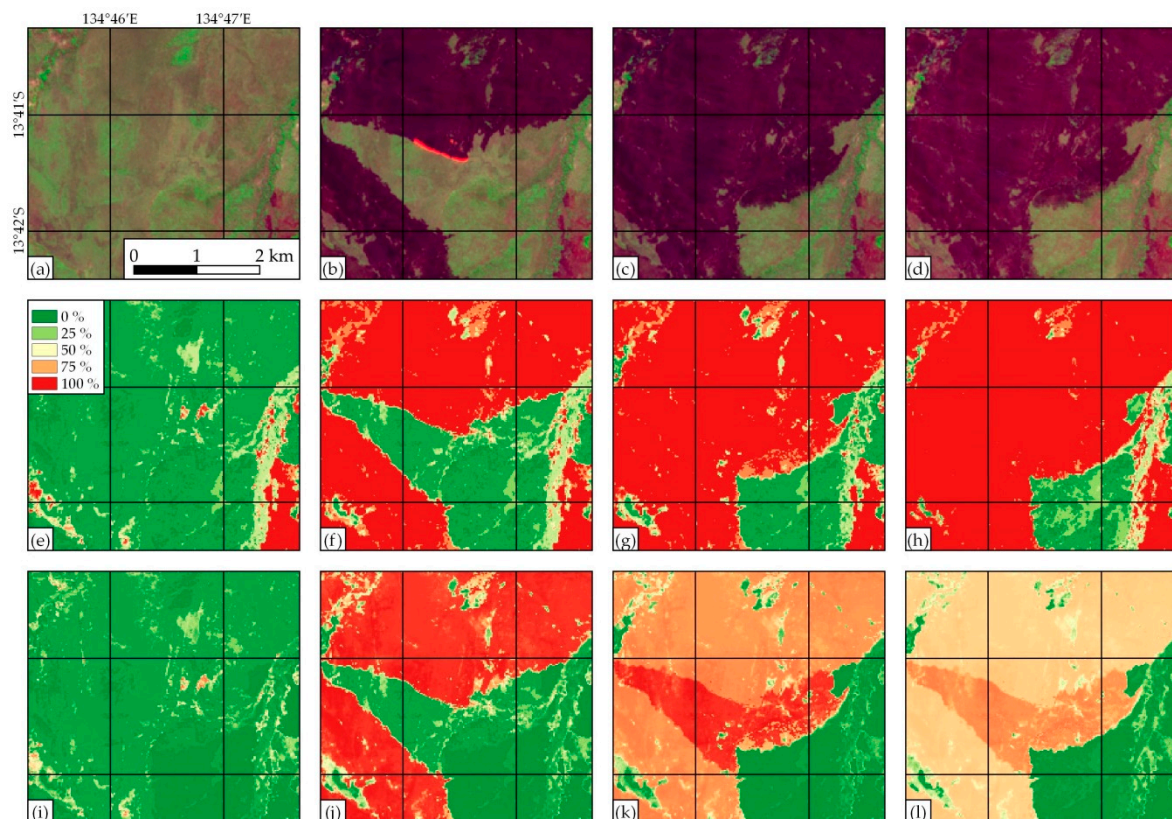
Figure 10. Evolution of the static and dynamic probabilities in the same sample area as in Figure 7. (**a**–**d**) LongSWIR/NIR/Red color compositions from the 8th, 13th, 18th and 23rd July 2018; (**e**–**h**) static probabilities for the same dates; and (**i**–**l**) dynamic probabilities.

The composite with the maximum P_{dy} may also contain pixels with low burn probability values and some areas burned on dates outside the processing month that should be removed (Figure 11a). The best option for removing these areas would be a two-phased strategy involving first identifying burned seeds (pixels with a strong-burned signal) and then extending the burned region around these seeds up to a threshold [66]; this strategy has already been used extensively for BA detection [12,13,16,18,22,25,39,41,61]. Several approaches were tested to implement this strategy, such as spatial dilation from burned seeds,

cumulative cost maps, and grouping of connected pixels, although they all proved to be too time- and memory-consuming and always ended up exceeding GEE's user memory limit. An alternative methodology was applied instead in the form of the Simple Non-Iterative Clustering (SNIC), a non-iterative superpixel segmentation algorithm [74] already implemented in GEE that has been shown to be efficient in terms of computation and memory requirements [75]. An 8-neighbor connectivity was used with a 0 compactness (disabling the spatial distance weighting) and 10 pixels as a superpixel seed location spacing parameter [74], which was observed as being a balanced value between the size of the objects and well limited burned patches. Once the object images are obtained, the mean value of each object is then computed in GEE. Only the objects with a mean P_{dy} higher than 50% are labeled as burned. The segmentation also removes single pixels with probabilities higher than 50% that are part of clusters with low BA probabilities, which would otherwise lead to commission errors (Figure 11b).
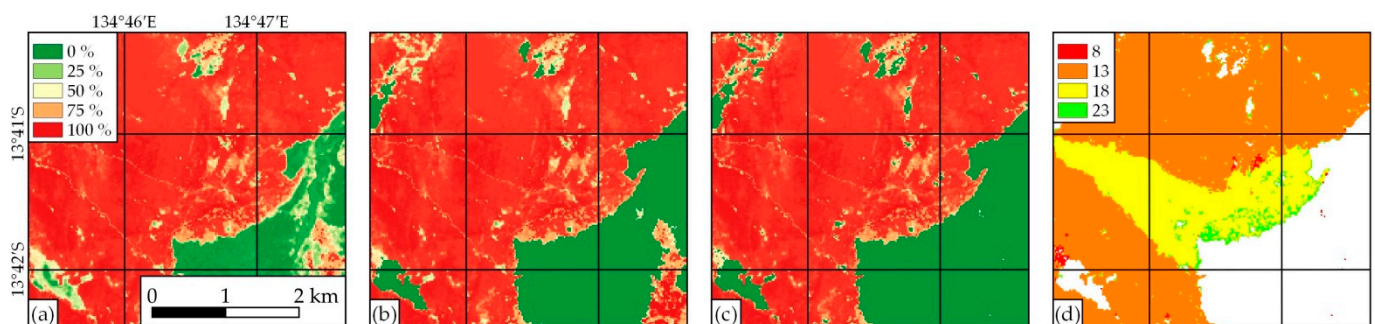
Figure 11. (**a**) Result by maximizing P_{dy} from the data series; (**b**) previous result after removing low probability clusters; (**c**) final BA map with dynamic probabilities after removing areas not burned in the processing month; and (**d**) day of the month on which the pixel was burned.

Finally, every pixel whose highest P_{dy} in the processing period was not observed in the processing month is labeled as unburned, and pixels that could not be observed on a single day throughout the processing month are assigned a special value of -1. The resulting BA map contains two bands (Table 3): the P_{dy} value as a confidence level of the burned pixel (Figure 11c), and the date of burn, which corresponds to the day of the year on which the highest P_{dy} was observed (Figure 11d). The final BA map is exported to a GeoTIFF image covering the corresponding MGRS tile in UTM coordinates, at 10, 20 (when using Sentinel 2 data) or 30 m (when using Landsat data) of spatial resolution.

Table 3. Bands and possible values of exported BA maps.

Confidence Level (%)	Day of Burn	Meaning
50–100	1–365	Burned
0	0	Unburned
−1	−1	Unobserved

2.3. Quality Assurance

2.3.1. Reference Data

The Committee on Earth Observing Satellites' Land Product Validation Subgroup (CEOS-LPVS) defined validation as the process of assessing by independent means the accuracy of the data products from the system outputs [76]. Out of four validation stages defined by CEOS-LPVS, Stage 3 requirements are usually followed by BA product validations [16,18,20,21,41,77,78], which consist of an assessment characterized in a statistically robust way over multiple locations [79]. BA products are validated by comparison with reference data (RD) created in multiple image pairs and located in validation sites typically selected by stratified random sampling [20,77,80,81]. These RD are generated by

visual analysis and supervised classification from independent higher-spatial-resolution images [82].

Validation of medium-spatial-resolution products in accordance with the CEOS protocol is challenging as the availability of multi-date higher-spatial-resolution data is expensive and often unavailable [31]. Although a standard BA reference database is already available for the scientific community, these data do not include information from 2016 onwards (the years in which sufficient S2 data can be found) or are limited to a country or continent (CONUS and Africa) [83], and could not be used to assess our algorithm's performance globally on S2 data. In this study, a quantitative assessment of our algorithm was carried out by comparing it with BA interpreted visually from multi-date S2 data at 10 m at 50 sites. This is a low number of sites if compared with other studies, where around 100 [77] or over 500 [21] validation areas were used, even though those sites were composed by only two images. A subset of 20×20 km^2 was selected for each site instead of a complete scene (110×110 km^2) to obtain an accurate result by supervised classification without requiring manual refinement. Similar sizes have already been used in other studies, especially when this has concerned Landsat data with SLC-off problems [18,77,84]. Unfortunately, both the RD and the results of the BA algorithm at 10 and 20 m were obtained from the same data—S2 imagery—because generating a similar global sample from higher-resolution data was unfeasible. Moreover, the stratified random sampling for site selection was based on S2 data, which means that all sites have frequent available cloud-free S2 images, making them optimum sites for BA detection using data from the same source. Therefore, due to the small size and low number of sites, same data being used for both the RD and the algorithm, and the site selection favoring S2 cloud-free areas, the authors prefer to use the term 'quality assurance' (QA) for this exercise, rather than a validation.

The areas where the QA analysis was carried out were selected using the stratified random sampling methodology [81], based on S2 data, with sampling units being 20×20 km^2 windows located at the center of each MGRS tile. Although a high number of areas is optimal in achieving an accurate estimation of errors in a global algorithm, processing of fewer albeit representative QA sites with temporally longer periods was preferred, which is especially crucial for assessing Landsat-based results and limiting the effect of any acquisition date disagreement. This QA exercise was limited to 50 areas—with several image pairs analyzed at each one—and is deemed to be sufficient since it covers several biomes. This sampling methodology has already been implemented in GEE as the VA tool from Burned-Area Mapping Tools (BAMT) [41] and, even though it could not be used globally because it exceeds the GEE user memory limit in large areas, part of its code was used in order to access the S2 catalog and analyze its availability in GEE. The whole analysis was carried out for data from 2019, which is the first year when S2 L2A data have already been consistently processed (Figure 1). First, long sampling units were selected, at least 2 months long, with a minimum frequency of one image every 20 days and cloud coverage lower than 20%. Then, these long sampling units were assigned the predominant Olson biome [85], reclassified into 7 main classes, and low or high fire activity in the unit's area. Global VIIRS active fires at 375 m were used in this study [86], which were observed as better detecting small fires [87] than the BA products at coarse resolution typically used as fire activity estimations [41,80,81], which tend to underestimate small fires [16,17]. Lastly, after splitting sampling units into 14 strata according to the 7 major Olson biomes and low and high fire activities, 50 QA areas were then randomly selected from each stratum. The number of sites in each stratum was proportional to the total number of sampling units and the mean fire activity in the stratum.

The 50 QA areas selected by the stratified random sampling can be seen in Figure 12. Despite sampling units being split among 7 major Olson biomes, half of the QA sites are in the tropical and subtropical savannas biome, because this is the biome with most African fires, constituting 70% of global BA. The following biome with most QA sites is tropical forests with 11 sites, most of them located either in Brazil or on the Indochinese Peninsula; the remaining biomes contain between 1 and 4 sites. The shortest periods are

two months long, while some cover the whole year of 2019, although most are less than 8 months long. Among all 50 sites, 419 cloud-free images were used, which means 369 pairs of consecutive images. The complete list of QA areas and their main characteristics are detailed in Appendix A Table A1.
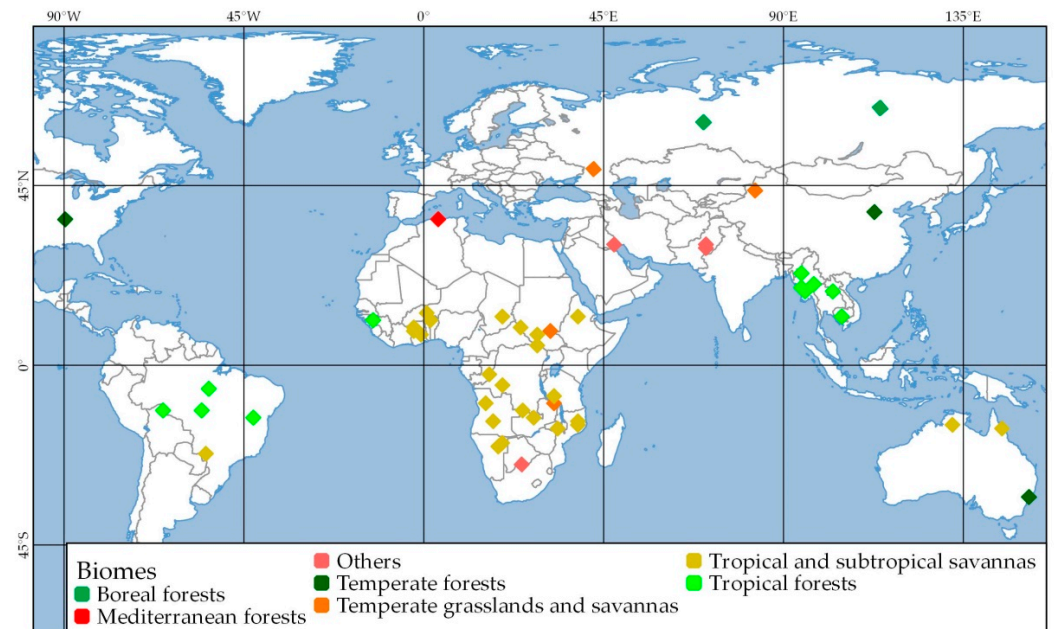
Figure 12. The location of the 50 QA areas selected by stratified random sampling, and their predominant Olson biomes.

For every pair of consecutive cloud-free images in each QA area, RD were created using a supervised classification, derived from S2 data at 10 m of spatial resolution. This task was done using the RP tool for reference data creation from BAMT, implemented in GEE [41]. Exported results were visually checked by comparing them with pre- and post-fire color images in a local machine and reprocessed in GEE where necessary, but were not refined or modified manually. Reference perimeters from different pairs of images at the same QA site were merged in one final image, in which every pixel was labeled as unburned, burned, or unobserved.

2.3.2. Accuracy Metrics

The algorithm presented in this study was run on all 50 QA sites, processing every month included between the first and last dates of each site, and at three different spatial resolutions: 10 and 20 m with S2 data, and 30 m with Landsat images. These BA maps shall be referred to BAS2-10, BAS2-20, and BAL-30 from now on.

Accuracy metrics were estimated based on the error matrix approach [88,89], by comparing BA maps with RD at the QA sites. Commission and omission errors (CE and OE) and the Dice coefficient (DC) were computed for each QA area, together with an aggregation from the sum of error matrices. DC is defined as the probability for a classifier to identify a pixel as burned, given that the other classifier also identifies it as burned [81,90,91], with the BA maps obtained by the automatic algorithm and the RD being the two classifiers in this case. In addition to the accuracy metrics for BAS2-10, BAS2-20, and BAL-30, the global products FireCCI51 and MCD64A1 were also assessed at these 50 QA sites. The only global product at medium resolution, GABAM, could not be assessed because this product lacks the date of burn. The accuracy of the BA maps and global products was also analyzed in different LC categories using the IGBP classification from the MCD12Q1 product at 500 m, reclassified into 9 main classes (Table 4).

Table 4. Reclassification of the 17 original categories from the IGBP classification in MCD12Q1.

| New Categories	Original LC Categories
Forests	Evergreen needleleaf forests Evergreen broadleaf forests Deciduous needleleaf forests Deciduous broadleaf forests Mixed forests
Shrublands	Closed shrublands Open shrublands
Savannas	Woody savannas Savannas
Grasslands	Grasslands
Wetlands	Permanent wetlands
Croplands	Croplands Cropland/Natural vegetation mosaics
Urban areas	Urban and built-up lands
Snow, ice, and water bodies	Permanent snow and ice Water bodies
Barren	Barren

2.3.3. Reporting Accuracy

A reporting accuracy analysis was carried out for all 5 BA products in these 50 QA areas by comparing burning dates from VIIRS active fires and those from BA products, following several previous studies [12,16,18,92]. After drawing a 375×375 m^2 window around each hotspot inside a QA site, the number of days between the hotspot and the first burned pixel detected by BA products in the window is measured, with this burned pixel being considered part of the BA whose fire was recorded by the hotspot. The purpose of this indicator is to measure the BA detection delay when labeling the date of the fire.

2.4. Test Sites

In addition to the QA exercise, performance of the proposed preliminary algorithm was tested in three large regions of 5×5 degrees, covering three representative biomes. The purpose of this analysis is to ensure that the algorithm is sufficiently robust to generate plausible results and assess the limitations of the medium-spatial-resolution algorithm, such as acquisition gaps owing to persistent clouds or issues related to active fires.

Stratified random sampling was used to select these three sites, similar to QA site selection; however, S2 image availability and cloud coverage were not taken into account in this case. Sampling units, consisting of MGRS tiles, were assigned the predominant Olson biome in the region, and the number of VIIRS hotspots detected in 2019 was used as fire activity. Once all units had been classified into 14 strata (7 major Olson biomes and low/high fire activity), the 3 strata with the highest mean fire activity were then selected. One sampling unit was randomly selected from each of these 3 strata, and 5×5-degree windows around these units were selected as test sites (Figure 13). The test site from Africa is located on the eastern half of the Central African Republic and contains predominantly tropical and subtropical savannas; the site from Central America is located between Mexico and Guatemala and includes tropical forests; the third one is in Siberia, north of lake Baikal, and is covered by boreal forests. The whole year of 2019 was processed at all three sites with S2 data at 20 m (BAS2-20), which was proven to be the fastest and one of the most accurate resolutions (see Sections 3.1 and 3.2).
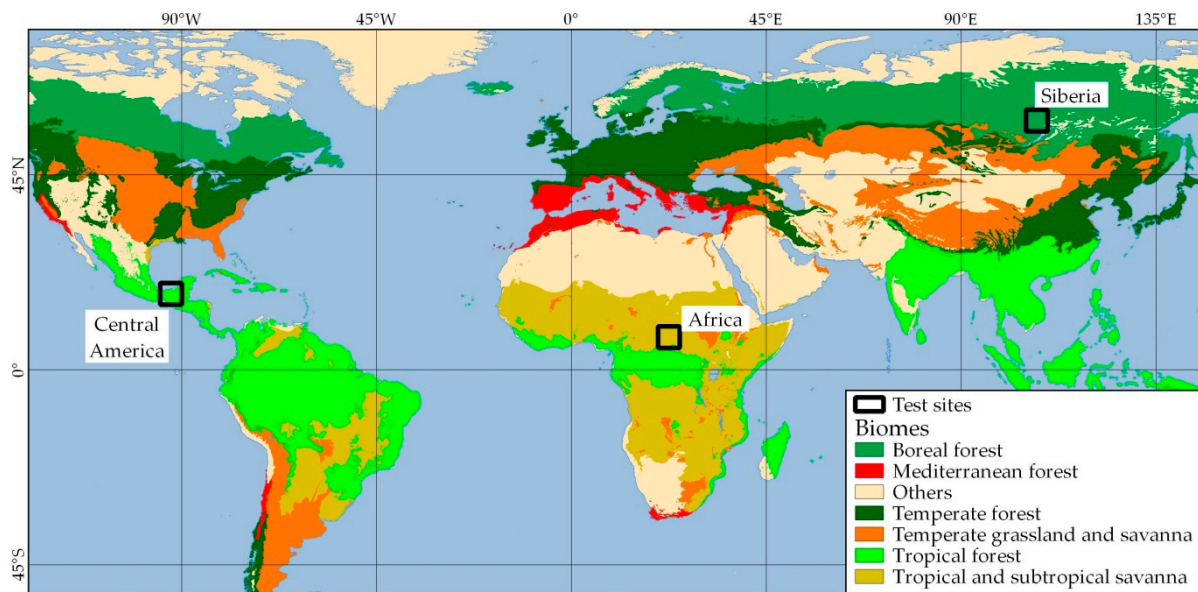
Figure 13. Location of the three 5 × 5-degree test sites and major Olson biomes.

The results obtained at these test sites at 20 m were compared with three global BA products at different resolutions: FireCCI51 at 250 m, MCD64A1 at 500 m and GABAM at 30 m. To analyze the spatial patterns of BA, the fraction of burned surface in a 0.05 × 0.05 degree grid (≈5.5 × 5.5 km^2 at the Equator) was compared between BAS2-20 and each global product.

3. Results

3.1. Algorithm

The algorithm presented in this study was run in the 50 QA areas at three different spatial resolutions (S2 at 10 and 20 m and Landsat at 30 m), with 321 monthly BA maps in total created at each resolution. Processing times depended on the resolution selected, with 20 m (BAS2-20) being fastest, which took 4.2 min per monthly map on average, followed by 30 m (BAL-30) at 4.5 min/map, and with the 10 m resolution (BAS2-10) being the slowest at 5.9 min per BA map.

3.2. Accuracy Metrics

Accuracy measures obtained by comparing the RD with our BA maps and global products are shown in Table 5. Commissions, initially between 18–19% for global products at coarse resolution (MCD64A1 at 500 m and FireCCI51 at 250 m), decreased up to 11% for BA maps derived from Landsat data (BAL-30), and around 9% at both resolutions with S2 images (BAS2-20 and BAS2-10). Similarly, omissions decreased from over 50% to less than 35% for BAL-30 maps, and between 27–28% for maps obtained from S2 data. Dice coefficients followed the same trend, since lowest values were found for products at coarser resolutions (56–62%), followed by 75% for BA maps at 30 m and over 80% at 20 and 10 m. Accuracy metrics at specific QA sites area are shown in Appendix A Table A2. No major improvement was found when processing S2 data at 10 m over 20 m, even though both commissions and omissions decreased slightly. Around 4300 and 4000 km^2 of burned areas were detected at these 50 sites by our algorithm using S2 and Landsat data, but significantly less by products at coarse resolution: 3355 and 2824 km^2 by FireCCI51 and MCD64A1, respectively. According to RD, however, 5421 km^2 had actually burned.

Table 5. Accuracy measures for our algorithm at 3 spatial resolutions and for 2 global BA products: commissions, omissions, and Dice coefficients, all expressed in percentages. Total burned area among all 50 sites is also shown.

Algorithm/Product	CE	OE	DC	BA (km^2)
BAS2-10	9.0	26.8	81.1	4359
BAS2-20	9.3	27.9	80.3	4309
BAL-30	11.2	34.8	75.2	3979
FireCCI51	19.1	50.0	61.8	3355
MCD64A1	18.3	57.4	56.0	2824

Figure 14 shows the accuracy measures in different LC categories. More than half the burned area in these 50 QA areas (56.9%) was in savannas, where our algorithm performed best with commissions between 8–9%, omissions between 18–27%, and Dice coefficients between 81–86%, depending on the spatial resolution. Next were grasslands, with 19.3% of total BA and slightly lower omissions but higher commissions, followed by croplands and forests (12.7 and 10.9% of total BA, respectively), both with low commissions but also very high omissions (45–70%). Very few areas were burned in shrublands (0.2%) or in urban areas (0.1%), and practically none in the remaining three LC categories (snow, ice, and water bodies, wetlands, and barren). In all these land covers, commissions were lower for BA maps obtained from S2 data (BAS2-10 and BAS2-20) than for those from Landsat images (BAL-30), while omissions remained in some cases. Global BA products at coarse resolution showed significantly higher omissions in most land covers, except in croplands, and similar or higher commissions; Dice coefficients were higher as spatial resolutions improved, being similar only in croplands.
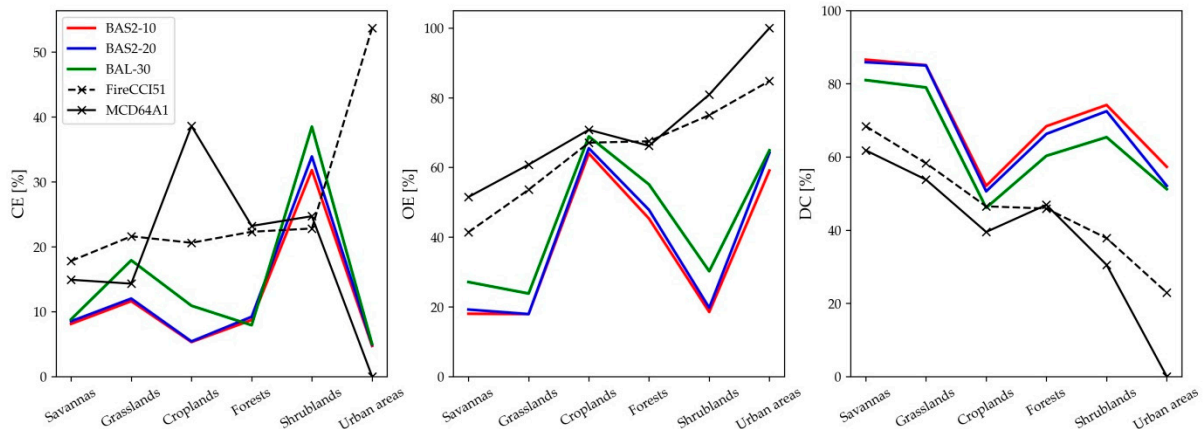
Figure 14. Accuracy measures for our algorithm at 3 spatial resolutions and for 2 global BA products, depending on the LC class: commissions, omissions, and Dice coefficients.

3.3. Reporting Accuracy

A total of 13,730 VIIRS hotspots were located at the 50 QA sites, detected between the corresponding first and last dates for each site. BAS2-10 maps contained some burned pixel around 87.4% of these hotspots, with lower ratios for BAS2-20 (84.5%) and BAL-30 (78.9%). Products at coarse resolution showed significantly lower detection percentages—41.0% and 35.9% for FireCCI51 and MCD64A1, respectively—which means omitting around 60% of the fires detected by VIIRS hotspots.

Over 26% of BA was detected the same day or the day after the hotspot's date in BAS2-10 and BAS2-20, and 17.5% in BAL-30 (Figure 15). All three of them had detected at least 81% of BA the first 5 (for BAS2-10 and BAS2-20) or 8 days (BAL-30), which correspond to the maximum time needed for S2 and Landsat satellites to revisit the area, respectively. Likewise, by the time a satellite revisited the area for the second time after the hotspot's

date (10 and 16 days for S2 and Landsat data), BA had already been observed and detected by the algorithm for nearly 92% of the hotspots. In comparison, global BA products detect burned areas earlier, due to their better temporal resolution (1 day). In particular, MCD64A1 detected 78.0% of BA the same day or one day after the hotspot, and 86.0% after two days; FireCCI51 took longer, with only 32.1% detected the same or next day, and not exceeding 80% of detection until the 5th day.
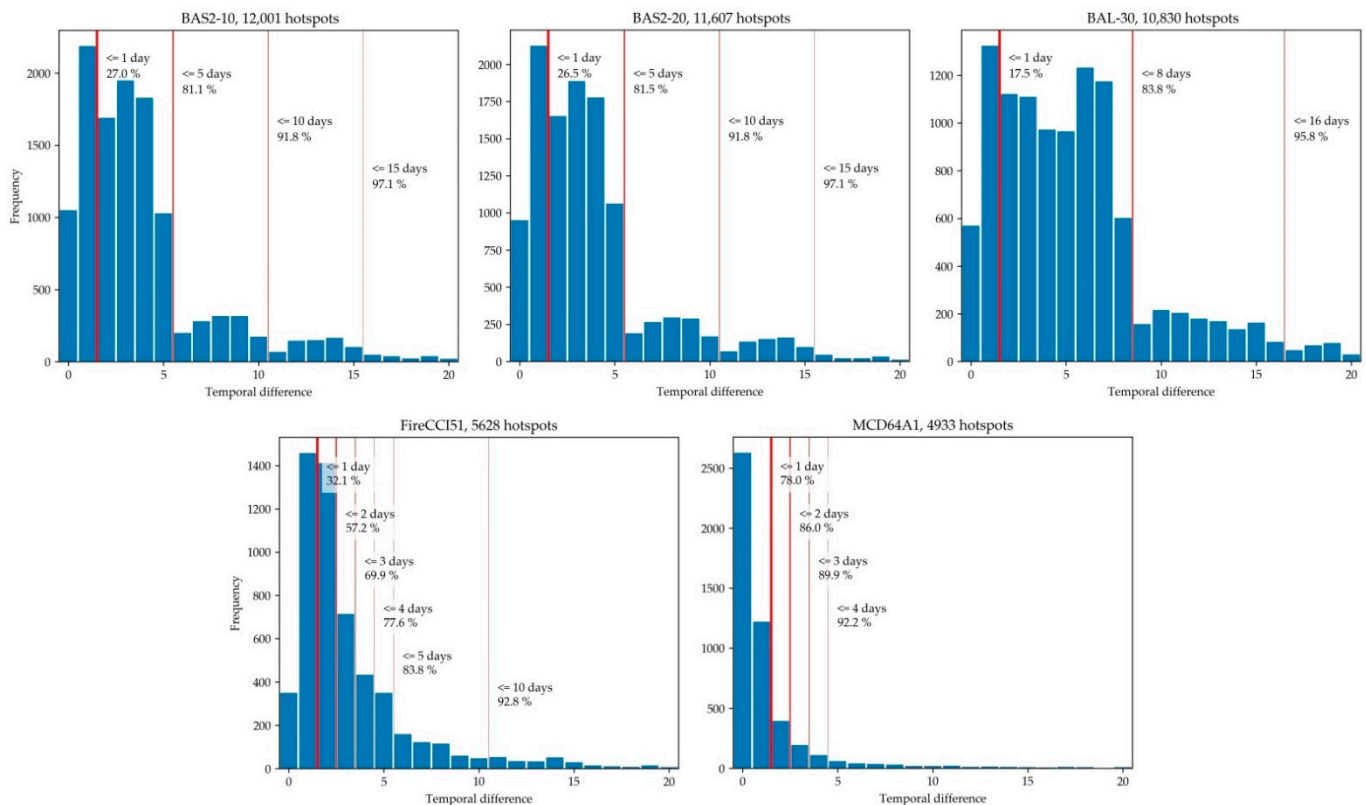
Figure 15. Reporting accuracy of our algorithm at 3 spatial resolutions and 2 global BA products, by comparing them with VIIRS hotspots.

3.4. Test Sites

The 3 test sites from Africa, Central America, and Siberia were covered by 122 MGRS tiles in total, with 1464 monthly BA maps in total processed for the whole year 2019. The process took around 5.5 days to process, or 5.4 min per monthly BA map on average. The results obtained from this algorithm and from global products at the test site from Africa are shown in Figure 16. A total of 144,000 km^2 were burned in total in 2019 at this site according to our algorithm, while this amount was lower in the case of FireCCI51 and GABAM (between 110,000 and 112,000 km^2), and only 87,000 km^2 were detected by MCD64A1. The largest differences are seen in the northeastern corner of the site, where many areas burned around November—according to BAS2-20—were omitted by all global products. Most large fire patches detected were consistent across all products, although the smallest fires were only mapped by BAS2-20 and GABAM. The scatter plots between burned fractions and regression lines in Figure 17 point to the same trend, since most cells have higher burned fractions in BAS2-20 than in global products. Spatially, the most similar patterns were found between BAS2-20 and FireCCI51 with the highest values for the slope of the regression line (0.872) and r^2 (0.588), followed by MCD64A1 (0.771 and 0.477, respectively), and with the lowest correlation being for GABAM (slope and r^2 below 0.4 and 0.2).
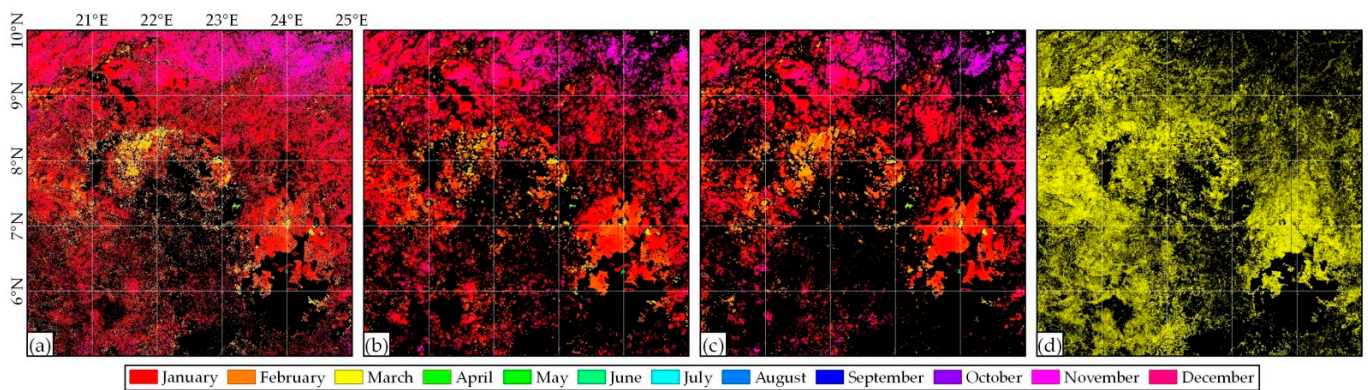
Figure 16. Comparison of different BA products at the test site from Africa. All areas burned in 2019 are shown, according to: (**a**) BAS2-20 map, (**b**) FireCCI51 product, (**c**) MCD64A1, and (**d**) GABAM (burning date unknown).
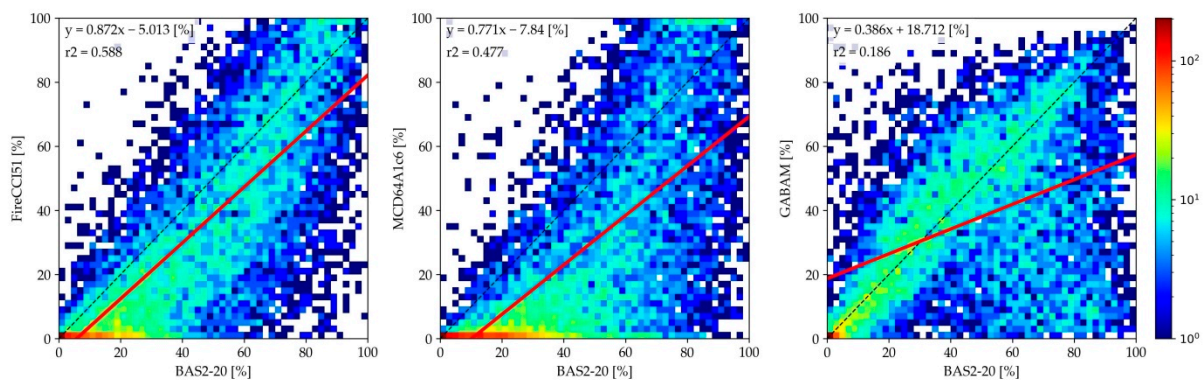
Figure 17. Scatter plots colored by density and linear regressions between BAS2-20 and global products, based on the BA fraction in each 0.05 × 0.05-degree cell, at the test site from Africa.

The same analysis at the test site from Central America is shown in Figures 18 and 19. More than 12,800 km^2 of BA were detected in 2019 according to BAS2-20, followed by both MODIS-derived products with only half the surface (between 6000 and 6200 km^2), and GABAM with 5500 km^2. The largest differences were found in areas affected by small size fires. Very similar results were obtained for FireCCI51 and MCD64A1 (slopes between 0.75 and 0.76, and r^2 around 0.59) when comparing their BA fractions with BAS2-20. At this test site, GABAM again showed the lowest correlation.

Figure 18. Comparison of different BA products at the test site from Central America. All areas burned in 2019 are shown, according to: (**a**) BAS2-20 map, (**b**) FireCCI51 product, (**c**) MCD64A1, and (**d**) GABAM (burning date unknown).

Figure 19. Scatter plots colored by density and linear regressions between BAS2-20 and global products, based on the BA fraction in each 0.05×0.05-degree cell, at the test site from Central Africa.

Figures 20 and 21 show the results from the third site in Siberia. Detected burned surfaces by global products at coarse resolution and our algorithm differed less than at other sites, with 6300 km^2, 4500 km^2, and 5200 km^2 found for BAS2-20, FireCCI51, and MCD64A1, respectively; GABAM only detected 1200 km^2. Higher correlations with FireCCI51 and MCD64A1 than at the other test sites were found at this one (r^2 of 0.697 and 0.785, respectively). The fact of the slope being higher than 1 between BAS2-20 and MCD64A1 indicates an underestimation of BA by our algorithm in boreal forests. The largest differences between BAS2-20 and coarse-resolution products were observed in the northwestern quarter of the site, where BAS2-20 incorrectly detected the decline of reflectance as having been burned at the end of summer in August and September.
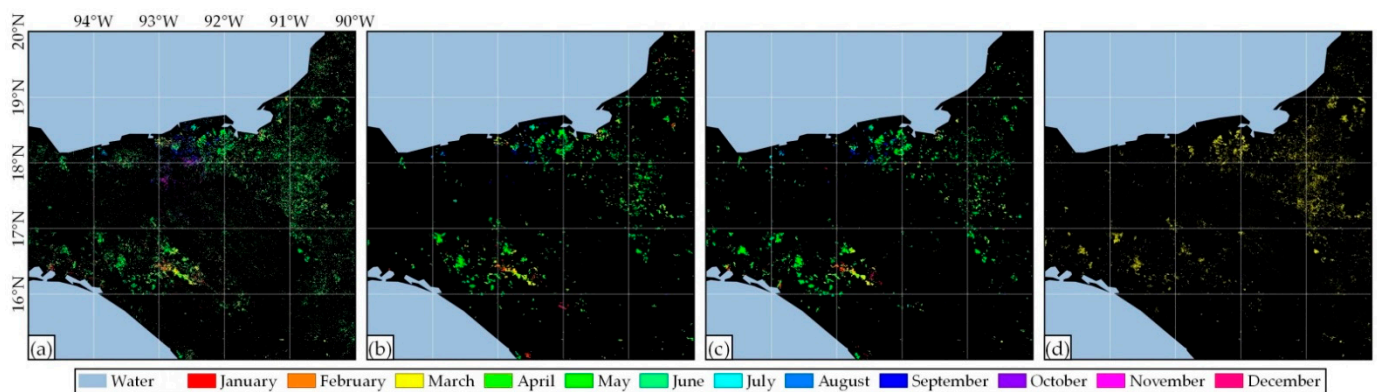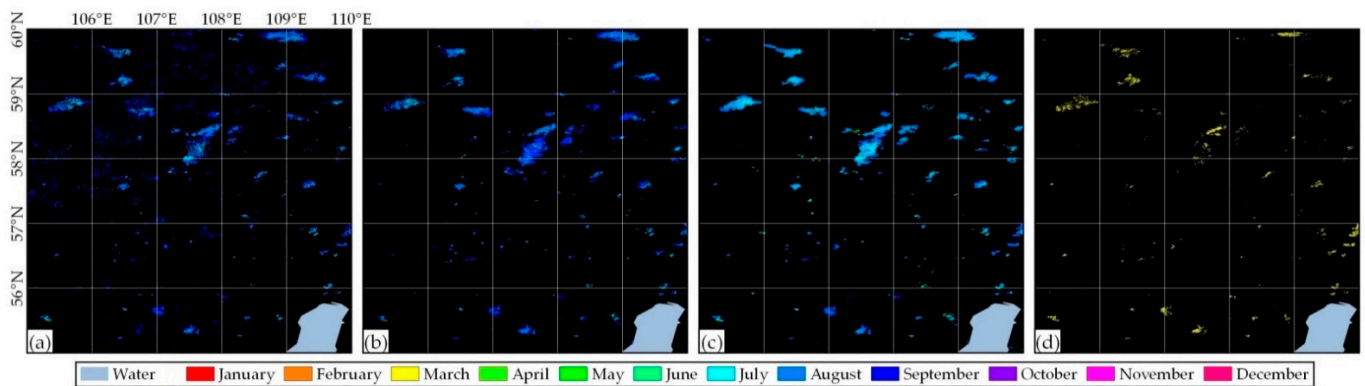

Figure 20. Comparison of different BA products at the test site from Siberia. All areas burned in 2019 are shown, according to: (**a**) BAS2-20 map, (**b**) FireCCI51 product, (**c**) MCD64A1, and (**d**) GABAM (burning date unknown).
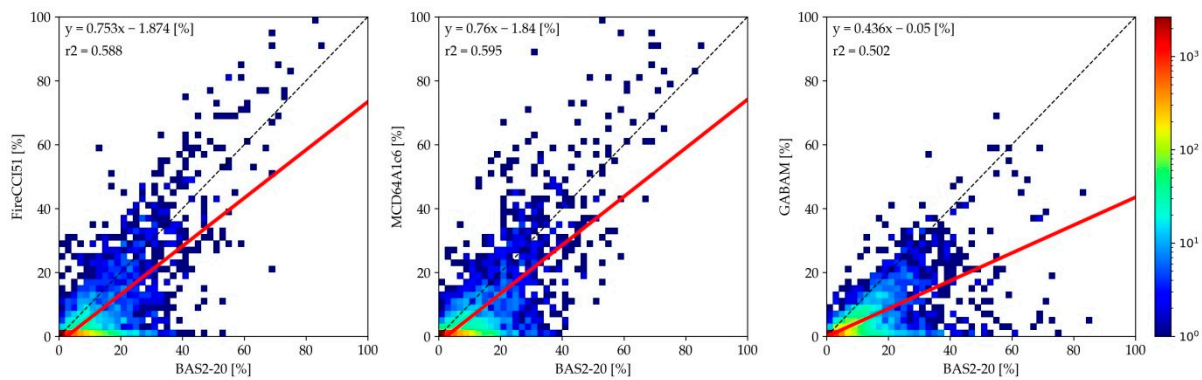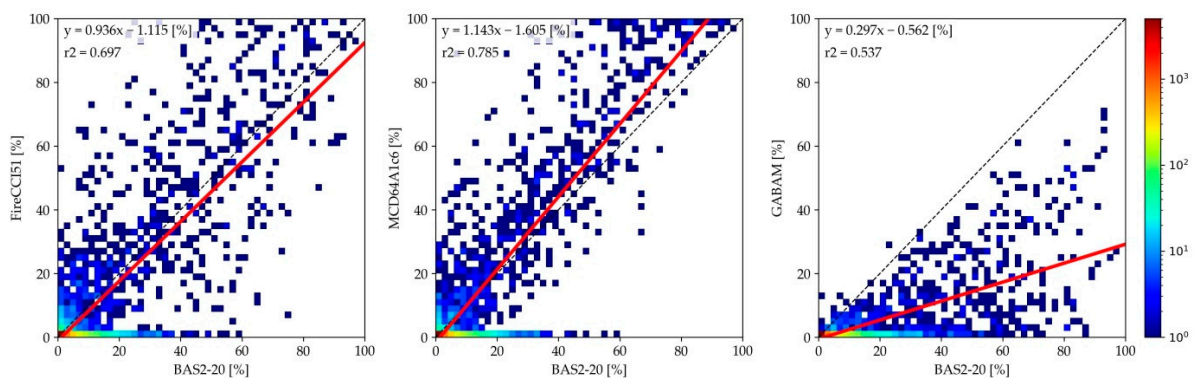

Figure 21. Scatter plots colored by density and linear regressions between BAS2-20 and global products, based on the BA fraction in each 0.05×0.05-degree cell, at the test site from Siberia.

4. Discussion

This paper presents a preliminary global automatic algorithm for BA detection at medium resolution, based on the MODIS active fire product MCD14DL and primarily on either Sentinel-2 (S2) or Landsat data. This is the only global BA algorithm based on S2 images so far, since only Landsat imagery has been used globally before [22], and algorithms with S2 data have been limited to national or continental scales [18,29–31]. Moreover, BA can be detected at both 20 and 10 m when using this dataset, even though the latter resolution has not proven to be more accurate. The algorithm is completely flexible when selecting the S2 or Landsat dataset and resolution, making it possible to produce BA in any year at the desired resolution, if S2 or Landsat datasets are available. BA from 2000 onwards can be processed with Landsat data at 30 m; previous years cannot be processed by this algorithm, despite Landsat images being available, because of the lack of MODIS hotspots for those dates. BA from 2016 onwards can also be processed at 10 or 20 m using S2 data; processing year 2015 with S2 data is possible but discouraged, because of the low number of available scenes (Figure 1).

The algorithm's main process involves sampling some burned candidate pixels (BC) around MODIS hotspots, and then classifying the image series in burn probabilities based on spectral characteristics of these candidate pixels and detecting burned areas and dates by analyzing their temporal trend. Using an active fire product to identify some BC pixels and using these to classify images is not a novel feature, since this is already done by most global or continental BA algorithms [11,13,15,16,18,32], even though many other studies do not use hotspots to identify burned areas [10,22], especially at regional scales [25–29,31]. However, this is one of the first studies at non-coarse resolution that analyze the temporal evolution of spectral signals in a time series in order to establish the earliest possible detection date, as well as requiring that a burned spectral signal continue on post-fire dates [27,29,31]; the temporal consistency requirement of unburned and burned signals before and after the fire improves BA detection by avoiding possible commissions unrelated to fires, such as clouds, cloud shadows, or flooding. This approach is similar to the way some global algorithms at coarse resolution perform [10,11]. On the other hand, most BA algorithms at medium resolution either detect burned pixels on one post-fire date [63], analyze spectral changes between two single dates [18,30], search for anomalies in comparison with a multi-annual average [28], or classify every image in the time series but then just select the date with the highest probability [22,25,26], but none of them verify whether the burned signal remains after the fire.

Unburned and burned pixels at medium resolution are usually classified either by a machine-learning approach [22,26,27,31,39], decision trees [32], thresholding [29], or by logistic regression [18]. Since a machine-learning approach in a time series focus was too memory-consuming in GEE, logistic functions were used instead by this algorithm, which allowed there to be a continuous transition between unburned and burned categories. This is often followed by a two-phase strategy to balance commissions and omissions at the end of the algorithm, first identifying burned seeds and then growing regions around them. However, the process was too heavy and exceeded GEE's user memory limits, even though several approaches were tested. Finally, an object-oriented image analysis focus was implemented using the SNIC algorithm, segmenting the burn probability and retaining the clusters with a mean probability higher than 50%.

The proposed algorithm is highly dependent on active fire products, which are required in the second step of the algorithm to identify BC pixels. Several active fire products have been developed and released in the scientific community, with the most prominent being those obtained from MODIS data at 1000 m, and from the VIIRS sensor at 375 m. Unfortunately, there is only one active fire product loaded in GEE, the near-real-time MCD14DL [52], and not the standard data product, which is internally consistent and well calibrated. FIRMS warns that the dataset is not considered to be of scientific quality [93] and, therefore, only hotspots with a confidence level over 80% are selected to overcome this limitation. Most other global BA algorithms also rely on active fire products but, since they

are not limited to the products available in GEE, usually use the standard MCD14ML product processed by the University of Maryland [94–96], which is a further-developed and more accurate active fire product than MCD14DL [12,13,16].

Using the near-real-time and non-standard product is a significant limitation of the algorithm. MODIS hotspots have been shown to be reliable in detecting actual BA, although detection of smaller fires is limited, and show low commission errors in all land covers except in urban areas, especially related to industrial heat sources [97]. Although our algorithm masks urban areas before identifying BC pixels, the spatial disagreement between the LC product and S2 or Landsat images generate residual unmasked urban areas where BC pixels can be identified, increasing commission errors. A crucial issue when developing and optimizing our algorithm was defining the limit where small fires were to be detected or BC pixels were considered insufficient, owing to lack of sufficient hotspots. Two empirical thresholds were used for the surface covered by hotspots and by the BC pixels (detailed at the end of Section 2.2.2). However, some tiles may omit all burned areas because the BC pixels were considered to be insufficient, while in some others the algorithm may detect enough BC pixels located in falsely detected hotspots causing significant commissions.

The quality assurance of the algorithm has been divided into three exercises. First, the BA results were compared with reference data derived from Sentinel-2 images at 10 m, by analyzing 369 pairs of images and located at 50 sites selected by stratified random sampling. The sampling process took into account both the predominant biome present in each sampling unit and the fire activity; image availability and cloud presence were also checked to obtain meaningful long-period samples. The preliminary algorithm showed higher omissions (27–35%) than commission errors (9–11%). It should be noted that there is a bias here since both the BA product at 10 and 20 m (BAS2-10 and BAS2-20) and the reference data were derived from the same dataset (S2 images). However, the BA product at 30 m (BAL-30) was generated from a fully independent dataset (Landsat images), and the results suggest the robust performance of the algorithm with omissions and commissions of 35% and 11%, respectively. When processing S2 images from 2016 onwards, the algorithm can detect BA at both 20 and 10 m of spatial resolution. According to QA, the product at 10 m performed only slightly better than the 20 m resolution, with omissions and commissions being only 1.1% and 0.3% lower. This is caused mainly by the way the static probabilities are computed, because it consists of a weighted average comprising four variables where NBR2 and MIRBI (at 20 m) tend to carry more weight than NIR and NBR (at 10 m). Moreover, processing BAS2-10 maps at the 50 QA sites took longer on average than for BAS2-20 maps (5.9 vs. 4.2 min per monthly BA map), which suggests that the 20 m resolution is more suitable when processing BA from S2 data. Accuracy metrics showed much better results for this algorithm than for existing global BA products at coarse resolution, especially in terms of omissions, which were reduced from over 50% to 35% with Landsat data at 30 m, or 27–28% with S2; commissions also decreased, albeit less significantly (Table 5). These results coincide with the trend observed for other global or continental BA products at medium resolution such as FireCCISFD11 and GABAM [18,22], where a greater decrease was found for omissions than for commissions, when compared with products at coarse resolution.

The second exercise computed the reporting accuracy for BA detection. MCD64A1 was the first product when detecting burned pixels after they had actually burned, followed by FireCCI51, BAS2-10 and BAS2-20, and BAL-30 (Figure 15). However, taking into account the revisit time of each satellite, our algorithm detected between 81–84% of the burned areas in the first acquired image after the fire (the first 5 days for BAS2-10 and BAS2-20, or the first 8 days for BAL-30), while products obtained from MODIS data, with an image every day, detected 78% (MCD64A1) or 32% (FireCCI51) after the first day. It should be mentioned that MCD64A1 at 500 m detects 53% of BA the exact same day as the active fire was recorded.

The third exercise was applied to three larger test sites of 5 × 5 degrees (about 550 × 550 km²), where our BA results were compared with existing global BA products

to assess the quality of the product. The comparison showed good concordance with FireCCI51 and MCD64A1, especially at the test site in boreal forests, Siberia, where highest values for r^2 and slopes closest to 1 were obtained. In Africa and Central America our BAS2-20 detected a larger burned surface, since both products at coarse resolution failed to identify small fires; however, they managed to detect larger BA. GABAM, in contrast, showed significant omissions when compared to other products at all three test sites, despite its medium spatial resolution at 30 m. This may have been caused by the way its algorithm works, since it is based on a comparison between two consecutive years, selecting the date with the strongest burned signal from each year [22] and may also omit burned pixels that had already burned the previous year. The total burned surface in 2019 was 163,000 km^2 at these sites, according to BAS2-20; this means an increase in BA of 35% when compared with FireCCI51 (121,000 km^2), or up to 65% if compared with MCD64A1 (99,000 km^2).

The performance of each product is illustrated in three representative sample areas located at QA site 30PWQ between Ghana and the Ivory Coast (Figure 22), QA site 46QGF in Myanmar (Figure 23) and the test site from Central America (Figure 24). BAS2-10, BAS2-20, and BAL-30 maps (in QA areas 30PWQ and 46QGF) detected practically the same BA, with very few differences, despite being at three different spatial resolutions and being derived from two independent datasets. However, products at coarser resolution omitted most small fires in all three sample areas, especially in 46QGF and Central America where most BA are small and dispersed. GABAM seems to have detected as much burned area as our algorithm in 30PWQ and Central America, but omitted a significant amount of BA in 46QGF, with similar results to those obtained by MODIS BA products despite its higher spatial resolution. There are also some BA in QA area 30PWQ that were only detected by GABAM, which may not actually be errors, but rather areas that had burned at another time of the year, since the burning date is unknown in GABAM and BA from the whole year 2019 are shown. The dates when BA were detected are also very similar, with coarse-resolution products generally identifying burned pixels some days earlier, although a few areas seem to have been detected first by BAS2-10 and BAS2-20 in tile 30PWQ.
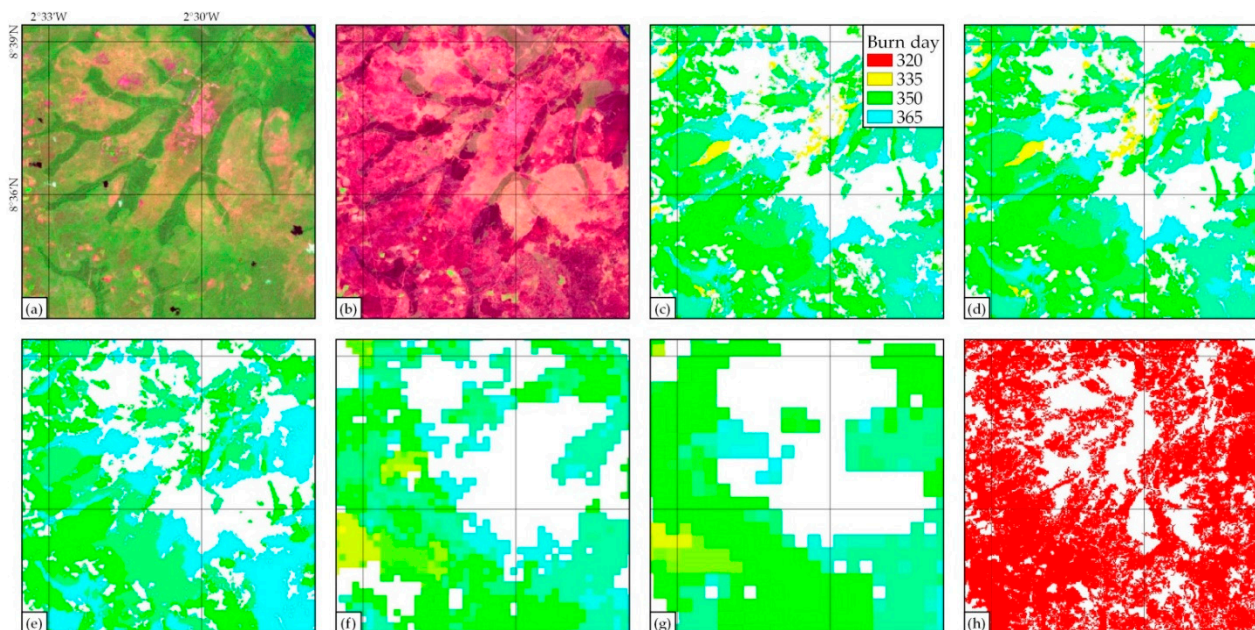
Figure 22. Different results in a sample area located at the QA site 30PWQ, between Ghana and Ivory Coast, the main LC classes being savannas and grasslands. (**a**) S2 image from the 320th day of 2019 (November 16th), with a LongSWIR/NIR/Red color composition; (**b**) S2 image from the 365th day of the same year (December 31st), with the same color; (**c–g**) areas burned between these images according to BAS2-10, BAS2-20, and BAL-30 maps and FireCCI51 and MCD64A1 global products, respectively; and (**h**) GABAM product from 2019, where the burning day is unknown.
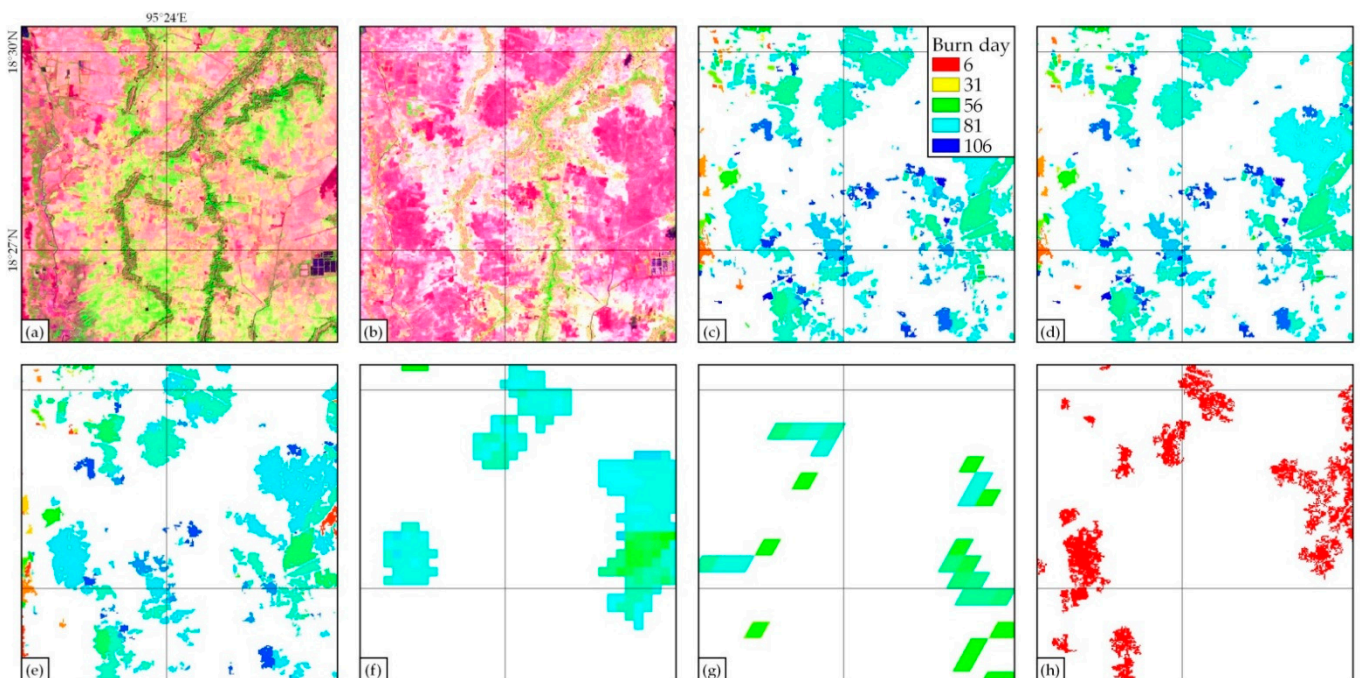
Figure 23. Different results in a sample area located at the QA site 46QGF, in Myanmar, the main LC class being croplands. (**a**) S2 image from the 6th day of 2019 (6th January), with a LongSWIR/NIR/Red color composition; (**b**) S2 image from the 106th day of the same year (16th April), with the same color; (**c**–**g**) areas burned between these images according to BAS2-10, BAS2-20, and BAL-30 maps and FireCCI51 and MCD64A1 global products, respectively; and (**h**) GABAM product from 2019, where the burning day is unknown.
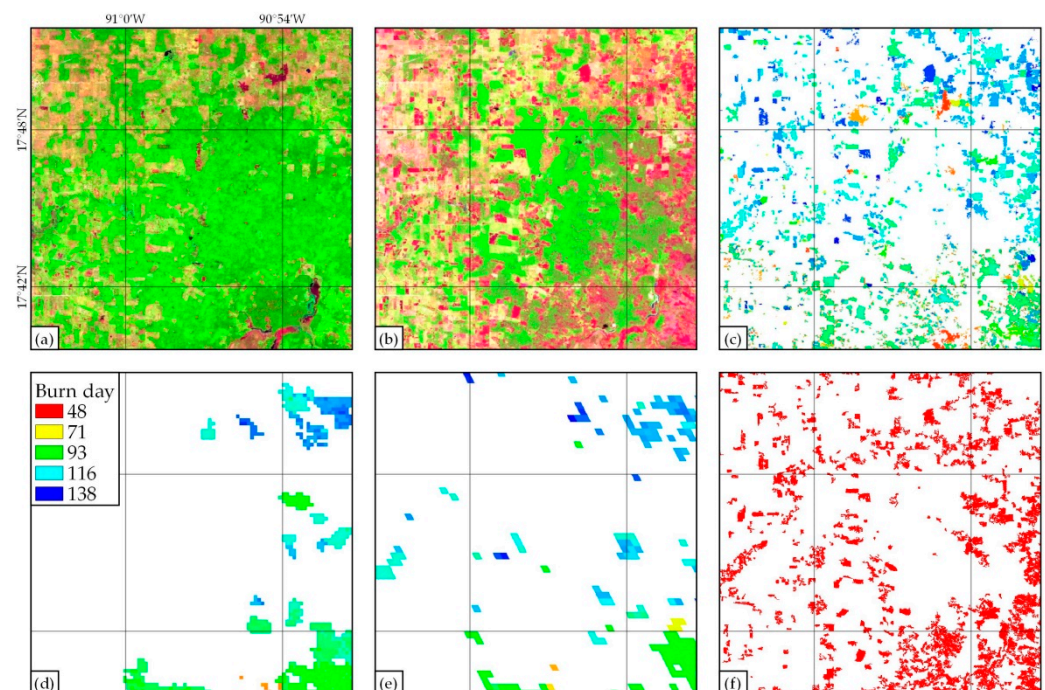
Figure 24. Different results in a sample area located at the test site from Central America, at the border between Mexico and Guatemala, the main LC class being woody savannas. (**a**) S2 image from the 48th day of 2019 (17th February), with a LongSWIR/NIR/Red color composition; (**b**) S2 image from the 138th day of the same year (18th May), with the same color; (**c**–**e**) areas burned between these images according to BAS2-20 maps and FireCCI51 and MCD64A1 global products, respectively; and (**f**) GABAM product from 2019, where the burning day is unknown.

According to the exercises for quality assurance, three main sources were found for commissions. One was partially caused by misclassifications in the land-cover map derived from MODIS data at 500 m (the IGBP classification from product MCD12Q1). The proposed BA algorithm applies many restrictions in croplands to avoid commissions, although not all croplands are correctly identified on the LC map. Many agricultural fields were found to be classified as grasslands, so they did not receive the restrictions that needed to be applied on croplands and therefore recently harvested fields were mapped as having burned. This is the reason most commissions in the QA are in grasslands, as shown in Figure 14—they actually belong to croplands. This issue could be solved if a more accurate and higher-resolution LC map were used, such as the Copernicus Land-Cover map [54], which is already available in GEE but not used by this algorithm because it does not cover as many years as the MCD12Q1 product. The second main source for the detected commissions is related to reporting accuracy. Especially in the case of BAL-30 maps obtained from Landsat data, acquisition dates did not coincide exactly with the RD period, and areas already burned on the first date, which were not part of the BA in the reference data, might be observed later in Landsat data. Since these areas appear as unburned in the RD but burned in BAL-30, they were labeled as commissions. To a lesser extent, BAS2-10 and BAS2-20 maps obtained from S2 data also displayed this type of commission, albeit in this case caused by a delay in the detection of the algorithm: around 15% of the total committed area among the 50 QA sites was detected in just one site (tile 30NYP, located in Ghana), and was caused by this delay in detection dates. The RP tool from BAMT used for reference data creation [41] and the BA algorithm presented here do not use exactly the same approach for cloud masking, and this causes areas to be observed as burned for the first time on different dates. Despite being estimated as commissions in this QA, these areas are actually not committed. A third source of commissions was found at the site from Siberia. Boreal forests were found to suffer a decrease in reflectance at the end of summer in September, and the vegetation spectral signal turned out to be similar to that of BA. If a continuous observation of the ground is possible, then the change would seem to be gradual and not classified as BA, although low observability due to high cloud coverage may result in this change appearing sudden, in which case these areas will be committed as burned.

As for omissions, another three sources were identified, with the first two affecting croplands and forests, respectively. As mentioned previously, several restrictions are applied on croplands to reduce usual commissions, since agricultural fields after harvesting and burned areas evidence similar spectral characteristics and are difficult to discriminate. These restrictions succeeded in reducing commissions considerably in croplands, but at the same time caused an increase in omissions. The second cause for omissions affects forests and is in MGRS tiles where areas were burned in both forests and other land covers. Because most burned forests display several degrees of burn severity, the BC pixels in the sampling step of the algorithm tend to gather in forested areas with high burn severity. Therefore, forests with medium to low burn severity are generally not well represented in the samples, and since these forested areas are closer to the unburned distribution in the samples, they are usually omitted in the final BA map. A third origin for omissions, albeit a less significant one, was found to be related to reporting accuracy, since some BA were detected after the last date in the RD period and labeled as omitted areas. Even though it has not been observed in the QA areas or at test sites, there could also be a fourth type of omission. To detect a burned pixel, the algorithm requires at least one previous and one further subsequent observation of the pixel, although one of these may be missing due to few available images or persistent clouds. In this case, omissions may increase considerably, even in areas that were labeled as having been observed in the exported BA map. This is likeliest to happen in tropical regions, where over 70% of Landsat scenes have been observed to be covered by clouds [98] and vegetation recovers in a few weeks after the fire [71,72]; in boreal regions, on the contrary, fire scars remain for several years [99,100], which makes it easier to detect BA even with persistent clouds.

Finally, the authors would like to note the importance of Google Earth Engine, a cloud-computing platform that enables its data catalogs to be accessed with huge processing capabilities. The use of GEE avoids the need for user technical expertise in information technology, and previously required enormous capacities for data acquisition and storage [35]. In this study, processing dense data series to detect BA proved feasible at high speeds, taking just 4–6 min on average per monthly BA map over 110×110 km^2 at 10, 20, or 30 m of spatial resolution. However, several limitations were also found when designing and implementing the algorithm on the platform. The most challenging job was finding an efficient approach to compare individual images, since iterating on a list of images was found to be quite memory-consuming for our algorithm implementation. Even though large data series can be handled, iterative analyses slowed down the process considerably—especially when computing P_{dy} maps, where every date needed to be compared to several previous and following images—and this required a reduction in data. Several filters were applied to the original list of images until no more than 50 images remained, so that our algorithm was able to conclude the BA detection. The platform also proved to be limited for patch and object identification, with the main limitation being a maximum size of 1024 pixels per patch, making it impossible to identify burned areas larger than 10, 41, or 92 ha, depending on spatial resolution (10, 20, or 30 m). This was tried by way of implementation of a two-phase strategy for seed identification and region growing at the end of the algorithm to reduce commissions, but was not achieved; similarly, other approaches such as spatial dilation and cumulative cost maps proved too time-consuming for GEE, as mentioned previously. The last issue was found when computing image statistics such as Otsu thresholds or sampling pixel values, which again requires some processing capacity; this can be solved by working at coarser scales (GEE allows extracting information at different spatial resolutions, despite the native resolution of the image), although some accuracy may be lost.

5. Conclusions

A new automatic global BA detection algorithm based on Landsat or Sentinel-2 reflectance and MODIS active fires is presented in this paper, which may be processed at three different spatial resolutions—10, 20, or 30 m—depending on whether S2 or Landsat data are chosen; this is still a preliminary algorithm, and a rigorous validation with independent data should still be done in order to statistically estimate the algorithm's accuracy, identify error sources and therefore propose necessary modifications for the algorithm before an operational global BA detection. The new methodology involves detecting some burned candidate pixels around hotspots based on their spectral changes, using these candidate pixels to classify single images from a dense time series with burn probability values, and then analyzing the temporal evolution of these probabilities to detect BA and their dates. The algorithm was implemented in Google Earth Engine, taking advantage of its huge cloud-computing and processing capabilities; since the platform's datasets are used exclusively, BA mapping can be extended globally to any year from 2000 up to the present.

The algorithm was processed at 50 sites from 2019 selected by a stratified random sampling, where commissions in the range of 9–11% were obtained, and omissions varied between 27–35%, while nearly 20% of commissions and over 50% of omissions were observed for existing products at coarse resolution (FireCCI51 and MCD64A1), respectively. Similarly, the algorithm was processed with Sentinel-2 data at 20 m at three larger sites, where an increase in BA of 65% was found when compared with MCD64A1, or 35% when compared with FireCCI51. This must be researched further to confirm a global trend, as it would impact on current estimations of greenhouse gas emissions into the atmosphere.

Author Contributions: E.R. developed the algorithm and generated the reference data in QA areas. A.B. supervised the process. E.R., A.B., A.I. and E.C. wrote the manuscript. All authors have read and agreed to the published version of the manuscript.

Institutional Review Board Statement: Not applicable.

Informed Consent Statement: Not applicable.

Conflicts of Interest: The authors declare no conflict of interest.

Appendix A

Table A1. 50 QA areas selected by the stratified random sampling methodology, and their biomes, first and last dates in YYYYMMDD format (with YYYY, MM, and DD standing for the year, month, and day of month), length in days, low or high fire activity, and number of images.

Biome	Tile	First Date	Last Date	Length (Days)	Fire Activity	Number of Images
Boreal forest	49WFM	20190617	20190913	88	high	5
	42VWN	20190716	20191004	80	high	2
Mediterranean forest	31SEA	20190415	20190902	140	high	9
Others	38RQU	20190111	20190327	75	high	2
	42RXT	20190114	20191205	325	high	24
	42RXU	20190114	20191205	325	high	25
	34JHT	20190103	20191219	350	low	13
Temperate forest	49SFC	20190630	20191028	120	high	7
	56HLJ	20190101	20191231	364	high	14
	16SBF	20190317	20191102	230	high	6
Temperate grassland and savanna	36LVQ	20190417	20191103	200	high	10
	36PUQ	20190103	20190403	90	high	6
	44TPP	20190515	20191029	167	high	3
	37UGQ	20190401	20191124	237	low	12
Tropical and subtropical savanna	33LYE	20190430	20191106	190	high	13
	33LWK	20190418	20190920	155	high	11
	35LNF	20190503	20191109	190	high	12
	30NYP	20190102	20190313	70	high	6
	35LKH	20190501	20191102	185	high	11
	34MCV	20190609	20190917	100	high	7
	31PCN	20191016	20191230	75	high	6
	37LDD	20190801	20191204	125	high	10
	36LWH	20190708	20191105	120	high	8
	37LDE	20190523	20191119	180	high	10
	35NPF	20190106	20190312	65	high	6
	36MVS	20190522	20191014	145	high	10
	55LBC	20190507	20191213	220	high	8
	35NPJ	20190923	20191227	95	high	5
	30PWQ	20191116	20191231	45	high	5
	34PHR	20191029	20191228	60	high	6
	33MXT	20190607	20190831	85	low	6
	52LHJ	20190127	20191223	330	low	8
	30PWR	20190110	20190420	100	low	8
	34KCD	20190124	20191210	320	low	15
	21KYR	20190916	20191230	105	low	4
	31PBQ	20190117	20190407	80	low	4
	34KBC	20190107	20191213	340	low	10
	34PCU	20190113	20190428	110	low	5
	37PDP	20190815	20191228	135	low	5

Table A1. *Cont.*

Biome	Tile	First Date	Last Date	Length (Days)	Fire Activity	Number of Images
	46QFL	20190101	20190531	150	high	13
	28PGT	20190102	20190527	145	high	10
	47QLC	20190113	20190428	105	high	8
	46QFG	20190101	20190426	115	high	9
	21MZP	20190701	20190830	60	high	4
Tropical forest	46QGF	20190101	20190421	110	high	10
	48PVU	20190106	20190411	95	high	6
	47QRA	20190117	20190422	95	high	9
	21LXH	20190427	20191004	160	low	7
	23LQF	20190422	20191113	205	low	4
	20LKN	20190509	20190916	130	low	2

Table A2. Accuracy measures for our algorithm at 3 spatial resolutions and for 2 global BA products by QA site: commissions, omissions, and Dice coefficients, all expressed in percentages. A dash in all 3 of the accuracy metrics means that no BA was detected by the algorithm or product, nor in the reference data.

MGRS Tile	BAS2-10			BAS2-20			BAL-30			FireCCI51			MCD64A1		
	CE	OE	DC	CE	OE	DC	CE	OE	DC	CE	OE	DC	CE	OE	DC
49WFM	77.6	0.7	36.5	79.7	0.4	33.7	46.0	3.6	69.2	20.0	22.7	78.7	8.4	12.4	89.6
42VWN	100.0	0.0	0.0	100.0	0.0	0.0	-	-	-	-	-	-	-	-	-
31SEA	2.7	30.5	81.1	2.5	30.6	81.1	3.3	36.1	77.0	41.8	36.4	60.8	32.8	49.4	57.7
38RQU	-	-	-	-	-	-	-	-	-	-	-	-	-	-	-
42RXT	14.2	95.4	8.8	15.8	96.3	7.1	13.6	93.4	12.2	28.2	87.0	22.0	41.9	83.7	25.4
42RXU	6.6	99.6	0.9	2.6	99.5	0.9	2.6	100.0	0.1	12.0	85.4	25.0	6.7	96.3	7.2
34JHT	-	-	-	-	-	-	-	-	-	-	-	-	-	-	-
49SFC	0.0	100.0	0.0	0.0	100.0	0.0	0.0	100.0	0.0	0.0	100.0	0.0	0.0	100.0	0.0
56HLJ	10.5	21.3	83.7	12.2	22.1	82.6	5.2	90.5	17.3	39.1	73.9	36.5	64.3	38.6	45.2
16SBF	34.8	90.2	17.1	28.5	86.5	22.8	79.6	95.6	7.3	39.5	74.0	36.4	93.7	55.2	11.0
36LVQ	6.2	14.6	89.4	6.1	16.0	88.6	6.9	23.5	84.0	8.0	61.0	54.7	6.7	71.8	43.4
36PUQ	0.2	2.9	98.4	0.3	2.9	98.4	1.1	3.5	97.7	3.4	15.0	90.4	8.1	6.5	92.7
44TPP	-	-	-	-	-	-	-	-	-	-	-	-	-	-	-
37UGQ	2.2	69.3	46.7	2.3	70.1	45.7	1.8	75.4	39.4	27.9	98.6	2.7	24.8	92.7	13.4
33LYE	1.5	13.9	91.9	1.7	14.5	91.4	2.4	21.0	87.3	13.9	51.6	62.0	15.9	55.9	57.9
33LWK	3.3	1.5	97.6	3.4	1.7	97.4	4.6	3.7	95.8	8.7	3.6	93.8	7.3	23.8	83.7
35LNF	2.2	50.7	65.5	2.3	52.5	64.0	3.7	54.6	61.7	20.2	38.4	69.6	19.6	53.7	58.8
30NYP	23.8	12.0	81.7	23.3	13.9	81.1	22.9	27.4	74.7	38.9	53.5	52.8	20.2	92.6	13.6
35LKH	2.3	15.3	90.8	2.8	16.2	90.0	6.6	22.3	84.8	18.8	37.2	70.9	16.0	53.4	59.9
34MCV	12.1	30.7	77.5	12.3	40.9	70.6	31.3	68.9	42.8	54.3	93.8	10.9	38.2	96.6	6.4
31PCN	0.5	29.6	82.5	0.6	29.6	82.4	0.9	32.0	80.7	12.5	1.1	92.9	10.8	5.2	91.9
37LDD	6.8	37.0	75.2	7.4	39.6	73.1	14.4	60.5	54.0	25.9	70.4	42.3	27.3	68.4	44.0
36LWH	5.8	11.3	91.4	6.2	11.8	90.9	10.3	20.3	84.4	22.5	44.6	64.6	16.7	71.6	42.4
37LDE	2.8	17.8	89.1	2.8	18.5	88.6	4.8	33.3	78.4	12.5	39.7	71.4	12.3	33.9	75.4
35NPF	11.8	35.0	74.8	12.4	36.1	73.9	22.2	31.8	72.7	46.2	56.5	48.1	32.5	88.3	20.0
36MVS	1.8	15.7	90.7	1.9	16.5	90.2	2.2	27.2	83.5	9.5	20.8	84.5	8.7	33.0	77.3
55LBC	5.6	11.7	91.2	5.6	11.7	91.2	5.9	18.7	87.2	15.3	7.0	88.6	10.3	24.6	81.9
35NPJ	4.2	14.3	90.5	4.6	14.2	90.4	8.2	20.9	85.0	13.1	56.3	58.1	15.0	57.7	56.5
30PWQ	3.8	6.1	95.0	4.2	6.0	94.9	5.7	6.9	93.7	23.1	32.0	72.2	17.6	35.0	72.7
34PHR	10.4	27.3	80.2	11.6	23.2	82.2	24.2	22.8	76.5	46.8	72.9	35.9	41.1	91.5	14.9
33MXT	4.6	42.7	71.6	4.4	45.8	69.2	8.1	64.6	51.1	40.2	87.8	20.2	60.7	89.5	16.6
52LHJ	22.2	2.3	86.6	18.8	3.0	88.4	65.6	3.9	50.7	13.0	2.3	92.0	7.2	10.3	91.2
30PWR	12.2	61.5	53.5	12.8	66.6	48.3	52.8	73.0	34.3	98.2	100.0	0.1	0.0	100.0	0.0
34KCD	4.7	11.9	91.5	5.6	12.5	90.8	9.7	20.0	84.8	0.0	100.0	0.0	20.4	69.1	44.5
21KYR	99.7	95.6	0.6	99.9	99.1	0.1	96.3	26.6	7.0	0.0	100.0	0.0	0.0	100.0	0.0
31PBQ	0.0	100.0	0.0	0.0	100.0	0.0	0.0	100.0	0.0	0.0	100.0	0.0	0.0	100.0	0.0
34KBC	-	-	-	-	-	-	-	-	-	-	-	-	-	-	-
34PCU	4.9	32.0	79.3	6.0	34.5	77.2	8.5	41.4	71.4	0.0	100.0	0.0	0.0	100.0	0.0
37PDP	0.0	100.0	0.0	0.0	100.0	0.0	0.0	100.0	0.0	0.0	100.0	0.0	0.0	100.0	0.0
46QFL	10.8	44.3	68.6	11.0	45.5	67.6	12.7	53.0	61.1	0.0	100.0	0.0	24.9	68.4	44.5
28PGT	4.9	33.0	78.6	5.1	34.8	77.3	9.0	44.7	68.8	24.5	65.0	47.8	31.0	55.1	54.4
47QLC	10.2	51.8	62.8	9.9	57.4	57.9	9.8	71.1	43.8	0.0	100.0	0.0	31.9	91.7	14.7
46QFG	8.5	58.5	57.1	7.7	61.6	54.2	8.9	70.2	45.0	33.5	89.1	18.7	48.4	68.6	39.1
21MZP	5.9	49.6	65.6	6.2	50.3	65.0	13.1	23.8	81.2	37.0	23.4	69.1	34.3	39.7	62.9
46QGF	4.3	22.6	85.6	4.7	27.6	82.3	15.5	33.1	74.7	40.1	70.4	39.7	41.2	88.0	20.0
48PVU	22.1	42.4	66.2	22.2	45.4	64.2	28.3	57.0	53.8	36.1	95.0	9.3	38.7	96.1	7.3
47QRA	33.1	41.5	62.4	31.9	56.0	53.5	26.4	76.3	35.9	0.0	100.0	0.0	0.0	100.0	0.0
21LXH	82.3	31.5	28.2	80.7	32.8	30.0	89.7	38.9	17.6	0.0	100.0	0.0	0.0	100.0	0.0
23LQF	98.9	50.2	2.2	99.2	59.6	1.6	99.4	68.9	1.3	0.0	100.0	0.0	0.0	100.0	0.0
20LKN	100.0	0.0	0.0	100.0	0.0	0.0	100.0	0.0	0.0	-	-	-	-	-	-

References

1. GCOS. The Global Observing System For Climate: Implementation Needs GCOS-200 (GOOS-214). Available online: https://library.wmo.int/doc_num.php?explnum_id=3417 (accessed on 25 October 2021).
2. Bowman, D.M.J.S.; Balch, J.K.; Artaxo, P.; Bond, W.J.; Carlson, J.M.; Cochrane, M.A.; D'Antonio, C.M.; DeFries, R.S.; Doyle, J.C.; Harrison, S.P.; et al. Fire in the Earth System. *Science* **2009**, *324*, 481–484. [CrossRef]
3. Van Der Werf, G.R.; Randerson, J.T.; Giglio, L.; Van Leeuwen, T.T.; Chen, Y.; Rogers, B.M.; Mu, M.; Van Marle, M.J.E.; Morton, D.C.; Collatz, G.J.; et al. Global fire emissions estimates during 1997–2016. *Earth Syst. Sci. Data* **2017**, *9*, 697–720. [CrossRef]
4. Roos, C.I.; Scott, A.C.; Belcher, C.M.; Chaloner, W.G.; Aylen, J.; Bird, R.B.; Coughlan, M.R.; Johnson, B.R.; Johnston, F.H.; McMorrow, J.; et al. Living on a flammable planet: Interdisciplinary, cross-scalar and varied cultural lessons, prospects and challenges. *Philos. Trans. R. Soc. B Biol. Sci.* **2016**, *371*, 20150469. [CrossRef] [PubMed]
5. Forkel, M.; Dorigo, W.; Lasslop, G.; Teubner, I.; Chuvieco, E.; Thonicke, K. A data-driven approach to identify controls on global fire activity from satellite and climate observations (SOFIA V1). *Geosci. Model Dev.* **2017**, *10*, 4443–4476. [CrossRef]
6. Tansey, K.; Grégoire, J.; Stroppiana, D.; Sousa, A.; Silva, J.; Pereira, J.M.C.; Boschetti, L.; Maggi, M.; Brivio, P.A.; Fraser, R.; et al. Vegetation burning in the year 2000: Global burned area estimates from SPOT VEGETATION data. *J. Geophys. Res.* **2004**, *109*, D14S03. [CrossRef]
7. Simon, M.; Plummer, S.; Fierens, F.; Hoelzemann, J.J.; Arino, O. Burnt area detection at global scale using ATSR-2: The GLOBSCAR products and their qualification. *J. Geophys. Res.* **2004**, *109*, D14S02. [CrossRef]
8. Tansey, K.; Grégoire, J.; Defourny, P.; Leigh, R.; Pekel, J.; Van Bogaert, E.; Bartholomé, E. A new, global, multi-annual (2000–2007) burnt area product at 1 km resolution. *Geophys. Res. Lett.* **2008**, *35*. [CrossRef]
9. Tansey, K.; Bradley, A.; Smets, B.; van Best, C.; Lacaze, R. The Geoland2 BioPar burned area product. In Proceedings of the EGU General Assembly Conference Abstracts, Viena, Austria, 22–27 April 2012; p. 4727.
10. Roy, D.P.; Jin, Y.; Lewis, P.E.; Justice, C.O. Prototyping a global algorithm for systematic fire-affected area mapping using MODIS time series data. *Remote Sens. Environ.* **2005**, *97*, 137–162. [CrossRef]
11. Giglio, L.; Loboda, T.; Roy, D.P.; Quayle, B.; Justice, C.O. An active-fire based burned area mapping algorithm for the MODIS sensor. *Remote Sens. Environ.* **2009**, *113*, 408–420. [CrossRef]
12. Giglio, L.; Boschetti, L.; Roy, D.P.; Humber, M.L.; Justice, C.O. The Collection 6 MODIS burned area mapping algorithm and product. *Remote Sens. Environ.* **2018**, *217*, 72–85. [CrossRef]
13. Alonso-Canas, I.; Chuvieco, E. Global burned area mapping from ENVISAT-MERIS and MODIS active fire data. *Remote Sens. Environ.* **2015**, *163*, 140–152. [CrossRef]
14. Chuvieco, E.; Yue, C.; Heil, A.; Mouillot, F.; Alonso-Canas, I.; Padilla, M.; Pereira, J.M.; Oom, D.; Tansey, K. A new global burned area product for climate assessment of fire impacts. *Glob. Ecol. Biogeogr.* **2016**, *25*, 619–629. [CrossRef]
15. Chuvieco, E.; Lizundia-Loiola, J.; Lucrecia Pettinari, M.; Ramo, R.; Padilla, M.; Tansey, K.; Mouillot, F.; Laurent, P.; Storm, T.; Heil, A.; et al. Generation and analysis of a new global burned area product based on MODIS 250 m reflectance bands and thermal anomalies. *Earth Syst. Sci. Data* **2018**, *10*, 2015–2031. [CrossRef]
16. Lizundia-Loiola, J.; Otón, G.; Ramo, R.; Chuvieco, E. A spatio-temporal active-fire clustering approach for global burned area mapping at 250 m from MODIS data. *Remote Sens. Environ.* **2020**, *236*, 111493. [CrossRef]
17. Randerson, J.T.; Chen, Y.; van der Werf, G.R.; Rogers, B.M.; Morton, D.C. Global burned area and biomass burning emissions from small fires. *J. Geophys. Res. Biogeosci.* **2012**, *117*. [CrossRef]
18. Roteta, E.; Bastarrika, A.; Padilla, M.; Storm, T.; Chuvieco, E. Development of a Sentinel-2 burned area algorithm: Generation of a small fire database for sub-Saharan Africa. *Remote Sens. Environ.* **2019**, *222*, 1–17. [CrossRef]
19. Ramo, R.; Roteta, E.; Bistinas, I.; van Wees, D.; Bastarrika, A.; Chuvieco, E.; van der Werf, G.R. African burned area and fire carbon emissions are strongly impacted by small fires undetected by coarse resolution satellite data. *Proc. Natl. Acad. Sci. USA* **2021**, *118*, e2011160118. [CrossRef]
20. Padilla, M.; Stehman, S.V.; Ramo, R.; Corti, D.; Hantson, S.; Oliva, P.; Alonso-Canas, I.; Bradley, A.V.; Tansey, K.; Mota, B.; et al. Comparing the accuracies of remote sensing global burned area products using stratified random sampling and estimation. *Remote Sens. Environ.* **2015**, *160*, 114–121. [CrossRef]
21. Boschetti, L.; Roy, D.P.; Giglio, L.; Huang, H.; Zubkova, M.; Humber, M.L. Global validation of the collection 6 MODIS burned area product. *Remote Sens. Environ.* **2019**, *235*, 111490. [CrossRef] [PubMed]
22. Long, T.; Zhang, Z.; He, G.; Jiao, W.; Tang, C.; Wu, B.; Zhang, X.; Wang, G.; Yin, R. 30m resolution Global Annual Burned Area Mapping based on Landsat images and Google Earth Engine. *Remote Sens.* **2019**, *11*, 489. [CrossRef]
23. Updated 30 m Resolution Global Annual Burned Area Map—Remote Sensing of Global Change. Available online: https://vapd.gitlab.io/post/gabam/ (accessed on 11 February 2021).
24. Wei, M.; Zhang, Z.; Long, T.; He, G.; Wang, G. Monitoring Landsat Based Burned Area as an Indicator of Sustainable Development Goals. *Earth's Future* **2021**, *9*, e2020EF001960. [CrossRef]
25. Hawbaker, T.J.; Vanderhoof, M.K.; Beal, Y.-J.; Takacs, J.D.; Schmidt, G.L.; Falgout, J.T.; Williams, B.; Fairaux, N.M.; Caldwell, M.K.; Picotte, J.J.; et al. Mapping burned areas using dense time-series of Landsat data. *Remote Sens. Environ.* **2017**, *198*, 504–522. [CrossRef]
26. Hawbaker, T.J.; Vanderhoof, M.K.; Schmidt, G.L.; Beal, Y.J.; Picotte, J.J.; Takacs, J.D.; Falgout, J.T.; Dwyer, J.L. The Landsat Burned Area algorithm and products for the conterminous United States. *Remote Sens. Environ.* **2020**, *244*, 111801. [CrossRef]

27. Goodwin, N.R.; Collett, L.J. Development of an automated method for mapping fire history captured in Landsat TM and ETM+ time series across Queensland, Australia. *Remote Sens. Environ.* **2014**, *148*, 206–221. [CrossRef]

28. Liu, J.; Heiskanen, J.; Maeda, E.E.; Pellikka, P.K.E. Burned area detection based on Landsat time series in savannas of southern Burkina Faso. *Int. J. Appl. Earth Obs. Geoinf.* **2018**, *64*, 210–220. [CrossRef]

29. Filipponi, F. Exploitation of sentinel-2 time series to map burned areas at the national level: A case study on the 2017 Italy wildfires. *Remote Sens.* **2019**, *11*, 622. [CrossRef]

30. Llorens, R.; Sobrino, J.A.; Fernández, C.; Fernández-Alonso, J.M.; Vega, J.A. A methodology to estimate forest fires burned areas and burn severity degrees using Sentinel-2 data. Application to the October 2017 fires in the Iberian Peninsula. *Int. J. Appl. Earth Obs. Geoinf.* **2021**, *95*, 102243. [CrossRef]

31. Roy, D.P.; Huang, H.; Boschetti, L.; Giglio, L.; Yan, L.; Zhang, H.H.; Li, Z. Landsat-8 and Sentinel-2 burned area mapping—A combined sensor multi-temporal change detection approach. *Remote Sens. Environ.* **2019**, *231*, 111254. [CrossRef]

32. Boschetti, L.; Roy, D.P.; Justice, C.O.; Humber, M.L. MODIS–Landsat fusion for large area 30m burned area mapping. *Remote Sens. Environ.* **2015**, *161*, 27–42. [CrossRef]

33. Belenguer-Plomer, M.A.; Tanase, M.A.; Chuvieco, E.; Bovolo, F. CNN-based burned area mapping using radar and optical data. *Remote Sens. Environ.* **2021**, *260*, 112468. [CrossRef]

34. Stroppiana, D.; Azar, R.; Calò, F.; Pepe, A.; Imperatore, P.; Boschetti, M.; Silva, J.M.N.; Brivio, P.A.; Lanari, R. Integration of optical and SAR data for burned area mapping in Mediterranean regions. *Remote Sens.* **2015**, *7*, 1320–1345. [CrossRef]

35. Gorelick, N.; Hancher, M.; Dixon, M.; Ilyushchenko, S.; Thau, D.; Moore, R. Google Earth Engine: Planetary-scale geospatial analysis for everyone. *Remote Sens. Environ.* **2017**, *202*, 18–27. [CrossRef]

36. Hansen, M.C.; Potapov, P.V.; Moore, R.; Hancher, M.; Turubanova, S.A.; Tyukavina, A.; Thau, D.; Stehman, S.V.; Goetz, S.J.; Loveland, T.R.; et al. High-resolution global maps of 21st-century forest cover change. *Science* **2013**, *342*, 850–853. [CrossRef]

37. Wang, L.; Diao, C.; Xian, G.; Yin, D.; Lu, Y.; Zou, S.; Erickson, T.A. A summary of the special issue on remote sensing of land change science with Google earth engine. *Remote Sens. Environ.* **2020**, *248*, 112002. [CrossRef]

38. Daldegan, G.A.; Roberts, D.A.; Ribeiro, F.d.F. Spectral mixture analysis in Google Earth Engine to model and delineate fire scars over a large extent and a long time-series in a rainforest-savanna transition zone. *Remote Sens. Environ.* **2019**, *232*, 111340. [CrossRef]

39. Roteta, E.; Oliva, P. Optimization of A Random Forest Classifier for Burned Area Detection in Chile Using Sentinel-2 Data. In Proceedings of the 2020 IEEE Latin American GRSS & ISPRS Remote Sensing Conference (LAGIRS), Santiago, Chile, 22–26 March 2020.

40. Seydi, S.T.; Akhoondzadeh, M.; Amani, M.; Mahdavi, S. Wildfire Damage Assessment over Australia Using Sentinel-2 Imagery and MODIS Land Cover Product within the Google Earth Engine Cloud Platform. *Remote Sens.* **2021**, *13*, 220. [CrossRef]

41. Roteta, E.; Bastarrika, A.; Franquesa, M.; Chuvieco, E. Landsat and Sentinel-2 Based Burned Area Mapping Tools in Google Earth Engine. *Remote Sens.* **2021**, *13*, 816. [CrossRef]

42. Verhegghen, A.; Eva, H.; Ceccherini, G.; Achard, F.; Gond, V.; Gourlet-Fleury, S.; Cerutti, P. The Potential of Sentinel Satellites for Burnt Area Mapping and Monitoring in the Congo Basin Forests. *Remote Sens.* **2016**, *8*, 986. [CrossRef]

43. Landsat Missions. Available online: https://www.usgs.gov/core-science-systems/nli/landsat (accessed on 24 January 2021).

44. The Worldwide Reference System | Landsat Science. Available online: https://landsat.gsfc.nasa.gov/about/worldwide-reference-system (accessed on 13 July 2021).

45. Arvidson, T.; Goward, S.; Gasch, J.; Williams, D. Landsat-7 long-term acquisition plan: Development and validation. *Photogramm. Eng. Remote Sens.* **2006**, *72*, 1137–1146. [CrossRef]

46. Masek, J.G.; Vermote, E.F.; Saleous, N.E.; Wolfe, R.; Hall, F.G.; Huemmrich, K.F.; Gao, F.; Kutler, J.; Lim, T.K. A landsat surface reflectance dataset for North America, 1990–2000. *IEEE Geosci. Remote Sens. Lett.* **2006**, *3*, 68–72. [CrossRef]

47. Vermote, E.; Justice, C.; Claverie, M.; Franch, B. Preliminary analysis of the performance of the Landsat 8/OLI land surface reflectance product. *Remote Sens. Environ.* **2016**, *185*, 46–56. [CrossRef] [PubMed]

48. ESA. Sentinel-2. Available online: http://www.esa.int/Applications/Observing_the_Earth/Copernicus/Sentinel-2 (accessed on 24 January 2021).

49. NGA. Geomatics—Coordinate Systems. Available online: https://earth-info.nga.mil/index.php?dir=coordsys&action=coordsys#tab_mgrs (accessed on 26 March 2021).

50. Gascon, F.; Bouzinac, C.; Thépaut, O.; Jung, M.; Francesconi, B.; Louis, J.; Lonjou, V.; Lafrance, B.; Massera, S.; Gaudel-Vacaresse, A.; et al. Copernicus Sentinel-2A calibration and products validation status. *Remote Sens.* **2017**, *9*, 584. [CrossRef]

51. Roy, D.P.; Boschetti, L.; Justice, C.O.; Ju, J. The collection 5 MODIS burned area product—Global evaluation by comparison with the MODIS active fire product. *Remote Sens. Environ.* **2008**, *112*, 3690–3707. [CrossRef]

52. MCD14DL | Earthdata. Available online: https://earthdata.nasa.gov/earth-observation-data/near-real-time/firms/c6-mcd14dl (accessed on 24 March 2021).

53. Sulla-Menashe, D.; Friedl, M. MCD12Q1 MODIS/Terra+Aqua Land Cover Type Yearly L3 Global 500 m SIN Grid V006. 2019. Available online: https://ladsweb.modaps.eosdis.nasa.gov/missions-and-measurements/products/MCD12Q1 (accessed on 25 October 2021).

54. Buchhorn, M.; Lesiv, M.; Tsendbazar, N.E.; Herold, M.; Bertels, L.; Smets, B. Copernicus global land cover layers-collection 2. *Remote Sens.* **2020**, *12*, 1044. [CrossRef]

55. Pekel, J.F.; Cottam, A.; Gorelick, N.; Belward, A.S. High-resolution mapping of global surface water and its long-term changes. *Nature* **2016**, *540*, 418–422. [CrossRef]
56. Key, C.H.; Benson, N. *The Normalized Burn Ratio (NBR): A Landsat TM Radiometric Measure of Burn Severity*; US Geological Survey, Northern Rocky Mountain Science Center: Bozeman, MT, USA, 1999.
57. García, M.J.L.; Caselles, V. Mapping burns and natural reforestation using thematic Mapper data. *Geocarto Int.* **1991**, *6*, 31–37. [CrossRef]
58. Trigg, S.; Flasse, S. An evaluation of different bi-spectral spaces for discriminating burned shrub-savannah. *Int. J. Remote Sens.* **2001**, *22*, 2641–2647. [CrossRef]
59. Huang, H.; Roy, D.P.; Boschetti, L.; Zhang, H.K.; Yan, L.; Kumar, S.S.; Gomez-Dans, J.; Li, J. Separability analysis of Sentinel-2A Multi-Spectral Instrument (MSI) data for burned area discrimination. *Remote Sens.* **2016**, *8*, 873. [CrossRef]
60. van Dijk, D.; Shoaie, S.; van Leeuwen, T.; Veraverbeke, S. Spectral signature analysis of false positive burned area detection from agricultural harvests using Sentinel-2 data. *Int. J. Appl. Earth Obs. Geoinf.* **2021**, *97*, 102296. [CrossRef]
61. Stroppiana, D.; Bordogna, G.; Carrara, P.; Boschetti, M.; Boschetti, L.; Brivio, P.A. A method for extracting burned areas from Landsat TM/ETM+ images by soft aggregation of multiple Spectral Indices and a region growing algorithm. *ISPRS J. Photogramm. Remote Sens.* **2012**, *69*, 88–102. [CrossRef]
62. Otsu, N. A Threshold Selection Method from Gray-Level Histograms. *IEEE Trans. Syst. Man Cybern.* **1979**, *9*, 62–66. [CrossRef]
63. Koutsias, N.; Karteris, M. Burned area mapping using logistic regression modeling of a single post-fire Landsat-5 Thematic Mapper image. *Int. J. Remote Sens.* **2000**, *21*, 673–687. [CrossRef]
64. Fraser, R.H.; Fernandes, R.; Latifovic, R. Multi-temporal burned area mapping using logistic regression analysis and change metrics. In Proceedings of the IEEE International Geoscience and Remote Sensing Symposium, Toronto, ON, Canada, 24–28 June 2002; Volume 3, pp. 1486–1488.
65. Pu, R.; Gong, P. Determination of burnt scars using logistic regression and neural network techniques from a single post-fire Landsat 7 ETM+ image. *Photogramm. Eng. Remote Sens.* **2004**, *70*, 841–850. [CrossRef]
66. Bastarrika, A.; Chuvieco, E.; Martín, M.P. Mapping burned areas from Landsat TM/ETM+ data with a two-phase algorithm: Balancing omission and commission errors. *Remote Sens. Environ.* **2011**, *115*, 1003–1012. [CrossRef]
67. Kaufman, Y.J.; Remer, L.A. Detection of Forests Using Mid-IR Reflectance: An Application for Aerosol Studies. *IEEE Trans. Geosci. Remote Sens.* **1994**, *32*, 672–683. [CrossRef]
68. Chuvieco, E.; Ventura, G.; Martín, M.P.; Gómez, I. Assessment of multitemporal compositing techniques of MODIS and AVHRR images for burned land mapping. *Remote Sens. Environ.* **2005**, *94*, 450–462. [CrossRef]
69. Lasaponara, R. Estimating spectral separability of satellite derived parameters for burned areas mapping in the Calabria region by using SPOT-Vegetation data. *Ecol. Model.* **2006**, *196*, 265–270. [CrossRef]
70. Smith, A.M.S.; Drake, N.A.; Wooster, M.J.; Hudak, A.T.; Holden, Z.A.; Gibbons, C.J. Production of Landsat ETM+ reference imagery of burned areas within Southern African savannahs: Comparison of methods and application to MODIS. *Int. J. Remote Sens.* **2007**, *28*, 2753–2775. [CrossRef]
71. Sader, S.A.; Stone, T.A.; Joyce, A.T. Remote sensing of tropical forests: An overview of research and applications using non-photographic sensors. *Photogramm. Eng. Remote Sens.* **1990**, *56*, 1343–1351.
72. Trigg, S.; Flasse, S. Characterizing the spectral-temporal response of burned savannah using in situ spectroradiometry and infrared thermometry. *Int. J. Remote Sens.* **2000**, *21*, 3161–3168. [CrossRef]
73. Chuvieco, E.; Mouillot, F.; van der Werf, G.R.; San Miguel, J.; Tanase, M.; Koutsias, N.; Garcia, M.; Yebra, M.; Padilla, M.; Gitas, I.; et al. Historical background and current developments for mapping burned area from satellite Earth observation. *Remote Sens. Environ.* **2019**, *225*, 45–64. [CrossRef]
74. Achanta, R.; Süsstrunk, S. Superpixels and polygons using simple non-iterative clustering. In Proceedings of the IEEE Conference on Computer Vision and Pattern Recognition (CPVR), Honolulu, HI, USA, 21–26 July 2017.
75. Yang, L.; Wang, L.; Abubakar, G.A.; Huang, J. High-resolution rice mapping based on snic segmentation and multi-source remote sensing images. *Remote Sens.* **2021**, *13*, 1148. [CrossRef]
76. Justice, C.; Belward, A.; Morisette, J.; Lewis, P.; Privette, J.; Baret, F. Developments in the "validation" of satellite sensor products for the study of the land surface. *Int. J. Remote Sens.* **2000**, *21*, 3383–3390. [CrossRef]
77. Padilla, M.; Stehman, S.V.; Chuvieco, E. Validation of the 2008 MODIS-MCD45 global burned area product using stratified random sampling. *Remote Sens. Environ.* **2014**, *144*, 187–196. [CrossRef]
78. Vanderhoof, M.K.; Fairaux, N.; Beal, Y.-J.G.J.G.; Hawbaker, T.J. Validation of the USGS Landsat Burned Area Essential Climate Variable (BAECV) across the conterminous United States. *Remote Sens. Environ.* **2017**, *198*, 393–406. [CrossRef]
79. CEOS. Land Product Validation Subgroup. Available online: https://lpvs.gsfc.nasa.gov/index.html (accessed on 15 July 2021).
80. Boschetti, L.; Stehman, S.V.; Roy, D.P. A stratified random sampling design in space and time for regional to global scale burned area product validation. *Remote Sens. Environ.* **2016**, *186*, 465–478. [CrossRef] [PubMed]
81. Padilla, M.; Olofsson, P.; Stehman, S.V.; Tansey, K.; Chuvieco, E. Stratification and sample allocation for reference burned area data. *Remote Sens. Environ.* **2017**, *203*, 240–255. [CrossRef]
82. Boschetti, L.; Roy, D.P.; Justice, C.O. *International Global Burned Area Satellite Product Validation Protocol Part I-Production and Standardization of Validation Reference Data (to Be Followed by Part II-Accuracy Reporting)*; Committee on Earth Observation Satellites: Silver Spring, MD, USA, 2009.

83. Franquesa, M.; Vanderhoof, M.K.; Stavrakoudis, D.; Gitas, I.Z.; Roteta, E.; Padilla, M.; Chuvieco, E. Development of a standard database of reference sites for validating global burned area products. *Earth Syst. Sci. Data* **2020**, *12*, 3229–3246. [CrossRef]

84. Padilla, M.; Wheeler, J.; Tansey, K. *ESA Climate Change Initiative-Fire_cci D4.1.1 Product Validation Report (PVR)*; Universidad de Alcala: Madrid, Spain, 2018.

85. Olson, D.M.; Dinerstein, E.; Wikramanayake, E.D.; Burgess, N.D.; Powell, G.V.N.; Underwood, E.C.; D'amico, J.A.; Itoua, I.; Strand, H.E.; Morrison, J.C.; et al. Terrestrial Ecoregions of the World: A New Map of Life on Earth. *Bioscience* **2001**, *51*, 933. [CrossRef]

86. Schroeder, W.; Oliva, P.; Giglio, L.; Csiszar, I.A. The New VIIRS 375m active fire detection data product: Algorithm description and initial assessment. *Remote Sens. Environ.* **2014**, *143*, 85–96. [CrossRef]

87. Oliva, P.; Schroeder, W. Assessment of VIIRS 375m active fire detection product for direct burned area mapping. *Remote Sens. Environ.* **2015**, *160*, 144–155. [CrossRef]

88. Congalton, R.G.; Green, K. *Assessing the Accuracy of Remotely Sensed Data: Principles and Practives*; CRC Press: Boca Raton, FL, USA, 2008; ISBN 9780429143977.

89. Stehman, S.V.; Foody, G.M. Key issues in rigorous accuracy assessment of land cover products. *Remote Sens. Environ.* **2019**, *231*, 111199. [CrossRef]

90. Dice, L.R. Measures of the Amount of Ecologic Association Between Species. *Ecology* **1945**, *26*, 297–302. [CrossRef]

91. Fleiss, J.L. *Statistical Methods for Rates and Proportions*; Wiley: Hoboken, NJ, USA, 1981; ISBN 0471064289.

92. Boschetti, L.; Roy, D.P.; Justice, C.O.; Giglio, L. Global assessment of the temporal reporting accuracy and precision of the MODIS burned area product. *Int. J. Wildl. Fire* **2010**, *19*, 705–709. [CrossRef]

93. FIRMS. Fire Information for Resource Management System. Available online: https://developers.google.com/earth-engine/datasets/catalog/FIRMS#description (accessed on 21 June 2021).

94. MCD14ML | Earthdata. Available online: https://earthdata.nasa.gov/earth-observation-data/near-real-time/firms/mcd14ml (accessed on 21 June 2021).

95. Giglio, L.; Descloitres, J.; Justice, C.O.; Kaufman, Y.J. An enhanced contextual fire detection algorithm for MODIS. *Remote Sens. Environ.* **2003**, *87*, 273–282. [CrossRef]

96. Giglio, L.; Schroeder, W.; Justice, C.O. The collection 6 MODIS active fire detection algorithm and fire products. *Remote Sens. Environ.* **2016**, *178*, 31–41. [CrossRef]

97. Hantson, S.; Padilla, M.; Corti, D.; Chuvieco, E. Strengths and weaknesses of MODIS hotspots to characterize global fire occurrence. *Remote Sens. Environ.* **2013**, *131*, 152–159. [CrossRef]

98. Ju, J.; Roy, D.P. The availability of cloud-free Landsat ETM+ data over the conterminous United States and globally. *Remote Sens. Environ.* **2008**, *112*, 1196–1211. [CrossRef]

99. Cuevas-González, M.; Gerard, F.; Balzter, H.; Riaño, D. Analysing forest recovery after wildfire disturbance in boreal Siberia using remotely sensed vegetation indices. *Glob. Chang. Biol.* **2009**, *15*, 561–577. [CrossRef]

100. Chu, T.; Guo, X.; Takeda, K. Remote sensing approach to detect post-fire vegetation regrowth in Siberian boreal larch forest. *Ecol. Indic.* **2016**, *62*, 32–46. [CrossRef]

V eranskina: AG1 – algoritmoen arteko konparaketa

Artikulua

Izenburua: Burned area detection and mapping: intercomparison of Sentinel-1 and Sentinel-2 based algorithms over Tropical Africa

Egileak: Mihai Tanase, Miguel Ángel Belenguer-Plomer, Ekhi Roteta, Aitor Bastarrika, James Wheeler, Ángel Fernández-Carrillo, Kevin Tansey, Werner Wiedemann, Peter Navratil, Sandra Lohberger, Florian Siegert eta Emilio Chuvieco

Argitaratze-data: 2020ko urtarrila

DOI: https://doi.org/10.3390/rs12020334

Erreferentzia bibliografikoa:

Tanase, M.A., Belenguer-Plomer, M.A., Roteta, E., Bastarrika, A., Wheeler, J., Fernández-Carrillo, Á., Tansey, K., Wiedemann, W., Navratil, P., Lohberger, S., Siegert, F., Chuvieco, E., 2020. Burned Area Detection and Mapping: Intercomparison of Sentinel-1 and Sentinel-2 Based Algorithms over Tropical Africa. *Remote Sens.* 12, 334. https://doi.org/10.3390/rs12020334

Aldizkaria

Izena: Remote Sensing

Sortze-urtea: 2009

Argitaratze-urteko inpaktu-faktorea: 4,848

Argitaratze-urteko posizioa *REMOTE SENSING* arloan:

  Postua: 10/32

  Pertzentila: %70

  Kuartila: Q2

VI eranskina: AG2 – erreferentzia-datuen datu-basea

Artikulua

Izenburua: Development of a standard database of reference sites for validating global burned area products

Egileak: Magí Franquesa, Melanie Vanderhoof, Dimitris Stavrakoudis, Ioannis Gitas, Ekhi Roteta, Marc Padilla eta Emilio Chuvieco

Argitaratze-data: diciembre de 2020

DOI: https://doi.org/10.5194/essd-12-3229-2020

Erreferentzia bibliografikoa:

Franquesa, M., Vanderhoof, M., Stavrakoudis, D., Gitas, I., Roteta, E., Padilla, M., Chuvieco, E., 2020. Development of a standard database of reference sites for validating global burned area products. *Earth Syst. Sci. Data*, 12, 3229-3246. https://doi.org/10.5194/essd-12-3229-2020

Aldizkaria

Izena: Earth System Science Data

Sortze-urtea: 2007

Argitaratze-urteko inpaktu-faktorea: 11,333

Argitaratze-urteko posizioa *GEOSCIENCES, MULTIDISCIPLINARY* arloan (ez dago *REMOTE SENSING* arloan):

> **Postua**: 4/200

> **Pertzentila**: %98

> **Kuartila**: Q1

VII eranskina: AG3 – sute txikien emisioak

Artikulua

Izenburua: African burned area and fire carbon emissions are strongly impacted by small fires undetected by coarse resolution satellite data

Egileak: Rubén Ramo, Ekhi Roteta, Ioannis Bistinas, Dave van Wees, Aitor Bastarrika, Emilio Chuvieco eta Guido van der Werf

Argitaratze-data: febrero de 2021

DOI: https://doi.org/10.1073/pnas.2011160118

Erreferentzia bibliografikoa:

Ramo, R., Roteta, E., Bistinas, I., van Wees, D., Bastarrika, A., Chuvieco, E., van der Werf, G., 2021. African burned area and fire carbon emissions are strongly impacted by small fires undetected by coarse resolution satellite data. *Proc. Natl. Acad. Sci. USA* 118, e2011160118. https://doi.org/10.1073/pnas.2011160118

Aldizkaria

Izena: Proceedings of the National Academy of Sciences of the United States of America

Sortze-urtea: 1915

Argitaratze-urteko inpaktu-faktorea: 12,779

Argitaratze-urteko posizioa *MULTIDISCIPLINARY SCIENCES* arloan (ez dago *REMOTE SENSING* arloan):

> **Postua**: 9/73

> **Pertzentila**: %88

> **Kuartila**: Q1

VIII eranskina: AG4 – Afrikako EAen bigarren produktua

Artikulua

Izenburua: Building a small fire database for Sub-Saharan Africa from Sentinel-2 high-resolution images

Egileak: Emilio Chuvieco, Ekhi Roteta, Matteo Sali, Daniela Stroppiana, Martin Boettcher, Grit Kirches, Thomas Storm, Amin Khairoum, M. Lucrecia Pettinari, Magí Franquesa eta Clément Albergel

Argitaratze-data: julio de 2022

DOI: https://doi.org/10.1016/j.scitotenv.2022.157139

Erreferentzia bibliografikoa:

> Chuvieco, E., Roteta, E., Sali, M., Stroppiana, D., Boettcher, M., Kirches, G., Storm, T., Khairoum, A., Pettinari, M.L., Franquesa, M., Albergel, C., 2022. Building a small fire database for Sub-Saharan Africa from Sentinel-2 high-resolution images. *Sci. Total Environ.* 845, 157139. https://doi.org/10.1016/j.scitotenv.2022.157139

Aldizkaria

Izena: Science of the Total Environment

Sortze-urtea: 1972

Argitaratze-urteko inpaktu-faktorea: 10,753 (2021)

Argitaratze-urteko posizioa *ENVIRONMENTAL SCIENCES* arloan (ez dago *REMOTE SENSING* arloan):

> **Postua:** 26/279 (2021)
>
> **Pertzentila:** %91 (2021)
>
> **Kuartila:** Q1 (2021)